Early Lunar Geology and Geophysics

by

Ian Garrick-Bethell

B.A., Physics, Wesleyan University (2002)
S.M., Aeronautics and Astronautics, Massachusetts Institute of technology (2004)

Submitted to the Department of Earth, Atmospheric and Planetary Sciences
in partial fulfillment of the requirements for the degree of

Doctor of Philosophy in Planetary Science

at the

MASSACHUSETTS INSTITUTE OF TECHNOLOGY

February 2009

Author.....
Ian Garrick-Bethell
Department of Earth, Atmospheric and Planetary Sciences
February 5, 2009

Certified by.....
Maria. T. Zuber
Department Head
E.A. Griswold Professor of Geophysics
Thesis Supervisor

Certified by.....
Daniel H. Rothman
Chair of the Graduate Committee
Department of Earth, Atmospheric and Planetary Sciences
Massachusetts Institute of Technology

Early Lunar Geology and Geophysics

By

Ian Garrick-Bethell

Submitted to the Department of Earth, Atmospheric and Planetary Sciences on February 5, 2009, in partial fulfillment of the requirements for the degree of Doctor of Philosophy in Planetary Science.

Abstract

Despite a number of human and robotic missions to the Moon, there are still important unanswered questions about its early evolution, and how it came to be the object we observe today. Here we use observational, experimental, and theoretical techniques to examine three important events that took place early in lunar history and have left a lasting signature. The first event is the formation of the largest basin on the Moon, the South Pole-Aitken Basin. We develop a systematic method to define the previously unknown boundaries of this degraded structure and quantify its gross shape. We also combine a number of remote sensing data sets to constrain the origin of heat producing elements in its interior. The second event we examine is the evolution of the lunar orbit, and the coupling between the Moon's early geophysical properties and the growth of orbital eccentricity. We use analytical models for tidal deformations and orbit evolution to show that the shape of the Moon suggests its early orbit was highly eccentric. However, we are also able to explain the presently high eccentricity entirely by traditional, secular tidal growth while the early Moon was hot. The third event we examine is the magnetization of lunar samples. We perform extensive paleomagnetic measurements of an ancient, deep-seated lunar sample, and determine that a long-lived magnetic field like that of a core dynamo is the most plausible explanation for its magnetic remanence. In sum, the earliest portion of lunar history has been largely obscured by later geologic events, but a great deal can still be learned from this formative epoch.

Thesis Advisor: Maria T. Zuber, Ph.D.
Title: E.A. Griswold Professor of Geophysics.

Acknowledgements

I thank my parents, who have always been very supportive of my work. I owe you a lot.

I thank Maria Zuber, who has shown incredible patience, support, and open mindedness as my advisor.

I thank Ben Weiss, who has been a great partner in our quest to unravel the story behind lunar magnetism.

I thank Jack Wisdom for many interesting discussions about tides and orbit evolution.

There are many friends and colleagues that deserve thanks as well. I would not have been able to get half as far as I did without you all.

Table of Contents

Chapter 1

Introduction

The geology, geophysics, and geochemistry of the Moon we see today have remained largely unchanged for the last 3 billion years. Free of plate tectonics, an atmosphere, and weather, the Moon has managed to preserve its greatest geologic structures with only a relatively thin veneer of dust. The Moon has been called Earth's attic [1], as it stores records of events that have taken place in the inner solar system long ago, and for which there is no longer any evidence on the Earth. For this reason, the Moon is a very useful tool for studying solar system history. However, even on the Moon there is a much earlier epoch for which we have comparably little information. This is because about 3.9 billion years ago the Moon suffered a number of major basin forming events that resurfaced the crust. Shortly thereafter, mare volcanism began to cover much of the nearside for the next ~1 billion years. These two events and other factors have made it difficult to study the earliest periods in lunar history. Knowledge of the geophysics and geology Moon at earlier times would provide information about the large-scale processes that controlled the evolution towards the Moon we see now. This thesis concerns the evolution of basins, lithosphere, core, and orbital parameters before 3.9 billion years ago.

For millennia, lunar geology was restricted to interpreting the Moon's dark, semicircular features with the naked eye. The very earliest telescopic observations of the Moon were made by Galileo in 1610, who was able to infer the existence of mountains from the shadows he observed. Eventually Hartmann and Kuiper [2] would use telescopic observations to map the Moon's largest circular structures and coin the term "basin" for these impact craters. Hartmann and Kuiper also observed several mountains on the nearside of the south pole, and inferred the existence of a large impact basin on the farside. These suspicions were confirmed when spacecraft visited the farside and imaged

an ancient basin now known as the South Pole-Aitken basin. Wilhelms [3] and Stuart-Alexander [4] attempted to map this structure and identified it as the Moon's oldest basin. Eventually, with global remote sensing data, the basin is now considered to form one of the Moon's three major geologic Terranes [5]. However, its exact shape has still not been adequately described. In Chapter 2 the structure and shape of the basin is defined in a consolidated and quantitative manner. This improved definition will enable a better understanding of large basin formation, the geology and geophysics of the region, and the effect of the basin on the Moon's orientation. One example of where the new basin definition might helpful is in explaining the high abundance of radioactive elements in the basin's northwestern quadrant. In Chapter 3, an interdisciplinary approach is used to address the origin of this anomaly, including the findings developed in Chapter 2. We establish that the anomaly is likely to be indigenous to the basin, and therefore it provides further insight into the formation of the basin, and its role in revealing the Moon's global budget of heat producing elements.

If we look back into lunar history even earlier than the South Pole-Aitken basin, we confront the formation of the lunar crust and lithosphere. The timing of crustal development reveals information about the early thermal state of the Moon, as does the timing for development of lithospheric strength. One way of assessing lithospheric strength is to consider the variations in the shape of the Moon and its gravity field, which are due to lithostatically supported masses. The clearest example of lithospheric strength is the nearside mascons, which are positive gravity anomalies that are likely due to a combination of supported mare fill and uplifted mantle material. Since the age of these structures are known, the age at which lithospheric support was possible, and thereby the cooling timescales of the Moon's outer layers, can be inferred. Another example is the strong degree-2 gravity signature of the Moon. The degree-2 gravity field on Earth and Mars is substantial because of their rapid rotation rates and the resultant oblate deformation. In contrast, the Moon rotates slowly now, but it rotated much faster in the past, which led Sedgewick [6] to suggest that the Moon may have locked-in a past oblate deformation as it cooled from a hotter, more deformable state. This would make the present degree-2 field a "fossil shape" that could be used to infer both the cooling and

orbital history of the Moon. In Chapter 4 we revisit this concept to explore nontraditional explanations for the fossil shape. We find that a past, highly eccentric orbit would produce precisely the right type of deformations that the Moon seems to have frozen in long ago. However, in Chapter 5 we take a different approach, and demonstrate that the early thermal history of the Moon can lead to tidal properties that generate the Moon's presently large eccentricity (compared to other satellites). In Chapter 6 we explore how the mascons and the South Pole-Aitken basin contribute to the degree-2 shape of the Moon. We find that the mascons and the South Pole-Aitken basin are not the sole cause of the degree-2 power, and therefore the fossil bulge hypothesis remains viable.

After considering the outer sections of the Moon, it becomes interesting to ask what is at the Moon's center. Growing evidence suggests the Moon has a small ~350 km iron core, but the seismic data that so unequivocally demonstrate a core on Earth are lacking for the Moon. Early proponents of a "cold-Moon" had argued that the Moon had never melted or differentiated, which would have made core formation very unlikely. However, this concept started to unravel as soon as in situ chemical analyses from the Surveyor V lander suggested Mare Tranquillitatis was composed of basalt. Eventually, the "hot-Moon" hypothesis became more attractive with the understanding of mare volcanism and the magma ocean hypothesis. The Moon had differentiated and a core was at least plausible. When it was discovered that lunar samples carry magnetic remanence, support for a lunar core and a core dynamo began to grow [7]. Unfortunately, a remarkably prescient suggestion in 1970 would prove to be a major difficulty in lunar magnetism for nearly 40 years. In their study of magnetized Apollo 11 basalts, Doell et al. [8] suggested that transient magnetic fields generated by impact-produced plasmas could magnetize rocks while the impactor's shock wave passes through them, even though the concept of shock magnetism did not yet exist. To avoid this issue entirely, and help determine if the Moon has a core, we perform a paleomagnetic study of the oldest unshocked lunar rock in Chapter 8. We find that the magnetic remanence in the rock is most consistent with being produced by a long-lived field like that of a core dynamo. In Chapter 7 we present calculations on the stability of lunar rock magnetism, which have previously been

available for Earth materials for 30 years. These calculations will be a useful tool to help assess how thermal events affect magnetism in metal-bearing samples.

In the next decade a number of lunar missions are planned. When new data and samples are analyzed from these missions, it is certain that new puzzles will emerge that require an understanding of the Moon's most ancient history.

References

1. Chapman, C.R., *Planetary science: Earth's lunar attic.* Nature, 2002. **419**(6909): p. 791-794.
2. Hartmann, W.K. and G.P. Kuiper, *Concentric structures surrounding lunar basins.* Communications of the Lunar and Planetary Laboratory, 1962. **1**: p. 55-66.
3. Wilhelms, D.E., *The geologic history of the Moon.* USGS Professional Paper 1348. 1987: U.S. Geological Survey. 327.
4. Stuart-Alexander, D.E., *Geologic map of the central far side of the Moon.* U.S. Geol. Surv. Map, I-1047, 1978.
5. Jolliff, B.L., et al., *Major lunar crustal terranes: Surface expressions and crustmantle origins.* J Geophys Res, 2000. **105**: p. 4197-4216.
6. Sedgewick, W.F., Mess. Math., 1898. **27**: p. 171.
7. Runcorn, S.K., et al., *Magnetic properties of lunar samples.* Science, 1970. **167**: p. 697-699.
8. Doell, R.R., et al., *Magnetic studies of lunar samples.* Science, 1970. **167**: p. 695-697.

Chapter 2

Elliptical Structure of the Lunar South Pole-Aitken Basin

In revision for Icarus, Ian Garrick-Bethell and Maria T. Zuber.

Abstract

The South Pole-Aitken basin (SP-A) is the largest and oldest basin on the Moon. The basin has usually been interpreted to exhibit a degraded circular structure, but here we demonstrate that the topography, iron and thorium signatures of the basin are well described by ellipses with axes measuring 2400 by 2050 km and centered at -53°, 191°E. Topography, abundances of iron, thorium, and the distribution of mare basalts are all elevated in the northern halves of the ellipses. We also identify an outer topographic ellipse whose semiminor axis scales with the main topographic ellipse by approximately $\sqrt{2}$. Taken together, these data imply that the basin was created by an oblique impact along an azimuth of approximately 19°, measured counterclockwise from longitude 191°E. The geometry of the elevated central farside topography surrounding SP-A suggests that it predates the impact. The elliptical ring structures of SP-A and their scaling relationships will help to understand the formation of large and elliptical basins elsewhere in the solar system. This refined basin shape will also inform local geology, geochemistry, and geophysics of the region.

2.1 Introduction

Located on the lunar southern farside between the crater Aitken and the south pole, the South Pole-Aitken basin (SP-A) is the largest verified basin on the Moon. The structure is large enough to be classified as one of the three major lunar terranes (Jolliff et al., 2000), and its highly-degraded appearance and abundance of superimposed craters suggests that it may predate all other lunar basins (Wilhelms, 1987). The impactor likely excavated lower crustal materials, and possibly even the upper mantle (Pieters et al., 2001). Samples returned from the basin would provide an opportunity to not only date the oldest preserved cataclysmic event on the Moon, but also to understand the mineralogy of the lunar crust. Because of its large size, SP-A is also important in understanding the formation of massive basins in general (Andrews-Hanna et al., 2008; Marinova et al., 2008).

Despite the importance of the basin, its gross shape and structure are not well understood, with most previous analyses assuming circularity (Hiesinger and Head, 2004; Petro and Pieters, 2004; Pieters et al., 2001; Pieters et al., 1997; Spudis et al., 2008; Spudis et al., 1994; Stuart-Alexander, 1978; Wilhelms, 1987; Wilhelms et al., 1979; Wood and Gifford, 1980; Yingst and Head, 1997). Schultz (1997) suggested an oblique impact based on the basin's relatively shallow depression, but did not address the shape of the depression (Schultz, 1997). Shevchenko et al. (2007) mapped generally oval-like structures in SP-A based on its topography and also proposed an oblique impact. Extending our preliminary work (Garrick-Bethell, 2004), we quantify the shapes of

boundaries of the topography, iron and thorium content of the region. We show that even under loose data selection criteria the distributions of these three quantities trace elliptical shapes that are oriented along the same azimuth, have nearby centers, similar eccentricities, and centers that lie along their common azimuth. This high coincidence of fit parameters from the three datasets suggests that ellipses represent a good fit to the data, and demonstrate that SP-A is an elliptical structure that formed from an oblique impact. We also expand the best-fit topographic ellipse outward to identify an additional elliptical-shaped topographic contour, concentric to the original fit, whose semiminor axis follows approximately $\sqrt{2}$-proportional spacing. This ellipse passes near massifs originally used to map the outer extent of the basin (Stuart-Alexander, 1978; Wilhelms, 1987; Wilhelms et al., 1979), and provides a better fit than the circular rings used in these earlier studies. Characterization of the elliptical shape of the South Pole-Aitken basin provides a context for understanding the basin's effect on regional geology, mineralogy, geochemistry, gravity, state of compensation, and the effect of the basin on the Moon's orientation.

2.2. Data

Topography data are from a spherical harmonic expansion of Clementine laser altimeter data, mapped at 0.25 pixel per degree resolution (Smith et al., 1997; Zuber et al., 1994). These data are truncated polewards of 70° latitude, leading us to also use global topography data from the Unified Lunar Control Network (ULCN2005) (Archinal et al., 2006). We use thorium and iron data from the Lunar Prospector gamma-ray

spectrometer, mapped at 0.5 pixel per degree resolution (Lawrence et al., 2003; Lawrence et al., 2002). We chose to use iron and thorium data because these data have the highest resolution and fidelity compared to data for other elements. Iron and thorium are also useful for estimating the depth of excavation of the impact, since iron is indicative of deeper crustal and upper mantle mineralogy, while thorium is a proxy for KREEP-rich material (potassium, rare earth elements, and phosphorous) that is believed to have crystallized between the lower crust and mantle.

An important test of the significance of our derived ellipses is their correlation with observable geologic features in SP-A. Our ellipses are derived from very large-scale patterns of relatively low-resolution data, and if they are representative of the formation mechanism and structure of SP-A, we would expect a correlation with smaller features that are characteristic of major lunar basins, such as arcuate mountains or ring-like structures. Traditionally, basin rings on the Moon have been identified using high phase-angle photographs (Hartmann and Kuiper, 1962; Head, 1974; Spudis, 1993; Wilhelms, 1987; Wilhelms et al., 1979), where shadows are exaggerated and morphology is readily apparent. Therefore, to test our predictions and compare them with the results of past efforts to map SP-A's rings, we examine two regions in SP-A where high phase-angle images are available. The first is an image from the Apollo 8 Hasselblad camera, taken of the northeastern rim of the basin, and the second is a mosaic of high latitude Clementine 750 nm reflectance images at the south pole (produced by the USGS). The two regions imaged are located on almost opposite sides of the basin.

Two additional useful data sets can be used to further constrain the utility of our ellipses. The first is the global Clementine 750 nm spectral reflectance mosaic, in which

the SP-A basin appears as a dark mafic anomaly (Belton et al., 1992). We will test if the anomalously low-albedo region is enclosed by the ellipses. We also apply a spectral band ratio scheme to Clementine UVVIS data to highlight soil maturity and mineralogical differences. The scheme was used by Pieters et al. (1994), and assigns red = 750/415 nm, green = 750/950 nm, and blue = 415/750 nm. This color scheme highlights many of the spectral features present in the lunar surface. In particular, high iron content is indicated by strong absorption near 1-μm (herein the 950 nm band), or stronger green and yellow tones. Soil maturity and composition are reflected by the steepness of the visible continuum slope, which is quantified by the 750 and 415 nm ratios (red to blue variations). The SP-A region has a distinctively orange and green (iron-rich and mafic) character that we can test for a correlation with the topographic ellipses. In addition to testing the validity the ellipses, both of these data sets are also essential for visualizing how the basin's ellipses correlate with other geologic features such as Mare Ingenii, Mare Australe, the Apollo basin, the Schrödinger basin, Jules Verne Crater, and the lunar south pole. We note that all of the Clementine spectral data are subject to high phase angle artifacts polewards of about 70^{o} latitude (which makes them useful for morphology, above). However, we included high latitude data in our figures so that features polewards of 70^{o} are identifiable, albeit not well represented.

2.3. Method and results

2.3.1 *Defining distributions of topography, iron, and thorium*

When topography, iron, and thorium data are plane-projected from a center of -56° and 180°E (the often-assumed SP-A basin center), it is clear that the quantities are distributed in elliptically-shaped patterns. Unlike a circular crater on a spherical Moon, whose perimeter defines a small circle that can be defined in a plane, the perimeter of an elliptical crater on a sphere is a three-dimensional curve. However, we can fit an ellipse, which is a much simpler shape, to the plane-projected shape to quantify several of the most intrinsic properties of the crater, including its boundaries, center, semimajor axis, a, and semiminor axis, b, and orientation. Because an ellipse is a planar feature that has a formally defined center, the natural choice for projection is an azimuthal projection centered on the ellipse center. Specifically, the stereographic projection is well suited for this task because it is the only commonly used conformal (angle or shape preserving) azimuthal projection[1], and does not distort small circles centered around the pole of the projection (scale is constant along the circle perimeter). Therefore, the stereographic projection assures that deviations from circularity are readily apparent and easily comparable to purely circular features.

To determine the best-fit ellipse for topography, iron and thorium, we selected data points at the perimeters of their distributions and performed a least-squares fit to the stereographic plane-projected data, while permitting a tilt angle (defined as a rotation within the page about the center of the ellipse). The fitting process was performed for 20 different sets of carefully selected data points and the parameters from each fit were then averaged. The center of the ellipse was determined, and the plane-projected ellipse was then recalculated using the new center, to avoid any minimal distortions due to an off-

[1] The Lambert conformal conic projection is another option, but would require the choice of two standard parallels. A natural choice may be to make one single standard parallel a pole at the center of the ellipse, but this projection then becomes a stereographic azumithal projection.

center projection. The true lunar coordinates of the ellipse edges were then determined and a and b were calculated as great circle arc lengths from the ellipse center to the edges, in both kilometers and degrees (Table 2.1). We also calculate the ratio a/b to quantify the crater's ellipticity. The final ellipse tilt angle reported is the azimuth of a great circle arc from the ellipse center to the northern end of the semimajor axis, defined relative to a meridian passing through the ellipse center (positive clockwise).

The most obvious uncertainty in this study is how to objectively select the data points that are used to the fit contours. We consider each dataset separately, since there are unique issues associated with each.

To define the primary topographic shape of the basin we used the Clementine laser altimeter data instead of ULCN2005 because ULCN2005 showed some ~1 km differences with the Clementine laser range values at several locations on the basin perimeter. Also, investigations showed that it made almost no difference which of these data sets is used (below). Later we compare our results with the ULCN2005 data and take advantage of its higher resolution to examine some small-scale geologic features, where relative elevations are of interest and absolute differences in topography are less important. We used 50 data points to establish the topography fit.

In the northern parts of the basin, the elliptical pattern of the topography is most clearly manifested around a –2000 m contour, Fig. 2.1A. Following the –2000 m contour counterclockwise from the northernmost part of the basin, we find that it is interrupted by a north-south directed feature (A), which we avoided. The contour is interrupted again by Mare Ingenii (B), but continues again by about 37° S. We used the contour from (–26°, 197°E) to (-48°, 160°E) in data selection, but did not use any portion within Mare

Ingenii, even though examination of the topography data in the ULCN2005 model show that a similar contour continues across Mare Ingenii, albeit at lower elevation. We then followed the –2000 m contour further southward, not including a depression that extends westward (C) or the crater Planck (D). We eliminated from consideration all data poleward of –70°, and picked up the –2000 m contour again in the east. At approximately (-60°, 240°E), there is an eastern-extending region of low topography (E) that could not be ruled out as part of any putative ellipse. We therefore selected points in this region but excluded data in the vicinity of the Apollo basin. A typical set of data points is shown in Fig. 2.1A, along with the mean best-fit ellipse and lines about its semiminor axis to illustrate the tilt angle. The best-fit ellipse parameters are listed in Table 2.1. While this ellipse fits most of the data, it is clear that it does not pass through region E, suggesting region E is not a part of the main ellipse. To indicate the uncertainty in the fit, we note that the standard deviation after averaging the 20 similar elliptical fits was about 1 degree for the basin center and 2 degrees for the tilt angle. Similar standard deviations were found to be true for the iron and thorium ellipses. Performing the same analysis with the ULCN2005 with 65 data points (compared with 50 for Clementine to allow for increased area coverage near the pole) produces a very similar mean ellipse center, (-53.2°, 191.8° E), a slightly greater tilt angle of 21.2°, and shorter semi axes, a = 960 km, b = 670 km. The similarity of the values speaks to the robustness of the technique even when limited portions of SP-A's topography contour are used. Second order corrections to our results can always be performed when superior topographic data become available.

The iron data are the most free of features that would complicate the choice of data points around the putative elliptical contour, Fig. 2.1B. The general approach was to follow the 7.5-8.0 % iron contour with 65 approximately equally-spaced data points. This contour level separates the "inner" and "outer" portions of the SP-A Terrane defined by (Jolliff et al., 2000) and is visibly the most obvious contour. Notably, the northern part of the basin shows the sharpest and most well-defined contour. In the northwest there is a small region of high iron that extends westward (A), which was avoided. On the east side of the basin the iron extends slightly eastward out from the Apollo basin (B), but the contour was still followed. The final mean best-fit iron ellipse is shown in Fig. 2.1B, as well as a typical set of 65 data points. The ellipse passes close to nearly all points, suggesting that the feature is well described by an elliptical shape.

For thorium, the general approach was to follow the 1.25-ppm contour with 50 approximately equally spaced points. Because the area of the enhanced thorium in SP-A is smaller than the area for iron, fewer data points were used. In the northwest the same region that was elevated in iron is elevated in thorium and was avoided, Fig. 2.1C (label A). Based on a correlation with basin topography and spectral similarity to other parts of the basin, the high-thorium anomaly in the northwest is likely indigenous to the basin and therefore likely a part of the putative thorium ellipse (Garrick-Bethell and Zuber, 2005; Haskin et al., 2004), but other possibilities include ejecta from Serenitatis (Wieczorek and Zuber, 2001). At any rate, we made no special effort to avoid it. In the east, the Apollo basin seems to have greatly affected the SP-A thorium distribution, as indicated by the c-shaped low-thorium feature (B), possibly because of its internal mare basalt flows. This region was not included in the data selection. Similar to the iron data, the

contour is again sharpest and most well defined in the northern part of the basin. The average best-fit ellipse and a typical set of selected data points are shown in Fig. 2.1C. Again, the data points selected are close to the best-fit ellipse.

We found that using other (non-conformal) azimuthal projections, such as orthographic, gnomonic, Lambert equal area, or Breusing harmonic mean, produced tilt angles that differed by ± 0.3 degrees, and semi axes that differed by ± 0.1% (in km) compared to the stereographic projection, when using the same plane-projected latitude-longitude points for topography, iron, and thorium. These differences are far lower than the uncertainty from choosing data points.

2.3.2 *Testing the technique*

The three best-fit ellipses and their parameters are consistently reproduced using as few as 15 data points, even if selected without care. However, to further test our methodology we fit ellipses around the Orientale basin using Lunar Prospector iron and Clementine topography data (not shown). We found a basin center of (-19.2°, 265.5°E) from topography and (-19.3°, 265.7°E) from iron, which compare quite favorably with the USGS value of (-19.4°, 267.2° W) for the center of the mare (http://planetarynames.wr.usgs.gov) and (-19°, 265°E) for the basin center (Spudis, 1993).

2.3.3 *Orientations, eccentricities, and great circle azimuths*

From Figure 2.1 and Table 2.1 it is clear that the SP-A topography, thorium, and iron distributions are well-fit by ellipses that are oriented towards the west at angles of -18.8°, -17.0°, and -14.1°, respectively. In addition, the azimuth of a great circle drawn from the topographic ellipse center (-53.2°, 191°E) to either the thorium or iron center lies along the same approximate azimuth as the ellipse tilt angles. For example, the azimuth from the topographic center to the center of the thorium ellipse is –33°, measured counterclockwise from longitude 191.1°E (clockwise positive). The azimuth from the topographic center to the center of the iron ellipse is –44°. The center of the iron ellipse is quite close to the center of the topographic ellipse, making the azimuth angle sensitive to changes in iron ellipse center. However, the azimuth to the more northern thorium ellipse center is less sensitive to small changes in location, and is a more reliable number. The thorium and iron ellipse centers are plotted as black squares in Figure 2C and 2D in a topographic-ellipse centered coordinate system to illustrate their relationships to the topographic ellipse center.

The ratio a/b for all ellipses are fairly large, 1.27-1.46, with the thorium ellipse the most circular of the three, 1.27, and the iron ellipse the most elliptical, 1.46. Considering the uncertainty in selecting data points, the agreement of the ellipses in tilt angle and axial ratios is quite good, and unlikely to be a coincidence or artifact of our technique. By comparison, the best-fit ellipse for Orientale's topography produces ratios of a/b the range of 1.05-1.07. While we cannot not rule out a modest ellipticity for Orientale, these values are likely large compared to the value defined by the basin's

characteristic rings. This is because the complete outline of the basin is difficult to resolve in the Clementine data, as well as the ULCN2005 data, even though the rings are well defined in images. Indeed, using the Cordillera and Outer Rook rings defined in the airbrush map of (Rosiek and Aeschliman, 2001) provides axial ratios of 1.00-1.05. Therefore, SPA may be considered to significantly deviate from circularity at least compared to Orientale, the often-assumed prototypical multiring basin. However, when compared to at least two other very massive basins, SPA's axial ratios appears to be typical (1.33 for Hellas and 1.25 for Borealis, both on Mars (Andrews-Hanna et al., 2008)), suggesting that massive basins may in general be more elliptical.

2.3.4 *Multiring structures?*

Large basins on the Moon and other bodies often exhibit ring spacing which is commonly proportional to approximately $\sqrt{2}$ (Pike and Spudis, 1987). Does the SP-A basin exhibit multiring structures? The best-fit iron and thorium ellipses show no other obvious structure outside of their bounds. However, the topography displays an arcuate structure north and northeast of the basin in the highlands terrain (Fig. 2.1, F). We found an optimal fit to the northern topography using a larger ellipse with a semiminor axis 1.428 times as large as the best-fit topographic semiminor axis, a semimajor axis 1.238 times as large, an ellipse center 2.0° lower in latitude, and the same tilt angle of –18.8°. Interestingly, the scaling in semiminor axis is close to $\sqrt{2}$. The derived outer topographic ellipse is shown plotted over Clementine and ULCN2005 topography data in Fig. 2.2A and B, respectively (rotated and centered on the best-fit center). The new

ellipse not only matches a long arc of topography in the north and northeast (label F in Fig. 2.1A and label V in Fig 2.2B), but also passes through high topography near the south pole in the ULCN2005 map (Fig. 2.2, X), high topography near label W in Fig. 2.2, and two other isolated high elevations in the west (labels Y and Z in Figs. 2.2A and 2.2B, more speculative). The axial ratio for this outer ring is 1.17, smaller than for the best-fit topographic ellipse (1.35), and closer to the value for the much larger martian Borealis basin. For convenience we define the area between the best-fit ellipse and the outer ellipse as the Outer Terrace.

We note that Shevchenko et al. (2007) proposed that the deeper topography in the south is a separate ring structure, which cannot be ruled out. However, we found existing topography data to be of inadequate quality to test this hypothesis using our ellipse-fitting method.

2.3.5 *Topography correlation with terrain*

To test whether the topographic ellipses are related to identifiable geologic features and compare our results with the often-used basin outlines of Wilhelms (1979, 1987) and Stuart-Alexander (1978), we examine in more detail regions A and B in Figure 2.2B. For region A, we use an oblique south-looking view of northeastern SP-A that shows high mountains on the horizon at approximately -21°, from 198-202° E (~150 km in extent, originally mapped by Stuart-Alexander (1978) and Wilhelms (1987) using a similar image). Also shown are several features, transects, and the outermost topographic ellipses mapped onto a Clementine 750-nm reflectance image, overlaid with ULCN2005

topography. Notably, two sections of the outer ellipse coincide with east-west trending hummocks, highlighted by transects 1 and 2. Topography becomes significantly higher when moving north and perpendicular to these hummocks, especially across transect 1. These units are roughly linear and do not perfectly follow the outer ellipse, but each trends generally in the direction of the ellipse and intersects it. The first transect was mapped by Stuart-Alexander (1978) as the northernmost section of SP-A's outer ring.

The prominent mountain range highlighted by transect 3 is between the outer and best-fit topographic ellipses and is nearly concentric with them, but it is not directly associated with either of them. These mountains, which we refer to here as the "Wilsing Mountains" (for the Nectarian age 73-km-diameter crater at (–21.5°, 204.8° E), that encloses the smaller crater labeled D), are also visible in Clementine topography data in Fig. 2.2A (Label U), and partly in ULCN2005 (Fig. 2.3). They are almost certainly the result of SP-A basin formation, and the band ratio scheme of (Pieters et al., 1994) shows a distinct change in mineralogy to more iron-rich materials on the south side of the mountains when the region is viewed close-up (not shown). The Wilsing Mountains appear to stop at label F. Determining whether the Wilsing Mountains are part of a large distinct ring system between the best-fit and outer ellipses, or are local in extent, will require higher-accuracy topography and better high phase-angle images. Overall, however, we find that the correlation of topography with transects 1 and 2 support our choice for the outer ellipse in this region, in agreement with (Stuart-Alexander, 1978).

We next examine terrain in region B of Fig. 2.2B using a Clementine 750 nm mosaic produced by the USGS, draped with ULCN2005 topography data, Fig. 2.4. Most importantly, the high topography at label X in Fig. 2.2B is correlated with arcuate massifs

along the dashed line indicated by label P in Fig. 2.4. These massifs were previously believed to be associated with SP-A based on Earth-based telescopic and Clementine observations (sometimes referred to as the Leibnitz Mountains (Shoemaker et al., 1994)). Massifs that are part of the same arc, but that are not readily apparent in the topography data are labeled at Q. Some of these massifs were also discussed by (Shevchenko et al., 2007) in their efforts to define SP-A's rings, and they are clearly visible in radar backscatter images (Margot et al., 1999). The elevated topography in the region at label S also matches the outer ellipse, but there is no morphologically obvious feature there. The high topography and massifs at R may also be part of the outer ellipse, albeit discontinuous and slightly recessed from the main structure. Wilhelms (1979) also mapped an outer SP-A ring near the poles, shown as a dashed line (label T), but this ring misses the more prominent massifs at P, and is not concentric with them. The correlation of our ellipse with terrain using superior photographic and topographic data suggest that our mapping is more appropriate.

Wilhelms (1987) mapped other parts of SP-A's rings, shown as long dashed lines in Fig. 2.2A and B (labels T). In some cases the agreement with the best-fit and outer ellipse is good, particularly in the east. However, in the west and northwest there are several mapped locations that appear unrelated to either topographic ellipse (Fig. 2.2A). For our outer ellipse to extend westward and match the ring mapped by Wilhelms (1987) would require an almost perfectly circular outer ellipse and a westward shift of the basin center (Wilhelms used a center 11° west of our center). In that case, the outer ellipse would differ substantially from the centers and axial ratios of the best-fit topographic ellipse, the thorium ellipse, and the iron ellipse, and it would then no longer arc around

the polar topography at P in Fig. 2.4. These considerations favor our outer ellipse for defining the western limit of the basin.

In summary, the validity of the outer ellipse is supported by 1) its derivation from a smaller best-fit topographic ellipse that is correlated with similarly elliptical geochemical data (Section 3.7-8), 2) its passage through high topography around an arc of ~100° from the north to the east, and another arc near the south pole, and 3) its correlation with arcuate massifs at two locations on opposite sides of the basin. In all, the SP-A depression is about 2400 km long by 2050 km wide, approximately the same size as the main depression of the Hellas basin on Mars (~2300 km), and larger than the lunar radius by a factor of 1.4.

2.3.6 *General trends in topography*

A major trend in topography is that elevations are generally higher within the northern half of the best-fit topographic ellipse. This is most apparent when comparing the high elevations east of Mare Ingenii, west of Apollo, and south of label A in Fig. 2.1A, with low elevations south of the ellipse center. Another trend is that the topographic contours are generally sharper in the north than in the south. While the topographic contour around the outer ellipse in the northeast and east is almost unbroken, it is much less obvious or nonexistent in the west. Moving radially outward from the basin, the topography between the best-fit ellipse and the outer ellipse in the Outer Terrace is high and slightly upward sloping.

2.3.7 *Topography correlation with iron and thorium*

As shown in Figs. 2.2C and D, the best-fit topographic ellipses also border the main concentrations of thorium and iron in SP-A. Both iron and thorium are in higher abundances in the northern halves of the topography and elemental abundance ellipses. For thorium, the outer topographic ellipse tightly borders the lowest thorium abundances in the north, while in the south the middle best-fit ellipse does the same, consistent with the thorium's more northern center. The Outer Terrace has little thorium in the southern half, but thorium is significantly more abundant in the northern portions. The northwest thorium anomaly also curves around the best-fit ellipse.

For iron, the outer topographic ellipse also borders the lowest abundances of iron in the north and northeast. High abundances of iron (>8%) appear to spill over the best-fit topographic ellipse into the Outer Terrace in the north. Iron abundances are lower in the southern and southeastern parts of the Outer Terrace.

2.3.8 *Topography correlation with mineralogy*

In Figs. 2.4A and 4B we plot the topographic ellipses over Clementine 750-nm reflectance data (A) and the band ratios from Pieters et al. (1994) (B). Fig. 2.4A shows that the best-fit topographic ellipse bounds the low-albedo mafic anomaly characteristic of the basin (Belton et al., 1992; Pieters et al., 1997). Fig. 2.4B shows that the interior of the basin is generally orange with lighter shades of green and yellow, suggesting higher abundances of iron-rich mineralogies. The feldspathic highlands terrain north of SP-A is

generally red, purple, or blue, and represents more feldspar-rich units. The best-fit topographic ellipse tightly bounds the brightest regions of orange iron-rich material, while the outer ellipse separates much of the remaining orange iron-rich material from the blue-red highlands material. Similar to the gamma-ray derived iron observed in the northern outer terrace (Section 3.7, Fig. 2.2D), iron-rich units are seen extending north of the best-fit topographic ellipse, in some cases reaching just beyond the outer ellipse. In all, the agreement between the best-fit topographic ellipse and the mafic mineralogy of the basin is quite strong.

2.4. Interpretation and discussion

2.4.1 *Basin formation*

On the basis of detailed analysis of the distributions of topography, iron and thorium, we hypothesize that an oblique impact caused the ellipse-shaped features and north-south asymmetries of excavation of lower crustal materials. The obliquity of the impact resulted in two major excavation structures that are represented by topographic lows: the Outer Terrace, whose border approximately follows $\sqrt{2}$ ring scaling in the semiminor axis, and a more deeply excavated central region that contains nearly all of the geochemical and mineralogical anomalies characteristic of the basin.

The first part of the hypothesis, that the basin was formed by an oblique impact, is well supported by data that show low-angle impacts cause elliptical craters (Melosh, 1989). Laboratory experiments indicate that at low energies elliptical structure appears

only at low impact angles (~ 12° threshold from the horizontal for planetary surfaces (Bottke et al., 2000)). However, since the scale of the SP-A basin is so much larger than experimentally-produced elliptical craters and the diameter of the basin is larger than the planetary radius, it is uncertain if a constraint on the impactor angle with the surface normal can be inferred from existing experimental data.

Scaling of ring diameters by multiples of $\sqrt{2}$ is a statistically-valid feature of large circular impact basins on the Moon, and possibly on Mars and Mercury (Clow and Pike, 1982; Neumann et al., 1996; Pike and Spudis, 1987). A number of hypotheses have been advanced to explain the scaling of ring diameters in basins (Hodges and Wilhelms, 1978; McKinnon and Melosh, 1978; Pascal and Piette, 1999; Pike and Spudis, 1987; van Dorn, 1968), but unfortunately no work has been done to address how rings would scale in elliptical basins. However, three unique features of SP-A's ring structure are worth noting because they may provide some clues to its ring-forming mechanism, and the mechanism of ring formation in general. The first is that the scaling factor for SP-A's outer ellipse is different for the semiminor and semimajor axis (1.428 and 1.238, respectively, Table 2.1), which suggests a scaling rule that changes as a function of the azimuth from the basin center, and indirectly the impactor trajectory. The second is that there is strong correlation of the most clearly manifested outer ellipse sections with high topography in the northeast and east, suggesting that preexisting high topography may have a role in determining which areas develop rings. The third is that the Outer Terrace generally has a less mafic character than the interior of the basin (Section 3.8), and may therefore represent upper crustal materials which may have slumped inwards, as advanced by the model of (Head, 1974). High-resolution multispectral data, terrain

mapping images, and superior gravity measurements of the Outer Terrace may help resolve the exact mechanism for its formation.

2.4.2 *Asymmetrical excavation and direction of impact*

Several observations suggest that depth of excavation was asymmetrical along the direction of impact: 1) higher iron and thorium abundances in the north, 2) thorium and iron ellipses displaced north of the topographic ellipse, 3) a smaller and more circular thorium ellipse. In the Moon both iron and thorium are expected to increase in concentration with depth, and there is support for this in remote sensing observations (Lawrence et al., 1999; Metzger et al., 1977; Wieczorek and Phillips, 1997). The higher abundances of these elements in the northern halves of their ellipses suggest that depth of excavation became progressively deeper moving northwards. This is also supported by the more northern displacements of these ellipses compared to the topographic ellipse. Thorium is a surrogate for KREEP, which is generally believed to have crystallized in a layer between the mantle and lower crust. Thorium is expected to appear at a greater and more well-defined depth than iron due to its incompatibility and late crystallization. Therefore, if the depth of excavation increased northward, the thorium ellipse would be displaced to the north more than either the iron or topographic ellipses. The ellipse would also be smaller due to the smaller area of the most deeply exposed material. These predictions are what are observed in the actual thorium distribution (Fig. 2.2c).

It is possible that the putative north-south asymmetry in depth of excavation is a result of differences between the up-range and down-range excavation flow fields.

Supporting this possibility are north-south structural and geologic asymmetries, such as sharper topography, thorium, and iron contours in the north, as well as higher topography. Mare volcanism is also much more prevalent in the north, with 90% of the total volume of basalts extruded located north of -55°, using the volumes and flow units identified by (Yingst and Head, 1997). Notably, the four largest craters in the northern half of SP-A, Ingenii (-33.7°, 163.5° E, 315 km), Apollo (-36.1°, 208.2°E, 537.0 km), Leibnitz (-38.3°, 179.2°E, 245.0 km) and Poincare (-56.7°, 163.6°E, 319.0 km, more central), are all nearly flooded with mare basalts, while the three largest and comparable size basins in the south, Planck (-57.9°, 136.8°E, 314.0 km), Schrödinger (-75.0°, 132.4°E, 312.0 km) and Zeeman (-75.2°S, 226.4°E, 190.0 km) are not at all, or are at least much less so (Shoemaker et al., 1994; Wilhelms et al., 1979). The greater abundance of volcanism in the north could be a reflection of regionally thinner crust or crust that is more mafic (above), either of which may have been an effect of asymmetry of excavation. The former would facilitate eruption via the overpressurized dyke model of (Head and Wilson, 1992), while the later would facilitate eruption via the buoyancy-controlled model of (Wieczorek et al., 2001).

An alternative explanation for the north-south asymmetries inside of SP-A is that the thorium was higher in the north prior to the impact, and the other asymmetries are secondary post-basin effects. In this case, the high abundance of mare basalts in the north could be related to the higher abundance of thorium and associated heat producing elements in the north, a correlation that is also observed in the nearside Procellarum KREEP Terrane (Jolliff et al., 2000). The higher surficial abundances iron in the north, as well as in the plains of cryptomaria southwest of Apollo (Pieters et al., 2001), could

then be a post-basin effect due largely to increased mare abundances. Higher temperatures may have also permitted greater relaxation and the observed higher northern topography. Obviously, the exact cause and effect relationships between geochemistry, geology, and geophysics of the region, and how pre- or post-excavation processes affected them, are complex and interrelated. In fact, many of these issues in SP-A are at the heart of long-debated problems in global lunar evolution, such as the mechanism that controls mare basalt eruption (Elkins-Tanton et al., 2004; Head and Wilson, 1992; Wieczorek et al., 2001), the role of heat producing elements in controlling magma production (Parmentier et al., 2002), viscous relaxation of large basins (Solomon et al., 1982; Zhong and Zuber, 2000), and the depth of excavation of large basins (Pieters et al., 2001; Wieczorek and Phillips, 1999). Despite this complexity, however, the elliptical shape and north-south alignment of SP-A's mineralogical and geochemical signatures suggest that the basin forming event, as well as the impactor trajectory, played an important role in determining the gross structures and relationships we see now.

It will not likely be possible to use the basin's north-south asymmetries to confidently determine the direction of the impactor until future missions return superior farside gravity data, and better models of large oblique impacts are developed. Schultz has argued for an up-range displacement of the uplifted central peak in oblique impacts (Schultz, 1992a; Schultz, 1992b; Schultz and Anderson, 1996), but these findings are disputed (Ekholm and Melosh, 2001; McDonald et al., 2008; Shuvalov, 2003). Ekholm and Melosh (2001) appear to consent to a model where simple craters may be deeper up-range, but argue that in complex craters the modification stage may undo this effect. More recent simulations (Elbeshausen et al., 2007; Poelchau et al., 2007) and field work

(Scherler et al., 2006) show evidence for asymmetries in central peak formation, but it is unclear if these asymmetries would be noticeable from orbital measurements. In all of these studies, the craters were much smaller, or much less elliptical than SP-A, making it uncertain how they would apply to SP-A.

2.4.3 *Farside topography and lunar orientation*

The highest lunar farside topography is almost exclusively on the eastern side of SP-A's long axis (Zuber et al., 1994), which suggests that it cannot be entirely due to emplaced SP-A ejecta. Ejecta from an oblique impact may have uprange/down range asymmetries, and a "forbidden zone" along the trajectory of impact (Melosh, 1989), but there is no existing model that would preferentially produce ejecta on one side of the axis along the impact direction. In fact, Jolliff et al (2000) find evidence in the iron distribution around SP-A that its ejecta may be distributed on both sides of the trajectory axis, as often observed for smaller oblique impacts. Therefore, the high central farside topography most likely predates SP-A.

The lunar principal moments of inertia, and thereby the orientation of the Moon, are affected by basins as large as SP-A (Melosh, 1975), and the elliptical structure of SP-A defined here can help quantify its contribution. Even small angular changes in lunar orientation (~10°) would be of interest, since a number of large-scale geologic and geophysical observations may be related to the history of the lunar orientation. For example, the lunar center of figure is displaced from its center of mass in the direction of the Earth-Moon axis within ~24° (Smith et al., 1997), even though any arbitrary

orientation is physically stable. The most stable position for a large uncompensated basin on a spherical Moon affected by tidal forces would be at the poles, and generally away from the sub-Earth and anti-Earth positions (0^o and 180^o longitudes) if there is preexisting J_2 gravitational potential. However, the basin is centered at (-53°, 191° E), suggesting that competing contributions to the global moments of inertia have affected its migration to the most stable location. It is possible that the changing compensation state of the basin with time has changed its contribution to the global moments of inertia and lunar orientation. Better farside gravity and an understanding of SP-A's state of compensation will help determine SP-A's contribution to the lunar orientation.

2.5. Conclusions

On the basis of the distributions of topography, thorium, and iron, we propose that the South Pole-Aitken Basin is an elliptical structure with axes measuring 2400 by 2050 km and centered at (53°S, 191°E). Within the best-fit ellipses, iron, thorium, and high topography are preferentially found in the north, suggesting that an oblique impact effected the north-south alignment of their distributions. A second, outer topographic ellipse is found to have a semiminor axis of $\sqrt{2}$ times the best-fit ellipse semiminor axis, which suggests a ring-scaling rule that is dependent on azimuth from the basin center. The outer ellipse is a discontinuous ring that is well defined near the south pole and in the northeast where surrounding topography is high, but is much weaker in the west. The best-fit topographic ellipse defines a much stronger geochemical anomaly and contains the main thorium and iron anomalies. Material between the outer ellipse and best-fit

ellipse (the Outer Terrace) is of intermediate composition between the interior and surrounding highlands, suggesting that deeper materials were not excavated there. Because SP-A is a large, multiring and elliptical structure, which exhibits $\sqrt{2}$ scaling in only one axis, it is a unique laboratory for understanding the generation and scaling of rings, elliptical crater formation, and the formation of massive basins in general (Andrews-Hanna et al., 2008; Marinova et al., 2008).

References

Andrews-Hanna, J. C., et al., 2008. The Borealis basin and the origin of the martian crustal dichotomy. Nature, 453, 1212-1215.

Archinal, B. A., et al., 2006. The unified lunar control network 2005. U.S. Geological Survey Open-file Report 2006-1367.

Belton, M. J. S., et al., 1992. Lunar impact basins and crustal heterogeneity: New western limb and far side data from Galileo. Science. 255, 570-576.

Bottke, W. F., et al., 2000. Interpreting the elliptical crater populations on Mars, Venus, and the Moon. Icarus. 145, 108-121.

Clow, G. D., Pike, R. J., 1982. Statistical test of the square root of 2 spacing rule for basin rings. Proc. Lunar Sci. Conf. 13th. 123-124.

Ekholm, A. G., Melosh, H. J., 2001. Crater features diagnostic of oblique impacts: the size and position of the central peak. Geophys. Res. Lett. 28, 623-626.

Elbeshausen, D., et al., 2007. Structural signatures of oblique impacts - insights from numerical modeling. Workshop on Impact Cratering II. 8047.

Elkins-Tanton, L. T., et al., 2004. Magmatic effects of the lunar late heavy bombardment. Earth and Planetary Science Lettes. 222, 17-27.

Garrick-Bethell, I., 2004. Ellipses of the South Pole-Aitken basin: Implications for basin formation. Proc. Lunar Sci. Conf. 35th. 1515.

Garrick-Bethell, I., Zuber, M. T., 2005. An indigenous origin for the South Pole-Aitken basin thorium anomaly. Geophys. Res. Lett. 32, L13203.

Hartmann, W. K., Kuiper, G. P., 1962. Concentric structures surrounding lunar basins. Communications of the Lunar and Planetary Laboratory. 1, 55-66.

Haskin, L. A., et al., 2004. Thorium anomalies in the NW qudrant of the South Pole-Aitken basin. Proc. Lunar Sci. Conf. 35th. 1461.

Head, J. W., III, 1974. Orientale mult-ringed basin interior and implications for the petrogenesis of lunar highland samples. The Moon. 11, 327-356.

Head, J. W., III, Wilson, L., 1992. Lunar mare volcanism: Stratigraphy, eruption conditions, and the evolution of secondary crusts. Geochimica et Cosmochimica Acta. 56, 2155-2175.

Hiesinger, H., Head, J. W., III, 2004. Lunar South Pole-Aitken basin: topography and mineralogy. Proc. Lunar Sci. Conf. 35th. 1164.

Hodges, C. A., Wilhelms, D. E., 1978. Formation of lunar basin rings. Icarus. 34, 294-323.

Jolliff, B. L., et al., 2000. Major lunar crustal terranes: Surface expressions and crust-mantle origins. J. Geophys. Res. 105, 4197-4216.

Lawrence, D. J., et al., 2003. Small-area thorium features on the lunar surface J. Geophys. Res. 108, 5102.

Lawrence, D. J., et al., 1999. Thorium abundances on the lunar surface. J. Geophys Res. 105, 20307-20331.

Lawrence, D. J., et al., 2002. Iron abundances on the lunar surface as measured by the Lunar Prospector gamma-ray and neutron spectrometers. J. Geophys. Res. 107, 5130.

Margot, J. L., et al., 1999. Topography of the Lunar Poles from Radar Interferometry: A Survey of Cold Trap Locations. Science. 284, 1658-1670.
Marinova, M. M., et al., 2008. Mega-impact formation of the Mars hemispheric dichotomy. Nature, in press.
McDonald, M. A., et al., 2008. Oblique impacts and peak ring position: Venus and Chicxulub. Geophys. Res. Lett. 35, L07203.
McKinnon, W., Melosh, H. J., 1978. The mechanism of ringed basin formation. Geophs. Res. Lett. 5, 985-88.
Melosh, H. J., 1975. Large impact craters and the moon's orientation. Earth and Planetary Science Letters. 26, 353-360.
Melosh, H. J., 1989. Impact cratering: a geologic process. Oxford University Press.
Metzger, A. E., et al., 1977. Thorium concentrations in the lunar surface. I: Regional values and crustal content. Proc. Lunar Sci. Conf. 8th. 949-999.
Neumann, G. A., et al., 1996. The lunar crust: Global structure and signature of major basins. J. Geophys. Res. 101, 16841-16843.
Parmentier, E. M., et al., 2002. Gravitational differentiation due to initial chemical stratification: origin of lunar asymmetry by the creep of dense KREEP? . Earth and Planetary Science Letters. 201, 473-480.
Pascal, A., Piette, T., 1999. Small-scale models of multiring basins. J. Geophys. Res. 104, 16501-16514.
Petro, N. E., Pieters, C. M., 2004. Surviving the heavy bombardment: Ancient material at the surface of South Pole-Aitken Basin. J. Geophys. Res. 109, E06004.
Pieters, C. M., et al., 2001. Rock types of South Pole-Aitken basin and extent of basaltic volcanism. J. Geophys. Res., 28001-28022.
Pieters, C. M., et al., 1994. A sharper view of impact craters from Clementine data. Science. 266, 1884-1848.
Pieters, C. M., et al., 1997. Mineralogy of the mafic anomaly in the South Pole-Aitken Basin: Implications for excavation of the lunar mantle. Geophys. Res. Lett. 24, 1903-1906.
Pike, R. J., Spudis, P. D., 1987. Basin-ring spacing on the Moon, Mercury, and Mars. Earth, Moon and Planets. 39, 129-194.
Poelchau, M., et al., 2007. Structural signatures of oblique impacts - insights from field observations. Workshop on Impact Cratering II. 8058.
Rosiek, M. R., Aeschliman, R., 2001. Lunar shaded relief map updated with Clementine data. Proc. Lunar Sci. Conf. 32nd. 1943.
Scherler, D., et al., 2006. Structural record of an oblique impact. Earth and Planetary Science Letters. 248, 43-53.
Schultz, P. H., 1992a. Atmospheric effects on ejecta emplacement and crater formation on Venus from Magellan. J. Geophys. Res. 97, 16,183-16,248.
Schultz, P. H., 1992b. Effect of impact angle on central peak/peak ring formation and crater collapse on Venus. LPI-Papers Presented to the International Colloquium on Venus, 103-104.
Schultz, P. H., 1997. Forming the South-Pole Aitken basin: The extreme games. Proc. Lunar Sci. Conf. 28th. 1787.

Schultz, P. H., Anderson, R. R., 1996. Asymmetry of the Manson Impact structure: evidence for impact angle and direction. Geological Society of America Special Paper 302. 397-417.
Shevchenko, V. V., et al., 2007. Structure of the South Pole-Aitken Lunar Basin. Solar System Research. 41, 447-462.
Shoemaker, E. M., et al., 1994. The south pole region of the Moon as seen by Clementine. Science. 266, 1851-1854.
Shuvalov, V. V., 2003. Cratering process after oblique impacts. 3rd International Conference on Large Meteorite Impacts. 4130.
Smith, D. E., et al., 1997. Topography of the Moon from the Clementine lidar. J. Geophys. Res. 102, 1591-1611.
Solomon, S. C., et al., 1982. The evolution of impact basins: Viscous relaxation of topographic relief. J. Geophys Res. 87, 3975-3992.
Spudis, P. D., 1993. Geology of Multiring Basins. Cambridge University Press, Cambridge.
Spudis, P. D., et al., 2008. The geology of the south pole of the Moon and age of Shackleton crater. Proc. Lunar Sci. Conf. 39th. abstract 1626.
Spudis, P. D., et al., 1994. Ancient multiring basins on the Moon revealed by Clementine laser altimetry. Science. 266, 1848-1851.
Stuart-Alexander, D. E., 1978. Geologic map of the central far side of the Moon. U.S. Geol. Surv. Map, I-1047.
van Dorn, W. G., 1968. Tsunamis on the Moon? Nature. 220, 1102-1107.
Wieczorek, M. A., Phillips, R. J., 1997. The structure and compensation of the lunar highland crust. J. Geophys Res. 102, 10933-10943.
Wieczorek, M. A., Phillips, R. J., 1999. Lunar multiring basins and the cratering process. Icarus. 139, 246-259.
Wieczorek, M. A., Zuber, M. T., 2001. A Serenitatis origin for the Imbrian grooves and South Pole-Aitken thorium anomaly. J. Geophys Res. 106.
Wieczorek, M. A., et al., 2001. The role of magma buoyancy on the eruption of lunar basalts. Earth and Planetary Science Letters. 185, 71-83.
Wilhelms, D. E., 1987. The geologic history of the Moon. U.S. Geological Survey.
Wilhelms, D. E., et al., 1979. Geologic map of the south side of the Moon, USGS special report I-1162, U.S. Geological Survey, Reston, VA.
Wood, C. A., Gifford, A. W., 1980. Evidence for the lunar big backside basin. Conference on Multi-ring Basins: Formation and Evolution. 414.
Yingst, A. R., Head, J. W., III, 1997. Volumes of lunar lava ponds in South Pole-Aitken and Orientale basins: Implications for eruption conditions, transport mechanisms, and magma source regions. J. Geophys. Res. 102, 10,909-10,931.
Zhong, S., Zuber, M. T., 2000. Long-wavelength topographic relaxation for self-gravitating planets and implications for the time-dependent compensation of surface topography. J. Geophys. Res. 105, 4153-4164.
Zuber, M. T., et al., 1994. The shape and internal structure of the Moon from the Clementine mission. Science. 266, 1839-1834.

Tables

Table 2.1. Best-fit ellipse parameters assuming a spherical Moon with a radius of 1738 km.

Parameter	Best-fit Topography	Outer Topography*	Iron	Thorium
Center latitude °S	-53.2°	-55.0°	-51.4°	-47.2°
Center longitude °E	191.1°E	191.1°E	188.4°E	185.6°E
Tilt angle (degrees)	-18.8°	-18.8°	-14.1°	-17.0°
Semimajor axis (km)	970	1.238 × 970	1030	940
Semiminor axis (km)	720	1.428 × 720	710	740
Semimajor axis (arc°)	32.0°	39.6°	33.9°	31.0°
Semiminor axis (arc°)	23.7°	33.9°	23.2	24.3°
Semimajor/semiminor axis	1.35	1.17	1.46	1.27
Surface area (% of sphere)	5.7	10.1	5.9	5.6
Northern edge	(-22.3°, 180.4°E)	(-16.6°, 178.7°E)	(-18.1°, 180.2°E)	(-17.2°, 176.5°E)
Southern edge	(-78.4°, 249.1°E)	(-77.7°, 293.3°E)	(-80.4°, 243.5°E)	(-74.4°, 219.7°E)
Eastern edge	(-41.0°, 221.3°E)	(-35.2°, 231.3°E)	(-41.1°, 219.0°E)	(-35.9°, 214.7°E)
Western edge	(-54.2°, 150.6°E)	(-51.6°, 133.0°E)	(-51.1°, 150.9°E)	(-48.6°, 149.0°E)
Great circle azimuth from best-fit topographic center to ellipse center	-	-	-44°	-33°

*Parameters partly derived from best-fit topography; see text for details.

Figures

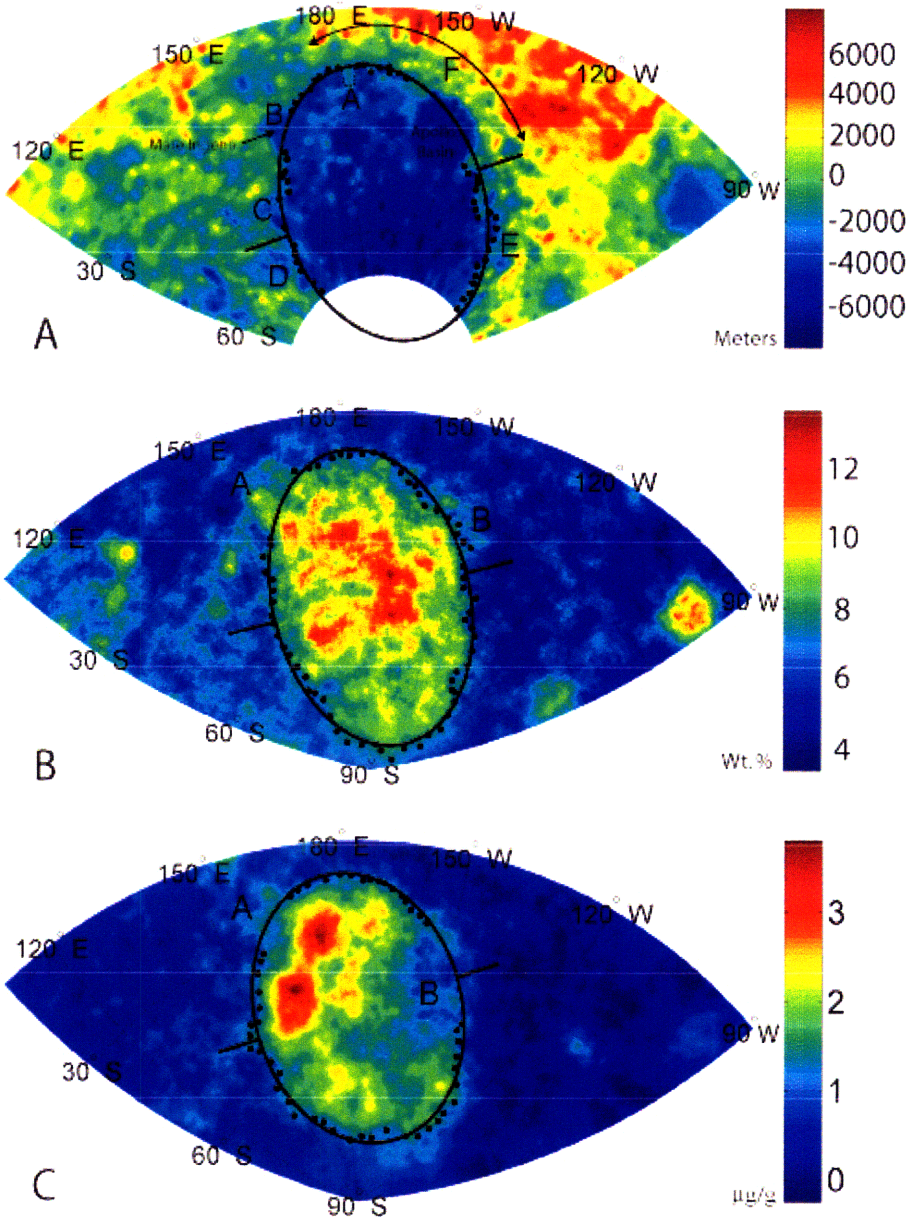

Figure 2.1. Best-fit ellipses and representative data used in the fit for: A) Clementine topography, B) Lunar Prospector iron, and C) Lunar Prospector thorium. Straight lines indicate the ellipse tilt angle. The projection is stereographic and centered on the best-fit center of each ellipse (Table 2.1). Part A labels: A) topography not included in fit (dotted line), B) topography not included in fit due to Mare Ingenii, C and D) topographic depressions topography not included in fit, E) topography considered part of the putative ellipse, despite its easterly displaced contour, F) arcuate topography contour used to derive the outer ellipse. Part B labels: A) iron data not included in fit due to Mare Ingenii, B) iron data incorporated into fit, despite the effects of the Apollo Basin. Part C labels: A) thorium data not included in fit due to Mare Ingenii, B) thorium data not included in fit due to the effects of the Apollo Basin. See main text for details.

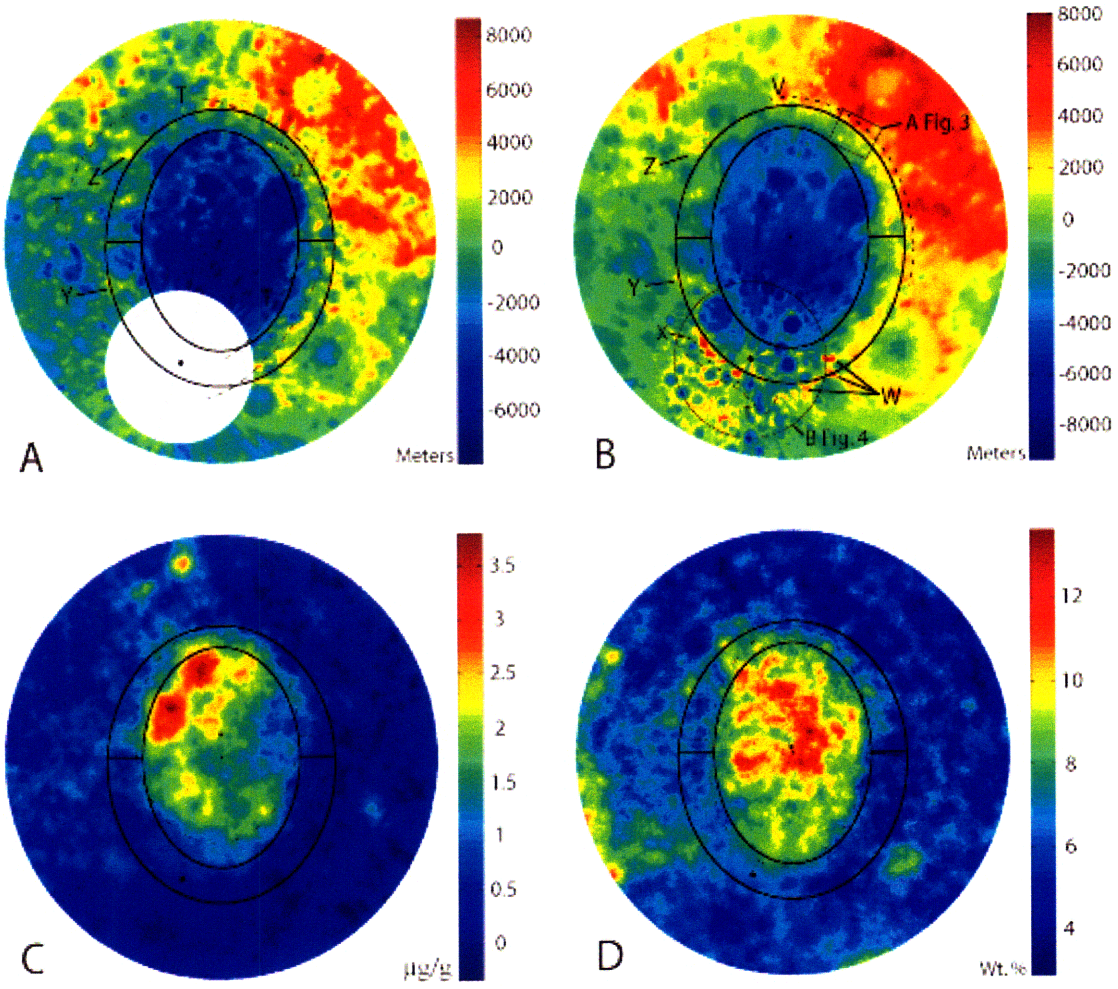

Figure 2.2. Best-fit topography ellipse and derived outer ellipse draped over: A) Clementine topography, B) ULCN2005 topography, C) Lunar Prospector thorium with best-fit thorium ellipse (dashed line), and D), Lunar Prospector iron with best-fit iron ellipse (dashed line). Straight lines indicate the ellipse tilt angle, black dots indicate the south pole, and black squares indicate the thorium and iron ellipse centers in parts C and D. The projections are stereographic centered on the best-fit topographic ellipse center (-53.2°, 191.1°E) and rotated 18.8° clockwise. The limit of the projection is 60° of latitude and gridline spacing is 30°. Part A labels: T) rings mapped by Wilhelms (1987), U) arcuate massifs in Figure 3, Y and Z) high topography possibly related to the outer ellipse. Part B labels: T) rings mapped by Wilhelms (1987), V) arc of high topography associated with the outer ellipse, W) isolated high topography associated with the outer ellipse, X) arcuate high topography at the south pole associated with the outer ellipse, Y and Z) isolated high topography possibly related to the outer ellipse.

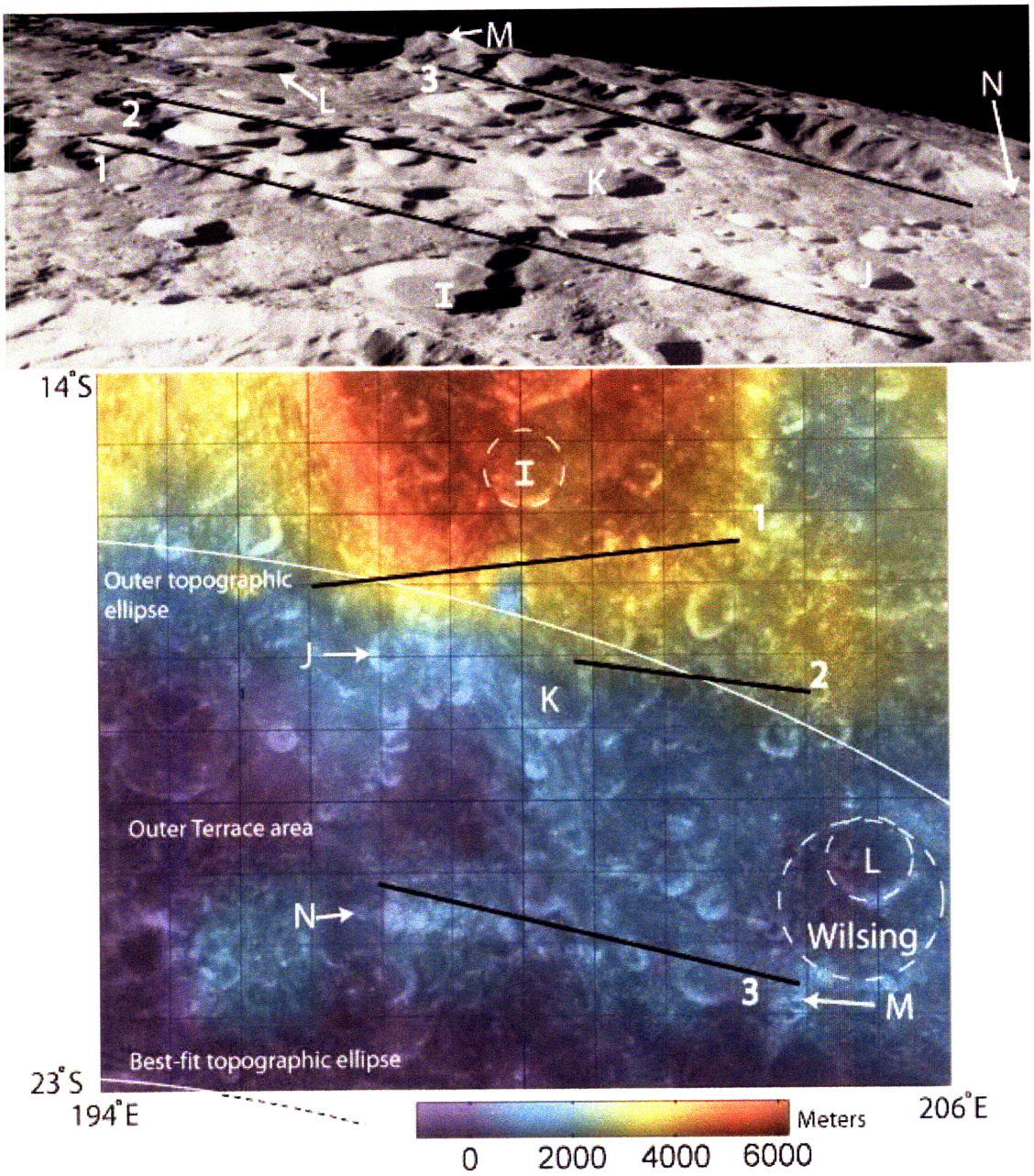

Figure 2.3. Top: South-looking oblique view of SP-A basin massifs on the edges of the outer and best-fit topographic ellipses, originally mapped by Stuart-Alexander (1978) and Wilhelms (1987) (Apollo 8 frame H-2319, high resolution image available online). Bottom: Clementine 750-nm reflectance image with transects from the top panel. Transects: 1 and 2) Massifs correlated with the outer ellipses and mapped as the basin's northern edge by Stuart-Alexander (1978), 3) arcuate massifs not associated with either topographic ellipse. Labels: J-N) Craters useful for comparing the top and bottom images.

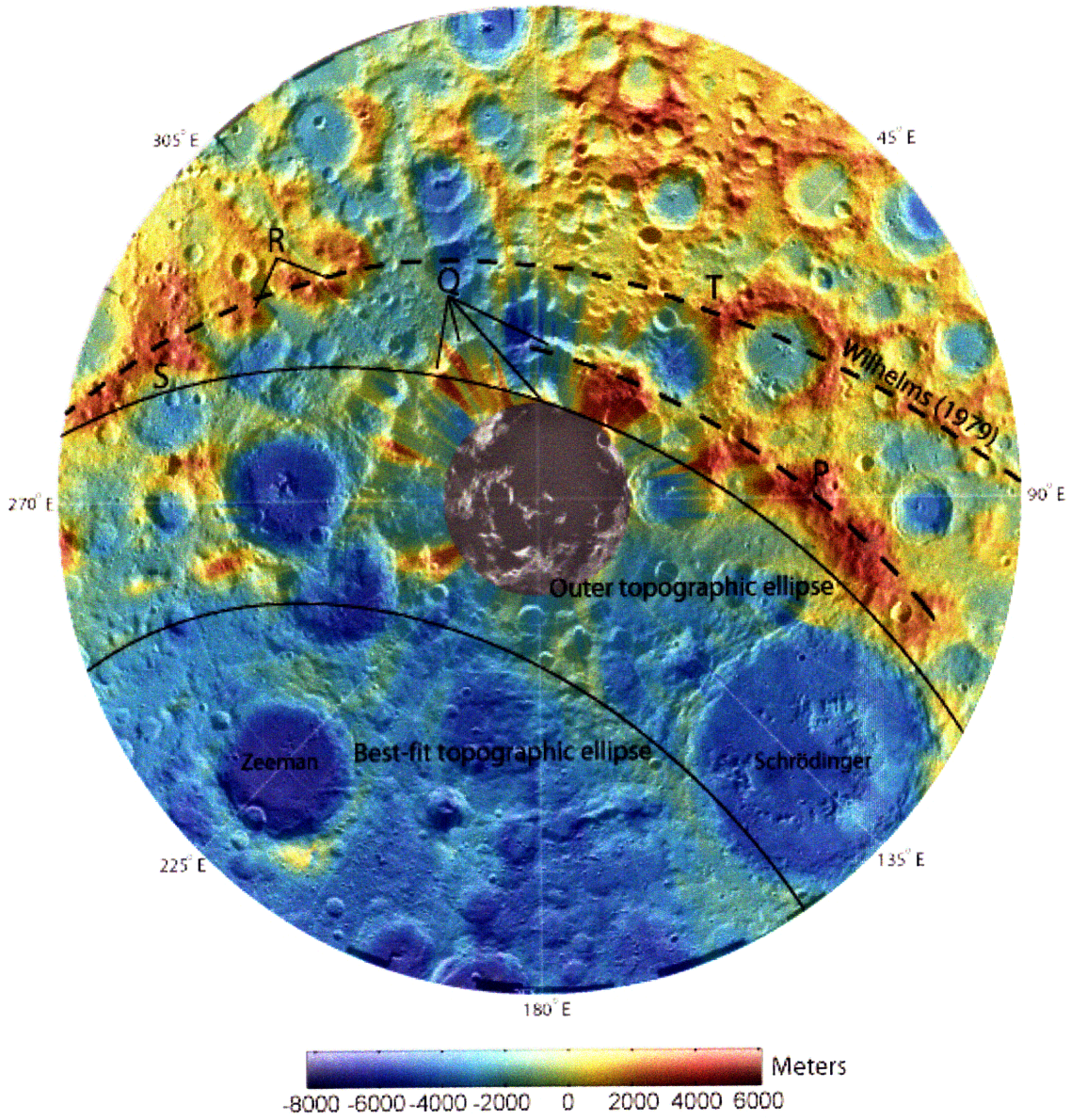

Figure 2.4. Orthographic projection of USGS-produced Clementine 750 nm reflectance mosaic draped with UCLN2005 topography, best-fit topographic ellipse, and outer topographic ellipse. The projection is centered at the south pole and extends to 70°S, with 5° parallels shown. Spurious topography data have been masked out near the pole. Labels: P) Arcuate massifs and high topography associated with the outer ellipse, Q) massifs not readily apparent in UCLN2005 topography data, R) massifs, possibly a discontinuous section of the outer ellipse, S) elevated topography associated with the outer ellipse, T) outer ring mapped by Wilhelms (1979).

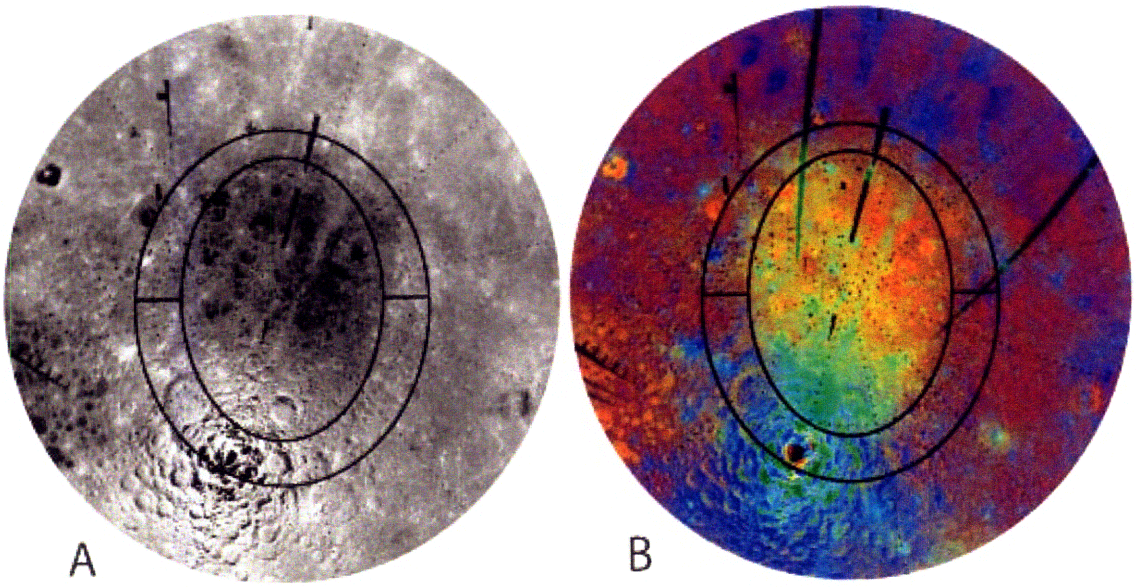

Figure 2.5. Best-fit topographic ellipse and derived outer ellipses draped over: A) Clementine 750-nm reflectance data, and B) band ratio technique from Pieters et al. (1994). Straight lines indicate the ellipse tilt angle. The projection is stereographic centered on the best-fit topographic ellipse center (-53.2°, 191.1°E) and rotated 18.8° clockwise. The limit of the projection is 60° of latitude and gridline spacing is 30°. Data near the poles suffer from high phase-angle artifacts, but are shown to aid in the identification of features.

Chapter 3

An indigenous origin for the South Pole-Aitken basin thorium anomaly

Originally published as Garrick-Bethell, I. and M.T. Zuber, An indigenous origin for the South Pole-Aitken basin thorium anomaly, Geophysical Research Letters 32, DOI: 10.1029/2005GL023142 (2005).

Abstract

The northwest portion of the Moon's South Pole-Aitken basin contains an anomalously high abundance of thorium as determined by Apollo and Lunar Prospector gamma-ray spectroscopy. The anomaly's proximity to the antipode of the Imbrium basin has led several investigators to suggest that the anomaly is the result of convergence of thorium-enriched ejecta from the Imbrium impact. Examination of this complex region with new higher resolution thorium data and several other datasets reveals that a convergence of ejecta cannot explain the anomaly. Alternatively, we propose an indigenous and likely ancient source.

3.1. Introduction

It is generally believed that as the Moon differentiated, plagioclase feldspar floated to the top of a magma ocean to form the anorthositic crust, while mafic minerals condensed to form the mantle. During this process trace incompatible elements concentrated in an

unincorporated magma ocean residue, eventually crystallizing last as the minerals observed in KREEP-rich rocks (i.e. enriched in potassium, rare earth elements and phosphorus). Among the elements found in KREEP, thorium is also abundant and serves as an adequate surrogate for detection of incompatible elements and KREEP. The global distribution of thorium is heterogeneous, with the strongest surficial expression found on the nearside in the Procellarum KREEP Terrane (PKT), centered around the Imbrium basin [*Jolliff et al.*, 2000]. The farside as a whole has far fewer expressions of significant abundances of thorium. The South Pole-Aitken (SP-A) basin contains most of the farside thorium in an oval shaped region centered at approximately (48°S, 188°E) [*Garrick-Bethell*, 2004], with abundances peaking at 3.8 μg/g in the northwest anomaly region, Figure 3.1 [*Lawrence et al.*, 2003]. Aside from the Compton-Belkovich region [*Lawrence et al.*, 2003], the SP-A thorium anomaly represents the highest concentration of thorium on the farside.

Noting the anomaly's proximity to the antipode of the Imbrium basin, and its rough association with units of ''grooves and mounds'', *Stuart-Alexander* [1978] suggested that the anomaly is due to a convergence of thorium enhanced ejecta from the nearside Imbrium basin. Models of ejecta deposition indicate that significant amounts of primary ejecta should land at the antipode [*Moore et al.*, 1974; *Haskin et al.*, 1996; *Haskin*, 1998]. *Wieczorek and Zuber* [2001] proposed on the basis of simple ejecta modeling that the Serenitatis basin is a more likely source of the thorium anomaly than the Imbrium basin. *Haskin et al.* [2004], however, have alternatively suggested that ejecta from Imbrium or Serenitatis is unlikely to produce the observed pattern. If the above impact-origin hypotheses are not correct, the SP-A thorium anomaly would have important implications for the thermal and chemical evolution of SP-A and the farside of the Moon. Here we show that an ejecta origin is untenable on the basis of careful analysis of a variety of data.

3.2. Data

Thorium abundance data comes from an updated version of low altitude (average 30 km) measurements of the Lunar Prospector gamma-ray spectrometer (LP-GRS) [*Lawrence et*

al., 2003]. Briefly, measured gamma-ray counts from 32-second spectra were binned onto a 0.5 × 0.5 degree/pixel grid, and smoothed to reduce statistical scatter with an equal area smoothing algorithm. The full width at half maximum (FWHM) of the LP-GRS becomes (80 km)^2 under the smoothing operations, with a full width at full maximum (FWFM) of 240 km (FWFM defined as where the spatial response function falls to 1%).

Topography data are from the Clementine laser altimeter. The 0.25 degree/pixel grid of interpolated elevation is obtained from filtered along-track range data [*Smith et al.*, 1997]. Clementine five-band UV-VIS multispectral image strips are taken from the published CDs and mosaiced together with the United States Geological Survey Map-a-Planet software at a maximum resolution of 100 meters/pixel [*Pieters et al.*, 1994]. In order to obtain qualitative mineralogical information from the multispectral images in an RGB color format, we utilized a ratio technique proposed by *Pieters et al.* [2001]. Under this scheme, noritic low-Ca pyroxene lithologies appear red (''band curvature''), high-Ca pyroxene and/or olivine rich materials are shown in green (''band tilt''), and blue tones represent anorthositic and/or mature materials (''band strength''). A shaded relief basemap from *Rosiek and Aeschliman* [2001] is also utilized.

3.3. Results

3.3.1. Anomaly Description

Figure 3.1 shows the thorium enhancement lies in the northwest corner of SP-A and ranges in concentration from 2.5 to 3.8 μg/g. The enhanced region can be divided into two northeast-southwest trending regions which we refer to as North and South Lobes. The lobes each have concentrations over 3.5 μg/g near their centers, with South Lobe being slightly higher, peaking at 3.8 μg/g. Thorium level contours ranging from 2.5 to 3.5 μg/g illustrate this morphology, and serve hereafter as a convenient quantitative means of characterizing the extent of the anomaly, Figure 3.2. The total anomaly area with regions of thorium above 2.5 μg/g is approximately 202,000 km^2. We note that the western edge

of the two lobes is continuous with the western edge of the entire inner SP-A thorium deposit (cf. Figure 3.1).

3.3.2. Correlation With Mapped Unit of Grooves

Smoothed thorium data shows that correlation with the mapped Imbrian unit of grooves, mounds and dissected crater walls (unit Ig) attributed to the Imbrium impact [*Stuart-Alexander*, 1978], is seen only in North Lobe (Figure 3.2a). To the northwest of North Lobe a large area greater in size than the FWHM thorium footprint is nearly filled with the mapped unit Ig, including the northwestern walls of Ingenii. However, the thorium signature falls to values below 1.0 μg/g in this region. In South Lobe unit Ig is hardly present except for several instances of crater wall dissection. Instead, Nectarian ''rolling terra'' constitutes the majority of South Lobe, as is the case for much of the interior of SP-A.

3.3.3. Relations With Eratosthenian Craters

Figure 2b shows that the highest abundance of thorium in South Lobe is associated with an unnamed 50-km-diameter Eratosthenian crater at (40°S, 165°E) [*Stuart-Alexander*, 1978], herein referred to as South Crater. In North Lobe the high thorium abundances are correlated with the mapped ejecta units of Birkeland (30.2°S, 173.9°E, 82.0 km) [*Blewett et al.*, 2000], but the thorium pattern is not as circular as for South Crater. Focusing on South Crater, we calculate from its diameter a crater depth of 3.4 km [*Pike*, 1974], and a depth of excavation of 1.1 km (from experiments of *Stoffler et al.* [1975]). Thus if earlier emplaced ejecta from Imbrium is responsible for the thorium deposit at South Crater, the ejecta would have to be at least 1.1 km thick to have remained exposed at the bottom South Crater and its immediate surroundings. Despite the fact that a purported ejecta blanket at least 1.1-km-thick fell in the vicinity of South Crater, there are no mapped Imbrian ejecta units bordering South Crater (Figure 3.3). Dissected crater walls of purported Imbrian origin are not present in the pre-Nectarian crater underlying South Crater, or in the larger pre-Nectarian crater Oresme (42.4°S, 169.2°E, 76.0 km) to the

southeast. In the crater Obruchev (38.9°S, 162.1°E, 71.0 km) the northern walls bordering Mare Ingenii show signs of dissection, but the walls closest to South Crater do not. If we use the more general numerically derived crater scaling laws of *Croft* [1980] we calculate the depth of excavation of South Crater to be 5.0 km. An Imbrium ejecta blanket of this thickness would have exceeded the depth of all pre-Imbrian craters currently observed inside the anomaly, likely filling the smaller ones completely, which is not observed.

3.3.4. Topography

Figure 3.2b shows that the western edge of the thorium anomaly is well aligned with topographic contours defining the inner part of the basin. Level contours between -1000 and -3000 m can be followed from approximately (23°S, 180°E) to (47°S, 158°E), over a distance of approximately 1200 km. The same contours also wrap around much of SPA and the Ingenii basin, which appears to have impacted on the border of SP-A's inner topographic depression. The northeast trending orientation of North and South Lobe is most likely due to correlation with this topographic trend in the same direction. Such strong correlation and bounding by terrain would not be expected if the material fell randomly as ejecta, but is more consistent with a process related to basin formation.

3.3.5. Mare-Thorium Relations

The most visually prominent feature of the thorium anomaly is that it is well defined by the eastern border of Mare Ingenii. When combined with the topographic contours described in Section 3.3, the two features completely outline the western portion of the anomaly (Figure 3.2b). We interpret this relationship to be due to mare cross-cutting a thorium-enriched subsurface that may extend approximately halfway into the Ingenii basin from the east. In a survey of all SP-A mare units we find that the majority are adjacent to or within the thorium anomaly. Total amounts of 68 percent of mare by volume, and 50 percent of mare by area are found either inside the 2.5 μg/g thorium contour, or with some component within 50 km of the exterior of the contour (including

all of Mare Ingenii, and mare in the craters Leibnitz and Von Karman), based on mare volumes and areas from *Yingst and Head* [1997]. We also note from the morphometric studies of *Yingst and Head* [1997] that Mare Ingenii has an approximate depth of 1.6 km, which places an upper limit on the thickness of the purported Imbrium ejecta. This thickness is less than the ejecta thickness estimate of 5.0 km implied by South Crater's maximum excavation depth (Section 3.2).

3.3.6. Multispectral Images

Using the multispectral ratio technique outlined in Section 2, we can compare the gross mineralogy of the thorium anomaly to nearside geologic units attributed to Imbrium basin ejecta (similar in spirit to *Spudis and Fessler* [2002]). Figure 3.4a shows that the thorium anomaly appears mostly green in both mare and non-mare regions, implying significant materials of mafic character. The anomaly region is similar to the mineralogy of SP-A as a whole. The Fra Mauro Formation, units mapped as Fra Mauro materials, and the Apennine backslope formations are all believed to have been deposited by the Imbrium event [*Wilhelms and McCauley*, 1971]. From Figure 3.4b it is apparent that under the same image stretch the mineralogy of these regions is much bluer than the thorium anomaly region, meaning there is more anorthositic and/or weathered material. Green areas surrounding the bluer units are Mare Imbrium, Mare Insularum, Mare Vaporum, Sinus Medii, and Sinus Aestuum.

3.4. Discussion

An alternative explanation to the antipodal ejecta hypothesis is that the anomaly is a province of slightly elevated thorium that was exposed by the SP-A impact event. This would explain the thorium correlation with inner-basin topography contours and the mafic mineralogies characteristic of SP-A's interior, while resolving the contradictions of association with the Imbrium unit Ig. An indigenous source explains the position and orientation of the anomaly lobes in relation to the entire SP-A thorium region, without invoking oblique nearside impacts [*Wieczorek and Zuber*, 2001]. South Crater may have

excavated thorium-rich indigenous material that had been covered by and mixed with ejecta from subsequent basins and craters [*Lawrence et al.*, 2003]. Beyond South Crater however, the lack of apparent association with any other features suggests that the deposit is an ancient province of material that has been homogenized by aeons of meteoroid bombardment. To the west of the pre-Nectarian Ingenii basin, we find low concentrations of thorium that would seem to contradict an ancient thorium province, which would have been ejected westward by the Ingenii impactor. However, Ingenii's western half is outside the anomaly's western edge (Figure 3.2b), where thorium is low and topography changes significantly. To the east, Ingenii would have contributed thorium-enriched ejecta to the anomaly region, in addition to the ejecta from Von Karman (44.8°S, 175.9°E, 180.0 km), and Leibnitz (38.3°S, 179.2°E, 245.0 km). To the east of Von Karman and Leibnitz we observe some thorium above 2.5 μg/g (Figure 3.2), which may be freshly exposed by local Copernican and Eratosthenian craters. The mare that fills Von Karman and Leibnitz appears to border loosely the eastern edge of the anomaly, implying that thorium may also be present beneath
these craters.

Thorium and other heat-producing elements at depth could provide the heating necessary for the extensive amount of mare flooding found around the anomaly (Section 3.4). Notably, this region not only contains most of the SP-A mare deposits, but a significant fraction of all farside volcanism. Work by *Hawke and Spudis* [1980] suggests that the thorium may be a result of extrusive volcanism, although the generally lower thorium abundances we observe in the nearby mare units contradict this idea. For insight into the relationship between thorium, mare materials, and non-mare materials, we look to the nearside PKT. The PKT is heavily enriched in radioactive elements that are believed to have led to most of the nearside's volcanism [*Jolliff et al.*, 2002]. In the PKT a topographically high circum-Imbrium ring of non-mare terrain surrounds Mare Imbrium materials that are relatively lower in thorium, though nonetheless enriched compared to terrain outside of the PKT [e.g., see *Lawrence et al.*, 2003]. Similarly, in the
SP-A thorium anomaly, non-mare thorium rich materials surround mare that is relatively lower in thorium, but enriched when compared to terrain outside of SP-A. Thus in both

cases, KREEP-related heating and volcanism apparently do not have to produce mare materials as rich in KREEP as adjacent non-mare crustal materials.

As for the mapped units of Imbrium ejecta, all of the above analysis indicates that they are not directly related to the region's enhanced thorium. These distinct and complex features may be unique local disturbances related to early Imbrian volcanism, the convergence of an antipodal impactor's seismic energy [*Schultz and Gault*,1975], or a combination of both [*Boslough et al.*, 1986].

3.5. Conclusions

The characteristics of the thorium anomaly can be linked to known geologic features and basin structures. When considering local geology, geophysics, and composition, as well as the merely rough correlation with mapped Imbrium ejecta deposits, we conclude the anomaly is an indigenous unit, likely emplaced at the time of basin formation. This region is important to understanding the nearside-farside dichotomy in REE, styles of lunar volcanism, and the general evolution of the SP-A basin.

References

Blewett, D. T., et al. (2000), Compositional studies of the South Pole-Aitken basin, Lunar Planet. Sci. [CD ROM], XXXI, Abstract 1501.

Boslough, M. B., et al. (1986) Axial focusing of impact energy in the Earth's interior: A possible link to flood basalts and hotspots, in The Cretaceous-Tertiary Event and Other Catastrophes in Earth History, edited by G. Ryder, D. Fastovsky, and S. Gartner, Geol. Soc. Am. Spec. Publ., 307, 541– 550.

Croft, S. K. (1980), Cratering flow field: Implications for the excavation and transient expansion stages of crater formation, Proc. Lunar Planet. Sci. Conf., XIth, 2347–2378.

Garrick-Bethell, I. (2004), Ellipses of the South Pole-Aitken Basin: Implications for basin formation, Lunar Planet. Sci. [CD ROM], XXXV, Abstract 1515.

Haskin, L. A. (1998), The Imbrium impact event and the thorium distribution at the lunar highlands surface, J. Geophys. Res., 103, 1679– 1689.

Haskin, L. A., et al. (1996), Could Imbrium ejecta be the source of the high-Th material in the Van de Graaff region of the Moon?, Proc. Lunar Planet. Sci. [CD ROM], XXVIIth, 501–502.

Haskin, L. A., et al. (2004), Thorium anomalies in the NW quadrant of the South Pole-Aitken basin, Lunar Planet. Sci. [CD ROM], XXXV, Abstract 1461.

Hawke, B. R., and P. D. Spudis (1980), Geochemical anomalies on the eastern limb and farside of the Moon, in Proceedings of the Conference on Lunar Highlands Crust, edited by J. J. Papike and R. B. Merrill, pp. 467– 481, Elsevier, New York.

Jolliff, B. L., et al. (2000), Major lunar crustal terranes: Surface expressions and crust-mantle origins, J. Geophys. Res., 105, 4197– 4216.

Lawrence, D. J., R. C. Elphic, W. C. Feldman, T. H. Prettyman, O. Gasnault, and S. Maurice (2003), Small-area thorium features on the lunar surface, J. Geophys. Res., 108(E9), 5102, doi:10.1029/2003JE002050.

Moore, H. J., et al. (1974), Multiring basins Illustrated by Orientale and associated features, Proc. Lunar Sci. Conf., Vth, 71– 100.

Pieters, C. M., et al. (1994), A sharper view of impact craters from Clementine data, Science, 266, 1844–1848.

Pieters, C. M., et al. (2001), Rock types of the South Pole– Aitken basin and extent of basaltic volcanism, J. Geophys. Res., 106, 28,001– 28,022.

Pike, R. J. (1974), Depth/diameter relations of fresh lunar craters: Revision from spacecraft data, Geophys. Res. Lett., 1, 291– 294.

Rosiek, M. R., and R. Aeschliman (2001), Lunar shaded relief map updated with Clementine data, Lunar Planet. Sci. [CD ROM], XXXII, Abstract 1943.

Schultz, P. H., and D. E. Gault (1975), Seismic effects from major basin formations on the Moon and Mercury, Moon, 12, 159–177.

Smith, D. E., M. T. Zuber, G. A. Neumann, and F. G. Lemoine (1997), Topography of the Moon from the Clementine LIDAR, J. Geophys. Res., 102, 1591–1611.

Spudis, P. D., and B. Fessler (2002), Searching for antipodal basin ejecta on the Moon, paper presented at The Moon Beyond 2002: Next Steps in Lunar Science and Exploration, Los Alamos Natl. Lab., Taos, N. M.

Stoffler, D., et al. (1975), Experimental hypervelocity impact into quartz sand: Distribution and shock metamorphism of ejecta, J. Geophys. Res., 80, 4062–4077.

Stuart-Alexander, D. (1978), Geologic map of the central far side of the Moon, U.S. Geol. Surv. Map, I-1047.

Wieczorek, M. A., and M. T. Zuber (2001), A Serenitatis origin for the Imbrian grooves and South Pole-Aitken thorium anomaly, J. Geophys. Res., 106, 27,853– 27,864.

Wilhelms, D. E., and J. F. McCauley (1971), Geologic map of the near side of the Moon, U.S. Geol. Surv. Map., I-703.

Yingst, R. A., and J. W. Head (1997), Volumes of lunar lava ponds in South Pole– Aitken and Orientale Basins: Implications for eruption conditions, transport mechanisms, and magma source regions, J. Geophys. Res., 102, 10,909– 10,931.

Figures

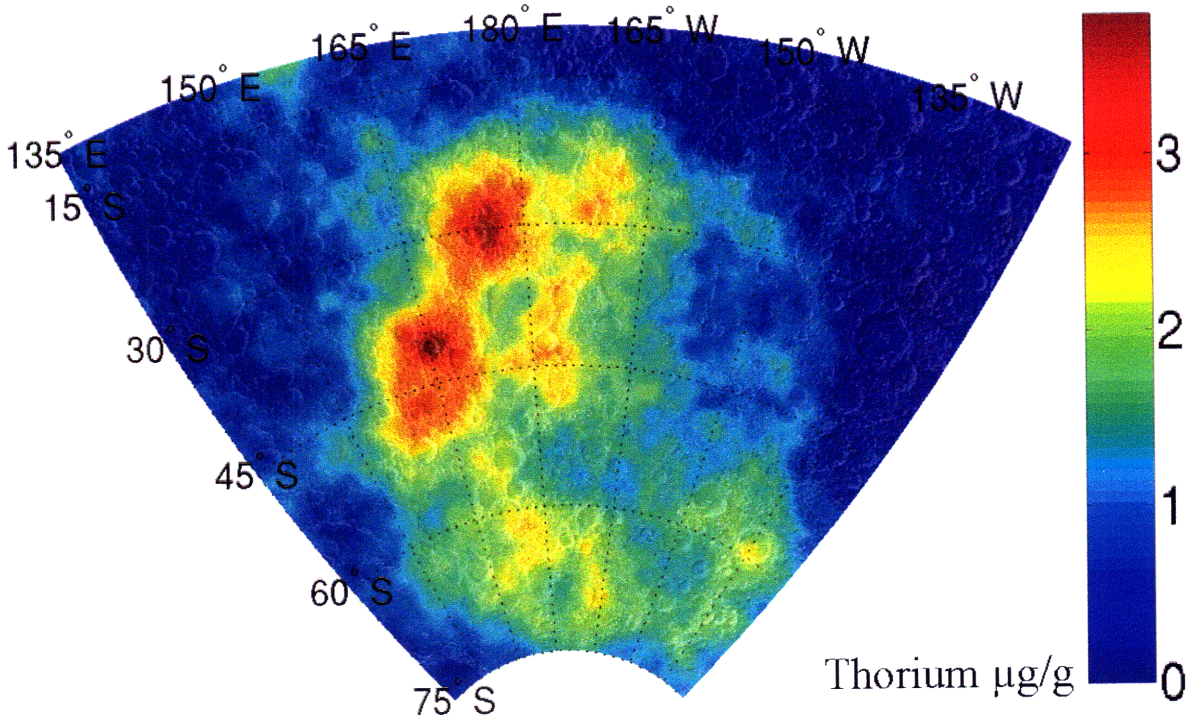

Figure 3.1 Map of thorium content in the South Pole-Aitken basin, in µg/g.

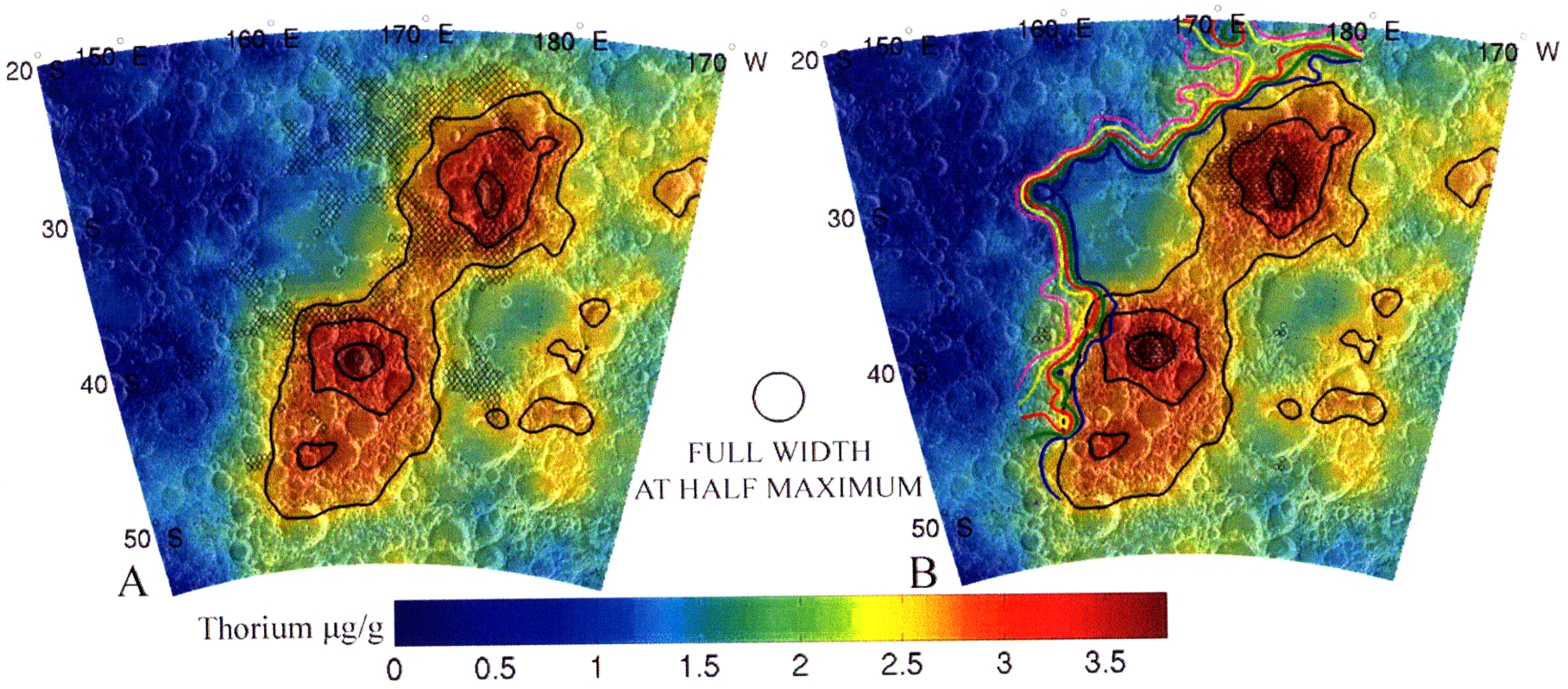

Figure 3.2 2.5–3.5 µg/g thorium contours in intervals of 0.5 µg/g, shown in black. (a) Small black diamonds represent mapped units of grooves and mounds from *Stuart-Alexander* [1978]; (b) small black circles represent units of Eratosthenian craters from *Stuart-Alexander* [1978], and multi-color contours show basin topography from -3000 to -1000 m, increasing westward in 500 m intervals.

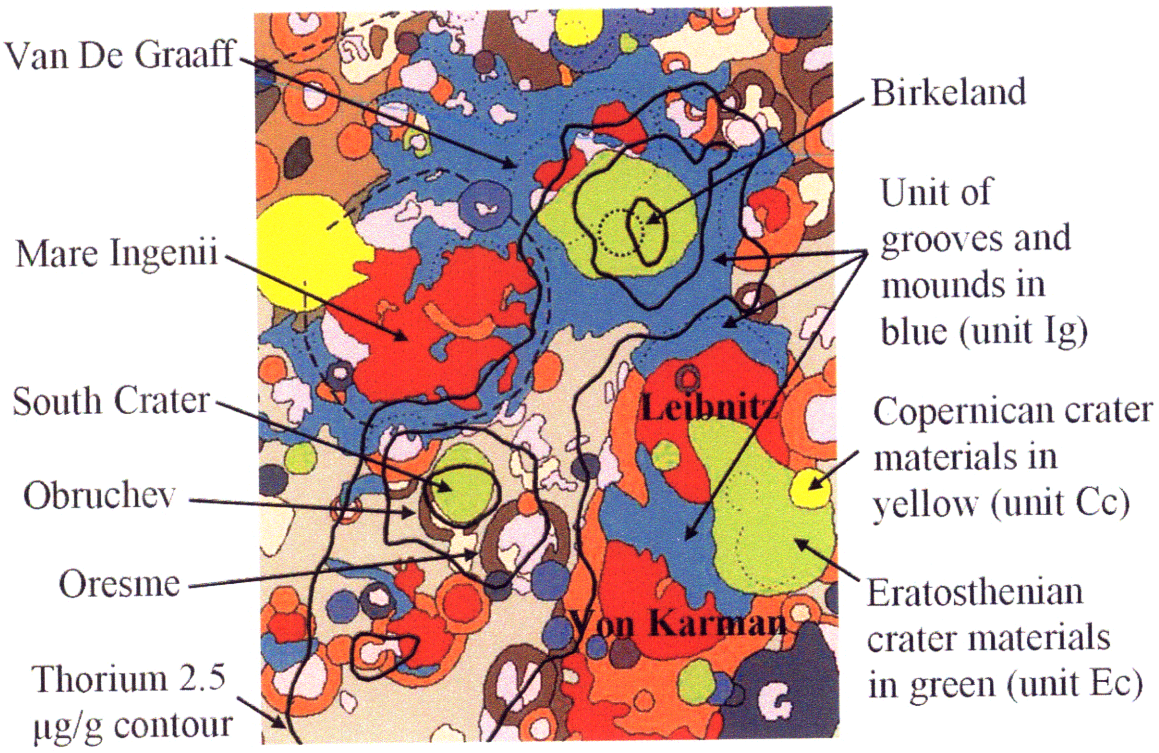

Figure 3.3 Geologic map of the anomaly region with superimposed thorium contours from Figure 3.2.

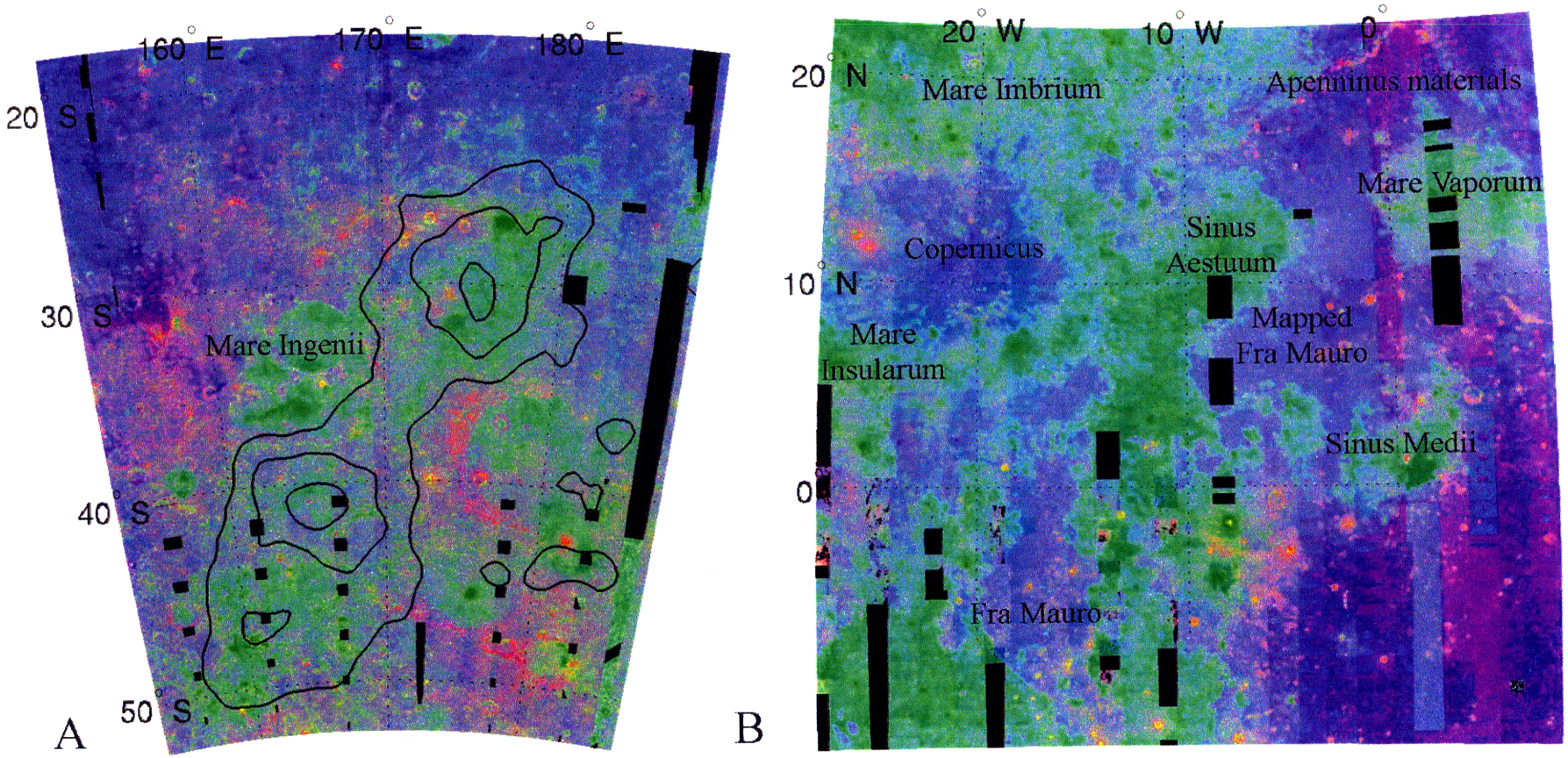

Figure 3.4 Multispectral ratio used to reveal dominant rock types. (a) Thorium anomaly; (b) imbrium ejecta formations.

Chapter 4

Evidence for a past high eccentricity lunar orbit

Originally published as Garrick-Bethell, I., J. Wisdom, and M.T. Zuber, Evidence for a past high-eccentricity lunar orbit, Science 313, 652-655 (2006):

Abstract

The large differences between the Moon's three principal moments of inertia have been a mystery since Laplace considered them in 1799. Here we present calculations that show how past high eccentricity orbits can account for the moment differences, represented by the low-order lunar gravity field and libration parameters. One of our solutions is that the Moon may have once been in a 3:2 resonance of orbit period to spin period, similar to Mercury's present state. The possibility of past high eccentricity orbits suggest a rich dynamical history, and may influence our understanding of the early thermal evolution of the Moon.

4.1. Evidence for a past high eccentricity lunar orbit

The Moon is generally thought to have accreted close to the Earth and migrated outwards in a synchronously-locked low-eccentricity orbit. During the early part of this migration the Moon was cooling and continually subjected to tidal and rotational stretching. The

principal moments of inertia $A < B < C$ of any satellite are altered in a predictable way by deformation due to spin and tidal attraction. The moments are typically characterized by ratios which are easier to measure, namely the libration parameters $\beta = (C - A)/B$ and $\gamma = (B - A)/C$, and the degree-2 spherical-harmonic gravity coefficients $C_{20} = (2C - B - A)/(2Mr^2)$ and $C_{22} = (B - A)/(4Mr^2)$, where M and r are the satellite mass and radius. Of these four values β, γ, and C_{20} can be taken as independent. Using the ratio $(C - A)/A$, Laplace was the first to observe that the lunar moments are not in equilibrium with the Moon's current orbital state (*1*). He did not, however, address the possibility of a "fossil bulge", or the frozen remnant of a state when the Moon was closer to the Earth. Sedgwick examined the lunar moments in 1898, as did Jeffreys in 1915 and 1937, and both authors effectively showed that β is too large for the current orbit, suggesting that the Moon may carry a fossil bulge (*2-5*). However, Jeffreys showed that the fossil hypothesis might be untenable because the ratio of $\gamma/\beta = 0.33$ does not match the predicted ratio of 0.75 for a circular synchronous orbit. In fact, using data from (*6*), none of the three independent measures of moments represent a low eccentricity synchronous-orbit hydrostatic form; $C_{20} = 2.034 \times 10^{-4}$ is 22 times too large for the current state, while $\beta = 6.315 \times 10^{-4}$ and $\gamma = 2.279 \times 10^{-4}$ are 17 and 8 times too large, respectively (*7, 8*). Another convenient means of representing the Moon's disequilibrium is the ratio of the normalized values of $\overline{C}_{20} = 9.096 \times 10^{-5}$ to $\overline{C}_{22} = 3.469 \times 10^{-5}$ (*9*), which gives 2.62, while synchronous rotators should have a ratio of order unity (0.97) at any location in the orbit (*10*).

The inappropriate ratio of C_{20}/C_{22} has led some to dismiss the fossil bulge hypothesis as noise due to random density anomalies (*11,12*). However, the power of the second-degree harmonic gravity field is anomalously high when compared to the power expected from back extrapolating the power of higher harmonics (*7, 13*). This suggests the bulge may be interpreted as a signal of some process. Special assumptions about mantle viscosity structure could lead to a stable two-cell second-degree convection pattern which could mimic a tidal bulge in the direction of the Earth, along the moment A axis (*14,15*). Since the moments A and B are not equal, however, a separate degree-2 pattern around the lunar polar axis would have to be superimposed on the first pattern to fully account for all moment differences (*14*). Hence, a complete explanation of the lunar moments using mantle convection has not been put forth, and would require very special circumstances. The Moon's center-of-mass/center-of-figure offset influences the moment parameters slightly, but that problem is geophysically separate and mathematically insignificant to the degree-2 problem (*8,10*).

Since C_{20} is due primarily to rotational flattening, and C_{22} is due to tidal stretching, the high C_{20}/C_{22} ratio seems to imply the Moon froze in its moments while rotating faster than synchronous. However, in such cases no constant face would be presented to the Earth for any C_{22} power to form in a unique lunar axis. This apparent dilemma can be avoided by considering that in any eccentric orbit with an orbit period to spin period ratio given by n:2, with n = 2, 3, 4, ... , the passage through pericenter results in higher C_{22} stresses throughout a single elongated axis, hereafter called the pericenter axis. When the stresses experienced over one orbit period are time-averaged, the highest stresses will still

appear in the pericenter axis, despite the shorter dwell time near pericenter. This is because, with respect to orbital distance, the tidal forces acting near pericenter increase faster than the decrease in time spent near pericenter. The time-averaged pericenter-axis stresses will nonetheless be lower than the peak stresses at pericenter.

Higher average stresses can form a C_{22} semi-permanent bulge through the pericenter axis because higher stresses lead to increased strain rate. Therefore, for lunar material having both viscous and elastic properties (e.g. approximated as a Maxwell material), any higher time-averaged stresses will accumulate as higher strains, as long as the material's relaxation time is significantly longer than the period of the orbit. Since the young lunar surface must at some point cool from a liquid to a solid, it will certainly pass through a state in which the relaxation time exceeds the orbit period. This pericenter axis deformation process will also take place for a high eccentricity synchronous orbit, where strong librational tides move the location of the C_{22} bulge over the lunar sphere, but on average the pericenter axis still attains the highest stresses.

Eventually, a semi-permanent bulge that is stable on timescales of the lunar orbit must be made permanent over billions of years. The lithosphere's ability to support degree-2 spherical harmonic loads for > 4 By is well established by theoretical calculations (*16*), and the overcompensation of large impact basins suggests the Moon has supported significant lithospheric loads from an early time (*17*). The transition between the state of short and long relaxation time must also happen relatively quickly for the shape to record a particular orbital configuration. Recent isotope studies have indicated the lunar magma

ocean crystallized approximately 30-100 My after lunar formation (*18*,), and Zhong and Zuber showed that a degree-2 deformation on a 100-My-old lithosphere will relax only 20% of its initial deformation after 4 By (*16*). Therefore, a conservatively late estimate of the start of bulge freeze-in, if it took place, would be between 100 - 200 My after lunar formation. We can obtain a rough estimate of the location of the Moon at this time by using established equations for the evolution of zero eccentricity synchronous orbits (*19*, *20*). With a current Earth potential Love number of ≈ 0.3, and the quality factor for a modern oceanless Earth, $Q_{Earth} = 280$ (*21*), the Moon reaches a semimajor axis of 24 r_E (Earth radii) by approximately 100 My and 27 r_E by 200 My. Therefore, over a 100 My timescale for fossil freeze-in, the orbit does not significantly evolve. It will also be shown that these semimajor axis estimates are consistent with the observed libration parameters and second-degree gravity harmonics, and that our solutions permit an average fossil to develop during orbit evolution. Without better constraints on the Love numbers and Q values for the Moon and Earth, and the evolution of eccentric and higher resonance orbits, no existing data rule out the development of a strong lithosphere on the relevant timescales.

To calculate eccentric orbits that may generate the time-averaged values of the three independent parameters β, γ, and C_{20}, we write the time-averaged tidal potential in each of three principal axes,

$$< U_{t,\hat{a}} > = \frac{-GMr^2}{a^3}\left(\frac{3}{4}X_{-3,p,q}(e) + \frac{1}{4}\right)$$

$$< U_{t,\hat{b}} > = \frac{GMr^2}{a^3}\left(\frac{3}{4}X_{-3,p,q}(e) - \frac{1}{4}\right)$$

$$< U_{t,\hat{c}} > = \frac{GMr^2}{2a^3}X_{-3,0,0}(e) \qquad (1)$$

where G is the gravitational constant, M is the Earth mass, r is the mean lunar radius, a is the orbital semimajor axis, and $\hat{a}$, $\hat{b}$, and $\hat{c}$ refer to the principal lunar axes with respective moments $A < B < C$. $X_{l,p,q}(e)$ is the eccentricity-dependent Hansen function that arises from time averaging the orbit (*22*). The instantaneous potentials are recovered by replacing a with R, and $X_{l,p,q}(e)$ with $\cos(2f - 2\omega t)$, where f is the true anomaly, ω is the lunar rotational velocity, and t is the time since passage of pericenter. The rotational potentials in the principal axes can be written (*19*)

$$U_{r,\hat{a}} = U_{r,\hat{b}} = -\frac{1}{2}U_{r,\hat{c}} = -\frac{1}{6}\omega^2 r^2. \qquad (2)$$

The lunar radii due to these potentials can be expressed by $r_{\hat{a},\hat{b},\hat{c}} = -h_2 < U_{\hat{a},\hat{b},\hat{c}} > r^2 / Gm$, where h_2 is the lunar secular displacement Love number, and m is the lunar mass (*23*). Without better constraints we approximate the young Moon as a strengthless homogenous body, for which $h_2 = \frac{5}{2}$. After summing the centrifugal and tidal potentials, we may obtain $r_{\hat{a},\hat{b},\hat{c}}$ for any orbit. Given the moment relations $A \propto r_{\hat{b}}^2 + r_{\hat{c}}^2$, $B \propto r_{\hat{a}}^2 + r_{\hat{c}}^2$, $C \propto r_{\hat{a}}^2 + r_{\hat{b}}^2$, the gravity harmonic $C_{20} = (r_{\hat{c}} - \frac{1}{2}(r_{\hat{a}} + r_{\hat{b}}))/5r^2$ (*24*), and the definitions of β and γ given previously, we obtain for 3:2 resonance:

$$C_{20} = \frac{Mr^3}{ma^3}\left(-\frac{1}{2}X_{-3,0,0}(e) - \frac{11}{8}\right)$$

$$\beta = \frac{5}{2}\frac{Mr^3}{ma^3}\left(\frac{1}{2}X_{-3,0,0}(e) + \frac{3}{4}X_{-3,2,3}(e) + \frac{11}{8}\right)$$

$$\gamma = \frac{15}{4}\frac{Mr^3}{ma^3}X_{-3,2,3}(e). \qquad (3)$$

Similarly, for synchronous rotation, we obtain:

$$C_{20} = \frac{Mr^3}{ma^3}\left(-\frac{1}{2}X_{-3,0,0}(e) - \frac{3}{4}\right)$$

$$\beta = \frac{5}{2}\frac{Mr^3}{ma^3}\left(\frac{1}{2}X_{-3,0,0}(e) + \frac{3}{4}X_{-3,2,2}(e) + \frac{3}{4}\right)$$

$$\gamma = \frac{15}{4}\frac{Mr^3}{ma^3}X_{-3,2,2}(e). \qquad (4)$$

These equations approximate the tidal and rotational effects for non-changing orbits of arbitrary eccentricity.

We searched the *a*-*e* space of Eq. 3 and 4 to find minimum error solutions to the observed values of β, γ and C_{20}. For synchronous rotation we find one solution at a = 22.9 r_E, e = 0.49, and for 3:2 resonance we find two solutions at a = 24.8 r_E, e = 0.17, and, a = 26.7 r_E, e = 0.61. One means of visualizing how closely these solutions match the observed values is to plot the *a*-*e* solutions for each parameter in *a*-*e* space (Fig. 4.1 and 4.2). For a Moon frozen instantaneously into the average potentials of a given orbit, the values of the

solution curves of β, γ and C_{20} will intersect at a single point. The insets in Fig. 4.1 and 4.2 show that the calculated solutions intersect quite near each other. That is, the Moon's observed moments closely satisfy a specific set of orbital constraints on the ratio of β, γ and C_{20}. To see this effect more clearly, imagine, for example, if the value of the observed C_{20} was smaller by 20%, i.e. closer to producing the value of unity for the ratio $\overline{C}_{20} / \overline{C}_{22}$. In this case the curves would no longer intersect so closely, and the results would be more inconclusive (Fig. 4.1). Currently, altering either β or C_{20} by about 2%, or γ by 8%, will bring the lines into a perfect intersection, a much smaller difference than the discrepancies discussed in the first paragraph. These results show that it is not necessary to invoke density anomalies or other processes to explain most of the power in the low-order lunar moment parameters.

The Moon may have relaxed somewhat since freeze-in, but because β, γ and C_{20} would have relaxed equally, the observed solution would merely be a horizontal displacement in semimajor axis from an earlier three-way intersection. For example, Fig. 4.2 shows a 3:2 resonance solution for the values of 2β, 2γ and $2C_{20}$ (a = 19.6 r_E, e = 0.17), i.e. if the current values are relaxed by 50%. More generally, the Moon need not have frozen instantaneously to produce the moments we observe. The average of the values of β, γ and C_{20} for any two solutions in a-e space produces a valid third solution, so that an evolving orbit may produce not a single true fossil, but a combination (*10*, *25*). For example, in the case of 3:2 resonance, if the Moon started freezing its figure at a = 23 r_E, e = 0.2, the observed values of β, γ and C_{20}, would be higher by a factor of 1.28, 1.43, and 1.27, respectively. Later, if the Moon evolved to an orbit at a = 27 r_E, e = 0.12, and

completed its freeze-in there, we would have at that location 0.73β, 0.57γ, and $0.78C_{20}$. These final and initial parameters average very close to the observed values, but they are not uniformly lower by a single factor, as would be expected for parameters changed by relaxation alone. Therefore, the requirement that the Moon changed rapidly from a state of short relaxation time to long relaxation time is not a stringent one. Combining relaxation and multiple averages over an evolving orbit, a rich history is permitted by the single observed solution.

The Moon's moments closely satisfy three different orbital states because the process that creates the time-averaged potentials is similar in all three cases. Since both eccentric synchronous rotation and 3:2 resonance involves smearing of the tidal potential over a range of lunar longitudes, it is not surprising that solutions can be found for each process at different values of a and e. For example, we also find solutions for 2:1 resonance at $a = 28.6\ r_E$, $e = 0.39$, and $a = 29.0\ r_E$, $e = 0.52$. No one solution for any orbital state is better constrained over the others by the values β, γ and C_{20}. However, we may interpret which state is more likely in the context of what we presently know about the orbital evolution of the Moon and Mercury.

Past high eccentricity orbits for the Moon have been considered possible for some time (*23*, *26*), and it is interesting to note that the Moon's eccentricity is the highest of all solar system satellites with radius > 200 km. In general, torques on a satellite from tides raised on the primary body will increase eccentricity, while energy dissipation in the satellite due to tides raised by the primary body will decrease eccentricity. Peale gives an

expression for the energy dissipation rate in a low eccentricity synchronous orbit (*27*), but there are no readily available expressions for orbits with higher order resonances. Deriving new expressions and interpreting plausible orbital histories is not possible in the limited space here, but we note that for any combination of e, k, and Q of the Earth and Moon there will be a critical initial eccentricity above which eccentricity may start to increase. Touma and Widsom have also studied in detail the process by which a synchronously rotating Moon can be excited into high eccentricity ($e = 0.5$) at $a = 4.6\ r_E$, in a resonance known as the evection (*28*). Numerical models of lunar accretion give eccentricities that range from 0 to 0.14 (*29*).

It has long been considered that the Moon may have passed through resonances higher than synchronous (*23*, *30*, *31*), and it is believed that Mercury passed through resonances higher than 3:2 (*30,32*). Among the solar system satellites, the Moon has one of the highest capture probabilities into 3:2 resonance (*31*). Formation by giant impact would leave the Moon to form near 4 r_E (*29*), where synchronous orbital periods would be greater than 10 hours. The initial spin rate of the Moon may be as low as 1.8 hours before reaching rotational instability (*31*), leaving open the possibility of sufficient angular momentum to permit greater than synchronous resonances.

The probability of capture into resonance generally decreases with the order of the resonance (*30*), so capture in the 3:2 resonance would is more likely than the 2:1 resonance. As for the high-*e* solutions for synchronous rotation and 3:2 resonance, these orbits dissipate energy faster and would change orbital parameters faster than their low-e

counterpart. The low-e 3:2 solution may therefore have the slowest evolving orbit, which may be more compatible with freeze-in. The Q value for the very young Moon and Earth, possible formation of the Moon nearer the evection point, and variations in eccentricity, all affect the probability of achieving a 3:2 resonance. In any case, the Moon must have eventually escaped any past 3:2 state, possibly through eccentricity damping. We note that none of the above processes in early lunar evolution are well explored. While it is difficult to unequivocally rule out the contribution of density anomalies, our high eccentricity solutions represent the first plausible scenarios in agreement with observations made since the 1700s, and may spawn new areas of investigation in the history of lunar dynamics and thermal evolution.

References and Notes

1. P. S. Laplace, *Traité de Mécanique Celéste*, Vol. II, Book V, Ch. II (Paris Duprat, Bachlier 1798-1827).

2. W. F. Sedgwick, *Messenger of Math.* 27, 171 (1898).

3. H. Jeffreys, *Memoirs of the Roy. Astro. Soc.* 60, Part 5, 187 (1915).

4. H. Jeffreys, *Mon. Not. of the Roy. Astro. Soc.*, Geophys. Supplement 4, No. 1 (1937).

5. H. Jeffreys, *The Earth* (Cambridge U. Press, Cambridge, 1970).

6. A. S. Konopliv *et al.*, *Science 281*, 1476 (1998).

7. J. G. Williams, D. H. Boggs, C. F. Yoder, J. T. Ratcliff, J. O. Dickey, *J. Geophys. Res.* 106, 27933 (2001).

8. Z. Kopal, *Proc. Roy. Soc. London Ser. A* 296, 254 (1967).

9. The normalized second-degree coefficients are given by $\overline{C}_{20} = C_{20}/\sqrt{5}$ and $\overline{C}_{22} = \sqrt{\frac{12}{5}} C_{22}$.

10. D. J. Stevenson, *Proc. Lunar and Plan. Sci. Conf.* XXXII, abstract 1175 (2001).

11. P. Goldreich, J. Toomre, *J. Geophys. Res.* 74, 2555 (1969).

12. M. Lefftz, H. Legros, *Phys. Earth Planet. Int.* 76, 317 (1993).

13. K. Lambeck, S. Pullan, *Phys. Earth Planet. Int.* 22, 29 (1980).

14. S. K. Runcorn, *Nature* 195, 1150 (1962).

15. P. Cassen, R. E. Young, G. Schubert, *Geophys. Res. Lett.* 5, 294 (1978).

16. S. Zhong, M. T. Zuber, *J. Geophys. Res.* 105, 4153 (2000).

17. G. A. Neumann, M. T. Zuber, D. E. Smith, F. G. Lemoine, *J. Geophys. Res.* 101, 16841 (1996).

18. T. Kleine, H. Palme, K. Mezger, A. N. Halliday, *Science 310*, 1671 (2005).

19. C. D. Murray, S. F. Dermott, *Solar System Dynamics* (Cambridge U. Press, Cambridge, 1999).

20. J. Touma, J. Wisdom, *Astronomical Journal* 108, 1943 (1994).

21. R. D. Ray, R. J. Eanes, F. G. Lemoine, *Geophys. J. Intl.* 144, 471 (2001).

22. The Hansen functions $X_{l,p,q}(e)$, satisfy $\left(\frac{R}{a}\right)^l \cos(pf) = \sum_q X_{l,p,q}(e)\cos(q\tilde{M})$ (*33*), where f is the true anomaly and $\tilde{M}$ is the mean anomaly. For our purposes $l = -3$. A 1:1 spin-orbit resonance is represented by $p = 2$ and $q = 2$, while a 3:2 and 2:1 resonance is represented by $p = 2$, $q = 3$, and $p = 2$, $q = 4$, respectively. The Hansen functions are also called Hansen coefficients, and the expansions in e to fourth order can be found in Table 3.2 of (*34*), albeit with a different subscript convention.

23. S. J. Peale, P. Cassen, *Icarus* 36, 245 (1978).

24. C. F. Yoder, *Global Earth Physics*, T.J. Ahrens, Ed. (AGU, 1995).

25. The simple average of two different sets of parameters β, γ and C_{20} may take place during the transition from the state of low relaxation time, to the state of long relaxation time. During this time, the Moon is plastic enough to accommodate changes in form, yet stiff enough to retain some signature of its state when freeze-in started. In fact, the Moon is necessarily a sum of different orbits, however close or far apart, if the fossil bulge hypothesis is valid.

26. P. Goldreich, *Mon. N. of the Roy. Astro. Soc.* 126, 257 (1963).

27. S. J. Peale, *Celest. Mech. Dyn. Astron.* 87, 129 (2003).

28. J. Touma, J. Wisdom, *Astron. J.* 115, 1653 (1998)

29. E. Kokubo, I. Shigeru, M. Junichiro, *Icarus* 148, 419 (2000).

30. P. Goldreich, S. J. Peale, *Astron. J.* 71, 425 (1966)

31. S. J. Peale, in *Satellites,* J. A. Burns, Ed. (U. Arizona Press, Tucson, 1978).

32. Mercury's unnormalized coefficients $C_{20} = 6\times10^{-5} \pm 2.0$ and $C_{22} = 1\times10^{-5} \pm 0.5$ (*35*) are not reproduced by any orbit-spin resonance at Mercury's current semimajor axis.

33. H. C. Plummer, *An Introductory Treatise on Dynamical Astronomy*, (Dover, New York, 1960).

34. W. M. Kaula, *Theory of satellite geodesy* (Dover, New York, 1966).

35. J. D. Anderson, G. Colombo, P. B. Espsitio, E. L. Lau, G. B. Trager, *Icarus* 71, 337 (1987).

Figures

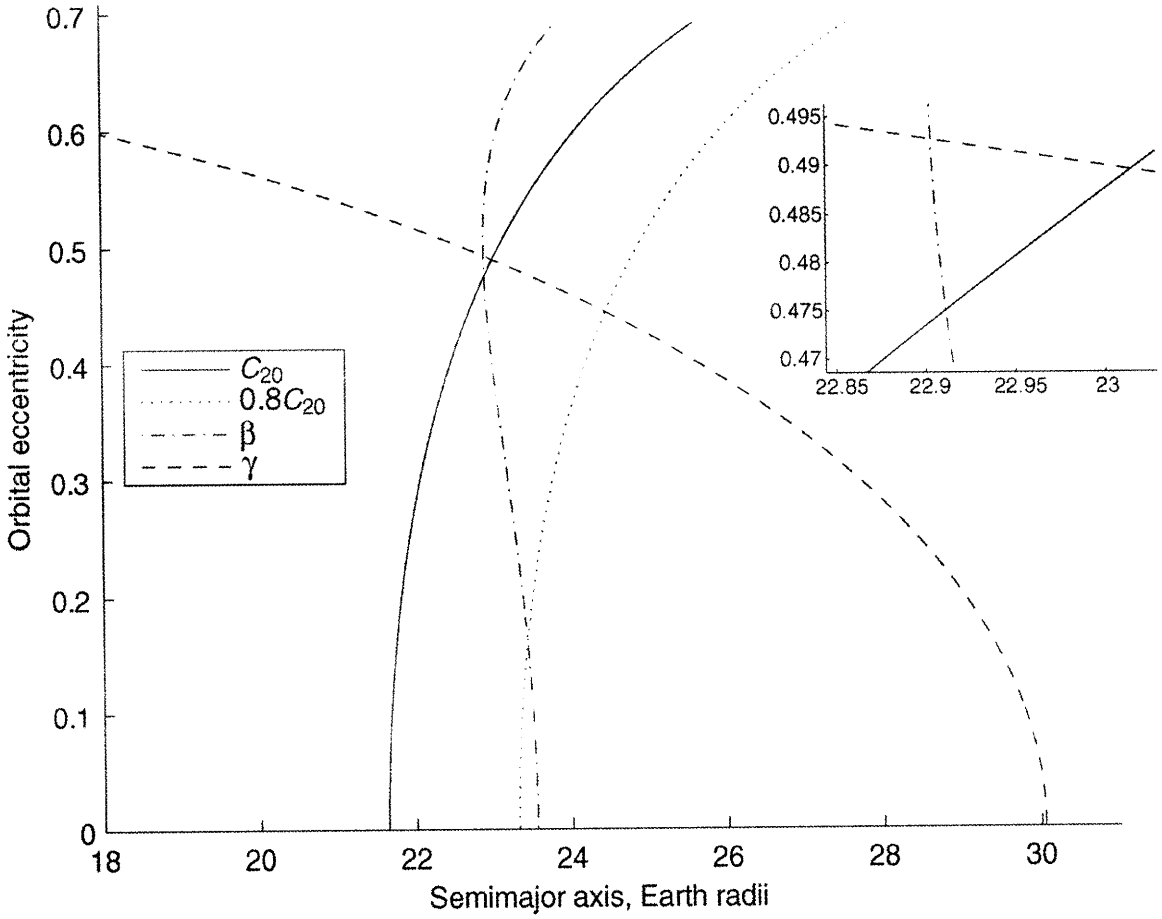

Figure 4.1. Synchronous spin-orbit solutions in a and e that give the observed values of β, γ and C_{20} (Eq. 4). The minimum error solution for the observed values is $a = 22.9\ r_E$, $e = 0.49$, near the intersection of the three curves. Valid a-e solutions to a hypothetical $0.8C_{20}$ are plotted to show the uniqueness of the observed parameters β, γ and C_{20}. Since the values β, γ and C_{20} are independent, there is no a priori reason to expect the curves to intersect so closely, other than the remanence of a past orbital state. Inset: Close-up of the near intersection of the three solutions to the observed values of β, γ and C_{20}.

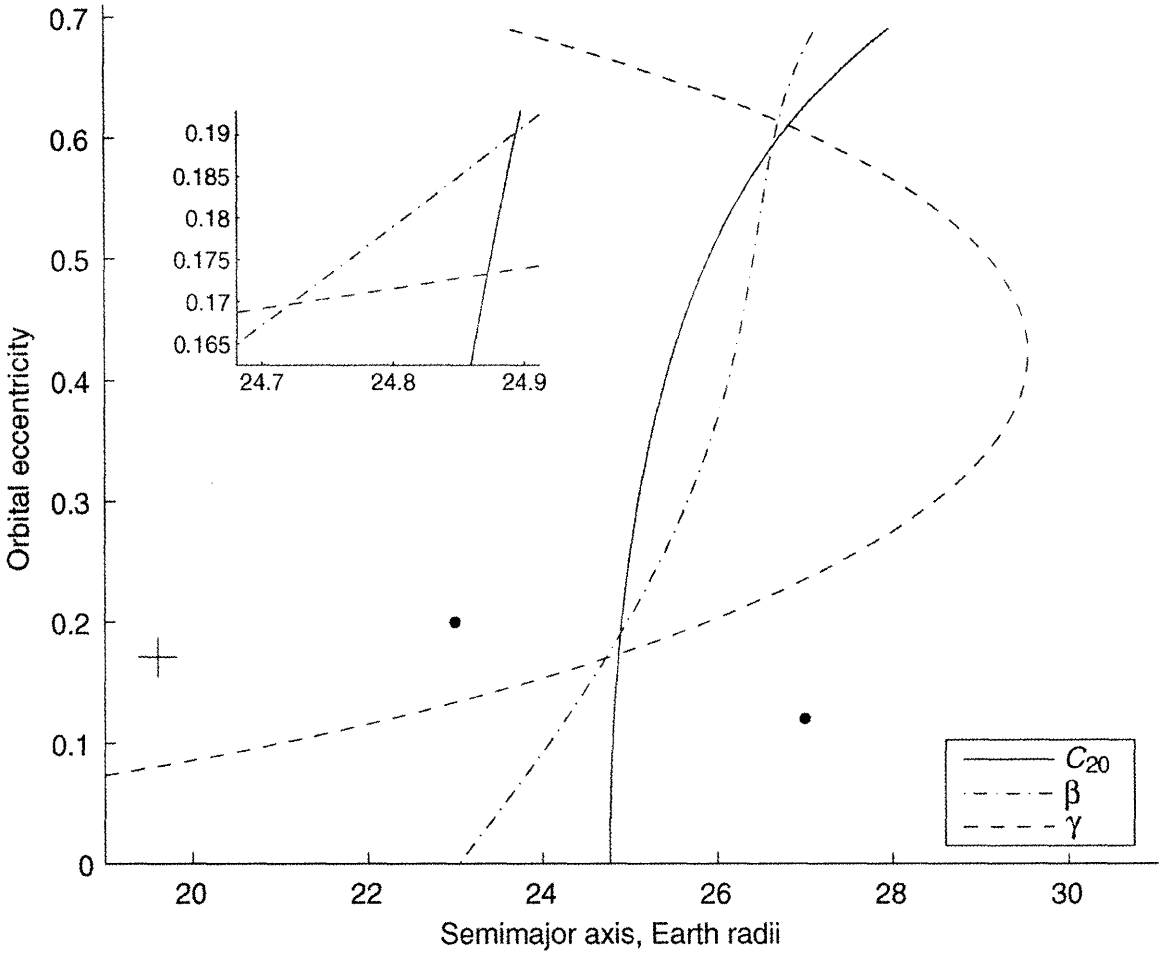

Figure 4.2. 3:2 spin-orbit solutions in a and e that give the observed values of β, γ and C_{20} (Eq. 3). The minimum error solutions are at $a = 24.8$, $e = 0.17$ and $a = 26.7$, $e = 0.61$. Since the values β, γ and C_{20} are independent, there is no a priori reason to expect the curves to intersect so closely, other than the remanence of a past orbital state. The cross at $r_E = 19.6$, $e = 0.17$, shows an orbit solution if the current values of β, γ and C_{20} are from a fossil bulge that has relaxed by 50%. The two dots show solutions that average to the observed values of β, γ and C_{20}. Averages of other sets of points are possible, including ones that do not fall on the line joining the two dots. Inset: close-up of the bottom intersection.

Chapter 5

A primordial origin for the lunar eccentricity

In revision for Astrophysical Journal Letters, Ian Garrick-Bethell and Maria T. Zuber.

Abstract

Using tidal parameters consistent with an Earth and Moon left hot by the Moon-forming impact, we apply an analytical model of tides to show that the present lunar eccentricity can be explained by a continuously increasing eccentricity since shortly after accretion. While initial high eccentricity lunar orbits are permissible, we focus on a simple, initially-damped lunar eccentricity and follow its evolution as the Moon and Earth cool. We find that simple tidal evolution alone can explain the current eccentricity.

5.1. Introduction

The Moon's mean eccentricity (e) of 0.055 is the highest for any large satellite in the solar system. For comparison, all of the major satellites (> 400 km diameter) of the gas giants have $e < 0.029$. Not only is the lunar eccentricity high, but it is also presently increasing (Williams et al. 2001). At first this high and increasing lunar eccentricity seems to make the Moon an outlier. However, extrasolar planets, comets, transneptunian objects, and irregular satellites all commonly have high eccentricities. How does the Moon fit into this spectrum?

Goldreich's development of eccentricity damping (Goldreich 1963) illustrates that dissipation in the primary body will increase the eccentricity, while dissipation in the satellite will decrease the eccentricity. Depending on the relative values of the tidal parameters of the two bodies, the net effect will be to increase or decrease eccentricity.

Of particular importance is ratio of the specific energy dissipation of the planet, Q_P, to that of the satellite, Q_s. For high Q_P/Q_S, the dissipation in the planet is low and the eccentricity will tend to damp. For the gas giants, $Q_P > 10^4$ (Yoder & Peale 1981), resulting in low tidally-damped free eccentricities for satellites close to the planet. However, the Earth and Moon are both rocky silicate bodies that are expected to have grossly similar tidal properties and therefore comparable relative dissipation in each body (Goldreich 1963). In fact, just after the putative giant impact that formed the Moon (Cameron & Ward 1976; Daly 1946; Hartmann & Davis 1975), the two bodies were both likely to have been hot and have similar Qs. The second-degree potential Love number for the Moon, k_2, which is the other important tidal parameter, was likely more than an order of magnitude higher during this time than it is today. It is also during this time, the first few million years after lunar formation, that the growth or decay of the eccentricity is the strongest and influences the present eccentricity the most. Previous studies have examined the eccentricity evolution of the Moon (Mignard 1980), but not in the context of the giant impact. Kaula and Yoder (1976), and Cuk (2007) have suggested that resonances with Jupiter and Venus could have increased an initially damped eccentricity to yield the present value. Cuk calculated that in order to achieve the present eccentricity a Jupiter evection resonance would require $e > 0.005$ when $a = 53R_E$. An earlier resonance with Venus would satisfy this requirement if $e > 0.001$ when $a = 46.6R_E$.

Here we show that the lunar eccentricity need not become low enough after the giant impact to require the evection resonances to produce the present eccentricity. Simple tidal growth of the eccentricity can increase the eccentricity to large values at very early times, and evidence suggests it may have (Garrick-Bethell, Wisdom, & Zuber 2006). However, here we will restrict our attention to an even simpler scenario, one in which the eccentricity was initially damped after the Moon's accretion from a debris disk after a giant impact. We show that in this case the simplest explanation for the lunar eccentricity is that it has been increasing continuously to reach its present value, just as it is increasing today. We use an analytical model of Earth and lunar tides and start the Moon near the Roche limit for silicates, and also at a semimajor axis a expected after the solar evection (if it occurred), $a = 6R_E$. The Earth and Moon are each initially given tidal

parameters expected for their hot, post-giant impact states. We then forward-evolve the lunar orbit and allow the parameters to vary towards the present values as they would if the Moon was cooling, while fine-tuning them to exactly reach the present state. In doing so, we obtain a minimum permissible initial eccentricity and limits on Q and k_2 for the Earth and Moon to reach the present eccentricity through tidal evolution. These limits are consistent with values expected from the giant impact and values for other silicate bodies in the solar system.

5.2. Methods

Mignard and Hut derived approximate expressions for the tidal evolution of eccentricity and semimajor axis (Hut 1981; Mignard 1980). Mignard's evolution equations can be written in terms of Hansen coefficients as

$$\frac{dX}{dt} = 6 \times 4\pi^2 k_{2,E} \frac{M_M}{M_S} \frac{M_M}{\eta} \frac{\Delta t_E}{\widetilde{P}^2} \frac{1}{X^7} \left[-(A+1) \times \frac{3}{7} e H_{-9,1,0}(e) - (A+1) \times (1-e^2) H_{-10,0,0}(e) \ldots \right.$$
$$\left. + \left(\frac{\dot{\theta}_E}{n} + A \frac{\dot{\theta}_M}{n} \right) (1-e^2)^{1/2} H_{-8,0,0}(e) \right]$$

$$\frac{de}{dt} = 3 \times 4\pi^2 k_{2,E} \frac{M_M}{M_E} \frac{M_M}{\eta} \frac{\Delta t_E}{\widetilde{P}^2} \frac{1}{X^8} \left[-(A+1) \times \frac{18}{7} (1-e^2) H_{-9,1,0}(e) \ldots \right.$$
$$\left. + \left(\frac{\dot{\theta}_E}{n} + A \frac{\dot{\theta}_M}{n} \right) \frac{11}{5} (1-e^2)^{1/2} H_{-7,1,0}(e) \right], \qquad (3)$$

where M is the Earth or lunar mass, X is the semimajor axis measured in Earth radii, n is the lunar mean motion, $\dot{\theta}$ is the rotation rate of the Earth or Moon, and η is the reduced mass, $M_E M_M/(M_E+M_M)$. The E and M subscripts refer to the Earth and Moon, respectively. The constant $\widetilde{P}$ is the period of the Moon at X = 1. The Hansen coefficients $H_{l,p,q}$ satisfy:

$$\left(\frac{r}{a}\right)^{l} \cos pv = \sum_{q} H_{l,p,q}(e) \cos q\tilde{M} , \qquad (4)$$

where r is the orbit radius, v is the true anomaly and $\tilde{M}$ is the mean anomaly. Table 1 lists the Hansen coefficients needed for equation 3. The variable Δt_E is the time required for the Earth to rotate by an angle equal to the geometric tidal lag angle ε, *i.e.* $\dot{\theta}_E \times \Delta t_E = \varepsilon = \delta/2 = 1/(2Q_E)$, where δ is the tidal phase lag. Mignard's tidal model assumes a constant Δt_E, or that the phase lag and $1/Q$ are proportional to frequency (see (de Surgy & Laskar 1997; Touma & Wisdom 1994)). This assumption is in contrast to tidal models that assume a constant Q. In reality, Williams et al. (2001) showed Q to be only weakly dependent on frequency, *i.e.* $Q \sim \dot{\theta}^{-0.19}$ (Williams, et al. 2001). As a compromise, we use Mignard's formulation of the frequency-dependent tidal torque within an instantaneous orbit in *a-e* space, but assume the phase lag (or Q) is constant as the orbit evolves in a and e. Therefore, when integrating equation 3, we continually convert a chosen constant Q to Δt_E using the Earth and lunar rotation rates. This procedure has the advantage of using a well tested and reasonable description of tidal accelerations, yet permits the use of a model of Q that is more easily interpretable from a geophysical perspective. We note that using Mignard's original frequency-dependent model produces qualitatively similar results, *i.e.* a sharp initial decay of eccentricity followed by an increase in eccentricity, comparable his figure 5 (Mignard 1980).

The parameter A in equation 3 is of particular importance and is defined by

$$A = \frac{k_{2,M}}{k_{2,E}} \frac{Q_E}{Q_M} \left(\frac{M_E}{M_M}\right)^2 \left(\frac{R_E}{R_M}\right)^5 . \qquad (5)$$

Higher values of A imply higher relative lunar dissipation and higher eccentricity damping. The current value of A is about 0.28 using $k_{2M} = 0.02$, $k_{2E} = 0.3$, $Q_E = 12$ and $Q_M = 29$ (J. Williams, personal communication). Using the present observed values for the Earth and Moon in equation 3, we obtain $\dot{a} = 3.7$ cm yr^{-1} and $\dot{e} = 1.4 \times 10^{-11}$ yr^{-1}, in

reasonable agreement with observed values of 3.8 cm yr^{-1} and 2.0×10^{-11} yr^{-1}, (Williams, personal communication, and (Williams, Boggs, & Ratcliff 2007; Williams, et al. 2001)).

The evolution equations are integrated while conserving the current Earth-Moon system angular momentum, which is satisfied by

$$\frac{\dot{\theta}_E}{n} = \frac{\eta}{M_E}\frac{M_E R_E^2}{C}\left[\frac{HX^{3/2}}{(GM_E M_M^2 R_E)^{1/2}} - X^2(1-e^2)^{1/2}\right], \qquad (6)$$

where H is the sum of the Earth and Moon angular momentum, C is the moment of inertia of the Earth (assumed to be the current value of $0.33M_ER_E^2$). The angular momentum of the lunar spin is negligible (<0.1% at all times). Solar tides on the Earth drain its angular momentum, but this too is a small effect, being 1.9% of the total system angular momentum and 11% of the Earth's angular momentum after 4.5 Ga, conservatively assuming a mean $Q_E = 20$ and $k_{2,E} = 0.3$ (predominantly drained after $a = 30R_E$).

The inclination I can also be included in equation 3 as a factor cos$I$, but I has generally been small and therefore does not significantly change the evolution of either eccentricity or semimajor axis. For simplicity we assume $I = 0$. Under these assumptions, the evolution equations are also unchanged by the inclusion of solar gravity (Mignard 1981). We assume synchronous rotation of the Moon throughout the analysis.

5.3. Tidal evolution scenarios

5.3.1 *Early tidal parameters*

Models of lunar accretion predict that the Moon should have accreted at about 1.3 times the Roche limit for silicate density materials ($2.9R_E$), or about $3.8R_E$ (Kokubo, Ida, & Makino 2000). The eccentricity at the time of accretion is unknown, but ranges from about 0.01-0.1 in simulations (Kokubo, et al. 2000), so we will explore e = 0.01, 0.025

and 0.1. Immediately after the Moon-forming giant impact, both the Moon and Earth were likely to have been hot and both bodies may have had magma oceans (Canup 2004). Therefore, for k_2 we assume that the newly-accreted Moon behaved like a homogenous fluid, yielding $k_2 = 1.5$. For the Earth we assume $k_2 = 0.92$, or about equal to the fluid Love number for the present Earth's density distribution (0.96) (Munk & MacDonald 1960). These values will tend to produce early eccentricity damping for $Q_M/Q_E < 5$, which is the focus of this paper. For comparison, Jupiter's satellite Io appears to currently have $k_2 = 1.27$ (Anderson et al. 2001), although this k_2 is the value determined gravity observations, and not the tidal effective value. The tidal effective k_2 for Mars is ~0.15 (Yoder et al. 2003).

For Q it is not certain if a magma ocean-like environment on the early Moon or Earth would produce a high or low Q. For example, the Earth is covered in a nearly global water ocean, yet land masses and resonances in the shallow oceans result in an effective global $Q_E = 12$, and Q_E ~280 for the solid Earth (Ray, Eanes, & Lemoine 2001). Global deep oceans could, however, tend to increase Q. Sagan and Dermott (Sagan & Dermott 1982) estimated a ~400 m deep global methane ocean on Titan could provide $Q > 200$, which is required to maintain Titan's high eccentricity (if it is assumed to be primordial, but see (Bills & Nimmo 2005)). The depth of magma ocean-like differentiation on the Moon is estimated to be 100-400 km deep, but the effective depth of the liquid and the thickness of solid rock on the near surface in the few millions of years after accretion, and its effect on Q is unknown. Even the source of dissipation that produces the relatively low present lunar Q, compared to that of the solid Earth and models of the lunar interior, is unknown (Williams, et al. 2001). For comparison, the estimated Q of Mars is ~90, measured using the 5.6 hr synodic forcing period of Phobos (Bills et al. 2005). Our models of orbit evolution lead us to use Q values between 32 and 150 for the early Earth and Moon, well within the limits of our uncertainty. For ease of comparison, we usually assume $Q_E = 50$.

Almost no work has been done to model how the enormous deformations of the Moon while in close proximity to Earth would have affected the dissipation process (Boss &

Peale 1986). For example, assuming $k_{2,M} = 1.5$, at the Roche limit ($a = 2.9R_E$) the tidal amplitude on the Moon is a remarkable 290 km, at $a = 3.8R_E$ it is 130 km, and at $a = 10R_E$ it falls to 7 km. Given the enormous deformations, it is not difficult to imagine that the effective k_2 could be different than the fluid values. Therefore, small uncertainties in Q and k_2 are overwhelmed by this uncertainty at very low semimajor axes.

5.3.2 *Evolution scenarios*

In Figure 5.1 we show the results of integrating equation 3 and plot a tidal evolution of the Moon from $a = 3.8R_E$ to the present semimajor axis and eccentricity. In this evolution we use three sets of tidal parameters in three time periods Δt that last for 5 My (hot early phase), 2 By (intermediate warm phase), and 2.495 By (similar to present values), for a total of 4.5 By of evolution. The tidal parameters in these and subsequent blocks are meant to represent average values over each time period. They are imperfect in that they are not derived from any specific physical model of cooling. In each block $k_{2,M}$ decreases from 1.5 to 0.2 to 0.035 to represent the gradual cooling and development of strength in the Moon, with A falling from >5.4 to 3.3 to 1.0. During these periods $k_{2,E}$ similarly decreases from 0.92 to 0.45, to 0.3. We also allow for three different initial eccentricities (0.01, 0.025 and 0.1) and find that during the hot early phase the initial Q values (150, 125, 107) and A values (5.4, 6.5, 7.6) for each of these eccentricities are very similar to reach the same location in a-e space 5 My later. From this location, lower lunar Q and k_2 values permit the Moon to reach the present eccentricity. All of the Q values used are well within range of values expected for silicate bodies, and within our uncertainty for the Moon and Earth at the time of formation (above). In the three cases shown, $\dot{e}$ eventually reaches a positive rate that continues until the present. In sum, nearly the entire eccentricity history can be explained using reasonable tidal parameters, and a range of initial eccentricities.

In Figure 5.1 we also show two evolution scenarios for a Moon that initially had a lower value of k_2 (0.1 and 0.3, labels A and B), relevant for the case of a Moon that accreted cold, yielding low values of A (1.3 and 2.2). These low-A evolutionary paths result in

large increases in eccentricity. Unfortunately, even if the Moon accreted cold and had a lower k_2, altering the Love number of the Earth and/or the Q parameters of either body could make A higher and damp the eccentricity to mimic the solution discussed in the previous paragraph. Therefore, from models of the eccentricity evolution alone, it is not possible to determine if the Moon accreted cold. If the eccentricity did increase substantially at early times, tidal dissipation would almost guarantee significant heating that would push the lunar Love number values closer to the fluid value, and cause eccentricity damping.

In Figure 5.2 we plot similar evolution scenarios as in figure 1, except that we assume the Moon has passed through a solar evection resonance (Touma & Wisdom 1998) and ended with a modest eccentricity of 0.01, 0.025 or 0.1. The tidal evolution parameters after the initial hot phase of 5 My are the same as the one shown in Figure 5.1. The initial Q_M values that are required to reach a similar location in a-e space after 5 My are generally lower than for the cases in Figure 5.1 for all starting eccentricities, (77, 63, and 51, for e = 0.01, 0.025, and 0.1, corresponding to A values of 10.6, 12.9 and 16.0). For comparison, we also plot two low A solutions with positive $\dot{e}$ (labeled A and B), even though they are less likely to have taken place after strong heating during the solar evection.

Can we use the present eccentricity to derive constraints on the past tidal properties of the very early Earth and Moon? In Figure 5.3 the solid line shows a highly-dissipative Moon with large eccentricity damping, although eccentricity is still increasing. Such high damping is unlikely to have been achieved for all of lunar history, as we have plotted, because this evolution uses a very large $k_{2,M}$ (0.45, 22 times the present value) and Q_E = 55, a value more than 4 times larger than the present. Therefore this line serves as an approximate upper limit on the eccentricity that can be achieved for $a > 19R_E$ and still permit tidal evolution of the Moon to its present value. We caution that depending on the tidal Love numbers of the Earth and Moon, higher dissipation rates are possible for short time periods, which would permit initially high-eccentricity orbits. Note that this line is only meaningful when examining initially-damped orbits. We plot calculated tidal

evolutionary paths from $a = 3.8$ and $6R_E$ that just intercept the bottom of this line in order to determine the minimum allowable initial lunar dissipation (minimum A). We find that A can be as low as 3.6 (starting from $a = 3.8R_E$ and $e = 0.01$), corresponding to an upper limit on the value $Q_M/Q_E = 158/35 = 4.5$, and still achieve the present eccentricity. The upper limit on Q_M/Q_E only applies to bodies with nearly fluid Love numbers (1.5 and 0.92), and not surprisingly, the limit on Q_M/Q_E is close to the limiting value that produces initially-damped orbits (instead of increasing eccentricity) when the Love numbers are fluid (~5). Unfortunately, we cannot constrain the actual value of Q_M or Q_E.

We also derive an upper limit on the early lunar dissipation and eccentricity damping for several initial scenarios in Figure 5.4. The solid top line shows an evolution with a weakly dissipative Moon (low A) value and high $\dot{e}$. Such a high $\dot{e}$ is unlikely to have been achieved for all of lunar history because it assumes a $k_{2,M}$ close to the present value. Any lower A makes it difficult to achieve the present eccentricity by 4.5 By. Therefore, this line serves as a lower limit on the eccentricity that can be achieved and still permit tidal evolution of the Moon to its present value. We plot four solutions that just intercept this line, starting from $a = 3.8$ or $a = 6R_E$, and from $e = 0.01$, $e = 0.025$, or $e = 0.1$ (solid lines). We find that A can be as high as 16.6 (for initial $e = 0.1$ after the evection at $6R_E$), corresponding to $Q_M/Q_E = 49/50 \sim 1$. As before, this lower limit on Q_M/Q_E is only valid assuming the Earth and Moon have values close to the fluid Love numbers. Considering both this upper limit and the lower limit from Figure 5.3, the ratio Q_M/Q_E may vary between 1 and 4.8 in hot, initially-damped, systems. The lowest eccentricity that is achieved is ~0.001.

Do the Venus or Jupiter resonances place any special constraints on the early tidal parameters that would cause these scenarios to be favored? In Figure 5.4 we plot two solid lines with similar A and very high $\dot{e}$ as the top solid line, except that each of these evolutionary paths reach the lower limits on a and e for the Jupiter and combined Venus-Jupiter resonance scenarios to have taken place (~0.001 at 46.6 RE, ~0.005 at $53R_E$, respectively) (Cuk 2007). Below these lines the eccentricity cannot have grown to reach the required value for each evection, and the present eccentricity could not be explained

by the resonances (or tides). We find the required tidal parameters to stay above these two lines during the first 5 My are not much different than the values required to stay above the top line that reaches the present a and e by tidal evolution alone. For the a = $3.8R_E$ case, the upper limit on A to meet the evection evolutionary paths ranges from 8.0-10.6 or Q_M/Q_E = 1.54-2.02, for e = 0.01-0.025, compared to A = 5.7-6.7 or Q_M/Q_E = 2.42-2.88 for the pure tidal evolution that reaches the present e. For the post-evection scenario, the upper limit on A to meet the evection evolutionary paths ranges from 16.6-25.2 or Q_M/Q_E = 0.50-0.98, for e = 0.01-0.1, compared to A = 11.3-16.6 or Q_M/Q_E = 0.98-1.44, for the pure tidal evolution to reach the present e. These results are not changed using different time intervals (*e.g.* 1 My initial evolution). Because the tidal parameters are similar, we cannot rule out the Jupiter and Venus resonances on the basis of unreasonable geophysical properties. However, the similarity also implies the resonances are not required to explain the present eccentricity.

5.4. Conclusions

We have shown that: 1) the present lunar eccentricity may be primordial; continuously increasing eccentricity from shortly after the giant impact to the present day requires no special conditions or resonances. With the Moon starting hot and cooling to its present state, the Q and k_2 values required for evolution to the present eccentricity are reasonable and within the expected range for silicate bodies. Our inability to model the exact cooling history and evolution of tidal parameters prevents us from guaranteeing that the present state is inevitably reached from tides alone, but our results demonstrate that it is plausible. 2) The permissible ratio of Q_M/Q_E that produces the present eccentricity by tides ranges from 1-4.5 for an initially-damped e, including eccentricities produced by the solar evection up to e_i = 0.1. The value of Q_M is greater than Q_E for all purely tidal models. 3) The required early tidal parameters to reach the Jupiter and Venus resonance lower a-e limits are similar to those of pure tidal evolution. Therefore, while such evolutionary scenarios cannot be ruled out, there is no special constraint placed on the early tidal parameters by these resonances.

We did not consider, and thus cannot evaluate, the relevance of early high-eccentricity orbits in which damping at later times can yield the present lunar eccentricity. Such a possibility is worthy of future scrutiny. These limitations aside, however, our study demonstrates that the giant impact model for the formation of the Moon is compatible with a suite of simple and plausible scenarios for the evolution of the lunar orbital eccentricity.

References

Anderson, J. D., Jacobson, R. A., Lau, E. L., Moore, W. B., & Schubert, G. 2001, J Geophys Res, 106, 32963

Bills, B. G., Neumann, G. A., Smith, D. E., & Zuber, M. T. 2005, J. Geophys. Res., 110, E07004

Bills, B. G., & Nimmo, F. 2005. in American Geophysical Union, Fall Meeting How Jupiter helped Titan retain a finite orbital eccentricity (San Francisco), abstract P33C

Boss, A. P., & Peale, S. J. 1986, Conference on the Origin of the Moon, 59

Cameron, A. G. W., & Ward, W. R. 1976, Proc. Lunar Planet. Sci. Conf., 7th, 120

Canup, R. M. 2004, Annual Reviews of Astronomy and Astrophysics, 42, 441

Cuk, M. 2007. in DDA meeting 38, Excitation of lunar eccentricity by planetary resonances (American Astronomical Society), Abstract 3.03

Daly, R. A. 1946, Proceedings of the American Philosophical Society 90, 104

de Surgy, N. O., & Laskar, J. 1997, Astron. Astrophys., 318, 975

Garrick-Bethell, I., Wisdom, J., & Zuber, M. T. 2006, Science, 313, 652

Goldreich, P. 1963, Monthly notices of the royal astronomical society, 126, 257

Hartmann, W. K., & Davis, D. R. 1975, Icarus, 24, 504

Hut, P. 1981, Astron. Astrophys., 99, 126

Kaula, W. M., & Yoder, C. F. 1976, Lunar and Planetary Science, 7, 440

Kokubo, E., Ida, S., & Makino, J. 2000, Icarus, 148, 419

Mignard, F. 1980, Moon and Planets, 23, 185

---. 1981, Moon and Planets, 24, 189

Munk, W., & MacDonald, G. J. F. 1960, The rotation of the Earth (New York: Cambridge University Press)

Ray, R. D., Eanes, R. J., & Lemoine, F. G. 2001, Geophysical Journal International, 44, 471

Sagan, C., & Dermott, S. F. 1982, Nature, 300, 731

Touma, J., & Wisdom, J. 1994, Astronomical Journal, 108, 1943

---. 1998, Astronomical Journal, 115, 1653

Williams, J. G., Boggs, D. H., & Ratcliff, J. T. 2007. in 38th Lunar and Planetary Science Conference, Lunar mantle and fluid core results and inner core possibilities (Houston, TX), Abstract 2004

Williams, J. G., Boggs, D. H., Yoder, C. F., Ratcliff, J. T., & Dickey, J. O. 2001, J. Geophys. Res., 106, 27933

Yoder, C. F., Konopliv, A. S., Yuan, D. N., Standish, E. M., & Folkner, W. M. 2003, Science, 300, 299

Yoder, C. F., & Peale, S. J. 1981, Icarus, 47, 1

Tables

Table 5.1. Relevant Hansen coefficients

$H_{-7,1,0}(e)$	$(1-e^2)^{-11/2}(\frac{5}{2}e+\frac{15}{4}e^3+\frac{5}{16}e^5)$
$H_{-9,1,0}(e)$	$(1-e^2)^{-15/2}(\frac{7}{2}e+\frac{105}{8}e^3+\frac{105}{16}e^5+\frac{35}{128}e^7)$
$H_{-8,0,0}(e)$	$(1-e^2)^{-13/2}(1+\frac{15}{2}e^2+\frac{45}{8}e^4+\frac{5}{16}e^6)$
$H_{-10,0,0}(e)$	$(1-e^2)^{-17/2}(1+14e^2+\frac{210}{8}e^4+\frac{35}{4}e^6+\frac{35}{128}e^6)$

Figures

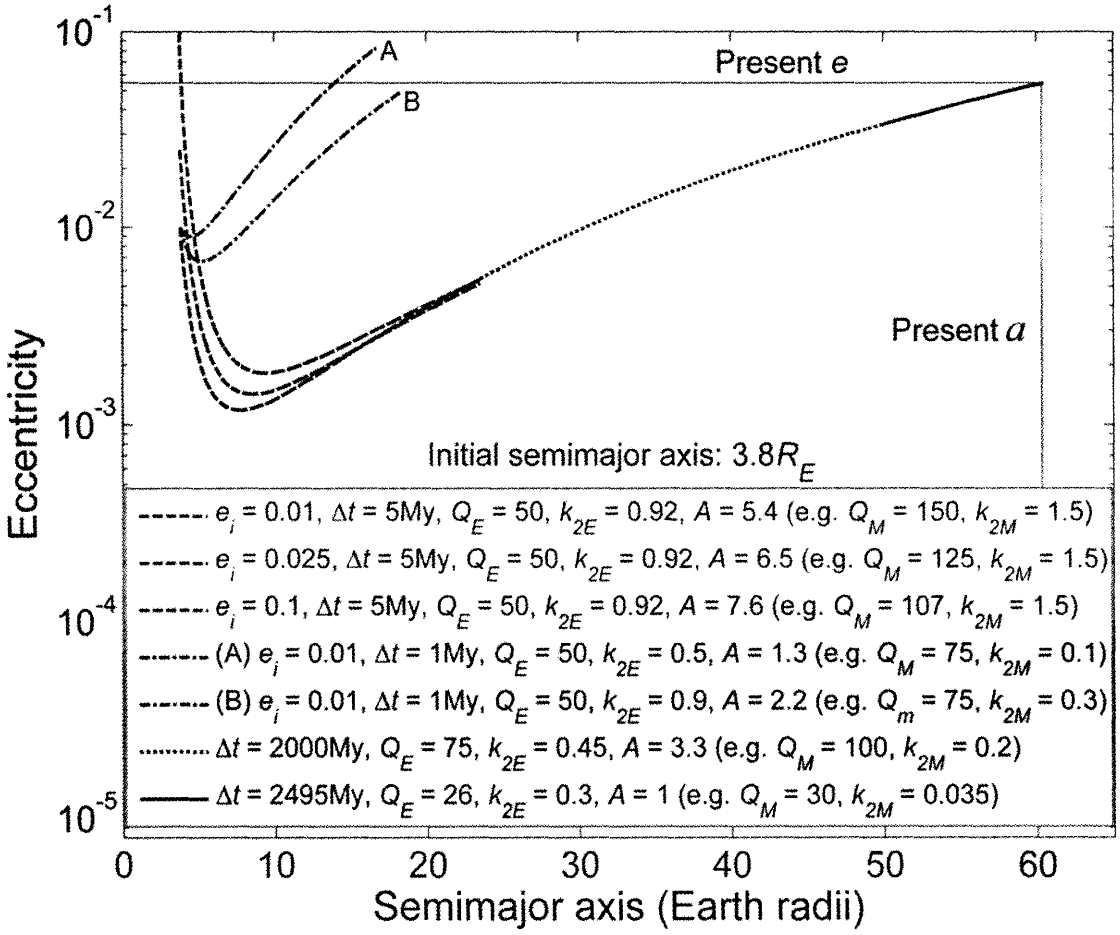

Figure 5.1. Calculated lunar eccentricity evolutions from $a = 3.8R_E$. The dotted and solid lines represent a Moon cooling to achieve tidal parameters close to its present values. Three different initial eccentricities are explored starting from a hot Moon and Earth (dotted lines): 0.01, 0.025, and 0.1. Two positive $\dot{e}$ solutions that may represent an initially cooler Moon are also shown (dash-dot lines A and B).

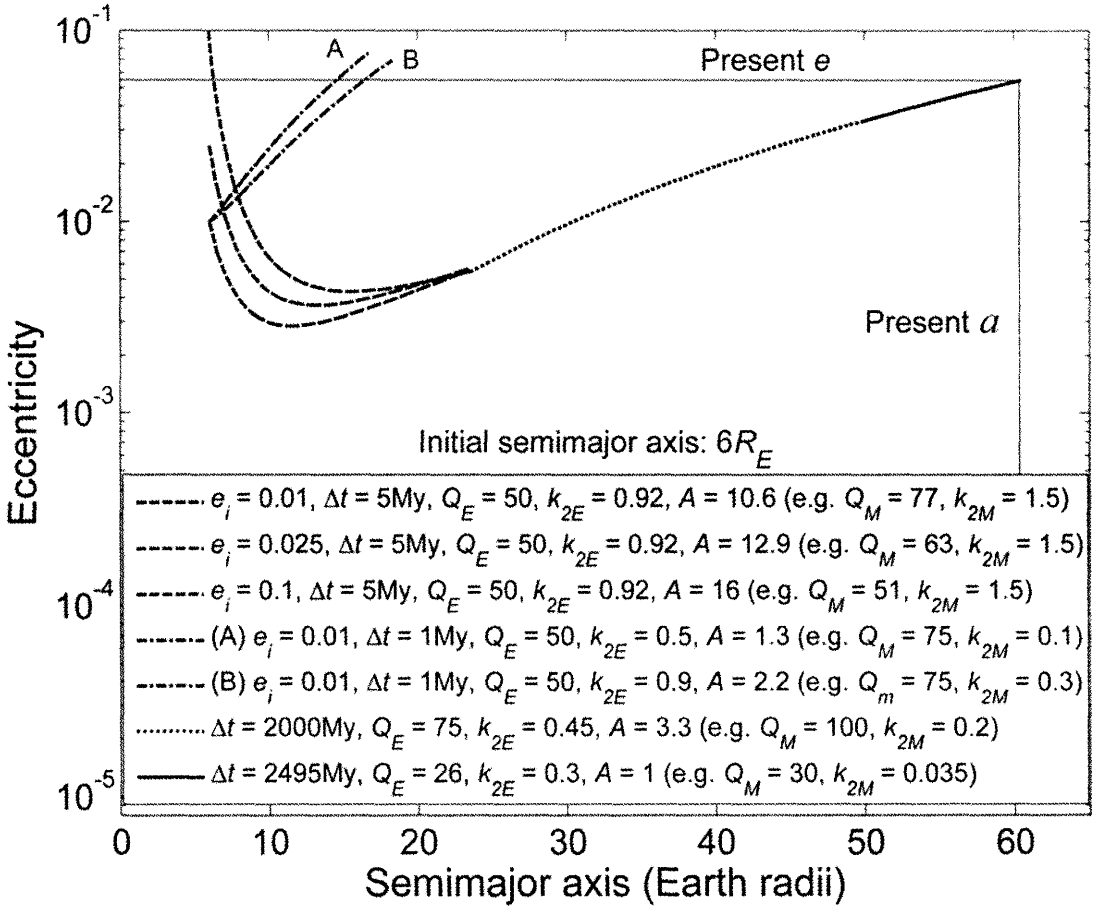

Figure 5.2. Calculated lunar eccentricity evolutions from $a = 6R_E$, the approximate post-solar evection location. The dotted and solid lines represent a Moon cooling to achieve tidal parameters close to its present values. Three different initial eccentricities are explored starting from a hot Moon and Earth (dotted lines): 0.01, 0.025, and 0.1. Two positive $\dot{e}$ solutions are also shown, but are less likely after tidal heating of the Moon during the evection (dash-dot lines A and B).

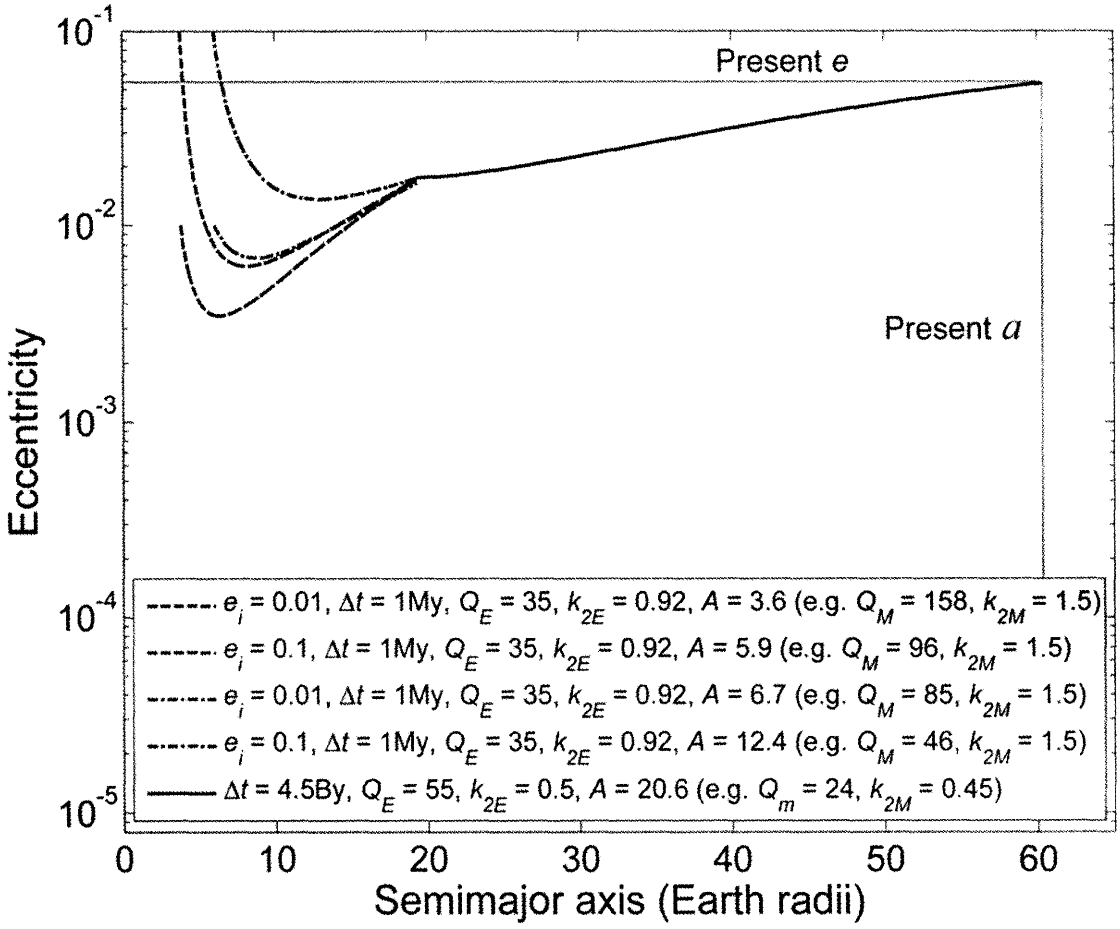

Figure 5.3. The solid line shows a highly dissipative Moon that serves as a lower limit on $\dot{e}$. Solutions significantly above this line could not achieve the present lunar eccentricity through damping, assuming an initially damped system with a hot Moon and Earth. The four early tidal evolutions that meet the solid line are used to derive a lower limit on the early A and an upper limit on Q_M/Q_E.

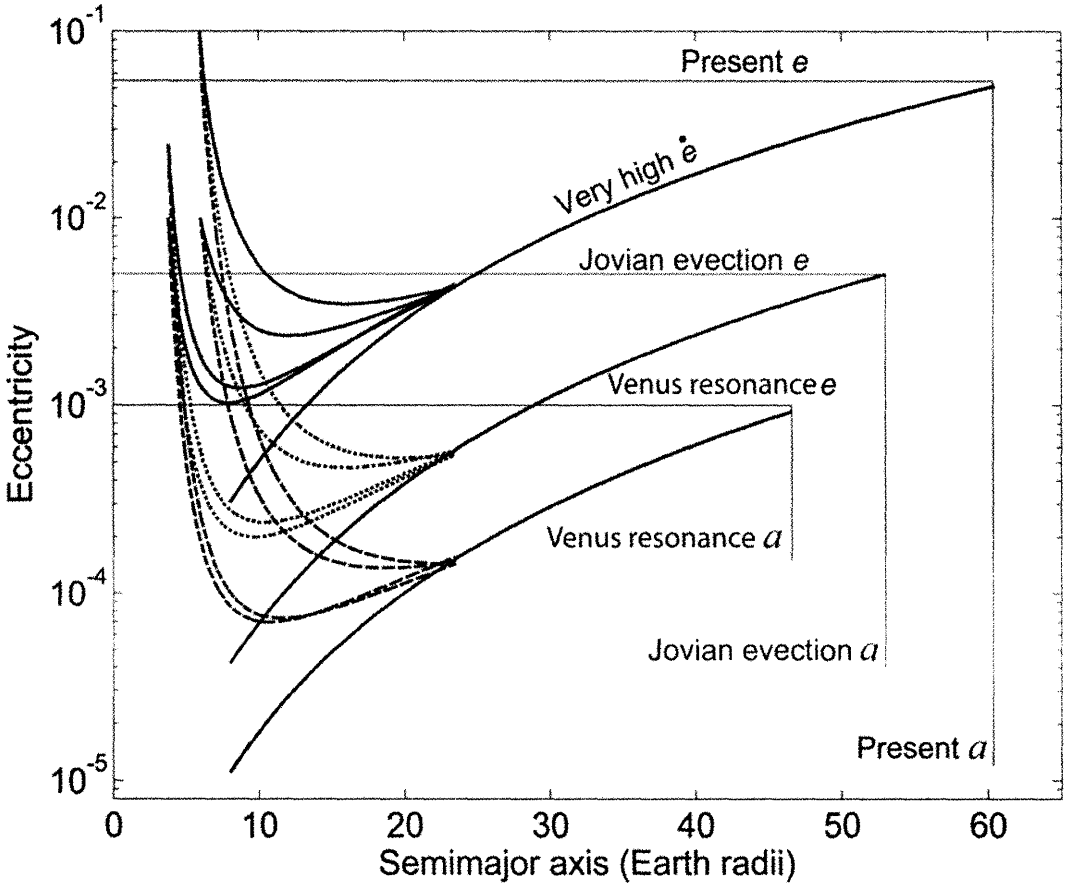

———	Q_E = 35, $k_{2,E}$ = 0.3, A = 0.5 (e.g. Q_M = 50, $k_{2,M}$ = 0.02)		Similar to present
a_i = 8	e_i = 0.000306: Δt = 4500 My		Present day orbit
	e_i = 0.000042: Δt = 2075 My		Jupiter evection
	e_i = 0.000011: Δt = 900 My		Venus evection

Δt = 5 My, Q_E = 50, $k_{2,E}$ = 0.92, $k_{2,M}$ = 1.5 — Post giant impact

	Accretion: a_i = 3.8		Post-evection: a_i = 6.0	
	e_i = 0.01	e_i = 0.025	e_i = 0.01	e_i = 0.1
———	Q_M = 144, A = 5.7	Q_M = 121, A = 6.7	Q_M = 72, A = 11.3	Q_M = 49, A = 16.6
·····	Q_M = 101, A = 8	Q_M = 90, A = 9	Q_M = 49, A = 16.6	Q_M = 37, A = 21.8
- - - - -	Q_M = 86, A = 9.5	Q_M = 77, A = 10.6	Q_M = 40, A = 20.2	Q_M = 32, A = 25.2

Figure 5.4. The three solid lines represent a very weakly-dissipative Moon that serves as an upper limit on $\dot{e}$. Solutions significantly below this line could not achieve the present lunar eccentricity through simple tidal growth (top solid line), the Jupiter evection (middle solid line), or the combined Venus then Jupiter resonance (bottom solid line). The other lines are used to drive upper limits on the early A and a lower limit on Q_M/Q_E to meet each of the three solid lines.

Chapter 6

Geologic contributions to the degree-2 structure of the Moon

Ian Garrick-Bethell and Maria T. Zuber

Abstract

The low-degree gravity and shape of the Moon has long been considered to be anomalously high compared to what is expected from a body that cooled from a magma ocean. To investigate the cause of the low-degree structure, we removed several of the major geologic features that contribute to the lunar shape and gravity. We find that the nearside mascons and South Pole-Aitken basin cannot explain the low order shape and gravity of the Moon. It appears that the combined geologic contribution to the degree-2 structure is relatively minor.

6.1. Introduction

The Moon is believed to have accreted from the debris of a giant impact with the proto-Earth [1-3], which eventually led to the formation of a magma ocean. As the body cooled and differentiated, a global, anorthositic crust likely formed by flotation of plagioclase crystals. Given this intense period of melting and single-plate mode of crustal development, it would not be unreasonable to expect the Moon to be very nearly spherical in shape and gravity. However, the Moon has long been known to possess a high amount of power in its degree-2 gravity coefficient [4-6]. A popular explanation has

been that the Moon acquired its lithospheric strength and present large-scale shape when it was more tidally and rotationally deformed while closer to the Earth, a theory known as the fossil bulge hypothesis [7]. In the last four decades, however, we have been able to observe the detailed topography and gravity of the Moon. The Moon has shown itself to have geologic features that are large enough compared with the lunar radius, and are therefore a possible "geologic component" of the low-order shape and gravity [8]. Here we will quantify some of these contributions to the lunar figure to determine if the low-degree power is due to some combination of geologic features, past tidal process, or some other mechanism. In doing so, we can also gain some insight into what controls the lunar orientation, and the structure of the lunar farside crust. A similar methodology was followed by [9] to determine the effect of Tharsis on Mars' low-degree shape and gravity. In particular, here we examine the effect of the Moon's major mascons and the South Pole-Aitken basin (SP-A). We test if the degree-2 gravity harmonics C_{20} and C_{22}, are changed by the removal of these features. We also examine the shape of the Moon after removing SP-A.

6.2. Data

Throughout the paper we use the degree-2 gravity harmonics to measure the degree-2 lunar gravity field. The definitions of the coefficients C_{20} and C_{22} are:

$$C_{20} = (2C - (B + A))/2MR^2$$
$$C_{22} = (B - A)/4MR^2$$

where R is the lunar radius, and M is the lunar mass. For a synchronous Moon:

$$C_{20}/C_{22} = 3.3.$$

Konopliv gives the observed values of C_{20}, C_{22} (unnormalized):

$$\widetilde{C}_{20} = 2.03428 \times 10^{-4}$$
$$\widetilde{C}_{22} = 0.22395 \times 10^{-4}$$
$$\widetilde{C}_{20} / \widetilde{C}_{22} = 9.1$$

The lunar center of figure (COF) is offset from the center of mass (COM) by about 2.2 km [8]. The COF is located in the central farside highlands terrain, at about 8°N, 203°E, which is displaced from the Earth-Moon line by 24°.

Figure 6.1 shows the lunar gravity, topography, and crustal thickness.

6.3. Results

6.3.1 – Effect of the major nearside mascons

To determine the effect of the major nearside mascons on the degree-2 gravity field we subtract the moment of inertia tensor of the mascons from the moment of inertia of the whole moon. This problem is similar to determining how glacial melting and unloading of the lithosphere affects the Earth's low-order properties such as J_2 and its rotation period [10-13]. In most glacial rebound studies the response of the Earth is calculated assuming it is composed of viscoelastic material. However, here we assume the Moon is completely rigid, and that the unloading of the mascons does not significantly affect the degree-2 shape of the Moon through viscoelastic effects. This is justified by noting the degree-2 elastic response to a surface load is reduced by the load deformation coefficient $k_2^{'}$, which in turn is related to the potential Love number k_2 by $k_2^{'} = -\frac{2}{3} k_2$ [14]. This formulation therefore accounts for self-gravitation [15]. Because $\left|k_2^{'}\right|$ is always less than unity (i.e. $k_{fluid}^{'}$ = -1 for a homogenous body) [14], the moments of inertia of the Earth will change by a smaller amount when including the elastic response, than without it [16, 17]. Therefore, our approximation of a rigid Moon is a conservative overestimate of the effect of removing the Mascons, which we shall see is relatively minor at any rate.

The first treatment of this problem assumes the mascons are represented by disc-shaped masses on the lunar surface, which was the assumption in [18], using the disc masses of [19], derived in 1971. The masses of the discs in [19] were constrained to fit gravity profile measurements from the Lunar Orbiters. Table 6.1 gives the masses used for the major nearside mascons [18]. The moment of inertia tensor of the Moon after subtracting the inertia tensor of these masses yields the following degree-2 coefficients and principal axes directions (in latitude and longitude, where 0°E is the sub-Earth longitude):

$$C_{20} = 0.93\widetilde{C}_{20} \qquad \hat{A} = (-4.3^\circ, 356^\circ\text{E})$$
$$C_{22} = 0.73\widetilde{C}_{22} \qquad \hat{B} = (-1.5^\circ, 84.0^\circ\text{E})$$
$$C_{20}/C_{22} = 11.58 \qquad \hat{C} = (-85.4^\circ, 193.3^\circ\text{E})$$

These slightly lower values suggest a modest effect of the mascons on the degree-2 gravity coefficients. Note that the ratio C_{20}/C_{22} is brought further from the synchronous fossil bulge value of 3.3.

While the disc model is sufficient for a first order estimate of the mascons' contributions, we also make use of more recent data. This is particularly important because it is now well established that the major nearside basins also contain a mass deficit in a ring-shaped area around the central mascon (a "masslite"), Figure 6.2. Some small amount of this apparent deficit may be due to "ringing" in the spherical harmonic expansion, but not all of it [20]. To model the excess mass in the central mascons and the mass deficit in the masslite rings, we use the crustal thickness and moho isostasy-level calculations of [20] (Figure 6.2). We assume a crustal thickness density of 2800 kg/m^3 and a mantle density of 3300 kg/m^3. In the future, these calculations could be redone with more modern crustal thickness data. The resulting mass excesses and deficits are given in Table 6.1. Generally, the agreement with the disc model for the mass excess from the mascons is good, except for the Orientale basin. The lunar degree-2 coefficients and principal axes directions when just the mascons under this model are subtracted from the Moon are given as:

$$C_{20} = 0.93\widetilde{C}_{20} \qquad \hat{A} = (-2.6^\circ, 355.3^\circ \text{E})$$
$$C_{22} = 0.89\widetilde{C}_{22} \qquad \hat{B} = (-1.9^\circ, 85.4^\circ \text{E})$$
$$C_{20}/C_{22} = 11.66 \qquad \hat{C} = (-86.8^\circ, 212.5^\circ \text{E})$$

We note that the mascon principal axes themselves (subscript *M*) using the data from [20] are:

$$\hat{A}_M = (18.7^\circ, 43.2^\circ \text{E})$$
$$\hat{B}_M = (14.3^\circ, -57.1^\circ \text{E})$$
$$\hat{C}_M = (66.1^\circ, 183.1^\circ \text{E})$$

which are slightly different from those reported by [18].

When the effects of the masslites surrounding the mascons are also removed from the Moon (the mass is added), they undo some of the contributions from the mascons, particularly for C_{20}. The removal of the effects of both the mascons plus masslites yields lunar degree-2 coefficients and principal axes directions:

$$C_{20} = 1.073\widetilde{C}_{20} \qquad \hat{A} = (1.2^\circ, 4.4^\circ \text{E})$$
$$C_{22} = 0.85\widetilde{C}_{22} \qquad \hat{B} = (-0.5^\circ, -85.6^\circ \text{E})$$
$$C_{20}/C_{22} = 11.4 \qquad \hat{C} = (88.7^\circ, -150.4^\circ \text{E})$$

The principal axes of the masslites themselves apparently have no association with the lunar principal axes (not shown). In summary, the generally small (~10%) changes in the low order gravity coefficients suggest that the mascons and masslites do not greatly affect the lunar moments of inertia.

We note that [18] shows the COM/COF offset is less than 3% for the mascons using the disc model, which is a value that would hold here as well, given the general agreement between the disc and mantle plug models.

6.3.2 South Pole-Aitken gravity

The gravity signature of SP-A is generally muted, which suggests that the basin has largely been compensated [20, 21]. However, even perfectly compensated terrain will have a small gravity anomaly and make a contribution to the global moments of inertia because of the slightly different radii of the compensating mass and mass deficit, compared to a perfectly spherical case [22]. Ojakangas and Stevenson [23] succinctly describe this effect by considering a water planet covered with compensated icebergs. The free air anomaly Δg for a fully compensated cavity of spherical harmonic S_n of degree n is given by equation 5.06.5 of [22]:

$$\Delta g = 4\rho G d S_n \frac{n-1}{2n+1}\left(1-\left(\frac{R-h}{R}\right)^n\right) \qquad (1)$$

where ρ is the crustal density, d is the depth of the harmonic S_n, G is the gravitational constant, and h is the crustal thickness (~45 km). This yields ~40 mgal or less for a feature of $d \sim 4$ km and $n <= 5$, which is appropriate for SP-A (~2400 km diameter outer cavity). The errors associated with the farside gravity field are of order 80-90 mgal in SP-A [24], making it difficult to determine its exact compensation state. However, we proceed working under the assumptions that SP-A is perfectly compensated to estimate its minimum contribution to the lunar moments of inertia. We note that it is plausible that the contribution is zero if the basin is slightly overcompensated.

Following the development of [23] we model both the moment of inertia contribution of the vacuum created by SPA's depression, as well as an uplifted mantle. The isostatic mantle height and equilibrium surface topography for a cavity, can be related by the following expressions:

$$\begin{aligned} X_1 &= h_{cm}(1-\rho_c/\rho_m) - h_c(1-\rho_c/\rho_m) \\ X_2 &= h_{cm} - h_{cm}(1-\rho_c/\rho_m) + h_c(1-\rho_c/\rho_m) - h_c \end{aligned} \qquad (2)$$

where h_{cm} is the mean planetary crustal thickness, h_c is the local crustal thickness at the anomaly, X_1 is the topography at planetary radius R after compensation, and X_2 is the mantle plug height referenced from R-h_{cm}. We use h_{cm} = 45 km, and we estimate the crustal thickness beneath SP-A as h_c = 20 km [25]. In this case, if the basin is completely compensated, this crustal thickness difference from the mean will produce topography X_1 = -3.8 km inside the basin, which is close to the mean observed topography in SP-A's main depression (not surprisingly). The surface area of the inner depression of SPA is about 0.055 times the lunar surface area [26]. The mass deficit produced by this is then 2.2×10^{19} kg, which is compensated by nearly equal mass excess in the underlying mantle plug. Note that the scalar moment of inertia contributions from each deficit and excess are given by:

$$\begin{aligned} \Delta I_{hole} &= \rho_c A X_1 (R - \tfrac{1}{2} X_1)^2 \\ \Delta I_{mantle} &= \Delta\rho A X_2 (R - \tfrac{1}{2} X_1 - \tfrac{1}{2} h_c - \tfrac{1}{2} X_2) \\ \Delta I_{net} &= \Delta I_{mantle} - \Delta I_{hole} \end{aligned} \qquad (3)$$

where A is the surface area of the cavity. Although these scalar equations are not used specifically in the inertia tensor calculation, they illustrate the relative contributions due to radial differences of the compensating mass excess and mass deficit. Taking the center of SP-A as (-51°, 191°E) [26], we compute the inertia tensor assuming the mass dipole produced by the basin's compensating excesses and deficits is located at the basin center, and add it to the global moments of inertia. We find that:

$$\begin{aligned} C_{20} &= 1.02\widetilde{C}_{20} & \hat{A} &= (-9.8^\circ, -5.6^\circ \mathrm{E}) \\ C_{22} &= 0.96\widetilde{C}_{22} & \hat{B} &= (-3.6^\circ, -95.0^\circ \mathrm{E}) \\ C_{20}/C_{22} &= 9.63 & \hat{C} &= (-79.6^\circ, 15.5^\circ \mathrm{E}) \end{aligned}$$

Overall, these perturbations are small, and therefore the hole created by SP-A has a negligible contribution to total moments of inertia. When this is combined with the value corrected from the lunar mascons we obtain:

$$C_{20} = 1.05\widetilde{C}_{20}$$
$$C_{22} = 0.92\widetilde{C}_{22}$$
$$C_{20}/C_{22} = 10.45$$

The combined contributions of SPA, the mascons, and the surrounding masslites do not greatly contribute to lunar degree-2 power. This must be validated in the future with superior gravity data from SP-A.

6.3.3 South Pole-Aitken basin ejecta and farside topography

It has often been suggested that the elevated topography in the central lunar farside may in part be from SP-A's ejecta (e.g. [21]). Here we determine if the estimated ejecta volume of SP-A is compatible with this hypothesis. Wieczorek and Phillips [28] estimate the volume of SP-A's excavated material to be ~30 × 10^6 km^3, based on a reconstruction of the excavation cavity from crustal thickness modeling. While this is not a fully constrained estimate, and the excavation cavity of SP-A is unusual in its shallowness compared to other smaller basins, it serves as a useful starting point.

The ejecta thickness as a function of radius from the center of a crater or basin has been studied [27, 28]. Numerical integration (not shown) of the ejecta thickness in [27] (their figure 5) reveals that 75% of the ejecta is located within 2.2 basin radii. We therefore conservatively assume that all of SP-A's ejecta is within 2.5 basin radii.

Figure 6.3A shows ULCN2005 [29] topography centered on SP-A (and rotated 18.8°), with the inner ellipse mapped in Chapter 2, and an outer ellipse 2.5 times the semi axes of the inner ellipse. More than one hemisphere is shown to illustrate the extent of the central farside highlands (compare also with Figure 6.1B). If we uniformly remove 30 × 10^6 km^3 of material from the area between the inner and outer ellipses, we obtain Figure 6.3B. Most importantly, in Figure 6.3B the surrounding farside terrain remains anomalously high beyond the region where most of SP-A's ejecta is expected. It is also important to note that in the areas where topography was removed, the elevation would

rise to a higher level due to isostasy, and therefore the topography between the inner and outer rings in Figure 6.3 is probably not a good estimate of the pre-SPA topography. For the same reason, no effort was made to reconstruct the pre-SP-A topography inside the inner ring by placing the excavated material back inside the cavity.

In summary, while the ejecta emplacement mechanisms and distribution functions for the largest basins are not well known, this coarse study demonstrates that even under a fairly conservative assumption, SP-A cannot be the sole cause of the high farside terrain.

6.4. Conclusions

The mascons do not greatly contribute to the lunar moments of inertia under two different models. The masslites that surround the mascons partially cancel out the small effect of the mascons. SP-A ejecta is not likely the sole cause of the anomalously high farside terrain. The cause of the degree-2 power in shape and gravity is not likely due to any combination of geological components. Future work could use a more rigorous treatment of the gravity contributions of the mascons or SP-A. Ongoing work is focusing on the gross structure of the farside highland terrain.

References

1. Daly, R.A., *Origin of the moon and its topography.* Proceedings of the American Philosophical Society 1946. **90**: p. 104-119.

2. Hartmann, W.K. and D.R. Davis, *Satellite-sized planetesimals and lunar origin.* Icarus, 1975. **24**: p. 504-515.

3. Cameron, A.G.W. and W.R. Ward, *The origin of the Moon.* Proc. Lunar Planet. Sci. Conf., 7th, 1976: p. 120-122.

4. Laplace, P.S., *Traité de Mécanique Celéste.* 1798-1827.

5. Lambeck, K., *The lunar fossil bulge hypothesis revisited.* Phys. Earth Planet. Inter., 1980. **22**: p. 29-35.

6. Jeffreys, H., *The Earth.* 1970, Cambridge: Cambridge University Press.

7. Sedgewick, W.F., Mess. Math., 1898. **27**: p. 171.

8. Smith, D.E., et al., *Topography of the Moon from the Clementine lidar.* J. Geophys. Res., 1997. **102**: p. 1591-1611.

9. Zuber, M.T. and D.E. Smith, *Mars without Tharsis.* J. Geophys Res., 1997. **102**: p. 28,673-28,685.

10. Nakiboglu, S.M. and Lambeck, K, *Deglaciation effects on the rotation of the Earth*, Geophys. J. R. astr. Soc. 1980. **62**: p. 49-58.

11. Sabadini, R., Yuen, D.A., and Boschi, E., *Polar wandering and the forced responses of a rotating, multilayered viscoelastic planet*, J. Geophys. Res. 1982. **87**: p. 2885-2903.

12. Wu, P. and Peltier, W.R., *Pleistocene Deglaciation and the Earth's rotation: a new analysis*, Geophys J. R. asr. Soc. 1984. **76**: p. 753-791.

13. Yoder, C., et al., *Secular variation of Earth's gravitational harmonic J_2 coefficient from Lageos and nontidal acceleration of Earth rotation,* Nature 1984. **303**: 757-762.

14. Munk, W.H. and MacDonald, G.J.F., *The Rotation of the Earth.* 1960, Cambridge: Cambridge University Press.

15. Hager, B.H., *Global isostatic geoid anomalies for plate and boundary models of the lithosphere*, Earth and Planet. Sci. Let. 1983. **63**: p. 97-109.

16. Longman, I.M., *A Green's function for determining the deformation of the Earth under surface mass loads*, J. Geophys. Res. 1963. **68**: p. 485-496.

17. O'Connell, R.J., *Pleistocene glaciation and the viscosity of the lower mantle*, Geophys. J. R. astr. Soc. 1971. **23**: p. 299-327.

18. Melosh, H.J., *Mascons and the Moon's orientation.* Earth and Planetary Science Letters, 1975. **25**: p. 322-326.

19. Wong, L., et al., *A surface-layer representation of the lunar gravitational field.* J. Geophys. Res., 1971. **76**: p. 6220-6236.

20. Neumann, G.A., et al., *The lunar crust: Global structure and signature of major basins.* J. Geophys. Res., 1996. **101**: p. 16841-16843.

21. Zuber, M.T., et al., *The shape and internal structure of the Moon from the Clementine mission.* Science, 1994. **266**: p. 1839-1834.

22. Jeffreys, H., *The Earth.* 1976, Cambridge: Cambridge University Press.

23. Ojakangas, G.W. and D.J. Stevenson, *Polar wander of an Ice Shell on Europa.* Icarus, 1989. **81**: p. 242-270.

24. Konopliv, A.S., et al., *Recent gravity models as a result of the Lunar Prospector mission.* Icarus, 2000. **150**: p. 1-18.

25. Hikida, H. and M.A. Wieczorek, *Crustal thickness of the Moon: New constraints from gravity inversions using polyhedral shape models.* Icarus, 2007. **192**: p. 150-166.

26. Garrick-Bethell, I. and M.T. Zuber, *Elliptical structure of the lunar South Pole Aitken basin.* Icarus, 2009, submitted.

27. Wieczorek, M.A. and R.J. Phillips, *Lunar multiring basins and the cratering process.* Icarus, 1999. **136**: p. 246-259.

28. Housen, K.R., R.M. Schmidt, and K.A. Holsapple, *Crater ejecta scaling laws: fundamental forms based on dimensional analysis.* J. Geophys. Res., 1983. **88**: p. 2485-2499.

29. Archinal, B.A., et al., *The unified lunar control network 2005.* U.S. Geological Survey Open-file Report 2006-1367, 2006.

30. Wieczorek, M.A., *Gravity and topography of the terrestrial planets.* Treatise on Geophysics, 2007. **10**: p. 165-206.

Table 6.1 Mass representations of nearside mascons used for inertia tensor calculations.

Mascon	Surface disk mass[a] 10^{18} kg	Uplifted mantle mass[b] 10^{18} kg	Subisostatic mantle mass[c] 10^{18} kg	Depth for inertia calculation (km)	Radial limits km[e]
Imbrium	1.68	1.11	2.26	50, 50	300, 650
Serenitatis	1.58	1.22	1.12	45, 55	275, 530
Crisium	0.676	0.63	0.48	45, 55	200, 440
Nectaris	0.617	0.55	0.89	45, 60	200, 420
Humorum	0.441	0.54	0.55	45, 60	160, 350
Sinus Aestuum	0.309	-	-	-	-
Smythii	0.228	0.23	0.55	45, 55	140, 400
Fecunditatis	0.191	0.17	1.11	45, 55	140, 500
Sinus Medii	0.147	-	-	-	-
Orientale	0.11	0.36	1.76	50, 70	130, 385

a) From a surface mass model of mascons by Wong et al. (1971), Melosh (1975).
b) Mantle mass excess ("mascon") represented by the superisostatic mantle plug, derived from Neumann et al. (1996). Estimated uncertainty 20%.
c) Mantle mass deficit ("masslite") represented by the subisostatic ring around the superisostatic mantle plug, derived from Neumann (1996). Estimated uncertainty 20%.
d) Approximate depth at which the mantle mass anomaly is effectively located, used to calculate the moment of inertia of the mascon, for the mantle plug, and subisostatic ring, respectively.
e) Outer boundary of the mantle plug, and the subisostatic ring, respectively. Used to calculate the volume of the super or subisostatic mantle. See Figure 6.2.

Figures

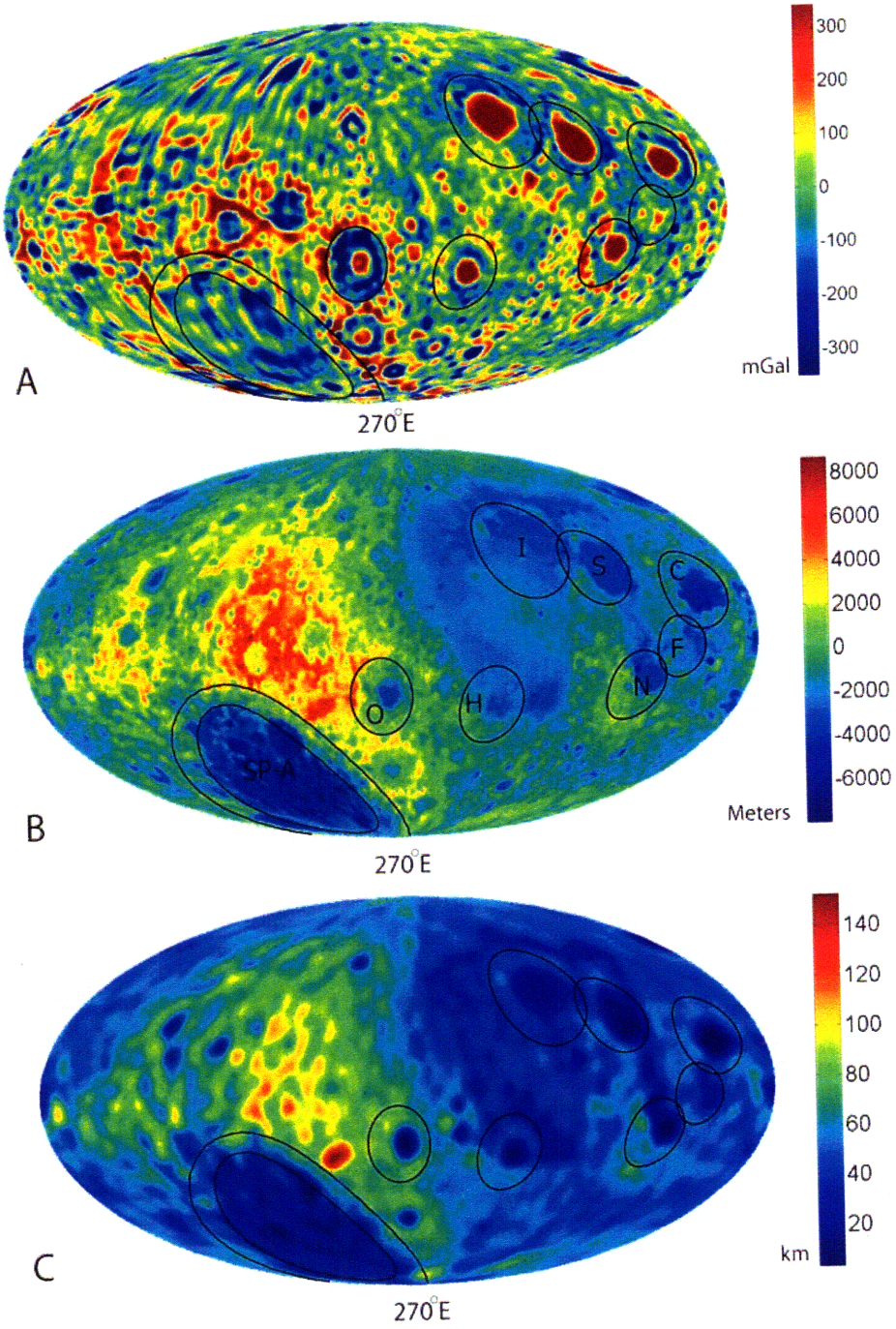

Figure 6.1. A) Lunar free air gravity anomaly from model JGL150Q1, a 150 degree expansion here truncated at degree 90, with the degree-2 terms included. B) ULCN2005 topography [29]. I: Imbrium, S: Serenitatis, C: Crisium, F: Fecunditatis, N: Nectaris, H: Humorum, O: Orientale, SP-A: South Pole-Atiken. C) Single layer model of crustal thickness from [30]. All projections are Molleweid centered at (0°, 270°E), and show the full lunar sphere.

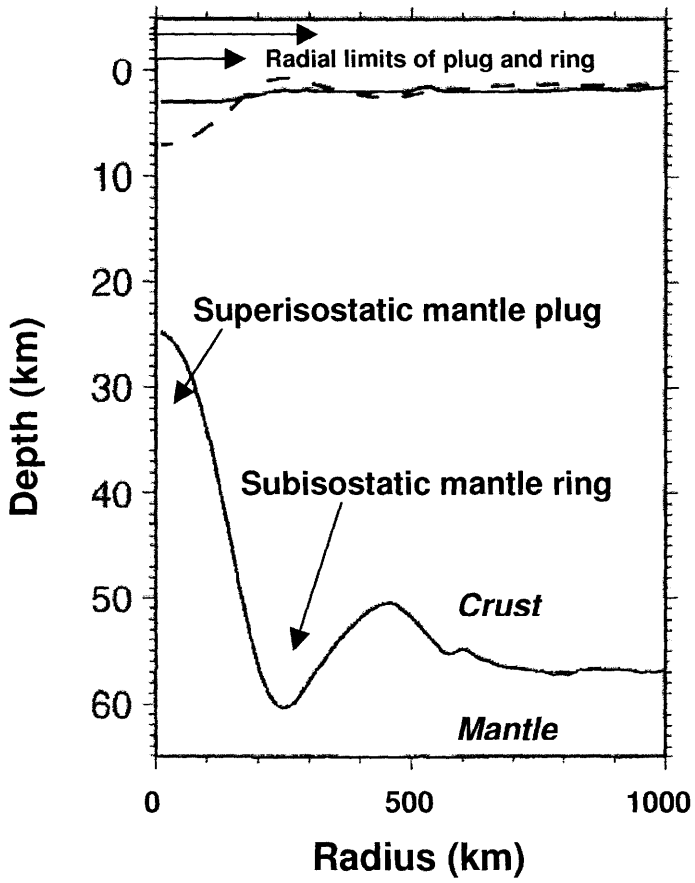

Figure 6.2. Radially averaged topography and moho of mare Humorum. Vertical exaggeration is 20:1. The dashed curve shows the topography, with an arbitrary reference level, that would result if the inferred moho and surface topography were in local isostatic equilibrium. This curve is used as a first-order estimate of the mass excess associated with the central mascon, and the mass deficit due to the surrounding masslite. Taken from Neumann et al. (1996).

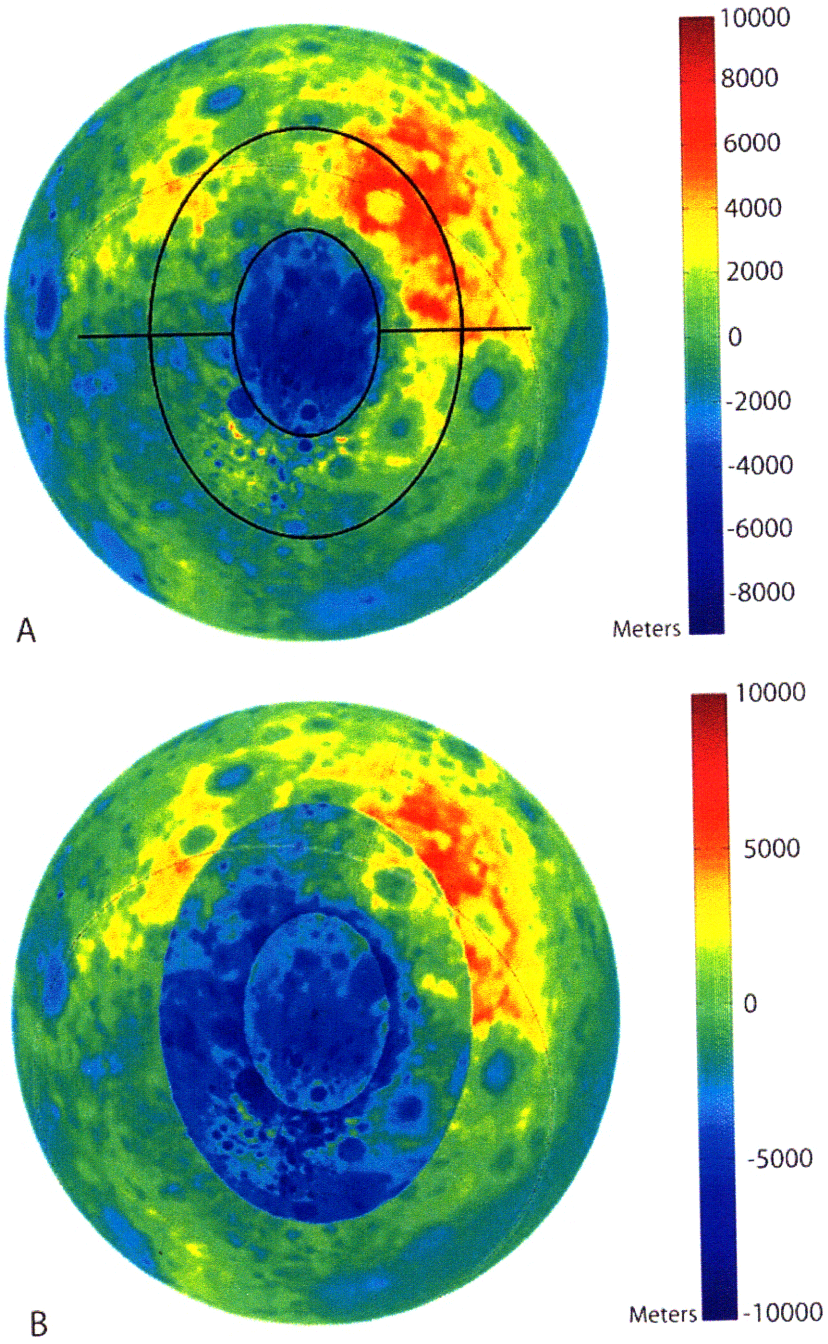

Figure 6.3. A) South Pole-Aitken inner elliptical boundary mapped by Garrick-Bethell and Zuber (2008) and an elliptical boundary with semi axes 2.5 times larger than the inner boundary, plotted over ULCN2005. Black horizontal lines are shown to indicate the central axis of the ellipse. B) Ejecta volume uniformly removed from the area between the two ellipses shown in part B. The original topography of the inner depression was not altered. The projection in both is Lambert equal area centered on (-53°, 191°E) and rotated counterclockwise 18.8°. The projection shows 120° of latitude (30° beyond one hemisphere). Grid lines are spaced 30° and the lunar equator is shown as a thin black line.

Chapter 7

Kamacite blocking temperatures and applications to lunar magnetism

In revision for Earth and Planetary Science Letters. Ian Garrick-Bethell and Benjamin P. Weiss.

Abstract

The long-term stability of remanent magnetization is a major assumption of paleomagnetism. Here we present calculations that predict the magnetic relaxation times of single domain crystals of the iron-nickel mineral kamacite as a function of their time-temperature history. Kamacite is one of the most abundant ferromagnetic minerals in the solar system and is the dominant remanence carrier on the Moon. We perform these calculations for a variety of grain sizes, times, and temperatures to derive a broad view of the remanence stability of kamacite over geologic timescales. Previously, such blocking temperature calculations were only available for the common Earth minerals magnetite, hematite, and pyrrhotite. Our results show that remanence in kamacite-bearing lunar samples is stable against typical thermal perturbations during the last several billion years of lunar history and residence on Earth. We find support for these predictions in previous thermal demagnetization experiments of lunar rocks and recommend that future studies exert caution in interpreting the remanence from grains with blocking temperatures below ~350°C. Our results imply that paleointensity experiments without laboratory thermal

demagnetization may underestimate the true paleofield. Our findings also help address any concerns that lunar rock paleomagnetism is a secondary artifact due to storage in the Earth's magnetic field. Future paleomagnetic studies of iron bearing samples can quickly use our blocking temperature diagram to determine the effects of geologic heating events on magnetic remanence.

7.1. Introduction

On Earth time-temperature events such as metamorphism are often important in interpreting a rock's natural remanent magnetization (NRM). Long-term heating in a magnetic field may impart a viscous overprint on the NRM and obscure the primary record of magnetization. In 1974 Pullaiah et al. [1] computed simple diagrams to quantify this effect for the common Earth minerals magnetite and hematite. Nearly three decades later, similar calculations were published for pyrrhotite [2, 3]. These diagrams are based on theory developed by Néel [4] and illustrate the tendency of an assemblage of single domain grains to relax its magnetization as a result of different time-temperature histories.

On the Moon and in some meteorites the primary carrier of remanent magnetization is native iron, which is usually alloyed with a minor amount of nickel and cobalt to form the body-centered cubic mineral kamacite. Although nearly ubiquitous on the lunar surface, kamacite is virtually absent from the Earth's crust, whose remanence is instead primarily carried by titanomagnetite. Because of the complexities and unfamiliarity of working with kamacite, some scientists have rightfully questioned the

reliability of lunar rock magnetism studies. One problem is that the NRM may be a mixture of thermoremanent magnetization (TRM) and crystallization remanent magnetization (CRM) due to phase transformations during cooling [5] (Section 2). Another problem is the prevalence of multidomain grains, which do not have discrete blocking and unblocking temperatures. A third problem is that alteration of iron during heating very often confounds thermal paleointensity experiments. A final problem—which forms the subject of this paper—is the uncertain effects of long time-temperature histories on the stability of the remanent magnetization. For example, most lunar samples have been exposed to diurnal surface temperature changes between 0-100°C for hundreds of millions of years, leaving open the possibility that their NRM has decayed in the presumably low-field environment of the recent Moon [6]. Apollo samples have also been stored at room temperature in the Earth's field for several decades, which has imparted a viscous remanence. In this paper we follow the methodology of Pullaiah et al. [1] to derive time-temperature stability diagrams for kamacite remanence. While these diagrams do not perfectly predict unblocking temperatures and do not apply to multidomain grains, they can provide guidance for samples with mixtures of single and multidomain crystals. They have particular relevance for paleomagnetic studies of lunar breccias and soils, which contain significant amounts of superparamagnetic and single domain grains.

Since the chemistry and magnetism of iron-nickel compounds is quite complex and not often discussed in the context of lunar magnetism, we will review some of the major points in Section 2. This discussion is important for establishing the range of nickel contents for which our kamacite calculations are relevant.

7.2. Iron-nickel alloys

7.2.1 *Equilibrium phase diagram*

Upon slow cooling from the liquid state, pure iron at low pressure passes through a series of equilibrium solid-state phases known as delta (δ), gamma (γ), and alpha (α), in order of their appearance. These phase changes correspond to crystallographic transformations from body centered cubic (bcc) to face centered cubic (fcc), and finally back to bcc, respectively. In steel formation, where iron is mixed with carbon, the three crystalline phases are known as δ, austenite, and ferrite, respectively. When iron is alloyed with nickel (as typically found in meteorites and lunar rocks), these phases are referred to as δ, taenite, and kamacite, as shown in the simplified equilibrium FeNi phase diagram in Fig. 7.1 [7]. Since carbon and nickel prefer fcc solvents, both constituents will diffuse out of ferrite (kamacite) into taenite (austenite) during cooling in the α + γ two-phase stability field. This exsolution process leads to mixtures of taenite enriched in nickel, and kamacite depleted in nickel, relative to the bulk composition of Ni. Below about 347°C, the α + γ stability field is believed to become a field with α + ordered $FeNi_3$ (awaruite, not shown in Fig.1). Below ~400°C and for low bulk nickel compositions, the kinetics of the formation of awaruite are very slow [8], but $FeNi_3$ has been observed in meteorites [9] with < 10% Ni.

High nickel taenite (>30% Ni) and kamacite are both ferromagnetic (Fig. 7.1). For bulk compositions with <3% Ni, equilibrium cooling produces a pure

thermoremanent magnetization (TRM) in the kamacite phase, which wholly makes up the cooled metal before the Curie temperature is reached. Kamacite with 3% Ni has a Curie temperature of approximately 760°C. For bulk compositions with >3% Ni, kamacite and taenite continually equilibrate below the Curie temperature during cooling to produce a phase-transformation CRM in the kamacite and taenite (if the taenite has >30% Ni). It is not known if such a remanence mechanism retains a memory of TRM acquired at earlier equilibrium states [6]. However, phase diagrams often depict a Curie temperature line for compositions up to about 7% Ni, or where the Curie temperature line intercepts the γ phase. Curie temperature measurements of kamacite with 3-7% Ni are made by rapid cooling to form a supersaturated nonequilibrium α phase (see below) [10]. The material is then heated relatively quickly to measure the Curie temperature before chemical equilibration alters the TRM-carrying supersaturated material. For compositions above 7%, the start of the taenite stability field is below the α phase Curie temperature, making it difficult to heat a supersaturated α compound rapidly enough to the Curie temperature before the γ transformation sets in.

7.2.2 *Non-equilibrium transformations*

The equilibrium transformations described in the previous section depend heavily on cooling rate. Volume diffusion kinetics can be very slow in FeNi alloys, so one may find non-equilibrium taenite and kamacite compositions as the end products of slow cooling. The diffusion rates for the decomposition of taenite into taenite plus kamacite can eventually slow to a point where equilibrium will not be reached over geologic times,

even at modest temperatures. Therefore, intermediate non-equilibrium taenite-kamacite mixtures may freeze in. An example of this process includes the Widmanstätten structures in iron meteorites. Derived equilibrium phase diagrams may illustrate the thermodynamics preferences of an alloy, but the domination of kinetics often makes them of little practical use.

If cooling from the taenite stability field is rapid enough, a variety of composition-invariant transformations can turn taenite of bulk composition into bcc supersaturated kamacite of bulk composition. The martensitic transformation is one example of this process, where in the case of nickel alloys a supersaturated bcc structure forms by a shearing dislocation in the crystal lattice. According to Wilson (1994), there are six different composition-invariant transformations in the nickel-iron system; equi-axed ferrite, massive ferrite, Widmanstätten ferrite, bainitic ferrite, lath-martensite (classic martensite, also known as "massive martensite"), and twinned martensite [11]. These transformations may also occur in pure iron, since they are crystal lattice dislocations that are do not require the presence of solute atoms [12]. However, addition of a solute such as nickel can greatly lower the start temperature of these reactions. Cooling rates to achieve these transformations can also vary by six orders of magnitude across reaction types and solute content. Many studies have been performed on the cooling rates necessary to achieve a given microstructure, e.g. [13-15]. In addition, the formation of $FeNi_3$ from taenite below ~347°C is suppressed by formation of metastable ordered states (Fe_3Ni and FeNi, tetrataenite), but these states are not likely to appear for <5-15% Ni, assuming cooling times substantially faster than meteorites (~1-100°C/M.y.) [7, 16, 17].

Some aspects of the effect of cooling rate, microstructure, and nickel content on kamacite magnetic properties have been examined by Wasilewski [5, 18]. Wasilewski [5] proposed nine new remanence mechanisms for FeNi alloys based on microstructure, and included samples transformed by both the massive and martensite transformations. Further experiments [18] concluded that microstructure is a major factor in determining intensity of remanence and stability to AF demagnetization. Other solutes such as carbon, cobalt, and phosphorous can also alter the likelihood and nature of phase transformations. Since almost all lunar kamacite has some nickel, cobalt, or other contaminants, and its grain size is often multidomain, its microstructure and remanence characteristics may be complex.

Clearly, the remanence of metals is more difficult to interpret than that of oxides. With these complexities in mind, we will calculate the relaxation times for homogeneous single domain bcc iron crystals and extrapolate the results to low nickel and cobalt alloys.

7.3. Time-temperature relaxation calculation

7.3.1 *Single domain iron*

Our calculations follow those of Pullaiah [1]. The relaxation time, τ, of a single domain particle in zero field can be written [4]:

$$\frac{1}{\tau} = C \exp\left(\frac{-vJ_s(T)H_c(T)}{2kT}\right) , \qquad (1)$$

where C is the characteristic frequency of thermal oscillation, v is the particle volume, $J_s(T)$ is the temperature dependent spontaneous magnetization, $H_c(T)$ is the temperature dependent microscopic coercivity, k is Boltzmann's constant, and T is temperature in Kelvins. Grains with a given v, H_c, and J_s will unblock their magnetization after heating to a temperature T for an unblocking time τ. We use a recent parameterization of the $J_s(T)$ curve from [19]:

$$J_s(T/T_c) = J_o\left(1 - s(T/T_c)^{3/2} - (1-s)(T/T_c)^p\right)^{1/3} \qquad (2)$$

where J_o is the saturation magnetization at $T = 0$ K, equal to 1750 kA/m, T_c is the Curie temperature, 1044° K, and $s = 0.35$ and $p = 4$ are empirically determined parameters (Fig. 7.2). Equation 1 is based on experimental data from [20] and its dependence on the parameters s and p has no physical basis other than to satisfy a steep drop in $J_s(T)$ as T gets close to the Curie temperature. Crangle and Goodman [20] measured 99.95% pure iron and make no remarks about rapid cooling in their work, so it is unlikely their data are greatly affected by nonequilibrium microstructure effects. Other experimental and theoretically determined curves for $J_s(T)$ [21] produce similar blocking temperature calculations as those presented here.

Complete data for the temperature dependence of the microscopic coercivity of iron do not appear in the literature. Fortunately, we may make a reasonable approximation for $H_c(T)$ by examining its dependence on the magnetic anisotropy of the grain and $J_s(T)$. Single domain magnetic anisotropy is due to three different effects: grain

shape, grain crystal structure, and stress on the grain. The $H_c(T)$ dependence on these anisotropies is, respectively:

$$H_{c,s}(T) = NJ_s(T) \tag{3a}$$

$$H_{c,c}(T) = \frac{4}{3}\frac{|K_1(T)|}{\mu_o J_s(T)} \tag{3b}$$

$$H_{c,r}(T) = \frac{3\lambda\sigma}{\mu_o J_s(T)}, \tag{3c}$$

where N is the difference between the demagnetizing factors in the easy and hard directions, $K_1(T)$ is the first term of the magnetocrystalline anisotropy constant, and λ is the magnetoelastic anisotropy constant. At 20°C $K_1 = 4.8\times10^4$ J/m^3 and $\lambda = -7\times10^{-6}$ [6].

We wish to understand which of these three anisotropies contributes the most to $H_c(T)$. We first note that at 20°C, $H_{c,s}$ is larger than $H_{c,c}$ when $N \geq 0.017$, which occurs when grains are elongated by 5% or more, using the shape demagnetizting factors from [6, 22] . To determine if this relationship holds true for all temperatures, we use the temperature dependent $K_1(T)$ function presented by Bozorth (Fig. 12-11) [21], shown in Fig. 7.3. The ratio of $H_{c,s}$ to $H_{c,c}$ is plotted in Fig. 7.4, for a value of N = 0.017 (5% elongation) and N = 0.12 (20 % elongation). The ratio rises with temperature, indicating the increased importance of shape anisotropy. For magnetoelastic anisotropy, even if we use the ultimate tensile strength of iron, $\sigma \approx$ 400 MPa, $H_{c,c}$ is 8 times larger than $H_{c,r}$.

Therefore, we conclude that for nearly all grain shapes and stress states, shape anisotropy dominates the coercivity of kamacite: $H_c = NJ_s(T)$. Pullaiah et al. reach the same conclusion for magnetite grains elongated by ≥ 10%.

Taking $C = 10^{10}$ Hz [1] we calculate equation (1) for a variety of temperatures (Fig. 7.5). For example, we can see that grains with a 1000 s (typical laboratory heating time) blocking temperature of 400°C will also unblock after heating at 200°C in zero field for 3 My. Relaxation in a non-zero field changes (1) to:

$$\frac{1}{\tau} = C \exp\left(\frac{-vJ_s(T)H_c(T)}{2kT} \left(1 - \frac{H_o}{H_c}\right)^2 \right) \qquad (4)$$

where H_o is the ambient field (equation 8.3 of [6]). For $H_o = 0.1$ mT compared to $H_c(T) =$ 37 mT (assuming shape anisotropy, $J_s(293°\text{ K}) = 1715$ kA/m, and $N = 0.017$ [6]), we obtain $(1 - H_o / H_c)^2 = 0.995$. Therefore predictions for τ from (4) for typical geomagnetic fields are essentially identical to that from (1).

7.3.2 *Extrapolation to low nickel and cobalt alloys*

Although we have calculated blocking temperature relations for pure iron kamacite, we can use apply these calculations to low nickel alloys because they have similar $J_s(T)$, $H_c(T)$, and T_c. The Curie temperature of α iron decreases slowly up to about 15% nickel ($T_c = 700$°C) [7]. Measurements show that the saturation induction at 20°C, which can be used as a proxy for $J_s(T)$, increases by only 3% percent with the

addition of 5% Ni, and then decreases again to the zero nickel value at 10% Ni, and 3% below the zero Ni value at 15% Ni [21] (his Fig. 5-8). In addition, measurements of the saturation induction as a function of temperature at 40% nickel follow a function that is similar in shape to that at 0% Ni [21] (his Fig. 5-10). The value of K_1 at 0°C decreases monotonically to 1.8×10^4 J/m^3 at 16% nickel [23]. Data on the change in K_1 with temperature could not be found for higher nickel contents, but the slowly and monotonically changing values of K_1 with temperature for pure Ni and Fe [21] (his Fig. 12-13) make it likely that shape anisotropy continues to dominate the anisotropy contribution to H_c at higher temperature. In summary, the slowly varying T_c and J_s(20°C) up to at least 15% Ni, the similar shape of the $J_s(T)$ function at high nickel, and the similarity of the anisotropy functions suggest that the above equations and assumptions for 0% Ni can be used for up to about 15% Ni. Using the reduced Curie temperature for 15% Ni, and the J_s(0°C) value at 0% Ni, the relaxation times for 15% Ni change by a negligible amount.

For iron with < 20% Co, T_c rises slowly with Co content, increasing by a few degrees at 3% Co [24]. J_s(T) data could not be found for low Co alloys, but the saturation induction at 20°C decreases less than 5% for Co < 10% (Fig. 5-80 of [21]). We could not find data on the temperature dependence of K_1 for Co < 10%, but for pure cobalt K_1 changes slowly and monotonically as a function of temperature (Fig. 12-12 of [21]). Given the small and monotonic changes in T_c, K_1, and saturation induction for alloys up to at least 10% Co, we may conservatively apply our calculations to kamacite with <3% Co. Using the available data for 3% Co do not change our results. Most lunar

kamacite has Ni < 10% [25], and Co < 3% (including the samples in Section 5, except for some grains of 15498).

For bulk nickel content greater than about 3%, Curie temperatures start to become less well defined for two reasons. The first is that if the metal is assumed to have been in complete equilibrium during cooling and subsequent heating, the magnetic remanence will be gained and removed by crystal structure changes in the kamacite + taenite stability field (Section 2). The second is that the metal may contain nonequilibrium reaction products that include kamacite with varying amounts of nickel, complicating the interpretation of which nickel-content Curie temperature is applicable. These complications are probably more significant for meteorites, where large multidomain grains of iron with high nickel contents may have formed with very slow cooling times. In any case, the blocking temperature calculations are not affected by these complications, as long as the user is aware of the crystallography of the kamacite in the sample.

7.4. Predictions

We can use Fig. 7.5 to predict the long-term stability of lunar rock magnetism for three major idealized thermal processes that nearly all Apollo samples have likely experienced: (Case 1) burial in the near-surface regolith, (Case 2) exposure to solar heating on the lunar surface, and (Case 3) residence on Earth. While these predictions are for lunar samples, similar thermal histories could be applied to kamacite-bearing meteorites.

In the lunar regolith the temperature gradient is about 1.7°C/m [26], and most regolith is on the order of 10 m thick [27]. Below the regolith, bedrock thermal gradients decrease markedly, so that rocks are not heated to very high temperatures in the upper few kilometers from which nearly all lunar samples have originated. At the surface the diurnal temperature variation is –140-110°C at the equator, but it is completely attenuated to a constant –20°C at approximately 30 cm depth. Therefore, the minimum temperature lunar rocks could have experienced during their pre-surface history of 1-4 B.y. is about -20°C at ~30 cm. We conservatively assume –20°C for our first part of the rocks's thermal history from 1-4 B.y.

On the Moon, rocks are often brought to the upper few meters of the lunar surface before being fully exposed. Near-surface exposure ages calculated from spallation-produced gases range from 1-300 M.y. [28], but the depth of burial is not often resolved to 30 cm accuracy, leaving open the possibility that they experienced some diurnal heating. Particle tracks and microcraters have been used to calculate the "suntan" ages of rocks, which can often span 1-300 M.y. Therefore, the second part of the rocks history will be exposure to the diurnal surface wave at 100°C for 1-300 M.y. (assuming the rocks are only heated during half of each lunar day during this period gives nearly the same results).

For the third part of the rock's history we assume storage on Earth for ~10 yr at 20°C.

We use Fig. 7.5 to calculate the 1000 s blocking temperatures that will demagnetize the same grains affected by each of the above three idealized thermal histories. We assume there were negligible ambient magnetic fields on the Moon for the

past 4 B.y. In Case 1, near-surface residence at –20°C for 1-4 B.y. yields an unblocking temperature of about 215°C. In Case 2, storage on the surface at 100°C for 1-300 M.y. leads to an unblocking temperature of 325-375°C. In Case 3, storage on Earth yields an unblocking temperature of 125°C. Therefore, grains with unblocking temperatures up to 125°C acquire magnetization from the Earth's field. This viscous contamination can be mostly removed by ~1 month of storage at 20°C in zero field, which resets grains up to blocking temperatures of 85°C. Additional histories such as mare volcanism heating, ejecta blanket heating, and shock heating, may also be explored using Fig. 7.5.

7.5. Comparison with published data

7.5.1 *Thellier-Thellier paleointensity determination*

Thermal demagnetization experiments are useful in determining which grains carry remanence and how the remanence of those grains has been affected by viscous overprinting. The most robust thermal demagnetization techniques for determining the paleofield H_o is the Thellier-Thellier double heating method [29]. Briefly, rocks are heated to a given temperature, and their remaining remanent magnetization is measured after cooling in a zero field environment. The samples are then reheated to the same temperature and allowed to cool in an ambient field, H_a. Ideally, the NRM lost in the first step will be equal to the partial thermal remanent magnetization (pTRM) gained in the second step, up to a factor equal to the ratio H_o/H_a. Each double heating step is plotted as NRM remaining vs. pTRM gained (the Arai plot), for which a straight line

indicates ideal single domain behavior (no thermal alternation), and the slope provides H_a/H_o.

Thellier-Thellier experiments are ideally suited for assessing our predictions because the stepped heating method allows the user to sense the effects of past thermal events without requiring knowledge of the blocking temperature distribution in the rock. For example, it may be that a rock has few grain sizes with low blocking temperatures, such that most of its remanence is carried by higher blocking-temperature grains. Merely heating such a rock and measuring the decrease in NRM would reveal small changes in NRM at low temperatures and greater changes at higher temperatures. However, this would not unambiguously distinguish between there being few grains of low blocking-temperature, or a significant amount of low blocking-temperature grains that had relaxed in a low field environment. In a Thellier-Thellier experiment, if there are few grains within a given blocking temperature range, this will be reflected as small differences in the distances between heating steps at those blocking temperatures (in an Arai plot), but the slope of the line will nonetheless be indicative of the field that those grains have acquired.

We note that Thellier-Thellier experiments assume single domain behavior, but an order of magnitude estimate of the paleofield can still be achieved with multidomain samples [6]. This level of accuracy is often sufficient in studies of extraterrestrial materials.

7.5.2 *Predicted Arai plot*

The three previously outlined lunar thermal histories predict an ideal Arai plot with three different slopes (Fig. 7.6). The first slope at low temperature heating steps represents acquisition of viscous remanence in the Earth's field. The second slope is shallower, representing the loss of remanence over 2-4 B.y. in a presumably low field environment on the lunar surface. It represents both the time spent in the shallow subsurface at cold temperatures and at the surface at diurnal temperatures. The second slope should ideally begin near 125°C and end at approximately 350-375°C. The third slope is steeper than the second, indicating acquisition of an NRM in a lunar paleofield and should end at the Curie temperature, 771°C. The third slope may or may not be higher than the first slope, depending on the lunar paleofield strength. Fig. 7.8.14 of ref. [6] shows examples of similar effects in Earth basalts.

7.5.3 Comparison with published data

We next examine the very limited published Thellier-Thellier experiments for comparison with the above predictions. We restrict our comparisons to generally decreasing Arai plots in order to exclude rocks that have undergone significant alteration during heating. All lines that we show on the Thellier-Thellier plots are the original best-fit lines reported by the authors. Heating times are not specifically reported in any of the studies, but appear to be on the order of 10 minutes, or 600 s, which is near the 1000 s

unblocking time we have assumed above. These Thellier-Thellier studies, which lack pTRM checks for alteration and may be affected by magnetic interactions, are not high-quality by terrestrial standards [30].

Two of our samples, 15498 and 60255, are glassy regolith breccias whose magnetic properties are probably dominated by single domain and superparamagnetic particles [30, 31]. These samples have relatively high ratios of saturation remanent magnetization (J_{rs}) to J_s ranging from 0.05 to 0.12 and relatively high ratios of J_s to initial susceptibility per unit mass (χ_0) from 7×10^{-2} to 9×10^{-2} m/A, suggesting that they contain predominantly a mixture of single domain and superparamagnetic grains. For these rocks, it has been argued that abundant superparamagnetic crystals rather than multidomain crystals are responsible for J_{rs}/J_s below the critical threshold of 0.5 for single domain iron dominated by shape anisotropy. However, one cannot rule out that some fraction of the grain sizes is multidomain.

Three other samples, 62235, 70215, and 75035, have the significant limitation that their remanence may be not be dominated by single domain grains, but rather by a spectrum of grain sizes from single domain to multidomain. A sixth sample, glassy regolith breccia 70019, has some glass-rich portions with a significant multidomain component but also has regolith-dominated fractions with finer grain sizes [32]. We have included these latter four samples in the discussion because most have some sections of their Arai plots that do not show concave up behavior that is characteristic of multidomain samples, suggesting that some single domain component is present. Nevertheless, we emphasize that our application of Néel theory calculations to these three samples must be regarded as provisional.

7.5.4 *Sample 15498*

Sample 15498 is a 2.34 kg glassy matrix regolith breccia of mare derivation collected at the rim of Dune Crater [33]. Its age is unknown but is almost certainly less than the ~3.3 Ga age of the surrounding basalts. Metal in the sample typically has 2-14% Ni, and < 2% Co [34]. The sample has $J_{rs}/J_s = 0.09$, a ratio of coercivity of remanence to coercivity $H_{cr}/H_c = 9$, and $\chi_0/J_s = 7\times10^{-2}$ m/A [31, 35], suggesting a modest single or PSD component. Gose and Carnes found that the sample's time-dependent magnetization attributes were in agreement with Néel's theory for single domain iron crystals [36]. The paleofield determined by [37] is 21 μT for temperatures 500-650°C (Fig. 7.7A). The initial NRM direction is rather stable upon heating. While there is some nonlinearity in the Thellier-Thellier low-temperature steps up to 400°C, they appear to form a region of low slope near that temperature. Taken at face value, the low temperature data are therefore again in reasonable agreement with our predictions of a slope break at 325-375°C.

7.5.5 *Sample 60255*

Of all the samples discussed here, 60255 is the one we can most confidently identify as having remanence with a large contribution from single domain iron. 60255 is a glassy matrix regolith breccia with a bulk composition of gabbroic anorthosite that matches the local soils at the Apollo 16 site [38]. It has $J_{rs}/J_s = 0.06$, $H_{cr}/H_c = 14$ and χ_0/J_s

$= 9\times10^{-2}$ m/A [30, 39]. Magnetic granulometry studies have found that ~15 volume % of the metallic iron in 60255 is in the superparamagnetic size range with an average size of 4 nm [40]. The Arai plot for two subsamples is shown in Figure 7B [41]. While the Thellier-Thellier experiment does not start until 225°C, some valuable inferences can be made from separate thermal demagnetization data starting at room temperature. In these experiments (not shown), a strong decrease in magnetization and change in direction is observed between 100-200°C. The authors attribute this change to a VRM acquired on Earth, which is in agreement the predicted slope break of ~125°C. In fact, the authors start the Thellier-Thellier experiments above 200°C on the basis of an unreported Néel theory calculation. If we examine the data for the subsample with filled data points in Figure 7B, we find that the slope gradually develops and becomes steeper near 300°C. This is suggestive of the predicted slope break at 325°C due to viscous relaxation on the lunar surface.

7.5.6 *Sample 70019*

Sample 70019 is a 160 g soil breccia [42] collected for lunar magnetism studies because of its high content of glass and proximity to a 3-meter glass-lined crater that implied a young age [43]. The total age is likely less than 200 My [44], and the exposure age of the rock based on ^{26}Al and ^{53}Mn abundances is between 2-8 M.y. [45, 46]. Kamacite in the sample has 1.7-2.6% Ni [47] and unknown cobalt content. The glass portions of the sample have $J_{rs}/J_s = 0.02$ and $\chi_0/J_s \sim 2\times10^{-2}$ m/A, while the regolith breccia portions have $J_{rs}/J_s = 0.06$-0.07 and $\chi_0/J_s \sim 8\times10^{-2}$ m/A (χ_0 estimated from plot of

J vs. *H*) [48], indicating that like lunar soils, the regolith breccia is likely dominated by single domain or and superparamagnetic grains. The paleointensities for two subsamples are 120 μT and 250 μT (Fig. 7.7C) [43]. Unfortunately, the relative glass and soil content for these two subsamples is not clearly reported in ref. [43], making it difficult to know whether the remanence is dominated by single or multidomain crystals. Both subsamples had been stored in a low field room for more than 6 months and their magnetization directions are stable upon heating. The very young age of the glass makes the sample of interest, since it is unlikely a dynamo was operating on the Moon within the last 200 My.

The Thellier-Thellier data in Fig. 7.7C show unusual behavior compared to the other samples. The slope in the low temperature (up to ~300°C) heating steps is steeper than the high temperature (> 300°C) fraction. A steep slope in the low temperature region could suggest viscous acquisition of the Earth field. However, this break is more than 175°C higher than the maximum predicted blocking temperature affected by terrestrial contamination. These results are as puzzling as the origin of its high temperature magnetization, and may suggest a strong isothermal remanence was overprinted on the rock, as has been noted previously for many lunar samples [49]. We note above about 500°C the data are affected by alteration products.

7.5.7 *Sample 62235*

Sample 62235 is an impact melt breccia with a total mass of 320 g collected at the rim of Buster Crater [38]. Its U-Pb systematics indicate a thermal disturbance at 3.9 Ga

[50], which probably sets an upper limit on the time when it acquired its magnetization. It has a noble gas exposure age of 104-163 M.y. [51], and a surface suntan age of 2-3 M.y. based on particle tracks and micrometeorite craters [52, 53]. Metal grains in the sample typically have < 6% Ni and < 0.5% Co [34]. The rock has $J_{rs}/J_s = 8.6\times10^{-3}$ and $H_{cr}/H_c = 52$ [54], putting it squarely in the multidomain size range. Two different laboratories found that the NRM was generally stable during demagnetization and reported similar paleointensities of 120 μT using the Thellier-Thellier technique [54, 55] (Figs. 7D and 7E). This field strength is twice that at the surface of the present Earth, making sample 62235 of great interest to lunar magnetism. Pearce et al. [34] also performed Thellier-Thellier experiments, but because their Arai plots are non-linear, no paleointensity was reported.

Figure 7D shows a clear slope break between 215-262°C, which falls between the predicted breaks at 100°C and 300-350°C. Because the slope before 262°C is shallower than the rest of the rock we may interpret it as due to viscous relaxation on the surface of the Moon, as also suggested in Sugiura and Strangway [54]. Since the suntan age of the rock is ~2 M.y., we would predict a slope break closer to 325°C due to surface exposure, which slightly overestimates the observed break between 215-262°C. Strangely, there does not appear to be any signature of viscous acquisition of the Earth's field. Sugiura and Strangway do not report if the rock was stored in a zero field environment. Although Figure 7E is a much lower resolution study, there is a subtle change in slope from shallow to steep between 260°C and 340°C. In all, we find that the agreement is fair considering the uncertainty.

7.5.8 *Sample 70215*

Sample 70215 is a fine-grained basalt collected 60 m from the Lunar Module, with a mass of 8.11 kg [42]. Its ^{40}Ar-^{39}Ar is 3.63-3.85 Ga [56, 57] and it has an exposure age ranging from 100-126 My [56, 58]. A surface exposure age from particle tracks and micrometeorites is not available and the Ni and Co content of metal in this sample could not be found in the literature. The sample has $J_{rs}/J_s = 7\times10^{-3}$ and $\chi_0/J_s = 2.6\times10^{-2}$ m/A [59], indicating a significant multidomain component. Thellier-Thellier data (Fig. 7.7F) suggest a paleofield of 2 μT at low blocking temperatures and 7.5 μT at high blocking temperatures [60]. Its magnetization direction wanders slowly upon heating. The Thellier-Thellier experiment shows a clear slope break between 260°C and 340°C. Given the low thermal resolution of this study, this agrees with our predictions of a break at 325-375°C.

7.5.9 *Sample 75035*

Sample 75035 is a medium-grained basalt collected near Camelot crater [42]. It has a ^{39}Ar-^{40}Ar age of 3.77 Ga [61], with an exposure age between 72-80 M.y. [51, 62, 63]. The sample contains kamacite-troilite intergrowths, with Ni < 0.1% and Co < 1.14% in both phases [64]. The value of J_{rs}/J_s is unavailable and it has $\chi_0/J_s = 2.5\times10^{-2}$ m/A . Upon thermal demagnetization all NRM disappeared by 250°C (Fig. 7.7G) [65], although

it is possible that this resulted from low instrument sensitivity rather than lack of stable magnetization above these temperature. Its magnetization direction is stable up to 200°C, after which the orientation of its magnetization vector changes by 100°. What is interesting about this sample is the gradual change in slope between 160-200°C. If the rock acquired the Earth's field for ~10 y, a gradual rounding out due to relaxation in the lunar subsurface is predicted to start at 125°C, but it appears the rounding out starts at higher temperatures than expected (160-200°C). A strong multidomain component cannot be ruled out.

7.6. Discussion

In general, we find support for our predictions in the highest quality Thellier-Thellier experiments available for lunar rocks, although it is clear that none of the plots look like the ideal plot in Fig. 7.6. For 60255, 15498, 62235, and 70215, and we see changes from low to high slope near 300°C, suggesting demagnetization on the lunar surface. For 62235, 70215, and 60255, the predicted break near 325-375°C overestimates the observed breaks, while for 15498 the lack of data between 300-400°C makes no conclusion possible. Samples 75035 and 60255 appear to gradually flatten out by 200°C, which suggests an overestimate of the temperature of acquisition of any Earth field. Since instrument sensitivity seems to be reached before 75035 is demagnetized, we cannot test if the slope changes again near 325-375°C. Sample 70019 has an anomalously high slope up to 300°C, a temperature well above our predictions. Despite these shortcomings, our calculations are useful as a general guideline for several reasons:

1) we can see consistent slope breaks even with the low resolution data available for four of the rocks (60255, 15498, 62235, 70215), 2) our underestimates of the slope break are not large, and may be explained by multidomain behavior (below), 3) multidomain grains, magnetic interactions, and the possible crystallization remanent magnetization from phase changes during initial cooling can explain some of the behavior in 70019 and 75035 (below). We note that Pullaiah et al. [1] performed experiments to verify their unblocking temperature predictions, and found they were not always in agreement.

If a rock has multidomain grains it will be more difficult to thermally demagnetize than if it had only single domain grains. The root of this difficulty is that a multidomain grain acquires its magnetization by rearrangement and pinning of its domain walls [6]. Increasingly elevated temperatures continually shift the domain magnetization through progressively lower-energy pinning states instead of rotating domains at a well-determined temperature as in single domain grains. This produces a spectrum of unblocking temperatures up to the Curie temperature [6]. Therefore, on the lunar surface, it may be more difficult to demagnetize rocks with multidomain grains up to the blocking temperatures of 325-375°C predicted by Fig. 7.6 for single-domain grains. This could account for our consistent underestimates of the slope breaks in 60255, 62235 and 70215.

The same wall pinning process that leads to difficulty in thermally demagnetizing a multidomain sample leads to concave-up Thellier-Thellier curves. Perhaps more than any of the others, sample 75035 shows evidence of concave-up behavior at all heating steps, suggesting it may be strongly multidomain. Samples 62235 and 70215 do not show this behavior, but they nonetheless may be multidomain enough to account for the overestimates described above. Samples 70019 (glass fractions) and 75035 may be of

sufficient multidomain character that lunar surface temperatures were not able to effectively cause noticeable breaks in slope.

It is important to note that there may be a self-reversal effect operating near 300°C. Between 250-300°C Pearce et al. [34] observed discontinuities in Thellier-Thellier heating experiments and pTRM acquisition experiments in a variety of lunar rocks (including 62235) and one synthetic sample. Their explanation was that upon cooling, troilite (FeS) was interacting with the TRM of nearby kamacite to form troilite TRM of opposite magnetization with unblocking temperatures near 250-300°C. This requires that troilite, an antiferromagnet with Néel point of 305°C, behave ferromagnetically by means of crystal defects. As kamacite cools and acquires a TRM above 305°C, adjacent ferromagnetic troilite is oppositely magnetized as it cools through its Néel point. During heating steps in a Thellier-Thellier experiment, acquired pTRM continues to increase normally up to 250-305°C. At around 250°C acquired pTRM decreases slightly before continuing to increase, since the canceling effect of troilite starts to affect the remanence. The model assumes most troilite blocking temperatures are between 250-305°C, and would therefore affect the Thellier-Thellier slope in the same region. The limited affect on the slope suggests self-reversal is probably not a factor in interpreting our predictions, but it should not be ruled out. At the very least, the self-reversal effect may be another reason to use caution near temperatures around ~300°C in thermal demagnetizing experiments.

Past studies of lunar samples have estimated the paleofield by normalizing NRM by saturation isothermal remanence (SIRM). The thermal demagnetizing effects of the lunar surface means that the NRM/SIRM technique of measuring the paleofield is only

measuring grains with unblocking temperatures above 325-375°C. Therefore, this technique may underestimate the paleofield by a factor of almost two (assuming the sample has evenly distributed blocking temperatures). Dunlop et al. [66] found that at least one lunar sample had almost half of its grain population with blocking temperatures below 300°C.

7.7. Conclusions

1) Néel theory demonstrates that despite storage on the lunar crust for billions of years, lunar rock magnetism is thermally stable. The available Thellier-Thellier experiments to verify this prediction are limited and of low resolution, but we observe what is likely a paleofield in the high temperature portions of some experiments. This is usually the same interpretation made by most of the original authors. Whatever the origin of these fields, nonequilibrium microstructures, self-reversal effects, thermal alteration during heating, and the multidomain character of the metal grains are likely to be more important than time-temperature effects in the interpretation of lunar rock magnetism.

2) Single domain grains with blocking temperatures up to ~325-375°C should have lost some of their remanence due to exposure to temperatures up to 110°C on the lunar surface. Therefore, remanence carried by such grains is unlikely to be a primary paleomagnetic record. Remanence carried by grains with blocking temperatures below ~125°C is probably a recent viscous remanence acquired on Earth.

3) Viscous contamination from storage in the Earth field for 10-30 years can be mostly removed by ~1 month of storage at 20°C in zero field, which should reset single domain grains with blocking temperatures up to 85°C. Alternatively, the sample can be heated in zero field to 125°C. This is an important consideration for planetary paleomagnetists, who are often reluctant or not permitted to perform potentially damaging heating experiments. Such a low-temperature heating step is unlikely to cause damage.

4) The unblocking of magnetism over millions of years implies that NRM/SIRM (otherwise known as total REM) measurements may underestimate the lunar paleofield, depending on the blocking temperature and grain size distribution in the rock.

5) These calculations can be used to assess a variety of other lunar thermal histories including mare volcanism and impact ejecta burial. They can also be used to interpret the magnetism of meteorites, asteroids, and any other iron-bearing bodies in the solar system.

6) The greater the multidomain character of the sample, the less applicable our calculations will be. A complete test our calculations will require more single domain samples with well documented time-temperature histories.

References

[1] G. Pullaiah, E. Irving, K.L. Buchan, D.J. Dunlop, Magnetization changes caused by burial and uplift, Earth Planet. Sci. Lett 28(1975) 133-143.

[2] D.J. Dunlop, O. Ozdemir, D.A. Clark, P.W. Schmidt, Time-temperature relations for the remagnetization of pyrrhotite (Fe_7S_8) and their use in estimating paleotemperatures, Earth Planet. Sci. Lett. 176(2000) 107-116.

[3] B.P. Weiss, J.L. Kirschvink, F.J. Baudenbacher, H. Vali, N.T. Peters, F.A. MacDonald, J.P. Wikswo, A low temperature transfer of ALH84001 from Mars to Earth, Science 290(2000) 791-795.

[4] L. Néel, Théorie due trainage magnétique des ferromagnétiques en grains fins avec applications au terres cuites, An. Geophys. 5(1949) 99-136.

[5] P. Wasilewski, Magnetic remanence mechanisms in iron and iron-nickel alloys, metallographic recognition criteria and implications for lunar sample research, Moon 9(1974) 335-354.

[6] D.J. Dunlop, Ö. Özdemir, Rock Magnetism: Fundamentals and Frontiers, Cambridge University Press, Cambridge, UK, 1997, 596 pp.

[7] L.J. Swartzendruber, V.P. Itkin, C.B. Alcock, Iron-Nickel, in: H. Okamoto, (Ed), Phase Diagrams of Binary Iron Alloys, ASM International, Materials Park, OH, 1993, pp. 256-278.

[8] A.D. Romig, J.I. Goldstein, Determination of the Fe-Ni and Fe-Ni-P phase diagrams at low temperatures (700-300°C), Metall. Trans. A 11A(1980) 1151-1159.

[9] C.-W. Yang, D.B. Williams, J.I. Goldstein, Low-temperature phase decomposition in metal from iron, stony-iron, and stony meteorites, Geochimica et Cosmochimica Acta 61(1997) 2943-2956.

[10] M. Peschard, Contribution to the study of ferro-nickels, Rev. Metall. 22(1925) 430-676.

[11] E.A. Wilson, The /gamma -> /alpha transformation in low carbon irons, ISIJ Int. 34(1994) 615-630.

[12] H.K.D.H. Bhadeshia, Diffusional formation of ferrite in iron and its alloys, Prog. Materials Sci. 29(1985) 321-386.

[13] T.B. Massalski, Distinguishing features of massive transformations, Metal. Trans. 15A(1984) 421-425.

[14] S.H. Chong, A. Sayles, R. Keyse, J.D. Atkinson, E.A. Wilson, Examination of microstructures and microanalysis of a Fe-9% Ni alloy, Materials Transactions 39(1998) 179-188.

[15] E.A. Wilson, S.H. Chong, Isothermal transformations in an Fe-9% Ni alloy, Metallurgical and Materials Transactions A 33A(2002) 2425-2431.

[16] K.B. Reuter, D.B. Williams, J.I. Goldstein, Determination of the Fe-Ni phase diagram below 400°C, Metall. Trans. A 20A(1989) 719-725.

[17] R.J. Reisener, J.I. Goldstein, Ordinary chondrite metallography: Part 1. Fe-Ni taenite cooling experiments, Meteorit. Planet. Sci. 38(2003) 1669-1678.
[18] P. Wasilewski, Magnetization of small iron-nickel spheres, Phys. Earth. Planet. Inter. 26(1981) 149-161.
[19] M.D. Kuz'min, Shape of temperature dependence of spontaneous magnetization of ferromagnets: quantitative analysis, Phys. Rev. Lett. 94(2005) 107204.
[20] J. Crangle, G.M. Goodman, The magnetization of pure iron and nickel, Proc. R. Soc. London A 321(1971) 477-491.
[21] R.M. Bozorth, Ferromagnetism, D. Van Nostrand, Princeton, 1951, 968 pp.
[22] F.D. Stacey, S.K. Banerjee, The physical principles of rock magnetism, Elsevier, Amsterdam, 1974, 195 pp.
[23] L.P. Tarasov, Ferromagnetic Anisotropy of Low Nickel Alloys of Iron, Phys. Rev. 56(1939) 1245-1246.
[24] T. Nishizawa, K. Ishida, Co-Fe (Cobalt-Iron), in: H. Okamoto, (Ed), Phase Diagrams of Binary Iron Alloys, ASM International, Materials Park, OH, 1993, pp. 93-101.
[25] T. Nagata, N. Sugiura, R.M. Fisher, F.C. Schwerer, M.D. Fuller, J.R. Dunn, Magnetic properties of Apollo 11-17 lunar materials with special reference to effects of meteorite impact, Proc. Lunar Sci. Conf. 5th(1974) 2827-2839.
[26] G.H. Heiken, D.T. Vaniman, B.M. Fench, Lunar Sourcebook: A User's Guide to the Moon, Cambridge University Press, Cambridge, UK, 1991, 756 pp.
[27] B.B. Wilcox, M.S. Robinson, P.C. Thomas, B.R. Hawke, Constraints on the depth and variability of the lunar regolith, Meteorit. Planet. Sci. 40(2005) 695-710.
[28] R. Arvidson, G. Corzaz, R.J. Drozd, C.M. Hohenberg, C.J. Morgan, Cosmic ray exposure ages of features and events at the Apollo landing sites, Moon 13(1975) 259-276.
[29] E. Thellier, O. Thellier, Sur l'intensité du champ magnétique terrestre dans le passe historique et geologique, An. Geophys. 15(1959) 285-376.
[30] M. Fuller, S.M. Cisowski, Lunar paleomagnetism, in: J.A. Jacobs, (Ed), Geomagnetism II, Academic Press, New York, 1987, pp. 307-455.
[31] M. Fuller, Lunar magnetism, Rev. Geophys. Space Phys. 12(1974) 23-69.
[32] G.W. Pearce, C.-L. Chou, On the origin of sample 70019 and its suitability for lunar magnetic field intensity studies, Proc. Lunar Sci. Conf. 8th(1977) 669-677.
[33] G. Ryder, Catalog of Apollo 15 Rocks, NASA Curatorial Branch Publication 72, Houston, 1985, 1296 pp.
[34] G.W. Pearce, G.S. Hoye, D.W. Strangway, Some complexities in the determination of lunar paleointensities, Proc. Lunar Sci. Conf. 7th(1976) 3271-3297.
[35] G.W. Pearce, W.A. Gose, D.W. Strangway, Magnetic studies on Apollo 15 and 16 lunar samples, Proc. Lunar Sci. Conf. 4th(1973) 3045-3076.
[36] W.A. Gose, J.G. Carnes, The time dependent magnetization of fine-grained iron in lunar breccias, Earth Planet. Sci. Lett. 20(1973) 100-106.
[37] W.A. Gose, D.W. Strangway, G.W. Pearce, A determination of the intensity of the ancient lunar magnetic field, Moon 7(1973) 196-201.
[38] G. Ryder, M.D. Norman, Catalog of Apollo 16 Rocks, NASA Lunar Curatorial Laboratory Publication JSC-16904, Houston, 1980.

[39] T. Nagata, R.M. Fisher, F.C. Schwerer, M.D. Fuller, J.R. Dunn, Magnetic properties and natural remanent magnetization of Apollo 15 and 16 lunar materials, Proc. Lunar Sci. Conf. 4th(1973) 3019-3043.

[40] F.C. Schwerer, T. Nagata, Ferromagnetic-superparamagnetic granulometry of lunar surface materials, Proc. Lunar Sci. Conf. 7th(1976) 759-778.

[41] N. Sugiura, D.W. Strangway, Comparisons of magnetic paleointensity methods using a lunar sample, Proc. Lunar Sci. Conf. 11th(1980) 1801-1813.

[42] G. Ryder, Catalog of Apollo 17 Rocks, Lunar and Planetary Institute, NASA publication JSC-26088, Houston, 1993, 644 pp.

[43] N. Sugiura, Y.M. Wu, D.W. Strangway, G.W. Pearce, L.A. Taylor, A new magnetic paleointensity value for a 'young lunar glass', Proc. Lunar Sci. Conf. 10th(1979) 2189-2197.

[44] P.P. Nunes, Pb loss from Apollo 17 glass samples and Apollo 16 revisited, Proc. Lunar Sci. Conf. 6th(1975) 1491-1499.

[45] J.S. Fruchter, L.A. Rancitelli, J.C. Evans, R.W. Perkins, Lunar surface processes and cosmic ray histories over the past several million years, Proc. Lunar Sci. Conf. 9th(1978) 2019-2032.

[46] Y. Yokoyama, J.L. Reyss, F. Guichard, 22Na-26Al chronology of lunar surface processes, Proc. Lunar Sci. Conf. 5th(1974) 2231-2247.

[47] G.W. Pearce, C.L. Chou, Y. Wu, Chemical compositions and magnetic properties in separated glass and breccia fractions of 70019, Lunar Science 8(1977) 759-761.

[48] G.W. Pearce, C.L. Chou, On the origin of sample 70019 and its suitability for lunar magnetic field intensity studies, Proc. Lunar Sci. Conf. 8th(1977) 669-677.

[49] G.W. Pearce, D.W. Strangway, Cause of secondary magnetization in lunar samples, in: R. Brett, A.W. England, J.E. Calkins, R.L. Giesecke, D.N. Holman, R.M. Mercer, M.J. Murphy, S.H. Simpkinson, (Eds), Apollo 16 Preliminary Science Report, NASA Special Publication SP-315, Houston, 1972, pp. 7-55 to 57-58.

[50] F. Tera, D.A. Papanastassiou, G.J. Wasserburg, Isotopic evidence for a terminal lunar cataclysm, Earth Planet. Sci. Lett 22(1974) 1-21.

[51] R.J. Drozd, C.M. Hohenberg, C.J. Morgan, C.E. Ralston, Cosmic-ray exposure at the Apollo 16 and other lunar sites: lunar surface dynamics, Geochim. Cosmochim. Acta. 28(1974) 1625-1642.

[52] G. Crozaz, R.J. Drozd, C.M. Hohenberg, C.J. Morgan, C.E. Ralston, R. Walker, D. Yuhas, Lunar surface dynamics: some general conclusions and new results from Apollo 16 and 17, Proc. Lunar Sci. Conf. 5th(1974) 2475-2499.

[53] G.H. Morrison, R.A. Nadkarni, J. Jaworski, R.I. Botto, J.R. Roth, Elemental abundance of Apollo 16 samples, Proc. Lunar Sci. Conf. 4th(1973) 1399-1405.

[54] N. Sugiura, D.W. Strangway, Magnetic paleointensity determination on lunar sample 62235, Proc. Lunar Sci. Conf. 13th(1983) A684-A690.

[55] D.W. Collinson, A. Stephenson, S.K. Runcorn, Magnetic properties of Apollo 15 and 16 rocks, Proc. Lunar Sci. Conf. 4th(1973) 2963-2976.

[56] T. Kirsten, P. Horn, Chronology of the Taurus-Littrow region III: ages of mare basalts and highland breccias and some remarks about the interpretation of lunar highland rock ages, Proc. Lunar Sci. Conf. 5th(1974) 1451-1475.

[57] O.A. Schaeffer, H.W. Muller, T.L. Grove, Laser 39Ar-40Ar study of Apollo 17 basalts, Proc. Lunar Sci. Conf. 8th(1977) 1489-1499.
[58] R.J. Drozd, C.M. Hohenberg, C.J. Morgan, F.A. Podosek, M.L. Wroge, Cosmic-ray exposure history at Taurus-Littrow, Proc. Lunar Sci. Conf. 8th(1977) 3027-3043.
[59] G.W. Pearce, D.W. Strangway, W.A. Gose, Magnetic properties of Apollo samples and implications for regolith formation, Proc. Lunar Sci. Conf. 5th(1974) 2815-2826.
[60] A. Stephenson, D.W. Collinson, S.K. Runcorn, Lunar magnetic field palaeointensity determinations on Apollo 11, 16, and 17 rocks, Proc. Lunar Sci. Conf. 5th(1974) 2859-2871.
[61] G. Turner, P.H. Cadogan, The history of the lunar basin formation inferred from 40Ar-39Ar dating of highland rocks, Lunar Sci. 5 (1975) 826-828.
[62] R. Arvidson, R.J. Drozd, E. Guiness, C.M. Hohenberg, C.J. Morgan, R. Morrison, V. Oberback, Cosmic ray exposure ages of Apollo 17 samples and the age of Tycho, Proc. Lunar Sci. Conf. 7th(1976) 2817-2832.
[63] G. Turner, P.H. Cadogan, Possible effects of 39Ar recoil in 40Ar-39Ar dating, Proc. Lunar Sci. Conf. 5th(1974) 1601-1615.
[64] H.O.A. Meyer, N.Z. Boctor, Opaque mineralogy: Apollo 17, rock 75035, Proc. Lunar Sci. Conf. 5th(1974) 707-716.
[65] N. Sugiura, D.W. Strangway, G.W. Pearce, Heating experiments and paleointensity determinations, Proc. Lunar Sci. Conf. 10th(1978) 3151-3163.
[66] D.J. Dunlop, W.A. Gose, G.W. Pearce, D.W. Strangway, Magnetic properties and granulometry of metallic iron in lunar breccia 14313, Proc. Lunar Sci. Conf. 4th(1973) 2977-2990.

Figures

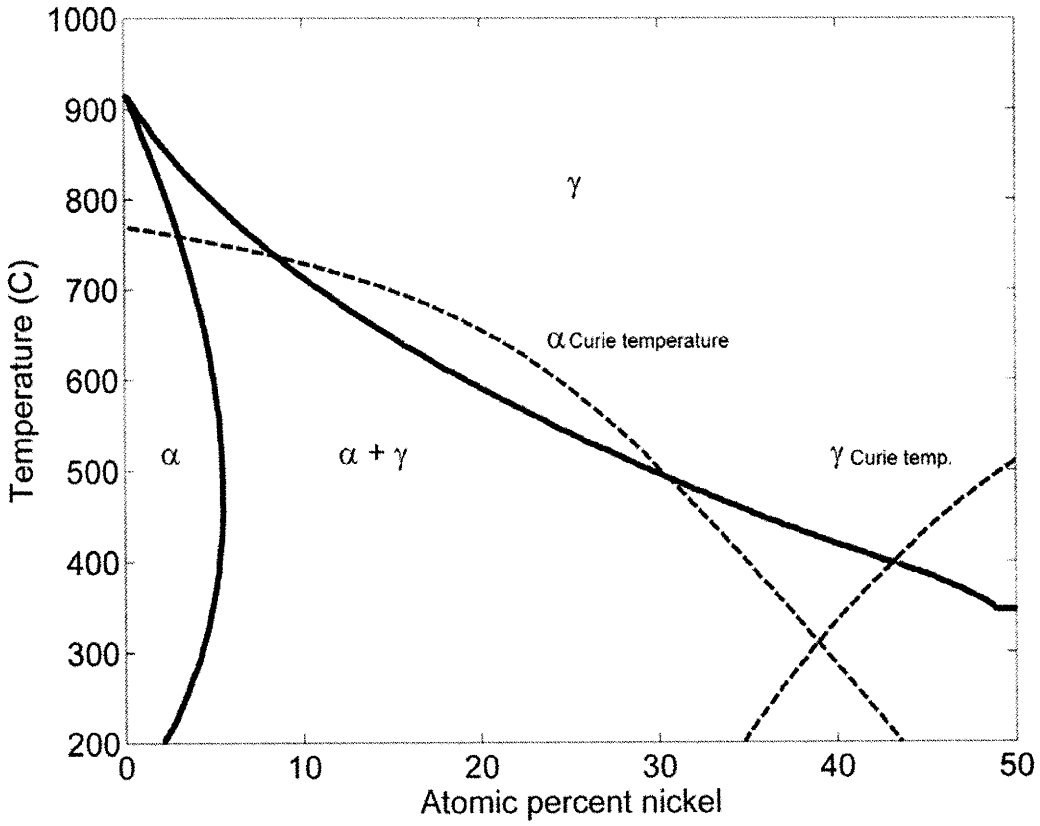

Figure 7.1. Equilibrium phase diagram for the Fe-Ni system [7]. The dashed lines show the Curie temperatures for taenite and kamacite.

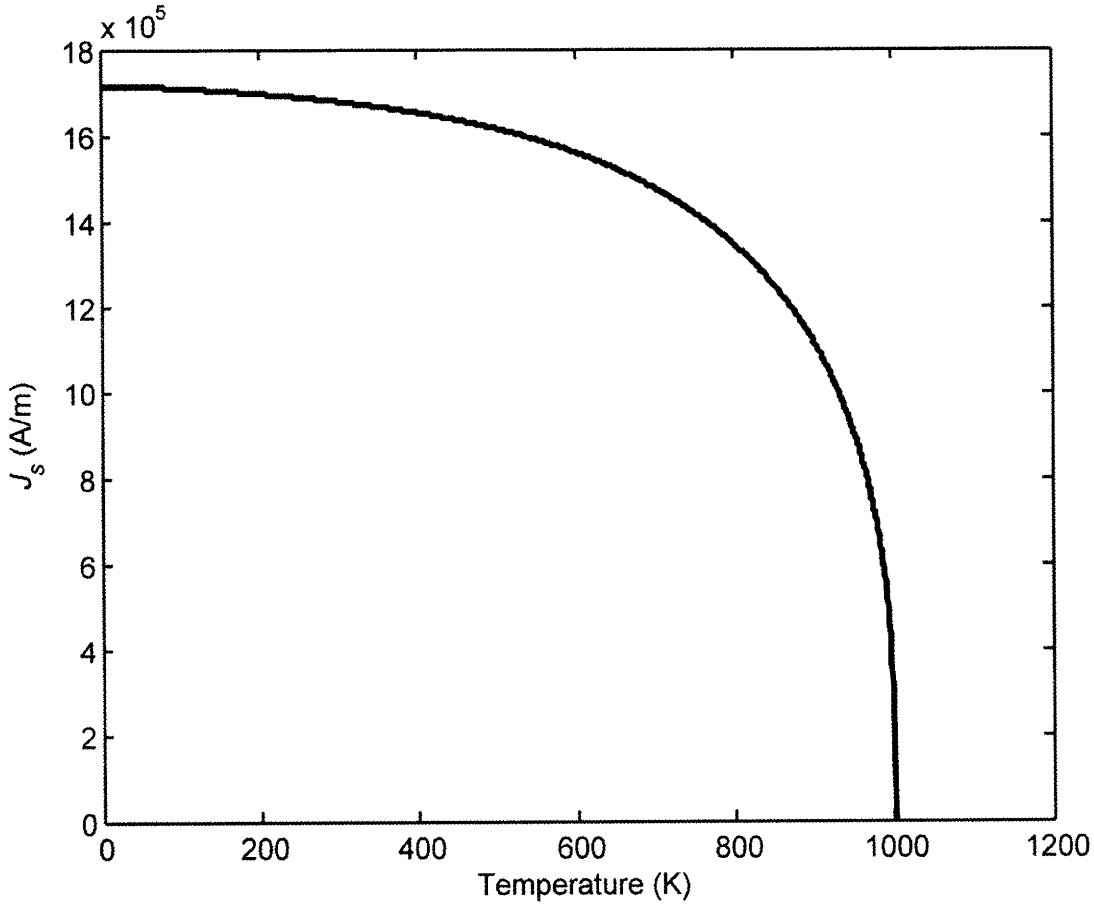

Figure 7.2. Saturation magnetization $J_s(T)$ of kamacite calculated using the parameterization of [19].

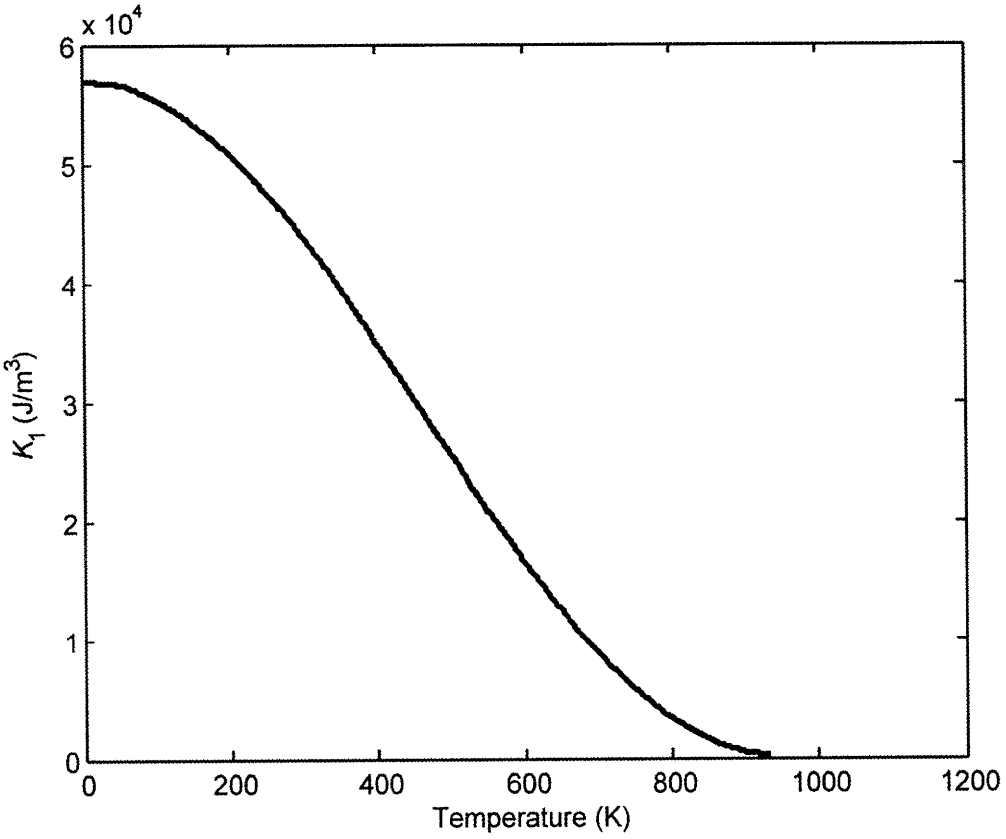

Figure 7.3. First order term of the magnetocrystalline anisotropy constant (K_1) vs. temperature for kamacite [21].

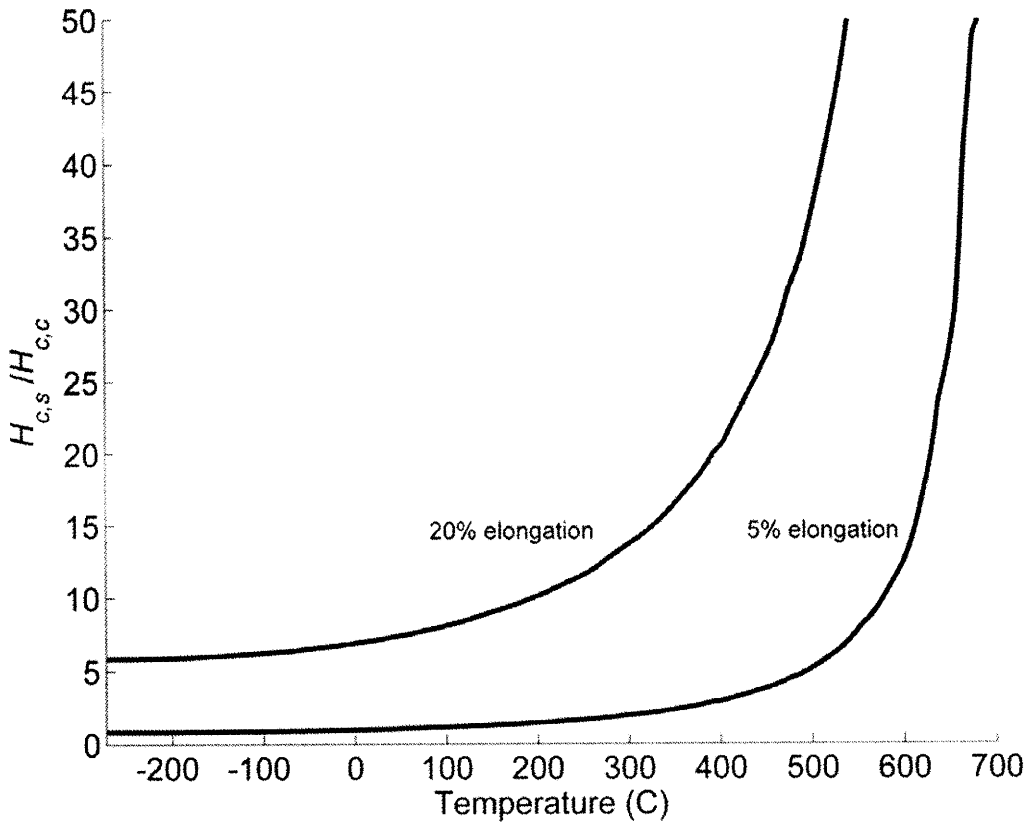

Figure 7.4. Ratio of coercivity from shape anisotropy ($H_{c,s}$) to coercivity from magnetocrystalline anisotropy ($H_{c,\,c}$) for kamacite, as a function of temperature. Data from [21].

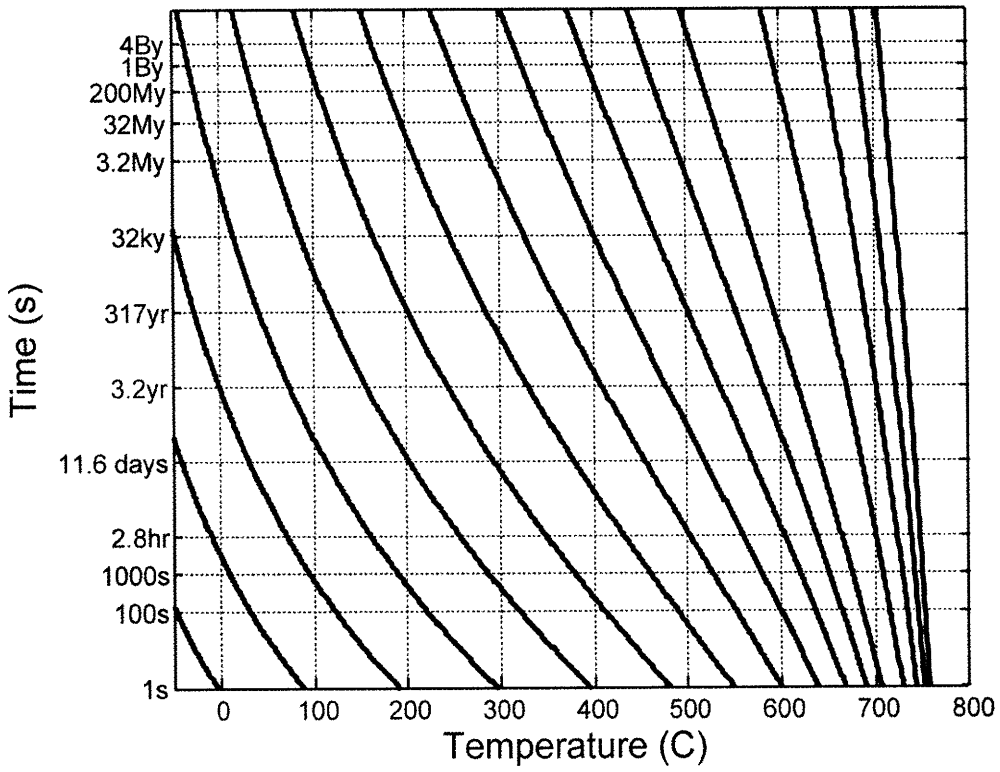

Figure 7.5. Time-temperature unblocking relationships for single domain kamacite grains. Each curve shows the time required to demagnetize or remagnetize a grain (in weak fields) for a particular value of the product $v\ H_c(T)$, where v is the grain volume and $H_c(T)$ is its microscopic coercivity. The curves here were calculated for grains with axial ratios (length/width) of 1.10 (dominated by shape anisotropy) and lengths from 11 to 28 nm, although they can represent the demagnetization behavior for grains with any value of $v\ H_c$. The critical superparamagnetic threshold (diameter at which a grain will demagnetize after 100 s at room temperature) is ~13 nm, in good agreement with experimental data [6].

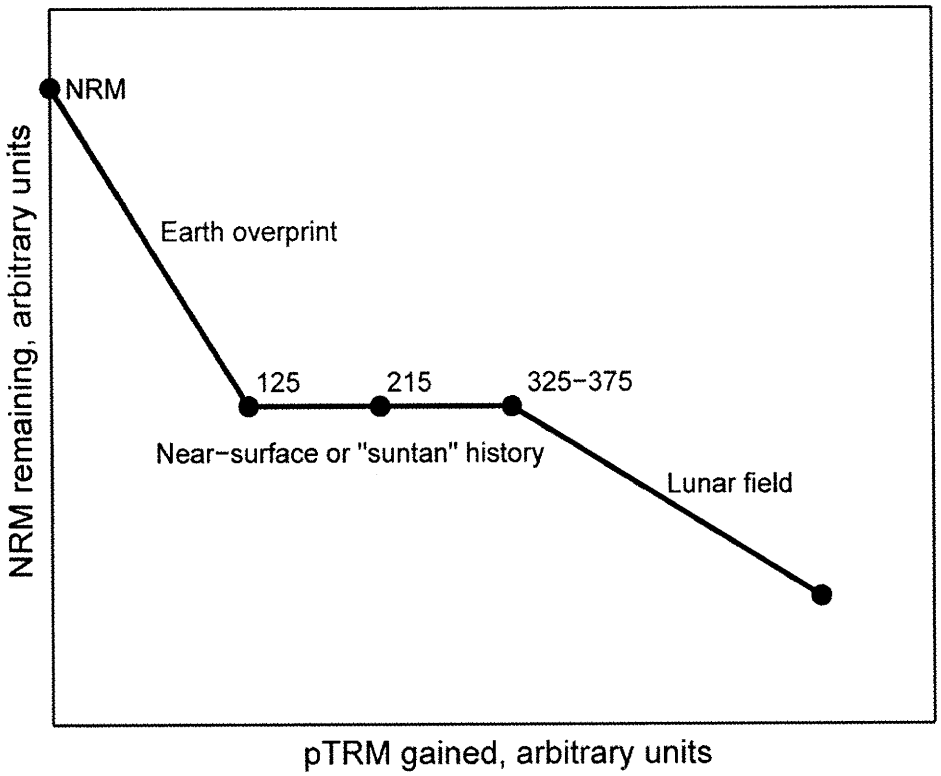

Figure 7.6. Ideal Thellier-Thellier experiment for an Apollo rock containing a population of single domain kamacite grains with a spectrum of blocking temperatures between room temperature and the Curie point.

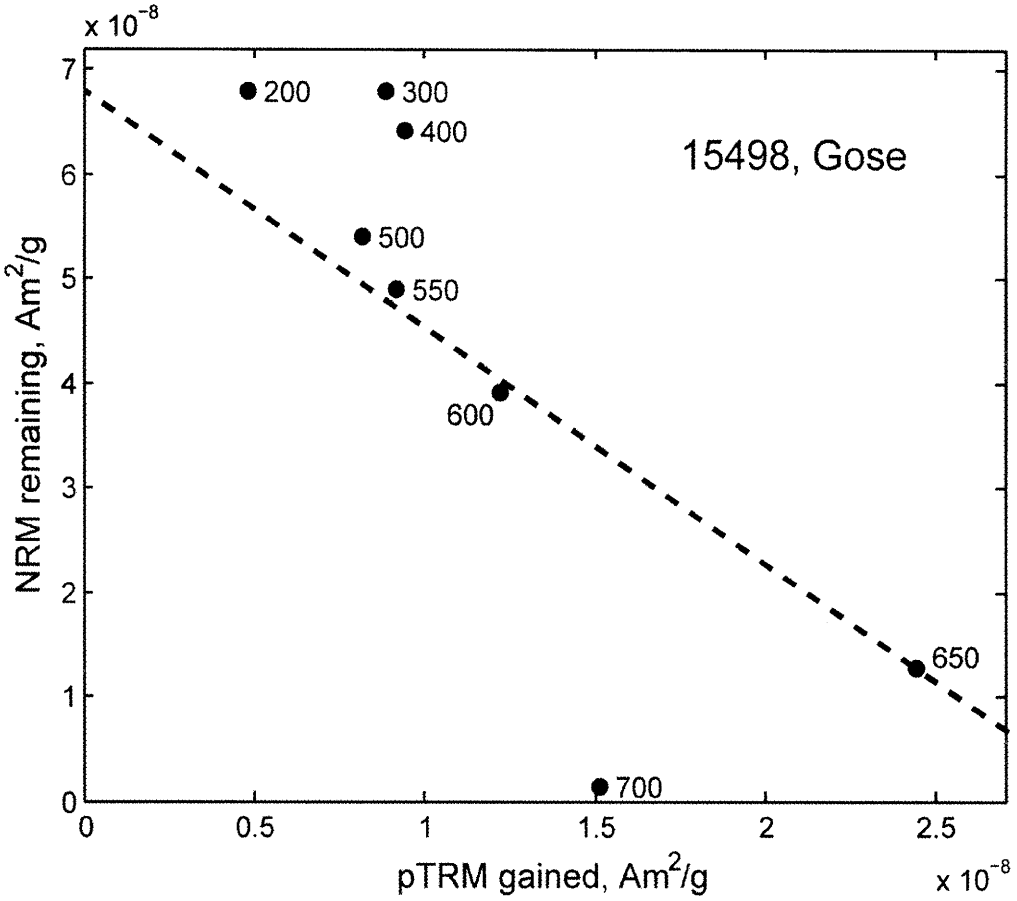

Figure 7.7A. Previously published Thellier-Thellier experiment (Arai plot) for lunar sample 15498 [37]. All temperature steps are in degrees Celsius, and the best-fit line is from the original work.

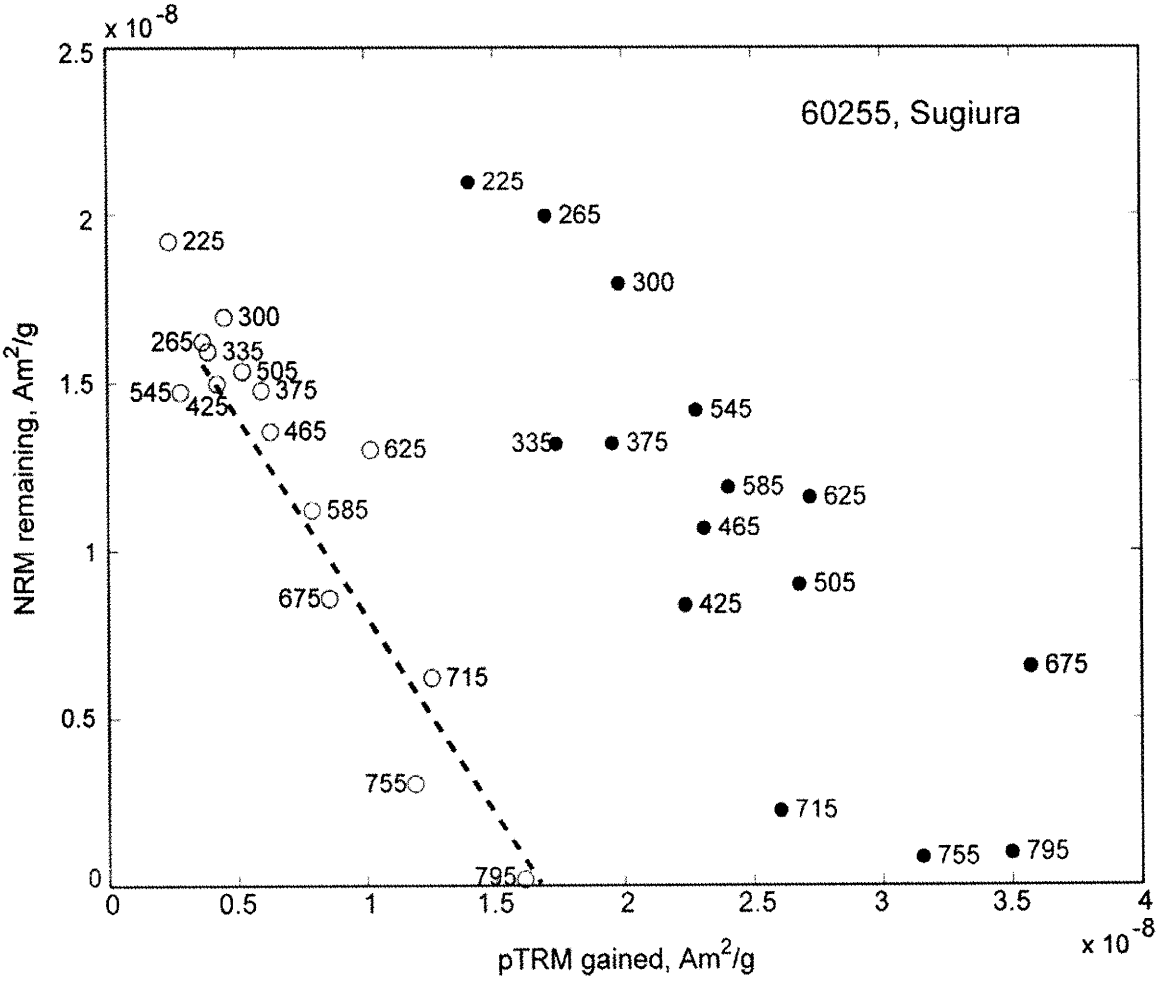

Figure 7.7B. Previously published Thellier-Thellier experiment (Arai plot) for lunar sample 60255 [41]. All temperature steps are in degrees Celsius, and the best-fit line is from the original work.

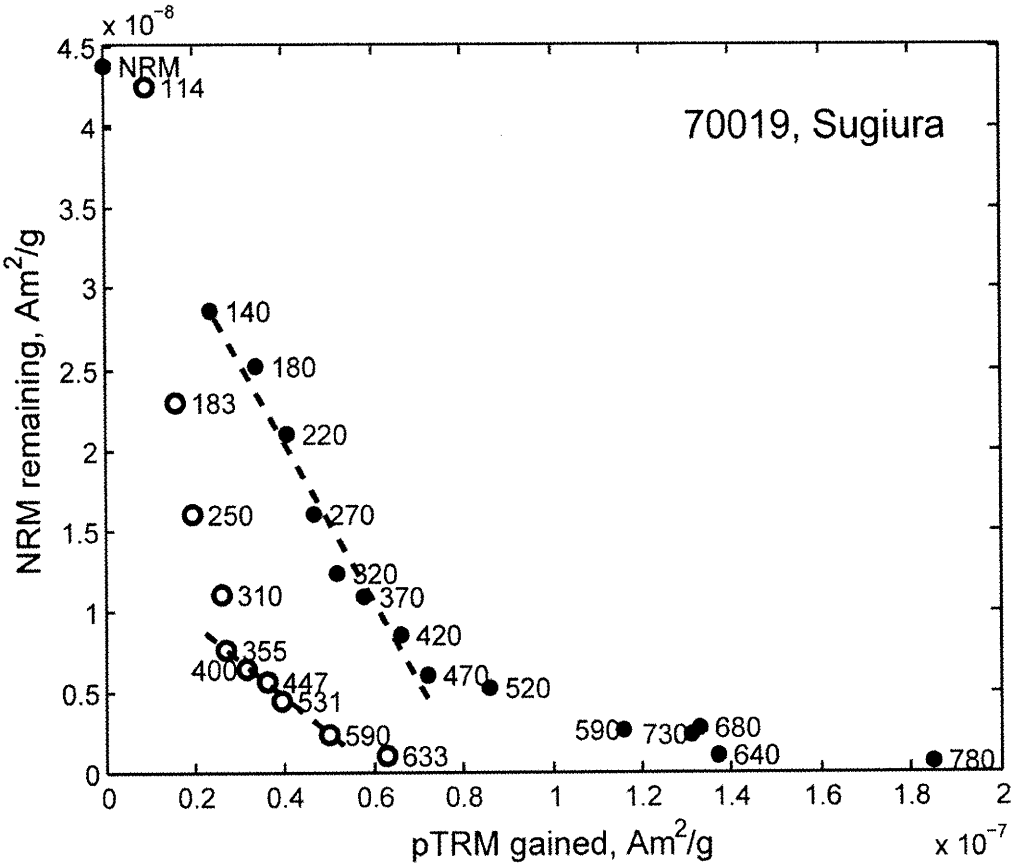

Figure 7.7C. Previously published Thellier-Thellier experiment (Arai plot) for lunar sample 70019 [43]. All temperature steps are in degrees Celsius, and the best-fit lines are from the original work.

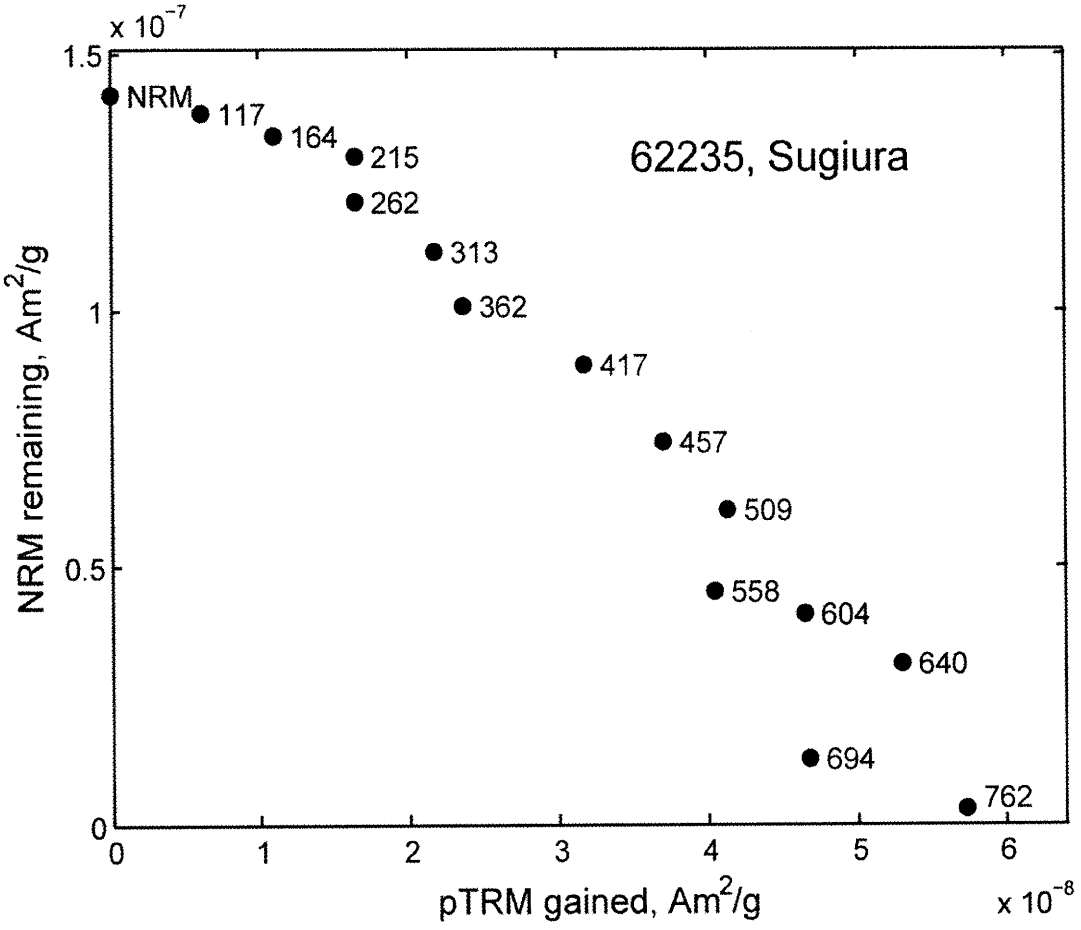

Figure 7.7D. Previously published Thellier-Thellier experiment (Arai plot) for lunar sample 62235 [54]. All temperature steps are in degrees Celsius.

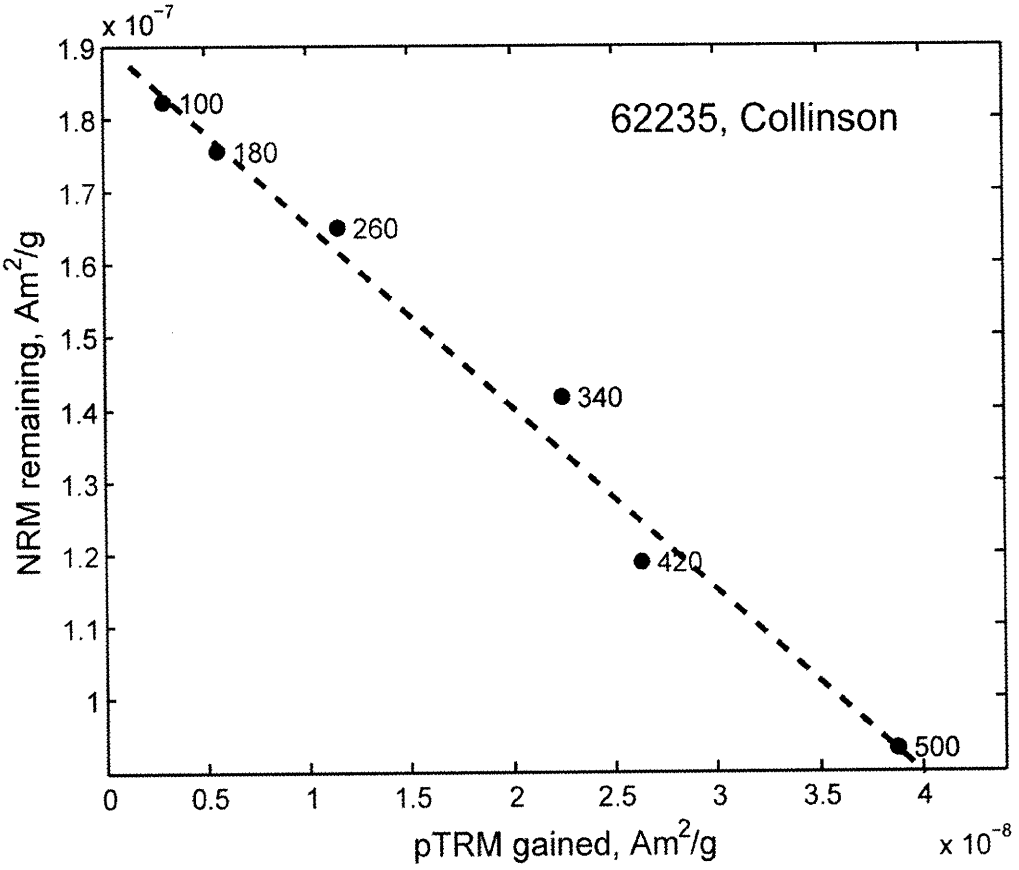

Figure 7.7E. Another previously published Thellier-Thellier experiment (Arai plot) for lunar sample 62235 [55]. All temperature steps are in degrees Celsius, and the best-fit line is from the original work.

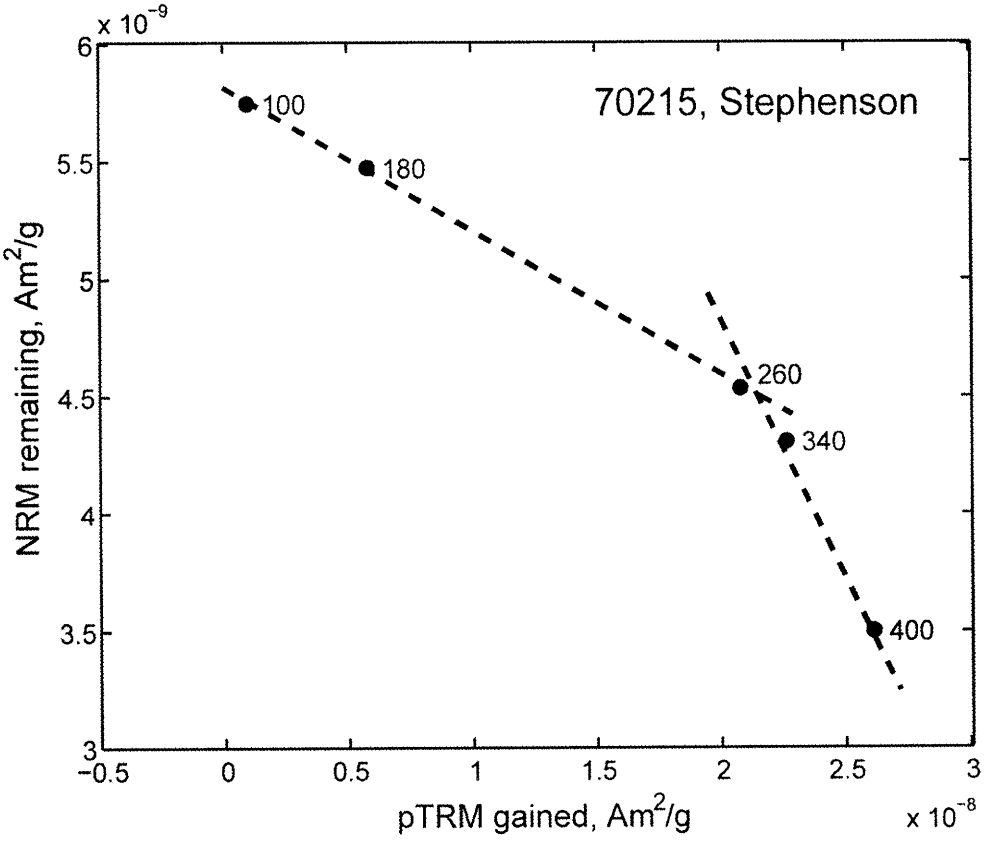

Figure 7.7F. Previously published Thellier-Thellier experiment (Arai plot) for lunar sample 70215 [60]. All temperature steps are in degrees Celsius, and the best-fit lines are from the original work.

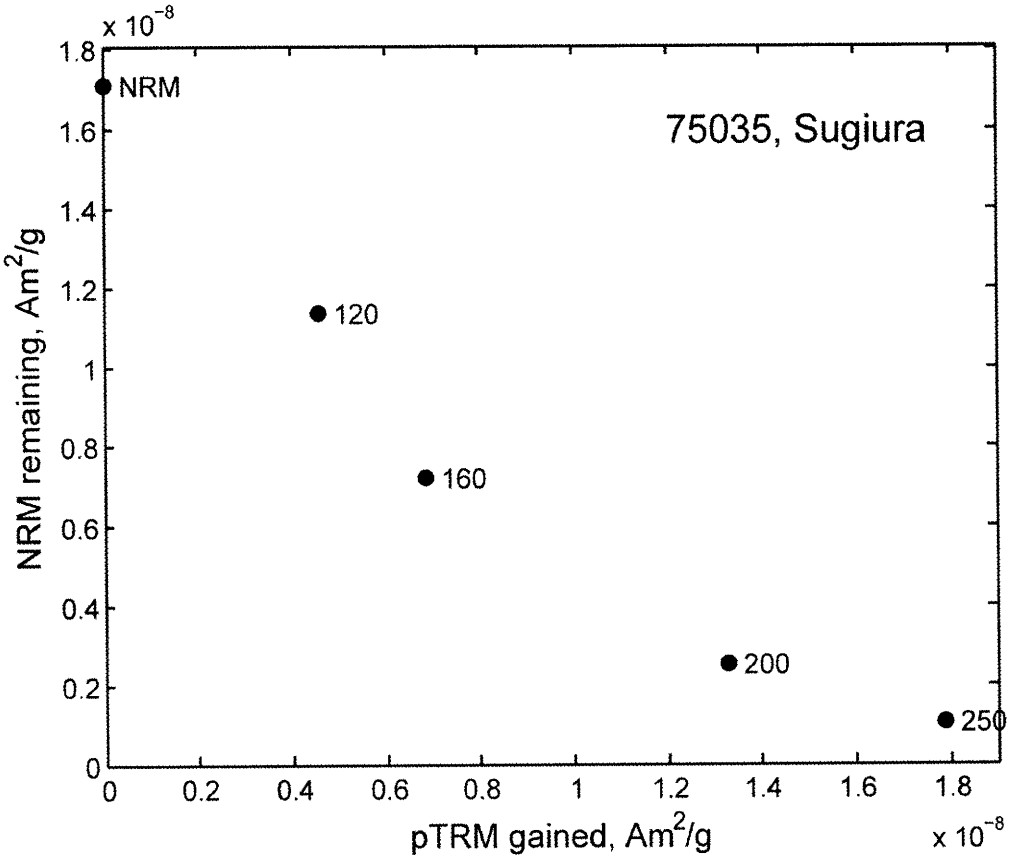

Figure 7.7G. Previously published Thellier-Thellier experiment (Arai plot) for lunar samples 75035 [37]. All temperature steps are in degrees Celsius.

Chapter 8

Early lunar magnetism

In press, Science. Ian Garrick-Bethell, Benjamin P. Weiss, David L. Shuster, Jennifer Buz.

Abstract

It is uncertain whether the Moon ever formed a metallic core or generated a core dynamo. The lunar crust and returned samples are magnetized, but the source of this magnetization could be meteoroid impacts rather than a dynamo. Here we report magnetic measurements and $^{40}Ar/^{39}Ar$ thermochronological calculations for the oldest known unshocked lunar rock, troctolite 76535. These data imply that there was a long-lived field on the Moon of at least 1 microtesla ~4.2-4.3 billion years ago. The early age, substantial intensity, and long lifetimes of this field supports the hypothesis of an ancient lunar core dynamo.

Early lunar magnetism

Before the Apollo missions the Moon was often thought to be a primordial, undifferentiated relic of the early Solar System (*1*) that had never formed a core or generated a magnetic dynamo. Because it was well known that the Moon has no global magnetic field (*2*), it was a surprise when the Apollo subsatellites and surface magnetometers detected magnetic fields originating from the lunar crust (*3*), and paleomagnetic analyses of returned samples identified natural remanent magnetization (NRM) (*4*). The magnetization of many samples must have been produced by ancient magnetic fields, but the association of crustal magnetization with impact structures (*5, 6*)

and the identification of NRM in <200 million year (Ma) old impact glasses (*7*) suggested that the field sources could have been impact-generated plasmas (*8-11*) rather than a core dynamo (*12*). Determining the source of lunar paleofields is critical for understanding the thermal evolution of the Moon, the limits of dynamo generation in small bodies, and, by implication, the magnetization of asteroids and meteorites.

A key difficulty is that available lunar rocks are often poor recorders of magnetic fields (*13, 14*). Most highlands samples are brecciated and/or shocked, making it difficult to distinguish between NRM acquired instantaneously during shock-magnetization or from long-lived dynamo fields (*11*). A further complication is that the precise thermal histories of most lunar rocks are unknown. Their magnetization ages have often been assumed equal to their radiometric ages (*14*), even though thermal events that can remagnetize rocks may have no effect on most geochronometers.

Here we report a magnetic study of an unshocked ancient rock with a well-constrained thermal history, troctolite 76535. We apply $^{40}Ar/^{39}Ar$ thermochronological constraints (*15*) in conjunction with paleomagnetism to determine when 76535 was last remagnetized and to constrain the nature and duration of the recorded paleofields. Because of the putative late heavy bombardment at ~3.9 Ga, there are few lunar rocks with $^{40}Ar/^{39}Ar$ ages older than ~4.0 Ga and no paleomagnetic analyses from before this time. However, it is during this early epoch when a convecting core dynamo is most thermally plausible (*16*). 76535 is the only known unshocked (*17-19*) whole-rock from this epoch (*20*).

76535 was found in a rake sample from the ejecta blanket of a 10-m-diameter impact crater (*21*). Four different chronometers (U/Pb, Th/Pb, Sm/Nd, and $^{40}Ar/^{39}Ar$) yield indistinguishable ages of 4.2-4.3 Ga (*22-26*). The Rb/Sr age is less certain due to spurious effects associated with olivine separates, ranging between 4.61 to 4.38 Ga (*24, 27*). The rock contains the ferromagnetic Fe-Ni-Co minerals kamacite and taenite as free grains and as inclusions of oriented linear arrays and needles (with axial ratios up to 45:1) in plagioclase (*17-19*). An unsuccessful Thellier-Thellier paleointensity experiment on 76535 (*14*) indicates that it contains a highly stable NRM composed of at least two components and that its Curie point is >780°C. The cobalt content of its iron metal, up to

6 wt%, among the largest measured for any lunar sample (*17, 28*), would indicate a Curie point of ~850°C [see (*29*)].

To determine if 76535 has a record of lunar magnetic paleofields, we conducted nondestructive AF demagnetization of six unoriented polycrystalline chips. AF data for our four most carefully controlled samples (137,1, 137,7, 137,8, and 138,2), demonstrate that the NRM consists of low coercivity (LC), medium coercivity (MC) and hard coercivity (HC) components (see Supplemental Material). The LC component, blocked below ~12 mT, is apparently a combination of viscous remanent magnetization and an IRM with a non unidirectional orientation relative to the MC and HC components (Figs. 8.1A and B, 8S.1, and 8S.2), resembling that observed in many other Apollo samples (*14, 30*) and meteorites (*31*). The MC component is much weaker than the LC component and extends from ~15 to 45-83 mT (Figs. 8.1C and D, 8S.1 and 8S.2, in blue). A final HC component trends to the origin from 45-83 to >250 mT, suggesting that it is the final, primary component (Figs. 8.1C and D, 8S.1, 8S.2, in red). The angular distances between the MC and HC components for all four subsamples after correction for anisotropy of remanence are similar (142-149°), and are consistent with the two components being unidirectional across the 76535 parent rock (Fig. 8.1G). The high coercivities of NRM are also consistent with the pseudo single-domain state of the iron in plagioclase-rich subsamples (Fig. 8S.11). The inferred paleointensities (see Supplemental Material) for the MC and HC components using the anhysteretic remanent magnetization (ARM) and IRM methods are at least 0.3-1 μT and possibly an order of magnitude larger (for comparison, the intensity of Earth's dynamo field at the Earth's surface is ~50 μT). Such paleointensities are far larger than that expected from external sources like the Earth, Sun, protoplanetary disk or galaxy at 4.2-4.3 Ga (see Supplemental Material), but are consistent with fields generated by meteoroid impacts and a lunar core dynamo.

The latter two possibilities can be distinguished using a diversity of petrologic and geochronologic data on 76535. The complete lack of shock features in 76535 [peak shock pressures < 5 GPa (*17*)] argues against isothermal shock remanent magnetization (SRM) [which for these pressures typically blocks below coercivities of <~30 mT (*32, 33*)], as well as the possibility of shock-produced thermoremanent magnetization (TRM)

[the temperature increase for any shock <5 GPa is negligible (*34, 35*)]. The low ratio of NRM to saturation IRM above 15 mT rules out magnetization by impact-generated (*36*) and artificial IRM fields. These data indicate that non-shock TRM is the most likely explanation for the MC component and much of the HC component (*37*).

Petrologic analyses indicate that 76535 experienced only two significant cooling events that could have blocked TRM (Fig. 8.2). The rock crystallized as a cumulate at ~45 km depth (*17, 18, 38*), and multiple thermobarometers indicate that it later experienced prograde metamorphism to peak temperatures >800-900°C (*38-42*). The observed equilibrium compositions of kamacite and taenite indicate that it then cooled slowly (at ~10°C per m.y.) to at least ~400°C (*17*), over which time five independent geochronometers closed to yield radiometric ages indistinguishable within their 50-100 Ma uncertainties. Observations of Fe-Mg ordering in 76535 orthopyroxene indicate that after excavation, it was heated again to at least 500°C and then cooled more rapidly to ~-20°C (the lunar near-surface temperature) over a period of ~10,000 years, probably in an ejecta blanket at ~200 m depth (*39*). Extrapolation of measurements of the diffusivity of Ni in taenite (*43, 44*) and the observation that the 400°C kamacite equilibrium composition was preserved after excavation imply that the peak temperature reached during burial was <500-600°C. This prediction is also in agreement with the 600°C temperature inferred from symmetry transitions in 76535 anorthite that formed during rapid cooling (*19, 45*). A final event excavated the rock to a depth of ~30 cm where it remained for much of the last ~220 million years (*23*).

Fission track data (*46*), in conjunction with our calculations using $^{40}Ar/^{39}Ar$ data (*25*), demonstrate that initial excavation took place at ~4.2 Ga. Because the rock was heated to 500-600°C after initial excavation, its fission track age (~4.2 Ga, when corrected for annealing at ambient lunar surface temperatures) must have been completely reset at this time (*47, 48*). The lack of evidence for Ar loss after 4.2 Ga places a conservative upper bound of heating for ~50 years at 500°C at 3.9 Ga, the time of major basin formation, or several hours at 800°C (Fig. 8.3, see Supplemental Material). Limits placed on events since 3.9 Ga are even more stringent even for brief events (Fig. 8.3C). Therefore, the simplest interpretation of these magnetic data is that the HC component was acquired during slow cooling in the deep crust at ~4.2 Ga and the

MC component was acquired just after excavation during cooling in an ejecta blanket over ~10,000 years. The cooling rates experienced by 76535 during both events require that the magnetizing fields persisted for far longer than expected for the longest-lived impact-generated fields [just ~1 day for the largest basins (*10*)]. The slow cooling rate for the HC component indicates that the field was stable over millions of years, comparable to superchrons on Earth during the last several hundred million years (*49*).

Although the Ar data are permissive of extremely brief, *ad hoc* heating events (such as those from deposition in shallow ejecta blankets) after 4.2 Ga, we can demonstrate that even if such events took place, the durations of the magnetic fields from such impacts are too short to be a plausible source of the magnetization in 76535. Conductive heating from a hot ejecta blanket would raise the temperature of the ~5 cm diameter rock (conservatively assuming it has always been no larger than its size as sampled by Apollo 17) from –20°C (ambient subsurface), to 770°C (the minimum Curie temperature) in approximately 1000 s (Fig. 8S.12). However, spontaneously generated fields due to plasma currents or motion of charged ejecta are believed to disappear in $<\sim 10^2$ s for craters < 100 km in diameter (*8, 9*), before the rock could even begin to cool and acquire TRM. Such short thermal events are also unlikely to have occurred during the last 4 billion years because they would require the rock to be in a thin ejecta blanket unrealistically close to the surface (<10 cm, Fig. 8S.12), in contradiction with its exposure age of 220 m.y. and neutron capture data (*23, 50*). Even the day-long impact-generated fields that may have been present during major basin formation at 3.9 Ga would require an unrealistically small, <~1-m-thick ejecta blanket to permit 76535 to acquire TRM (see Supplemental Material). Therefore, the most reasonable remaining origin for the high-coercivity NRM in 76535 is from long-lived magnetic fields like those expected from a core dynamo.

The plausibility of a lunar dynamo has been questioned because of the unconfirmed existence of a fluid metallic core (*51*), the difficulty of sustaining a dynamo at least 600 million years after accretion (*16, 52*), and large paleointensities of ~100 μT that are difficult to reconcile with theoretical predictions (*51, 53*). However, recent predictions of the effect of dissipation at a liquid-core mantle boundary on the orientation of the lunar spin axis (*54*) and refined measurements of the tidal Love number (*55*) have

provided growing evidence that the Moon has a small (~350 km radius) liquid core. Furthermore, the field that magnetized 76535, which is ~300 million years older than that recorded by all previously studied lunar samples, is from the early epoch when the Moon would have most likely had a convecting core due to enhanced heat flow and a possible cumulate overturn event (*52*). Finally, the NRM in 76535 indicates that minimum paleointensities were of order microteslas, consistent with the theoretical expectations for a lunar core dynamo (*53*). Our data and these considerations indicate that at 4.2 Ga the Moon possessed a dynamo field, and by implication a convecting metallic core.

References and Notes

1. H. C. Urey, *Geochim. Cosmochim. Acta* **1**, 209 (1951).
2. N. F. Ness, K. W. Behannon, C. S. Scearce, S. C. Cantarano, *J. Geophys. Res.* **72**, 5769 (1967).
3. P. Dyal, C. W. Packer, C. P. Sonett, *Science* **169**, 762 (1970).
4. S. K. Runcorn *et al.*, *Science* **167**, 697 (1970).
5. J. S. Halekas, R. P. Lin, D. L. Mitchell, *Meteorit. Planet. Sci.* **38**, 565 (2003).
6. D. L. Mitchell *et al.*, *Icarus* **194**, 401 (2008).
7. N. Sugiura, Y. M. Wu, D. W. Strangway, G. W. Pearce, L. A. Taylor, *Proc. Lunar Planet. Sci. Conf. 10th*, 2189 (1979).
8. L. J. Srnka, *Proc. Lunar Sci. Conf. 8th*, 785 (1977).
9. D. A. Crawford, P. H. Schultz, *Int. J. Impact Eng.* **23**, 169 (1999).
10. L. L. Hood, N. A. Artemieva, *Icarus* **193**, 485 (2008).
11. R. R. Doell, C. S. Gromme, A. N. Thorpe, F. E. Senftle, *Science* **167**, 695 (1970).
12. S. K. Rucorn, *Nature* **275**, 430 (1978).
13. M. Fuller, S. M. Cisowski, *Geomagnetism* **2**, 307 (1987).
14. K. P. Lawrence, C. L. Johnson, L. Tauxe, J. Gee, *Phys. Earth Planet. Inter.*, doi:10.1016/j.pepi.2008.05.007 (2008).
15. D. L. Shuster, B. P. Weiss, *Science* **309**, 594 (2005).
16. D. J. Stevenson, *Rep. Prog. Phys.* **46**, 555 (1983).
17. R. Gooley, R. Brett, J. R. Smyth, J. Warner, *Geochim. Cosmochim. Acta* **38**, 1329 (1974).
18. R. F. Dymek, A. L. Albee, A. A. Chodos, *Proc. Lunar Sci. Conf. 6th*, 301 (1975).
19. G. L. Nord, *Proc. Lunar Sci. Conf. 7th*, 1875 (1976).
20. D. E. Wilhelms, *USGS Professional Paper 1348*, (1987).
21. E. W. Wolfe, *The Geologic Investigation of the Taurus-Littrow Valley: Apollo 17 Landing Site*. (USGS Professional Paper 1080, 1981), pp. 220.
22. J. C. Huneke, G. J. Wasserburg, *Lunar Sci. VI*, 417 (1975).
23. G. W. Lugmair, K. Marti, J. P. Kurtz, N. B. Scheinin, *Proc. Lunar Sci. Conf. 7th*, 2009 (1976).
24. W. R. Premo, M. Tatsumoto, *Proc. Lunar Planet. Sci. Conf. 22nd*, 381 (1992).
25. L. Husain, O. A. Schaeffer, *Geophys. Res. Lett.* **2**, 29 (1975).
26. D. D. Bogard, L. E. Nyquist, B. M. Bansal, H. Wiesmann, C.-Y. Shih, *Earth Planet. Sci. Lett.* **26**, 69 (1975).
27. D. A. Papanastassiou, G. J. Wasserburg, *Proc. Lunar Sci. Conf. 7th*, 2035 (1976).
28. G. Ryder, M. D. Norman, R. A. Score, *Proc. Lunar Planet. Sci. Conf. 11th*, 471 (1980).
29. R. M. Bozorth, *Ferromagnetism*. (IEEE Press, New York, 1951), pp. 968.
30. G. W. Pearce, D. W. Strangway, *Apollo 16: Preliminary Science Report. NASA SP-315, Ch. 7-55*, (1972).
31. J. Gattacceca, P. Rochette, *Earth Planet. Sci. Lett.* **227**, 377 (2004).
32. J. Gattacceca *et al.*, *Phys. Earth Planet. Inter.* **166**, 1 (2008).
33. J. Pohl, A. Eckstaller, *Lunar Planet. Sci. 12*, 851 (1981).
34. A. Bischoff, D. Stoffler, *Eur. J. Mineral.* **4**, 707 (1992).
35. N. Artemieva, B. Ivanov, *Icarus* **171**, 84 (2004).
36. L. Carporzen, S. A. Gilder, R. J. Hart, *Nature* **435**, 198 (2005).

37. Because some kamacite would have exsolved from taenite during slow-cooling in the deep lunar crust, the HC component is likely a mixture of non-shock TRM and phase-transformation crystallization remanent magnetization (see Supplemental Material).
38. I. S. McCallum, J. M. Schwartz, *J. Geophys. Res.* **106**, 27969 (2001).
39. I. S. McCallum *et al.*, *Geochim. Cosmochim. Acta* **70**, 6068 (2006).
40. D. H. Lindsley, D. J. Andersen, *Proc. Lunar Planet. Sci. Conf. 13th*, A887 (1983).
41. C. T. Herzberg, *Lunar Planet. Sci. 10*, 537 (1979).
42. R. H. Hewins, J. I. Goldstein, *Lunar Planet. Sci. 6*, 356 (1975).
43. K. Righter, A. J. Campbell, M. Humayun, *Geochim. Cosmochim. Acta* **69**, 3145 (2005).
44. A. Meibom *et al.*, *Science* **288**, 839 (2000).
45. J. R. Smyth, *Proc. Lunar Planet. Sci. Conf. 17th*, E91 (1986).
46. D. Braddy, I. D. Hutcheon, P. B. Price, *Proc. Lunar Sci. Conf. 6th*, 3587 (1975).
47. C. W. Naeser, H. Faul, *J. Geophys. Res.* **74**, 705 (1969).
48. R. A. Ketcham, R. A. Donelick, W. D. Carlson, *Am. Mineral.* **84**, 1235 (1999).
49. R. B. Merrill, *The Magnetic Field of the Earth: Paleomagnetism, the Core, and the Deep Mantle*. M. W. McElhinny, Ed., (Academic Press, 1998), pp. 531.
50. It is plausible that a small (<10 cm), highly localized magmatic dike could heat a sample for short timescales, but such an event would be highly fortuitous, and even more fortuitous for it to take place simultaneously with an impact event.
51. D. W. Collinson, *Surv. Geophys.* **14**, 89 (1993).
52. D. R. Stegman, M. A. Jellinek, S. A. Zatman, J. R. Baumgardner, M. A. Richards, *Nature* **421**, 143 (2003).
53. M. A. Wieczorek *et al.*, *Reviews in Mineralogy and Geochemistry* **60**, 221 (2006).
54. J. R. Williams, D. H. Boggs, C. F. Yoder, J. T. Ratcliff, *J. Geophys. Res.* **106**, 27933 (2001).
55. S. Goossens, K. Matsumoto, *Geophys. Res. Lett.* **35**, L02204 (2008).
56. H. Fechtig, S. T. Kalbitzer, in *Potassium Argon Dating,* O. A. Schaeffer, J. Zahringer, Eds. (Springer-Verlag, New York, 1966), pp. 68-107.

Figures

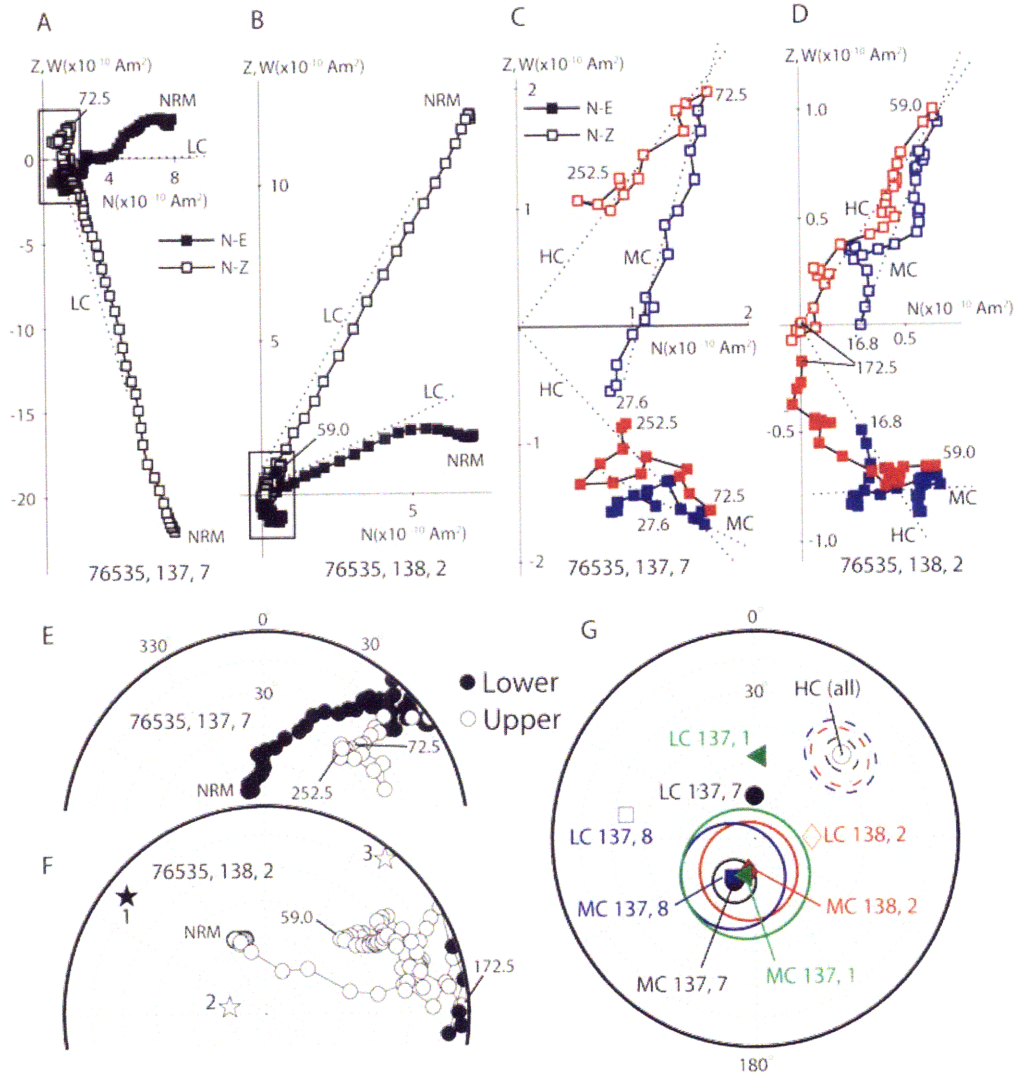

Fig. 8.1. Natural remanent magnetization in troctolite 76535. (**A-D**) two-dimensional projection of the NRM vector during AF demagnetization. Closed (open) symbols represent end points of magnetization projected onto the horizontal N-E (vertical N-Z) planes. Peak fields for selected AF steps are labeled in mT. Dashed lines are component directions determined from principal component analyses (PCA). (**A**) AF demagnetization of 76535,137,7 up to 252.5 mT and its LC component. (**B**) AF demagnetization of 76535,138,2 up to 172.5 mT and its LC component. (**C**) Zoom of boxed region in (**A**), showing data for the MC (blue) and HC (red) components. Data points are from averages of a total of 185 AF measurements. The HC direction is anchored to the origin. (**D**) Zoom of boxed region in (**B**), showing data for the MC (blue) and HC (red) components. Data points are from averages of a total of 1450 AF measurements. The HC direction is anchored to the origin. (**E**) Equal area projection of the remanence shown in (**A**). (**F**) Equal area projection of the remanence shown in (**B**), and first, second, and third principal axes of the anisotropy of remanence ellipsoid (stars), calculated with a 100 μT bias field ARM in a peak AF field of 57 mT. (**G**) LC, MC, and HC components obtained from PCA of four subsamples studied (four symbols/colors), rotated so that all HC directions overlap with the HC direction of 137, 7. Circles indicate maximum angular deviations.

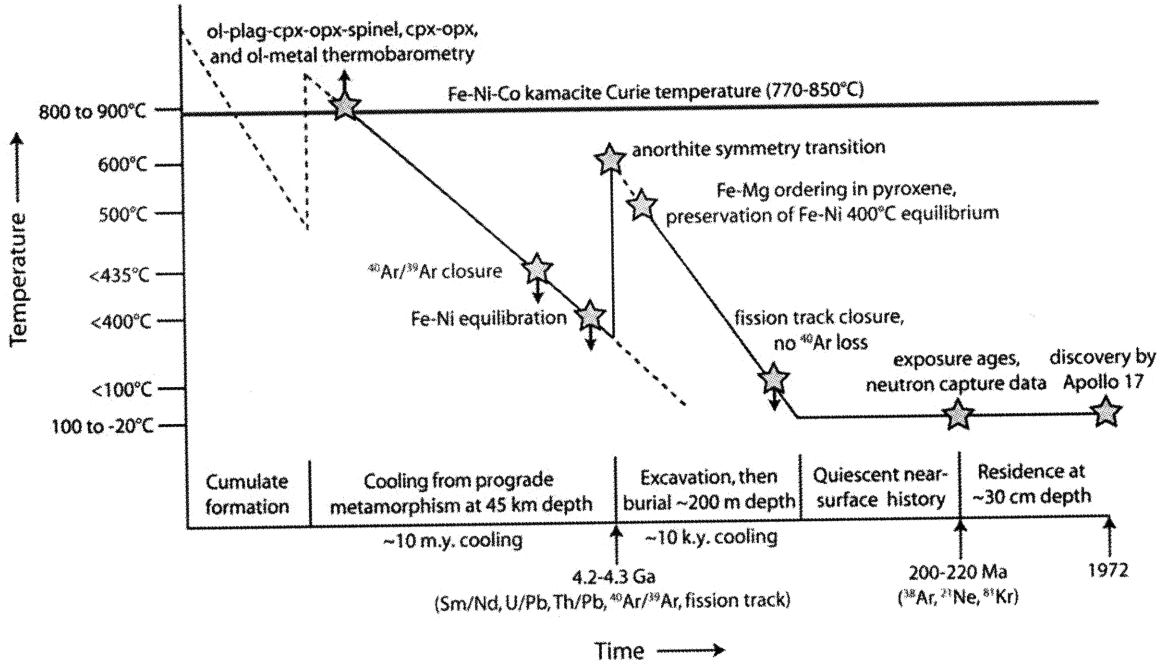

Fig. 8.2. Thermal history of troctolite 76535 as inferred from a variety of petrologic and geochronometric measurements. Stars and solid lines indicate relatively well-constrained times and temperatures. Dashed lines indicate less certain time-temperature histories. References for the various datasets described here are found in the main text. Axes are not linearly scaled.

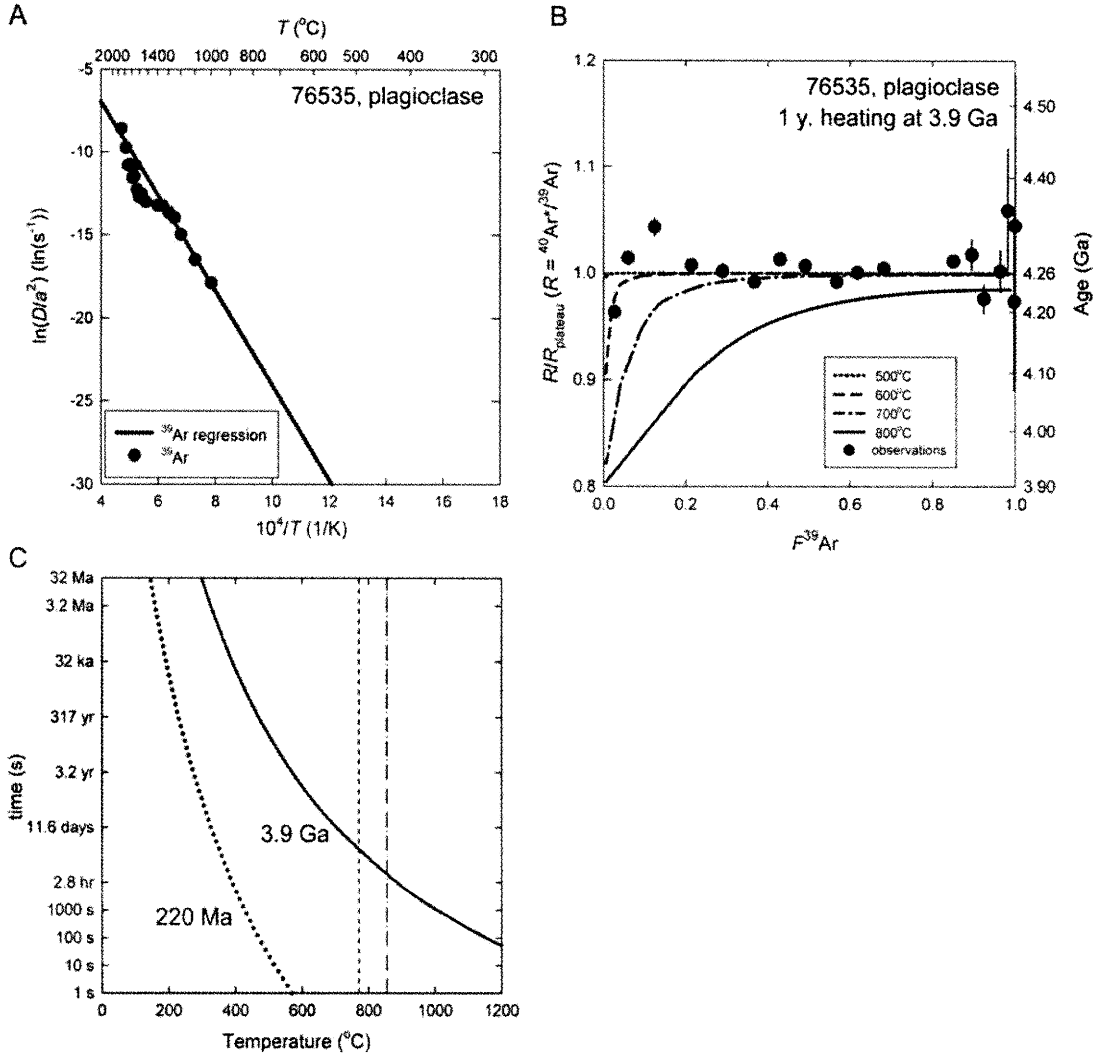

Fig. 8.3. $^{40}Ar/^{39}Ar$ thermochronological constraints on troctolite 76535. (**A**) Diffusivity as a function of temperature (Arrhenius plot) calculated from ^{39}Ar release data of Husain and Schaeffer (*25*). Circles are the diffusion coefficients calculated following (*56*). Solid line is model $D(T)/a^2$ obtained from the linear regression to data collected below 1350°C, where D is the diffusivity as a function of temperature T and a is the radius of the diffusion domain. (**B**) Measured and modeled $^{40}Ar^*/^{39}Ar$ ratio evolution spectra. $^{40}Ar^*/^{39}Ar$ ratios, R (normalized to the plateau ratio, $R_{plateau}$). Circles are the $^{40}Ar^*/^{39}Ar$ data of (*25*) with associated uncertainties. The model spectra were calculated using a spherical one-domain model with the diffusivity shown in part A for thermal disturbances at 3.9 Ga lasting for 1 year at various constant temperatures: 500°C (dotted line), 600°C (dashed line), 700°C (dash-dot line), and 800°C (solid line). (**C**) Time-temperature constraints derived from $^{40}Ar^*/^{39}Ar$ data. Shown is an *upper limit* on the temperature experienced by the rock for a thermal disturbance at 3.9 Ga (solid curve) and 220 Ma (dotted curve) for various assumed heating times. Short dashed line shows lower limit on Curie point derived from the data of (*14*) and long dashed line shows best estimate of Curie point using Co-content of 76535 metal measured by (*17*).

Chapter 8 Supplemental Material

8S.1 Introduction

Our subsamples of 76535 were collected as chips from the interior of the parent rock (76535,0) clear of any space-weathered or saw cut surfaces. Measurements of natural remanent magnetization (NRM) were performed in the MIT Paleomagnetism Laboratory (http://web.mit.edu/paleomag) with a 2G Enterprises Superconducting Rock Magnetometer 755 (sensitivity ~1×10^{12} Am^2) housed inside a magnetically shielded room (DC field < 150 nT). Nearly all sample handling was conducted inside a class 10,000 clean laboratory within this shielded room.

To assess the nature of the multicomponent NRM in our samples, we conducted room-temperature, three-axis alternating field (AF) demagnetization using a robotic sample handling system integrated with the magnetometer (*S1*). This automation permitted us to collect many more AF and rock magnetic measurements per sample than previous lunar experiments. Prior to this analysis our samples had been stored for 6-15 months in our magnetically shielded clean room. After AF demagnetization our samples were subjected to paleointensity analyses, selected rock magnetization experiments, hysteresis analyses, and magnetic viscosity experiments. In the following sections we describe each of these analyses and then end by providing further details about our $^{40}Ar/^{39}Ar$ thermochronology calculations and our models of the thermal history of 76535.

8S2. Alternating field demagnetization

To reduce spurious anhysteretic remanent magnetization (ARM) noise from our AF system (see Section 3), we performed each AF step multiple times (2-30) and computed the vector mean. A four-point vector running average was then performed on the AF measurements at progressively higher AF fields to produce the data shown in Figs. 1, S1 and S2. The reported AF field at each step is the median field of the four steps. Because we found that 76535 is susceptible to gyroremanent magnetization (GRM) (see Section 3.2), the data in Figs. 1, S1 and S2 have been corrected using the Zijderveld-Dunlop averaging method (*S2*). Taking the average of multiple AF steps at a single AF level also

improves the accuracy of the GRM correction. The data for two of our subsamples were processed using over 1300 individual AF steps at coercivities above 25 mT (1450 steps for 138,2 and 1320 steps for 137,8).

While thermal demagnetization is traditionally the favored mechanism for assessing the remanence in terrestrial samples, there are several reasons why AF demagnetization is advantageous for lunar studies. Firstly, lunar and other extraterrestrial materials are rare, and heating permanently alters the samples such that they are often unsuitable for any subsequent petrologic and geochronological studies. While terrestrial datasets often have dozens of samples from one rock type, the mass of lunar materials typically allocated to investigators is far more limited. Previous thermal demagnetization of 76535 has shown that it alters substantially during heating (*S3*).

A second and related reason for using AF demagnetization is that extensive studies of rock magnetic properties can be conducted on the very same unaltered subsample that was AF demagnetized. Such studies, which can include magnetic anisotropy, acquisition of ARM and isothermal remanent magnetization (IRM), hysteresis properties, and viscous magnetization acquisition, have proven critical for determining the nature of the remanence in our samples. A third but unexpected advantage of AF demagnetization over thermal demagnetization methods is that it allowed us to identify and completely remove secondary IRM observed in 76535. The major disadvantages of performing room temperature demagnetization are AF-related noise sources like GRM and spurious-ARM, the inability to assess the blocking temperature distribution of NRM, and the inability to conduct Thellier-Thellier paleointensity analyses. Fortunately, our automated high-resolution AF demagnetizer (*S1*) can rapidly acquire thousands of AF measurements per sample, enabling very detailed studies of the behavior of the remanence vector and allowing us to average many measurements to reduce spurious-ARM noise, as described above.

8S.3. Spurious remanence acquired during alternating field demagnetization

During AF demagnetization, 76535 increasingly acquires spurious remanence with growing peak AF field. This spurious remanence consists of (*i*) randomly oriented ARM

due to imperfections in the AF equipment and (*ii*) GRM acquired as a result of the rock's anisotropy and our static three-axis AF protocol. The collective effect of these two artificial magnetization sources is substantial directional scatter of the NRM vector during AF demagnetization.

We can reproduce this scatter by AF demagnetizing a laboratory remanence equivalent to that inferred from our AF demagnetization of NRM experiments. For example, we applied to sample 137,1 an ARM with a DC bias field of 0.05 mT in a peak AF field of 290 mT oriented in the approximate direction of the MC component. This ARM was chosen to mimic a natural TRM acquired in a paleofield approximately equivalent in strength to that inferred from our paleointensity experiments (Fig. 8S.3). We then rotated the sample and applied an IRM of 15 mT in the approximate direction of the LC component. AF demagnetization of this two-component remanence (ARM 0.05 mT + IRM 15mT) up to 13 mT revealed a linear monotonic decay of the vector to the approximate direction of the ARM (Fig. 8S.4B), just as observed for NRM. The sample moment then remained in the vicinity of the ARM until at least AF 126.3 mT, with nearly identical scatter as observed for NRM in this range. The fact that this scatter is reproducible indicates that noise encountered during AF demagnetization of NRM is not inconsistent with an underlying NRM acquired in paleofields with substantial (Earth-strength or greater) paleointensities. We next explain how we substantially reduced this ARM noise and spurious GRM to recover an accurate estimate of the NRM.

8S.3.1. Spurious anhysteretic remanent magnetization. It is well known that secondary harmonics in the AF waveform due to current fluctuations and imperfections in the AF equipment can cause a sample to acquire a spurious ARM (*S4-8*). This often appears as a random component added to the residual NRM and can be identified as directional scatter during repeat AF measurements at the same peak field. As discussed in Section 2, we have reduced ARM noise by making repeat AF measurements (up to 30) at the same peak field, and then averaging the repeated steps.

83.2. Gyroremanent magnetization. During static AF demagnetization, anisotropic samples will acquire a GRM that is oriented orthogonal to the direction of the AF axis

(*S9*). To test for GRM acquisition we conducted two experiments. In the first experiment, we compared the NRM of 76535,137,7 measured after each of three uniaxial (*x* (N-S), *y* (E-W), *z* (U-D)) AF steps for a given AF field. We found that above AF ~40 mT, the moment inclination after AF in the *z* direction, for example, is consistently shallower (closer to the *x*-*y* plane) than after AF in the *x* and *y* direction (Fig. 8S.5A), with the degree of shallowing growing with increasing AF level. This growth in remanence in the plane orthogonal to the *z*-axis suggests acquisition of GRM. In the second experiment, after AF demagnetization of NRM to 290 mT we again conducted three-axis AF demagnetization of 76535,137,7 from 0 to 290 mT, following the methods of (*S10*). During this AF sequence, when measuring the remanence after the (final) *z*-axis AF demagnetization step only, we observed first a drop in sample moment followed by a rise in moment at AF levels above ~40 mT (Fig. 8S.5B). Like (*S10*), we can ascribe the initial drop in moment to AF demagnetization of GRM acquired during the last steps of our previous AF sequence (AF of NRM), and the subsequent rise in moment to progressive reacquisition of GRM in the equatorial *x*-*y* plane. Note that the scatter away from these trends in Fig. 8S.5 is very likely a manifestation of ARM noise superimposed on the GRM signal.

The results of both experiments are consistent with 76535 being susceptible to GRM acquisition during AF demagnetization. Except where noted, all measurements presented in Figs. 1, S1, S2 and used for our principal component analyses were corrected with the Zijderveld-Dunlop method (*S2*). Our AF demagnetization scheme proceeded in the following order: *y*, *z*, *x*, *y*, and finally *z*. The GRM-corrected magnetization is computed as the vector average of the latter three orthogonal measurements.

8S.4. Obtaining magnetization components

8S.4.1. Principal component analyses. After AF demagnetization, low coercivity (LC), medium coercivity (MC), and high coercivity (HC) components were identified with principal component analysis (*S11*). AF demagnetization data for samples 76535,137,1

and 76535,137,8 (not shown in main text) are shown in Figs. S1 and S2. The AF steps, maximum angular deviation (MAD), anisotropy-corrected directions, and angular differences between the MC and HC components for all fits are summarized in Table S1. We note that the variability in the range of AF fields required to remove the MC component in different subsamples (from 44.5-82.9 mT) is likely a result of the inefficiency of AF demagnetization in removing two thermal components that are blocked across a mixture of coercivity levels.

Sample 76535,137,1 was only demagnetized in one axis above 85 mT, and it was therefore not possible to GRM-correct its remanence above AF 85 mT. However, above this AF level the sample shows the same well-defined origin-trending HC component as the other samples (Fig. 8S.1B, green points). Because the HC component in 76535,137,1 manifests itself near the end of the three-axis demagnetization data (at approximately AF 83-93 mT), to obtain a fit to the HC component we used the last point in the three-axis demagnetized GRM-corrected data (AF 82.9 mT) and the origin. While such a two-point fit by itself would not be a robust measure of the final HC component, the fit passes through many points of the single-axis data that trend to the origin, which justifies its use. In addition, it produces an anisotropy-corrected angular difference between the MC and HC components that is nearly identical to the MC-HC angular differences seen in the other three samples (143.9°).

We note that while the slow cooling and blocking of the HC component in the lower crust may have produced a mixed crystallization remanent magnetization (CRM) and TRM, due to the continuing equilibration of kamacite and taenite to ~400°C (main text), the much more rapidly acquired MC component should be nearly free of any CRM effects (see also Section 6.2).

8S.4.2. Identifying primary magnetization. We have argued in the main text that the HC component in 76535 is the characteristic magnetization which originated during cooling in the lower crust of the Moon. A key test of this conclusion is the demonstration that the HC component trends to origin. One such proposed quantitative test is to compute the direction of the maximum dispersion axis in the component's centroid-centered reference frame ("unconstrained line fit"), determined by PCA. The direction is then computed for

a line that joins the centroid and the origin. If the angular difference between these directions, dANG, is less than some pre-defined value (e.g., the MAD for the PCA fit or else some *ad hoc* maximum threshold), then it can be said that the component trends to the origin (*S12*). While this kind of metric is arbitrary because it does not assign a confidence interval, the lack of more robust alternatives has led us to use it to test whether our components trend to the origin. However, instead of using the direction of the line from the centroid to the origin to compute dANG, we use the direction of the first point of the HC component, which has the advantage of weighting data further from the origin more heavily than data closer to the origin, where noise is higher. We then use the criterion of dANG < MAD to determine if HC trends to the origin, where MAD in this case is the MAD from the *unconstrained* line fit (not listed in Table S1).

We find that the HC component for sample 76535,137,8 has a dANG of 16.2°, which is < MAD = 18.5°, and it can said that its HC component trends to the origin. For sample 76535,137,7 we find dANG = 19.9°, which is < MAD = 21.7°, and it can be said that its HC component trends to the origin. For comparison, dANG for the MC component of 76535,137,7 is 108.5°, far greater than MAD = 8.5°, and therefore its MC component does not trend to the origin, as expected. For sample 76535,138,2, we find dANG = 7.4° for its HC component, which is < MAD = 13.0°, and it can be said that its HC component trends to the origin. For sample 76535,137,1, only two points were used to determine the direction of HC (described above). However, if we use the non-GRM corrected single-axis demagnetized data between 94.7 and 142.0 mT (Figure S1), we find that dANG = 21.7°, which is < MAD = 32.5°, and therefore it can be said that its HC component trends to the origin. In summary, it can be said that all four HC components trend to the origin within the limitations of the dANG metric.

8S.4.3. Correction for anisotropy of remanence. As discussed in Section 9.1, some of our subsamples of 76535 have anisotropy of remanence, which deflects their remanence directions from that of the magnetizing field. The LC, MC, and HC directions were therefore corrected for this anisotropy. For most samples, this involved computing anisotropy ellipsoids with IRM fields representative of the coercivity range of each component (10, 40, and 105 mT, for LC, MC, and HC, respectively). The anisotropy

data for each sample are presented in Table S3, and the corrected directions are shown in Table S1, along with the total angular change after anisotropy correction. Sample 76535,137,7 showed negligible changes in remanence direction after correction, and the original uncorrected directions were used. In the case of 76535,138,2, the directions changed by ~10° for all components, which led us to perform corrections using anisotropy of ARM, which is likely a better analog for TRM anisotropy. The results using ARM with a DC field of 100 μT in AF fields of 57.0 and 120.0 mT, for the MC and HC components, respectively, yielded an MC-HC angular difference of 141.6°, comparable to the IRM-corrected value of 134.4° (a difference of 7.2°). Using the MC-HC angular distance calculated from the IRM-corrected data would not affect our main conclusions.

8S.5. Magnetic homogeneity test

A key test of whether 76535's MC and HC components are the product of a spatially uniform external magnetic field like that of a core dynamo is that each component should be unidirectionally oriented throughout the rock (*S13*). Because our allocated subsamples of 76535 are very small, and the rock is extremely friable and not easily broken apart into mutually oriented subsamples, we used a comparison of the relative orientation of the MC and HC components as a proxy test for magnetic homogeneity. A necessary but not sufficient condition for homogeneity is that the angular distance between the two components should be constant, and indeed we observe this for all of our well-controlled subsamples of 76535 (Fig. 1G, Table S1).

We were also able to break apart one sample, 76535,138,1 into two mutually oriented subsamples (138,2, and 138,3). The two subsamples were AF demagnetized and the directions corrected for anisotropy and GRM. After successful removal of a well-defined LC component, the demagnetization behavior of 138,3 was anomalous and unlike our other samples did not reveal clear MC or HC components, likely because of the sample's tiny size (22 mg, our smallest subsample) and relatively small number of crystals. The sample also showed particular susceptibility to GRM. We conducted a least squares fit to a possible HC component from 53.0-61.0 mT (MAD = 12.2°) that

decreased monotonically in intensity from 2.3×10^{-11} to 1.1×10^{-11} Am^2. After ARM anisotropy correction (DC field of 100 μT, peak AF field of 57.0 mT), the direction of this component is 65° from the ARM-anisotropy corrected HC component of its pair 138,2. This angular distance is comparable to the total angular error between the two components (55°), estimated by the sum of the HC MAD values for each sample (11.8° + 12.2°), the estimated relative orientation error of the two pieces (15°), and the estimated orientation errors during calculation of the anisotropy ellipsoids (~8° per sample), not including the formal error estimate for the anisotropy ellipsoids. Notably, the HC components of each sample moved towards each other after anisotropy correction. For comparison, the LC components (MAD values of 0.9° and 4.0°, for 138,2 and 138,3, respectively) were 18.0° apart after anisotropy correction using IRM fields of 10 mT. The similar LC directions for these two pieces contrasts with the non-unidirectionality of the LC components in our unoriented samples. This difference is not surprising since although IRM fields from localized sources can be highly non-uniform on the centimeter scale, they must be unidirectional below some spatial scale [typically, millimeters and below; see Fig. 8S.1 of (*S14*)].

8S.6. Paleointensity measurements

For terrestrial igneous samples, the Thellier-Thellier heating experiment is the preferred method for estimating paleofield because thermal demagnetization reproduces the way that the sample naturally acquired its NRM (*S15, 16*). However, numerous previous Thellier-Thellier studies of lunar rocks, including a recent such analysis of 76535, have failed to obtain accurate paleointensities due to severe sample alteration (*S3, 17-20*). Therefore, we made a fundamental decision to use nondestructive, order-of-magnitude room-temperature techniques to demagnetize the NRM and obtain paleointensity estimates. Following (*S14*), we have normalized the NRM to a laboratory ARM and IRM rather than to a laboratory TRM like the Thellier-Thellier technique. The artificial ARM and IRM were stepwise AF demagnetized using the same AF steps as used to demagnetize the NRM, permitting us to compute NRM/ARM and NRM/IRM for each coercivity bin and therefore for each NRM component. Our paleointensity methods are

therefore multicomponent techniques: our IRM method is essentially the REM' technique (*S19*), while our other paleointensity technique is philosophically equivalent to REM' except that ARM is used as the normalizer in place of IRM.

8S.6.1. Paleointensity techniques. The IRM technique typically provides an order-of-magnitude estimate of the absolute paleofield, with the major source of error being the dependence of TRM/IRM on the unknown grain volume and microscopic coercivity distribution (*S21*). For example, Yu (*S21*) found that in terrestrial basalts, the IRM and Thellier-Thellier methods agreed within a factor of two using calibration data for meteorites, and a factor of three using the calibration for lunar samples. Weiss et al. (*S22*) used terrestrial basalts to find that a simple NRM/IRM metric reproduced the Earth's field within a factor of ~2. In addition, laboratory experiments with synthetic metal-bearing samples reproduced the ambient field within an order of magnitude for a wide range of field values (*S23*). However, narrow acicular shape distributions like that expected for 76535 can have TRM/IRM 50 times higher than that of equant grains (*S23-25*), and we incorporate this factor into our uncertainty estimates (Section 6.2).

Similar to the IRM method, NRM can also be normalized by laboratory ARM to obtain an estimate of the paleofield (*S20, 26-29*). Traditionally, this technique has only been applied to the total remanence. Analogous to our IRM paleointensity method, here we calculate the derivative of AF of NRM for separate magnetization components in each sample. The paleofield is obtained by multiplying NRM/ARM by the ARM bias field [ideally equal to the paleofield (*S30*)], and dividing by a calibration coefficient f', which is the ratio of TRM to ARM for a given magnetizing field. There is some uncertainty in the value of f' because it changes as a function of grain size, bias field, and degree of interactions (*S31*), but a number of experiments have shown that a value of $f' = 0.9\text{-}1.6$ (typically $f' = 1.34$) is fairly constant across different lunar samples (*S20, 26, 32, 33*). A recent analysis of ARM (*S34*) suggests that samples with elongate grains could have a f' perhaps 10 times larger than this. Generally, we expect the ARM method to also be accurate to within an order of magnitude (*S35-37*).

For each sample, we first conducted three paleointensity experiments in which ARM was acquired in increasing AF fields for constant bias fields of 50, 100, and 200

μT. These samples were then demagnetized completely and given a near-saturation IRM (260-290 mT) that was then AF demagnetized and GRM-corrected (the multicomponent IRM method used here does not require saturating the rock because it measures remanence lost at each AF demagnetization step). We also AF demagnetized and GRM-corrected an ARM (DC bias field of 200 μT, peak field 85 mT) to obtain a paleofield estimate analogous to the ARM acquired estimate. This was done to assess if GRM made a significant contribution to our ARM acquired paleointensity estimate (it did not). Paleointensity estimates (Table S2) were obtained from plots of NRM lost versus ARM gained [similar to the Stephenson method (*S38*)] and NRM lost versus IRM lost [essentially the REM' method of (*S19*) and REM(AF) method of (*S39*) but using the visualization method of (*S38*)]. NRM lost was computed using vector subtraction for each component. For example, for the MC component observed in 76535,137,7 (Fig. 1), NRM lost values between AF 27.6 and 72.5 mT were computed by vector subtraction from the AF 27.6 mT step, while for the HC component, NRM lost values were computed by vector subtraction from the AF 72.5 mT step. We calculated the IRM and ARM paleointensities using the following formulas:

$$\text{ARM paleointensity in } \mu\text{T} = (\Delta\text{NRM}/\Delta\text{ARM})/f' \times (\text{bias field in } \mu\text{T})$$

$$\text{IRM paleointensity in } \mu\text{T} = (\Delta\text{NRM}/\Delta\text{IRM}) \times a,$$

where f' and a^{-1} are the ratio of TRM to ARM and IRM, respectively, and ΔNRM, ΔARM, ΔIRM are, respectively, the vector-subtracted gain or loss of NRM, ARM, and IRM as derived from least squares fits to the paleointensity plots in the AF range for a given component. Although the uncertainty in the calibration coefficients is almost certainly higher than the uncertainty from the linear regressions to estimate the paleofield, we also compute the 95% confidence interval for all paleofield estimates in order to demonstrate that the slopes are statistically distinguishable from zero.

Because f' and a are known to vary depending on grain size and shape, we calculated a range of paleointensities for each paleointensity method. The upper limit is obtained assuming $f' = 1.34$ and $a = 3000$ (typical for equant grains of multidomain iron). The lower limit for IRM paleointensities is calculated assuming the smallest yet

measured a = 3000/50. The latter value has been observed for an anorthosite from the Archean Stillwater Complex containing exsolved single-domain magnetite needles in plagioclase with aspect ratios up to 50:1 (*S23*); other single domain acicular magnetites as well as Fe-Ni-Co wires with axial ratios up to 14:1 also have been observed to have intermediate values of a (*S24, 25*). We believe a = 3000/50 is a conservative lower limit on our paleointensities because although 76535 contains acicular needles of Fe-Ni-Co with axial ratios up to 45:1 (*S40-42*), our hysteresis data (Fig. 8S.11) indicate that unlike the Stillwater anorthosite, the most abundant Fe-Ni metal in 76535 is in the form of approximately multidomain crystals. The latter metal is probably the large (~10-100 μm diameter) approximately equant grains observed in the mesostasis and "mosaic assemblages" [see Fig. 6 of (*S40*) and Figs. 5D and 6 of (*S42*)]. Although the dependence of f' on shape is not well known, a recent study (*S34*) suggests that for magnetite with similar aspect ratios, TRM/ARM should exceed by at least the same factor of 50 as the TRM/IRM ratio that of equant grains. Therefore, we adopt a lower limit for ARM paleointensities computed using $f' = 1.34 \times 50$.

8S.6.2. Paleointensity estimates. Figure S3 shows the results of ARM and IRM paleointensity experiments for the MC and HC components in 76535,137,7 and 76535,138,2. The labels in each plot give the slope calculated by linear regression. Table S2 summarizes the computed slopes, formal 95% confidence intervals for the regression, and paleointensity estimates assuming the ARM and IRM calibration factors defined above. The slopes derived from GRM-corrected AF of ARM (open uncolored data points) are nearly equivalent to the slopes from the analogous ARM-acquired experiment, suggesting that GRM does not significantly affect our paleointensity estimates. In the case of 76535,137,7, the ARM acquired with a bias field of 50 μT was too noisy at the coercivities blocked by the HC component (likely due to ARM noise) and did not yield a statistically significant slope.

Generally, the slopes and fields for the HC component are higher than those for the MC component. The slope changes between the two components are sharp and well defined, which suggests that the higher HC values are not due exclusively to changes in grain size or AF field but possibly to real differences in paleointensity. Note that the MC

component was blocked just after the end of the period during which the HC component was acquired. While this would at first seem to suggest that the paleointensity plots should have exactly the same slope across the final AF steps of the MC component and the first AF steps of HC component, recall that upon initial excavation the rock was heated up to 600°C, which is at least ~200°C (and possibly as much as 400°C) above its final temperature acquired while in the lower crust. Therefore, given the slow cooling rate in the lower crust (several tens of °C per Ma or less), the remaining HC remanence unaffected by this reheating could be millions of years older than the MC remanence. This means there is in fact no reason to expect that the MC and HC components should have the same paleointensity. In any case, our paleointensity technique is sufficiently uncertain that it probably prevents us from accurately determining the relative strength of the MC and HC fields.

While the MC component was acquired relatively quickly, and its TRM paleointensity is likely unaffected by the effects of CRM, it is possible that the HC paleointensity is being underestimated due to the equilibration of kamacite and taenite during slow cooling to ~400°C. This is because kamacite grains will acquire some CRM as they grow during cooling, which is theoretically a less efficient magnetization process than TRM [e.g. equation 13.5 of (*S16*)]. This would effectively mean that the values used for a are lower limits and the values used for f' are upper limits. However, in the absence of experimental work on the effects of CRM on paleointensities for the Fe-Ni system, we cannot definitely determine how the HC paleointensity estimate would be affected.

As shown in Table S2, the minimum estimate from all of the paleofield experiments is 0.3-1.3 μT. We suspect the upper range of paleointensities (in some cases exceeding 100 μT), which would be difficult to reconcile with the expected small size of the lunar core (*S43*), are likely overestimates given the unusual shape distribution of metal in 76535 (see Section 6.1). The minimum paleointensities are so large that they rule out most potential field generation processes as the source of the HC and MC magnetization. Such fields are too strong to have been the product of the early T Tauri Sun (*S44*) and protoplanetary disk dynamo (*S45*) [neither of which should have been present at ~4.2 Ga anyway (*S46*)], the solar wind or galactic field. The magnitude of

fields from a dynamo on the early Earth would have also been too weak. For example, using equation 4.213 of (*S47*) to estimate the timescale for tidal growth of the lunar semimajor axis, we find that the Moon reached a semimajor axis of 20 Earth radii 0.3-30 Ma after accretion, assuming a wide range of k/Q = 0.1-0.001, where k is the Earth's second-degree tidal effective Love number and Q is its tidal specific dissipation factor (presently k/Q = 0.025). These timescales are in agreement with timescales obtained using the treatment of (*S48*) and results reported by (*S49*). Assuming the early Earth had a dipole moment like today, its field at the Moon at 20 Earth radii would have been only 0.006 μT, and by 4.2 Ga the Moon was almost certainly beyond 20 Earth radii. All of these field sources have the additional problem that it is difficult for them to uniformly magnetize the spinning, orbiting Moon. Lunar crustal fields like those observed today are also mostly too weak to have produced the magnetization in 76535. This leaves core dynamo fields and impact-generated fields as the two remaining explanations. As described in the main text, the well-constrained slow cooling history and lack of shock features in 76535 strongly favors a core dynamo.

8S.7. Isothermal remanent magnetization in 76535

During AF demagnetization of 76535, we found that all of our subsamples contained a strong, near-saturation LC component that is removed by AF ~11-13 mT. This component is distinctly non-uniform both spatially (its orientation relative to the MC and HC components varies for different subsamples) as well as in coercivity (it is curved in orthographic plots). Similar features are observed for the IRM magnet overprints commonly found in meteorites (*S14, 19*). The LC component also demagnetizes very similarly to a 15 mT laboratory IRM (Fig. 8S.6). Any mismatch of the NRM with the laboratory IRM below ~13 mT in the samples is almost certainly due to viscous decay of the original IRM and acquisition of a terrestrial VRM. The nonlinearity of the remanence direction observed during AF demagnetization at such low fields is also probably partly due to overprinting by this VRM, as well as to the fact that natural IRM field sources are usually highly nonuniform on the sample's spatial scale (such that when the IRM source was removed from 76535, it may have progressively blocked different coercivity ranges

in different directions and also produced magnetization directions varying throughout the sample). In addition, the directionality of the IRM remanence is largely controlled by anisotropy, which is greatest for low coercivity grains in 76535 (Section 9.1 and Fig. 8S.7). All of these features strongly indicate that, like many other Apollo samples (*S3, 50, 51*) and meteorites (*S14, 19*), 76535 acquired an IRM overprint prior to our analyses. The coercivity range of the IRM overprint is in the range of fields inferred to have been present in the Apollo spacecraft and also typical of hand magnets, but its true origin is unknown.

Fortunately, AF demagnetization is the ideal method for removing IRM overprints (*S50, 52*). Six experiments on three subsamples repeatedly demonstrated that a laboratory 15 mT IRM is completely removed by AF ~12-13 mT [slightly less than the IRM field, presumably due to assistance by internal demagnetizing fields (*S53*)]. For example, following AF demagnetization of the NRM of 76535,137,1 to 290 mT, we applied a 15 mT IRM in the approximate LC direction and then AF demagnetized the sample again. Up to AF ~11 mT, the laboratory IRM moment decayed monotonically with increasing AF field, and a least squares fit from AF 7.6 to 11.0 mT yielded a MAD of 9.0°. This behavior was similar to that of the LC component (MAD = 9.6° over the same AF range). By AF 14.0 mT, the remanence vector was within 10° of the pre-laboratory IRM direction (Fig. 8S.4A), which was 90.5° away from the IRM direction. This demonstrates that the MC and HC components are unlikely to be contaminated by a low-field IRM like that which produced the LC component. These results are in agreement with a previous study (*S50*) that demonstrated how a low-field IRM from the Apollo 16 spacecraft that overprinted an Apollo 12 basalt brought back to the Moon could be essentially completely removed by AF 2 mT (as indicated by the return of the sample's moment to its pre-Apollo 16 direction).

8S.8. Magnetic viscosity

Lunar rocks have been immersed in the Earth's magnetic field since their return during 1969-1972. It is important to establish that the MC and HC components in 76535 are not entirely VRM acquired during this period. For instance, in previous studies, fine grained

iron in lunar breccias has been suspected of giving artificially high paleointensities due to recent acquisition of VRM in the Earth's field (*S28, 54*). In these studies, below AF fields of 10-20 mT it was found that both laboratory- and naturally acquired-VRM yielded relatively high slopes in the low coercivity portions of ARM-paleointensity plots, implying large paleofields (*S28*). However, at higher coercivities it was found that the slope breaks cleanly towards a shallower value that remained constant up to the limit of the demagnetizer, suggesting that VRM was removed and that the high coercivity magnetization components represented primary remanence (*S28*). These results are also in agreement with similar VRM experiments on breccias by (*S55*), where terrestrial VRM was removed by AF ~20 mT.

We also find marked direction changes and suspected VRM components that are removed by at most AF 10 mT. Consider 76535,137,1, which from a comparison of AF demagnetization of NRM and IRM 15 mT has by far the largest VRM component of all of our subsamples (Figs. S1A, S6B). The responsibility of low coercivity grains for the VRM is clearly demonstrated by (a) the directional change and decay of the LC component at AF 3.6 mT and near 8.2 mT and by (b) the relatively small amount of NRM lost by AF 15 mT relative to that lost by a 15 mT IRM. Because the LC component was apparently viscously affected only in grains with coercivities <8.2 mT and was directionally stable between AF 8.2-11 mT (and compared favorably with low-field laboratory IRM) despite years of storage in the Earth's field, we can be confident that higher coercivity grains have not been affected by VRM.

We tested this conclusion by conducting our own VRM-acquisition experiments on 76535. Three subsamples were exposed to the Earth's field after AF demagnetization of NRM up to 290 mT. Two of these subsamples (76535,137,3 and 137,5) exhibited little apparent viscous demagnetization of their natural LC IRM during AF demagnetization of their NRM. During the subsequent artificial VRM experiments, these samples indeed showed no detectable evidence of VRM (<1% of the sample's pre-VRM moment) after exposure to the Earth's field for 42 days (measured within 100 s of reentry into the shielded room). On the other hand, sample 137,1, which as described above exhibits the effects of substantial natural viscous demagnetization of its LC IRM, acquired after 42 days of Earth-field exposure a moment of 3.2×10^{-10}Am^2, which is 44%

of its NRM, 60% of the NRM lost up to AF 8.2 mT (5.4×10^{-10}Am^2), and 73% of its pre-VRM moment. If VRM acquisition is approximated as linear with the logarithm of time, the predicted VRM after 10 years of undisturbed storage at Johnson Space Center and 6 months of storage in a shielded room would be 0.6×10^{-10}Am^2. This is only 11% of the NRM lost up to AF 8.2 mT. However, this is not unexpected given that VRM acquisition is nonlinear with time (*S56*) and the LC component is a mixture of IRM and VRM. No detectable change (<1%) from the post-VRM moment was observed during 100 continuous measurements performed over one hour after removal from the Earth's field. However, after 7 days of storage in a shielded room the moment of 137,1 had returned to 96.5% of its original value, and after 23 days the sample moment had returned completely to its previous magnitude (99%) and direction (3°), suggesting a very soft component of low coercivity grains was the carrier of the VRM, as observed for other lunar samples.

8S.9. Other rock magnetic data

8S.9.1. Anisotropy of remanence. 76535 is a coarse grained rock with plagioclase and olivine crystal sizes ranging from ~0.2 to ~3 mm in diameter. The relatively small size of our analyzed subsamples means that they each contain several dozen or fewer olivine and plagioclase crystals. The plagioclase contains oriented arrays and needles (with axial ratios sometimes exceeding >50) of metallic inclusions (*S40-42*). This would suggest that our subsamples could exhibit significant anisotropy of remanence. Such anisotropy would influence the remanence directions inferred from our PCA fits [i.e., (*S57*)] as well as the magnitude of our paleointensity analyses [i.e., (*S58*)].

To characterize the anisotropy of remanence, we applied an IRM in three orthogonal directions and then solved for the principal axes of the IRM anisotropy ellipsoid following (*S59, 60*). We conducted this experiment for at least four different IRM fields (10, 40, 105 and 205 mT) in order to determine how the anisotropy varies as a function of coercivity. Table S2 summarizes some of the data at fields relevant for the LC, MC, and HC components. We found that the degree of anisotropy, P (*S61*) decreases monotonically as coercivity increases for all samples, suggesting that

anisotropy of higher coercivity grains is lower than those of lower coercivity. The continually changing anisotropy as a function of coercivity could be responsible for some of the deviations from ideal linear demagnetization observed in Figs. 1, S1 and S2. The shape factor T (*S62*), was generally positive, indicating that the anisotropy ellipsoid is oblate.

The directions of the LC components with respect to the principal anisotropy axes are a direct manifestation of the high anisotropy carried by low coercivity grains described above. The LC component directions for all seven samples are either close to the easy axis direction or in the easy-intermediate plane as computed from a low field IRM. There is no such trend for the MC and HC components. Figure S7 shows the uncorrected LC directions and the first, second, and third principal axes of the anisotropy ellipsoids calculated with an IRM of 10 mT. Three LC components cluster very close to the sample's first axis, and the remaining four points lie within or near the easy-intermediate plane. This strong correlation of the IRM with anisotropy axes is consistent with other findings in meteorites and lunar rocks (*S63*). However, in this case the anisotropy is not due to shock related processes, but rather the rock's naturally coarse grain size.

8S.9.2. Anhysteretic remanent magnetization and isothermal remanent magnetization acquisition and demagnetization. Samples 76535,137,3 and 137,5 were given stepwise ARM in increasing DC bias fields from 0.5 to 2 mT in a peak AC field of 200 mT (Fig. 8S.8). These data can be used to infer the degree of magnetostatic interactions in the sample (*S53*). Following ARM acquisition, the ARM was then stepwise AF demagnetized, and the median destructive field was found to be 13.5 and 11.0 mT for 137,3 and 137,5, respectively. The samples were then given an IRM with a DC field of 200 mT that was also subsequently stepwise AF demagnetized (Fig. 8S.9), and the median destructive field was found to be 13.5 and 11.2 mT, for 137,3, and 137,5, respectively. The IRM acquisition and AF demagnetization of IRM data are indicators of the coercivity spectrum of the sample. Comparison of the AF demagnetization of ARM and IRM constitutes the Lowrie-Fuller test (Fig. 8S.10), an indicator of grain size and stress state (*S64, 65*). The data indicate that the rock exhibits H-type (IRM more stable

than ARM) behavior, consistent with kamacite and ferromagnetic taenite in the pseudo single domain to multidomain size range (see also Section 9.3).

High ARM susceptibility (Fig. 8S.7) and Cisowski *R* values (*S53*) ranging from 0.42-0.44 (Fig. 8S.9) indicate that 76535 contains relatively weakly interacting grains or some multidomain grains. IRM acquisition and demagnetization data (Fig. 8S.8) and coercivity of remanence values (18.5, 16.0, and 36.0 mT for 137,3, 137,5, and 137,1, respectively) are consistent with the presence of kamacite and taenite [and not the high coercivity mineral tetrataenite (*S66, 67*)] as the main ferromagnetic phases in 76535.

8S.9.3. Hysteresis loops. Room temperature hysteresis data for 76535,137,1 and 76535,137,3 were obtained with a Digital Measurement Systems vibrating sample magnetometer in C. Ross's laboratory in the MIT Department of Materials Science and Engineering. The high-field slope of each hysteresis loop was used to estimate the contribution of paramagnetic and diamagnetic minerals. Their contribution has been subtracted from the loops shown in Fig. 8S.11. We found that the subsample containing significant amounts of both olivine and plagioclase (137,1) is predominantly multidomain (Fig. 8S.11A), with a ratio of saturation remanence to saturation magnetization M_{rs}/M_s = 0.016 and a ratio of coercivity of remanence to coercivity of H_{cr}/H_c = 9 [see (*S68*), with the caveat that the results of this study are formally only applicable to magnetite]. On the other hand, the very plagioclase-rich sample (137,3) is apparently pseudo-single domain, with M_{rs}/M_s = 0.027 and H_{cr}/H_c = 3 (Fig. 8S.11B). The latter is the first lunar plutonic rock sample observed to have such fine-grained remanence carriers and is in fact one of the most single-domain like lunar samples known [see (*S51*)]. This may be because the metal in this sample is likely mostly in the form of exsolved needle-shaped inclusions in the plagioclase, whereas the metal in 137,1 may be in larger interstitial grains. The observed saturation field near 1 T and the M_{rs}/M_s and H_{cr}/H_c values indicate that kamacite and taenite rather than tetrataenite (*S66, 67*) are the major ferromagnetic phases in 76535. This is also consistent with the thermal history of the rock (Fig. 2), during which any tetrataenite formed during slow cooling in the lunar crust should have been destroyed upon heating to ~500°C and cooling over 10 ka in an ejecta blanket [i.e., (*S67, 69-74*)].

8S.10. $^{40}Ar/^{39}Ar$ thermochronology

Three different groups have dated 76535 using K/Ar and $^{40}Ar/^{39}Ar$ geochronology and have obtained plateau and integrated ages ranging from 4.2-4.3 Ga (*S75-77*). The most thoroughly documented of these studies is that of Husain and Schaeffer (*S77*). We used their data to conduct $^{40}Ar/^{39}Ar$ thermochronology calculations in order to constrain the temperature history of the 76535. Using their plagioclase ^{39}Ar release data assuming that their heating steps lasted ~ 1 h (*S78, 79*), we calculated the temperature-dependence of the ^{39}Ar diffusion coefficients $D(T)$ through 76535 assuming a spherical diffusion domain geometry (Fig. 3A). We then conducted thermochronological modeling following our previous analyses of Martian meteorites (*S80-82*). We assumed that the colinearity observed for the first 6 heating steps (1000-1350°C) of the released ^{39}Ar indicates that the diffusion of Ar in 76535 plagioclase is thermally activated over this range. Assuming the diffusivity is described by an Arrhenius relationship, a least squares regression to these data gave an activation energy E_a = 236.9 ± 27.6 kJ mol^{-1} and $\ln(D_0/a^2)$ = 4.43 ± 0.95 $\ln(s^{-1})$ for diffusivity at infinite temperature D_0 and diffusive length scale a. This diffusivity is at the retentive end of that typically observed for plagioclase (*S83, 84*).

Consistent with the lack of deformational textures in this rock, we assume that this Arrhenius relationship and corresponding diffusive length scale, a, have held for 76535 since the deep crustal metamorphic event. Using a numerical solution to the radiogenic production-diffusion equation described by (*S82, 85*) and using a radius of 2.5 cm for the parent rock (*S82, 86*), we simulated the expected radiogenic ^{40}Ar ($^{40}Ar^*$) distributions within the sample following various thermal perturbations at 3.9 Ga (the putative late heavy bombardment) and 220 Ma [the time of recent excavation of 76535 given by its cosmic ray exposure age (*S87*)]. We found that there is *no evidence for any ^{40}Ar loss since 4.2 Ga*. From this we derived a *conservative upper bound* on the time-temperature history for thermal events at 3.9 Ga and 220 Ma assuming no gas loss at any other time in the rock's history (Fig. 3C).

8S.11. Conductive cooling timescales

As described in the main text, establishing the conductive heating and cooling timescale for 765335 is critical for establishing the origin and duration of the field that magnetized it. We have already established that the rock could not have been shock heated (see main text). Quick heating and cooling (< 1 day) as a result of heating in an impact ejecta blanket might permit the rock to acquire a TRM from any associated impact-generated fields (which are thought to persist for as long as ~1 day for the largest, basin-forming impacts), while slower heating and cooling would mean that impact-generated fields would not be present long enough to block a TRM. To determine the typical conductive heating and cooling timescales for 76535, we modeled the rock as a sphere of radius R at initial temperature T_0 surrounded by an infinite medium with initial temperature T. The temperature at a radius r within the sphere can then be computed using equation (6) from Section 10.2 of (*S88*) [see also (*S82*)]. For these calculations, we assumed a thermal diffusivity of 10^{-6} m^2s^{-1}, a specific heat of 815 J kg^{-1} K^{-1}, and a density of 2800 kg m^{-3}. Fig. 8S.12 shows the heating time for a rock with T_0 = –20°C, the approximate lunar near-surface temperature at depths not subject to diurnal fluctuations (*S89*), to reach a temperature of T = 770°C, the Curie temperature of pure iron, at a radius of $r = R/2$, for several values of R. During this time, the rock could not acquire magnetization, yet any impact-generated fields would be decaying. An extreme minimum heating timescale for 76535 can be computed using only the size of the rock recovered by the Apollo astronauts (R = 2.5 cm). For this radius, we find that the rock will heat up to the ambient temperatures of an ejecta blanket in ~1000 s, long compared to the expected lifetimes of impact-generated and -amplified fields. Fig. 8S.12 also shows the time required for conductive cooling of a rock, which is representative of the cooling timescale for an ejecta blanket. The total time required for the rock to acquire TRM is the sum of both the heating and cooling times. Even very small ejecta blankets of ~1 m diameter would remain hot for ~1 day.

Supplemental Material References

S1. J. L. Kirschvink, R. E. Kopp, T. D. Raub, C. T. Baumgartner, J. W. Holt, *Geochem. Geophys. Geosys.* **9**, Q05Y01 (2008).
S2. A. Stephenson, *J. Geophys. Res.* **98**, 373 (1993).
S3. K. P. Lawrence, C. L. Johnson, L. Tauxe, J. Gee, *Phys. Earth Planet. Inter.*, doi:10.1016/j.pepi.2008.05.007 (2008).
S4. C. Snape, *Geophys. J. R. Astr. Soc.* **23**, 361 (1971).
S5. E. A. Hailwood, L. Molyneux, *Geophys. J. R. Astr. Soc.* **39**, 421 (1974).
S6. D. W. Collinson, *Methods in Rock Magnetism and Paleomagnetism.* (Chapman and Hall, New York, N.Y., 1983), pp. 503.
S7. S. J. Morden, *Phys. Earth. Planet. Inter.* **71**, 189 (1992).
S8. G. Acton *et al.*, *J. Geophys. Res.* **112**, doi:10.1029/2006JB004655 (2007).
S9. A. Stephenson, *J. Geophys. Res.* **98**, 373 (1993).
S10. S. Hu, E. Appel, V. Hoffmann, W. W. Schmahl, S. Wang, *Geophys. J. Int.* **134**, 831 (1998).
S11. J. L. Kirschvink, *Geophys. J. R. Astr. Soc.* **62**, 699 (1980).
S12. L. Tauxe, H. Staudigel, *Geochem. Geophys. Geosyst.* **5**, doi:10.1029/2003GC000635 (2004).
S13. D. W. Collinson, *Earth Moon Planet.* **33**, 31 (1985).
S14. B. P. Weiss *et al.*, *Science*, in press (2008).
S15. E. Thellier, O. Thellier, *Ann. Geophys.* **15**, 285 (1959).
S16. D. J. Dunlop, O. Ozdemir, *Rock Magnetism: Fundamentals and Frontiers.* (Cambridge University Press, 2001).
S17. M. Westphal, *Phys. Earth Planet. Inter.* **43**, 300 (1986).
S18. J. R. Dunn, M. Fuller, D. Clauter, *Proc. Lunar Planet. Sci. Conf. 12th*, 1747 (1981).
S19. J. Gattacceca, P. Rochette, *Earth Planet. Sci. Lett.* **227**, 377 (2004).
S20. K. A. Hoffman, J. R. Baker, S. K. Banerjee, *Phys. Earth Planet. Inter.* **20**, 317 (1979).
S21. Y. Yu, *Earth Planet. Sci. Lett.* **250**, 27 (2006).
S22. B. P. Weiss, E. A. Lima, L. E. Fong, F. J. Baudenbacher, *Earth Planet. Sci. Lett.* **264**, 61 (2007).
S23. G. Kletetschka *et al.*, *Phys. Earth Planet. Inter.* **154**, 290 (2006).
S24. G. Kletetschka, M. H. Acuna, T. Kohout, P. J. Wasilewski, J. E. P. Connerney, *Earth Planet. Sci. Lett.* **226**, 521 (Oct 15, 2004).
S25. Y. Yu, L. Tauxe, J. S. Gee, *Phys. Earth Planet. Inter.* **162**, 244 (2007).
S26. A. Stephenson, D. W. Collinson, *Earth Planet Sci. Lett.* **23**, 220 (1974).
S27. A. Stephenson, S. K. Runcorn, D. W. Collinson, *Proc. Lunar Sci. Conf. 8th*, 679 (1977).
S28. N. Sugiura, D. W. Strangway, *Proc. Lunar Planet. Sci. Conf. 11th*, 1801 (1980).
S29. S. J. Morden, *Phys. Earth Planet. Inter.* **71**, 189 (1992).
S30. M. E. Bailey, D. J. Dunlop, *Phys. Earth Planet. Inter.* **13**, 360 (1977).
S31. S. Levi, R. T. Merrill, *Earth Planet. Sci. Lett.* **32**, 171 (1976).
S32. A. Stephenson, D. W. Collinson, S. K. Runcorn, *Proc. Lunar Sci. Conf. 7th*, 3373 (1976).
S33. T. Nagata, *Proc. Lunar Planet. Sci. Conf. 10th*, 2199 (1979).

S34. R. Egli, W. Lowrie, *J. Geophys. Res.* **107**, doi:10.1029/2001JB000671 (2002).
S35. D. J. Dunlop, K. S. Argyle, *J. Geophys. Res.* **102**, 20199 (1997).
S36. D. J. Dunlop, M. E. Bailey, M. F. Westcott-Lewiss, *Proc. Lunar Sci. Conf. 6th*, 3063 (1975).
S37. S. Levi, R. T. Merrill, *Earth Planet Sci. Lett.* **32**, 171 (1976).
S38. A. Stephenson, D. W. Collinson, S. K. Runcorn, *Proc. Tenth Lunar Planet. Sci. Conf.*, 2859 (1974).
S39. T. Kohout, G. Kletetschka, F. Donadini, M. Fuller, E. Herrero-Bervera, *Stud. Geophys. Geod.* **52**, 225 (2008).
S40. R. Gooley, R. Brett, J. R. Smyth, J. Warner, *Geochim. Cosmochim. Acta* **38**, 1329 (1974).
S41. G. L. Nord, *Proc. Lunar Sci. Conf. 7th*, 1875 (1976).
S42. R. F. Dymek, A. L. Albee, A. A. Chodos, *Proc. Lunar Sci. Conf. 6th*, 301 (1975).
S43. M. A. Wieczorek *et al.*, *Reviews in Mineralogy and Geochemistry* **60**, 221 (2006).
S44. J.-P. Vallée, *New Astron. Rev.* **47**, 85 (2003).
S45. S. A. Balbus, *Annu. Rev. Astron. Astrophys.* **41**, 555 (2003).
S46. S. S. Russell *et al.*, in *Meteorites and the Early Solar System II,* D. S. Lauretta, H. Y. McSween, Eds. (University of Arizona, Tucson, 2006), pp. 233-251.
S47. C. D. Murray, S. F. Dermott, *Solar system dynamics.* (Cambridge University Press, Cambridge, 2000), pp. 606.
S48. F. Mignard, *Moon and Planets* **23**, 185 (1980).
S49. S. J. Peale, P. Cassen, *Icarus* **36**, 245 (1978).
S50. G. W. Pearce, D. W. Strangway, *Apollo 16: Preliminary Science Report. NASA SP-315, Ch. 7-55*, (1972).
S51. M. Fuller, S. M. Cisowski, *Geomagnetism* **2**, 307 (1987).
S52. F. Rimbert, *Ph.D. Thesis, University of Paris*, (1958).
S53. S. M. Cisowski, *Phys. Earth Planet. Inter.* **26**, 56 (1981).
S54. D. J. Dunlop, *Rev. Geophys. Space Phys.* **11**, 855 (1973).
S55. W. A. Gose, G. W. Pearce, D. W. Strangway, E. E. Larson, *Moon* **5**, 106 (1972).
S56. Y. Yu, L. Tauxe, *Phys. Earth Planet. Inter.* **159**, 32 (2006).
S57. H. Hyodo, D. J. Dunlop, *J. Geophys. Res.* **98**, 7997 (1993).
S58. P. A. Selkin, J. S. Gee, L. Tauxe, W. P. Meurer, A. J. Newell, *Earth Planet. Sci. Lett.* **183**, 403 (2000).
S59. A. Stephenson, S. Sadikun, D. Potter, K., *Geophys. J. R. Astr. Soc.* **84**, 185 (1986).
S60. J. F. Nye, *Physical Properties of Crystals: Their Representation by Tensors and Matrices.* (Oxford University Press, Oxford, 1985).
S61. T. Nagata, *Rock Magnetism.* (Maruzen Company, Tokyo, 1961), pp. 350.
S62. V. Jelinek, *Tectonophys.* **79**, 63 (1981).
S63. J. Gattacceca, P. Rochette, M. Bourot-Denise, *Phys. Earth Planet. Inter.* **140**, 343 (2003).
S64. W. Lowrie, M. Fuller, *J. Geophys. Res.* **76**, 6339 (1971).
S65. S. Xu, D. J. Dunlop, *J. Geophys. Res.* **100**, 22533 (1995).
S66. T. Nagata, *Proc Lunar Planet. Sci. Conf. 13*, A779 (1983).
S67. P. Wasilewski, *Phys. Earth Planet. Inter.* **52**, 150 (1988).
S68. D. J. Dunlop, *J. Geophys. Res.* **107**, doi:10.1029/2001JB000486 (2002).

S69. L. Larsen, H. Roy-Paulsen, N. O. Roy-Paulsen, L. Vistisen, *Phys. Rev. Lett.* **48**, 1054 (1982).
S70. J. F. Petersen, M. Aydin, J. M. Knudsen, *Phys. Lett.* **62A**, 192 (1977).
S71. J. F. Albertsen, M. Aydin, J. M. Knudsen, *Phys. Scripta* **17**, 467 (1978).
S72. R. Gooley, R. B. Merrill, J. R. Smyth, *Meteoritics* **10**, 410 (1975).
S73. S. J. Morden, D. W. Collinson, *Earth Planet. Sci. Lett.* **109**, 185 (Mar, 1992).
S74. T. Nagata, *Proc. Lunar Planet. Sci. Conf. 13th*, A779 (1983).
S75. D. D. Bogard, L. E. Nyquist, B. M. Bansal, H. Wiesmann, C.-Y. Shih, *Earth Planet. Sci. Lett.* **26**, 69 (1975).
S76. J. C. Huneke, G. J. Wasserburg, *Lunar Sci. VI*, 417 (1975).
S77. L. Husain, O. A. Schaeffer, *Geophys. Res. Lett.* **2**, 29 (1975).
S78. L. Husain, *Science* **175**, 428 (1972).
S79. L. Husain, *J. Geophys. Res.* **79**, 19 (1974).
S80. H. Fechtig, S. T. Kalbitzer, in *Potassium Argon Dating,* O. A. Schaeffer, J. Zahringer, Eds. (Springer-Verlag, New York, 1966), pp. 68-107.
S81. D. L. Shuster, B. P. Weiss, *Science* **309**, 594 (2005).
S82. B. P. Weiss, D. L. Shuster, S. T. Stewart, *Earth Planet. Sci. Lett.* **201**, 465 (2002).
S83. W. A. Cassata, P. R. Renne, D. L. Shuster, *Goldschmidt Conf. Abs.*, A142 (2008).
S84. I. McDougall, M. T. Harrison, *Geochronology and thermochronology by the $^{40}Ar/^{39}Ar$ method.* (Oxford University Press, 1999), pp. 269.
S85. D. L. Shuster, K. A. Farley, *Earth Planet. Sci. Lett.* **217**, 1 (2004).
S86. O. Eugster, H. Busemann, S. Lorenzetti, D. Terrebilini, *Meteorit. Planet. Sci.* **37**, 1345 (2002).
S87. G. W. Lugmair, K. Marti, J. P. Kurtz, N. B. Scheinin, *Proc. Lunar Sci. Conf. 7th*, 2009 (1976).
S88. H. S. Carslaw, J. C. Jaeger, *The conduction of heat in solids.* (Oxford University Press, London, 1959).
S89. G. H. Heiken, D. T. Vaniman, B. M. French, *Lunar Sourcebook: A User's Guide to the Moon.* (Cabridge University Press, London, 1991), pp. 756.

Table S1 - Summary of magnetization components from principal component analysis and corrected directions from anisotropy of remanence computed using IRM fields of 10, 40, and 105 mT for LC, MC, and HC, respectively, except where indicated. MAD = maximum angular deviation.

Sample, component	AF range (mT)	Fit type *	Dec., Inc. (°)	Dec., Inc. anisotropy-corrected (°)	Angular Change (°)†	MC-HC Distance (°)	MAD	Points
76535,137,1								
LC	7.6-10.5	L	104.9, 34.2	100.5, 28.4	6.9	-	9.6	6
MC	35.9-82.9	L	176.6, 54.5	156.8, 48.9	13.4	-	25.7	18
HC	82.9-origin‡	AL	40.7, -62.5	40.3, -67.5	5.0	143.9	-	2
76535,137,7								
LC	8.9-11.3	L	359.5, 73.2	Neg.§	0	-	3.2	7
MC	27.6-72.5	L	206.9, 71.3	Neg. §	0	-	8.5	10
HC	72.5-252.5	AL	47.2, -41.0	Neg. §	0	148.0	6.5	12
76535,137,8								
LC	6.8-11.8	L	226.0, -44.5	229.3, -47.9	4.1	-	2.8	11
MC	19.8-34.5	L	152.6, 57.4	159.4, 55.3	4.3	-	20.9	5
HC	44.5-205.0	AL	22.9, -41.4	23.7, -42.6	1.3	148.9	14.1	22
76535,138,2								
LC	6.8-11.8	L	335.5, -57.1	8.0, -34.0	31.9	-	0.9	11
MC	25.0-59.0	L	178.8, 69.4	198.6, 56.5	15.6||	-	19.4	17
HC	59.0-172.5	AL	59.5, -36.8	46.8, -24.0	16.8||	141.6||	11.8	28

* Fit type: L = line. AL = line anchored to the origin.
† Difference between directions before and after anisotropy correction.
‡ Only one measurement point used in fit. See text for details.
§ Negligible change (less than 2°).
|| Remanence corrected with ARM(100 μT) at peak AC fields of 57 and 120 mT for MC and HC, respectively. Remanence corrected with IRM(57 mT) and IRM(120 mT) gives similar angular changes (8.9° and 12.7°) in the same directions, with an MC-HC angular distance of 134.4°.

Table S2: Paleointensity estimates for medium coercivity (MC) and high coercivity (HC) components in 76535. See Section 6 for details.

Sample, Experiment	MC slope	Paleointensity (μT)	HC slope	Paleointensity (μT)*
76535,137,7				
ARM 50 μT	0.68 ± 0.23	0.50 ± 0.2 to 25 ± 8	-	-
ARM 100 μT	0.38 ± 0.09	0.56 ± 0.1 to 28 ± 7	0.53 ± 0.18	0.8 ± 0.2 to 40 ± 10
ARM 200 μT	0.22 ± 0.04	0.64 ± 0.1 to 32 ± 7	0.42 ± 0.14	1.2 ± 0.4 to 62 ± 20
AF ARM† 200 μT	0.22 ± 0.07	0.66 ± 0.2 to 33 ± 10	-	-
AF IRM†	0.019 ± 0.004	1.2 ± 0.2 to 58 ± 10	0.058 ± 0.01	3.5 ± 0.6 to 170 ± 30
76535,138,2				
ARM 50 μT	0.36 ± 0.035	0.26 ± 0.02 to 13 ± 1	1.50 ± 0.30	1.2 ± 0.2 to 58 ± 10
ARM 100 μT	0.23 ± 0.04	0.34 ± 0.06 to 17 ± 3	1.50 ± 0.40	2.2 ± 0.6 to 110 ± 30
ARM 200 μT	0.11 ± 0.02	0.32 ± 0.04 to 16 ± 2	0.86 ± 0.08	2.6 ± 0.2 to 130 ± 10
AF ARM† 200 μT	0.12 ± 0.02	0.38 ± 0.06 to 19 ± 3	0.73 ± 0.08	2.2 ± 0.2 to 110 ± 10
AF IRM†	0.02 ± 0.003	1.3 ± 0.2 to 66 ± 8	0.13 ± 0.02	7.9 ± 1.0 to 390 ± 50

Note: ARM paleointensity in microteslas = (NRM/ARM)/f' × (bias field in microteslas), and IRM paleointensity in microteslas= NRM/IRM × a. The limits of the given paleointensity range were computed using two extreme values of f' = 1.34 and 1.34×50 and a = 3000 and 3000/50. Uncertainties on each limit are formal 95% confidence intervals on the slope fit using Student's t-test.

* These values may be lower limits given the possible contribution of phase transformation crystallization remanent magnetization to the HC component.
† GRM-corrected.

Table S3. Anisotropy of remanence data for 76535, at IRM fields of 10, 40, and 105 μT. *P* = degree of anisotropy. *T* = shape factor.

Sample	Mass (mg)	NRM (Am^2)	*P* (10 μT)	*T* (10 μT)	*P* (40 μT)	*T* (40 μT)	*P* (105 μT)	*T* (105 μT)
76535,137,1	68	7.20×10^{-10}	2.79	-0.32	1.89	-0.36	1.50	-0.32
76535,137,3	55	7.73×10^{-9}	5.00	0.15	4.14	0.04	3.00	-0.30
76535,137,7	109	2.32×10^{-9}	1.22	0.80	1.16	-0.49	1.10	0.33
76535,137,8	48	3.39×10^{-9}	1.56	-0.04	1.39	0.82	1.44	0.25
76535,138,2	38	1.41×10^{-9}	3.31	-0.08	2.27	0.31	1.65	0.43
76535,138,3	22	5.82×10^{-10}	2.61	0.41	1.93	0.24	1.18	-0.29

Supplemental Material Figures

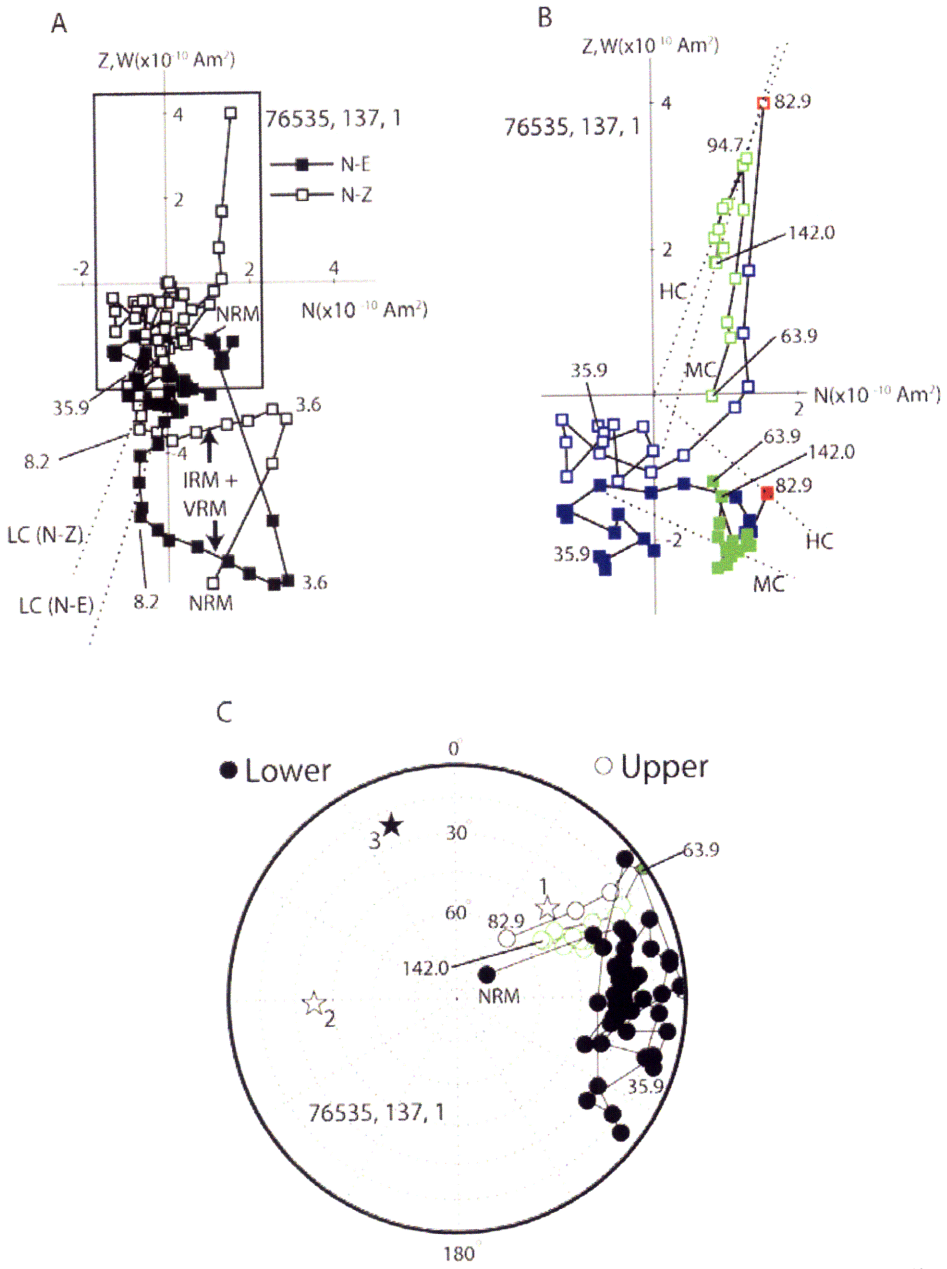

Fig. 8S.1. Natural remanent magnetization in 76535,137,1. (A, B) two-dimensional projection of the NRM vector during AF demagnetization. Closed (open) symbols represent end points of magnetization projected onto horizontal N-E (vertical N-Z) planes. Peak fields for selected AF steps are labeled in mT. Dashed lines are component directions determined from principal component analyses. (A) AF demagnetization up to 89.2 mT and the LC component. (B) Zoom of boxed region in part A, showing MC (blue) and HC (red) components, determined from a total of 80 AF measurements. The HC fit is anchored to the origin. Green points show data that are not GRM corrected and only AF demagnetized in one axis above 85.0 mT (not used in any fits). (C) Equal area projection of the remanence shown in part A.

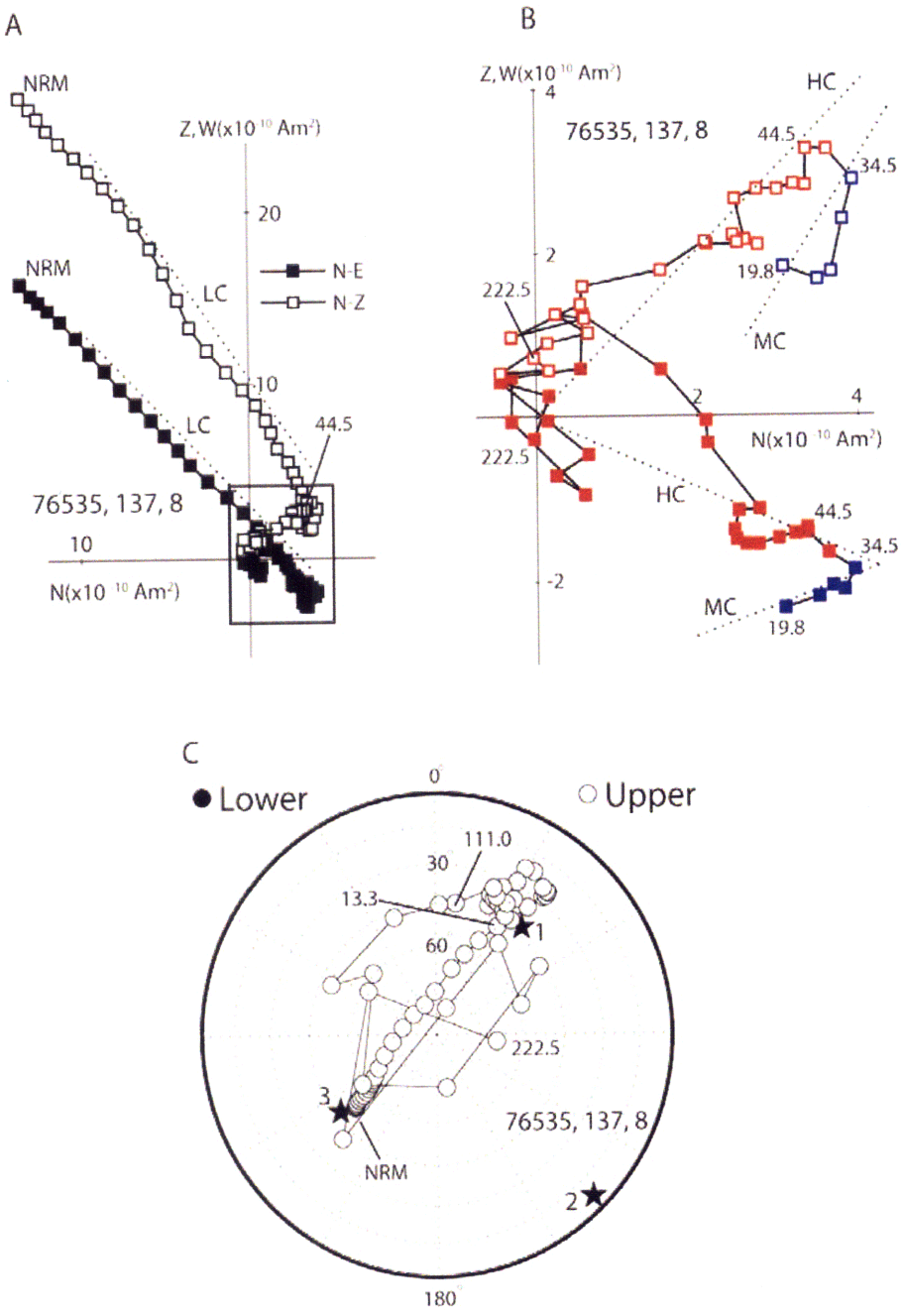

Fig. 8S.2. Natural remanent magnetization in 76535,137,8. (A, B) two-dimensional projection of the NRM vector during AF demagnetization. Closed (open) symbols represent end points of magnetization projected onto horizontal N-E (vertical N-Z) planes. Peak fields for selected AF steps are labeled in mT. Dashed lines are component directions determined from principal component analyses. (A) AF demagnetization up to 205.0 mT and the LC component. (B) Zoom of boxed region in part A, showing MC (blue) and HC (red) components, determined from a total of 1320 AF measurements. The HC fit is anchored to the origin. (C) Equal area projection of the remanence shown in part A.

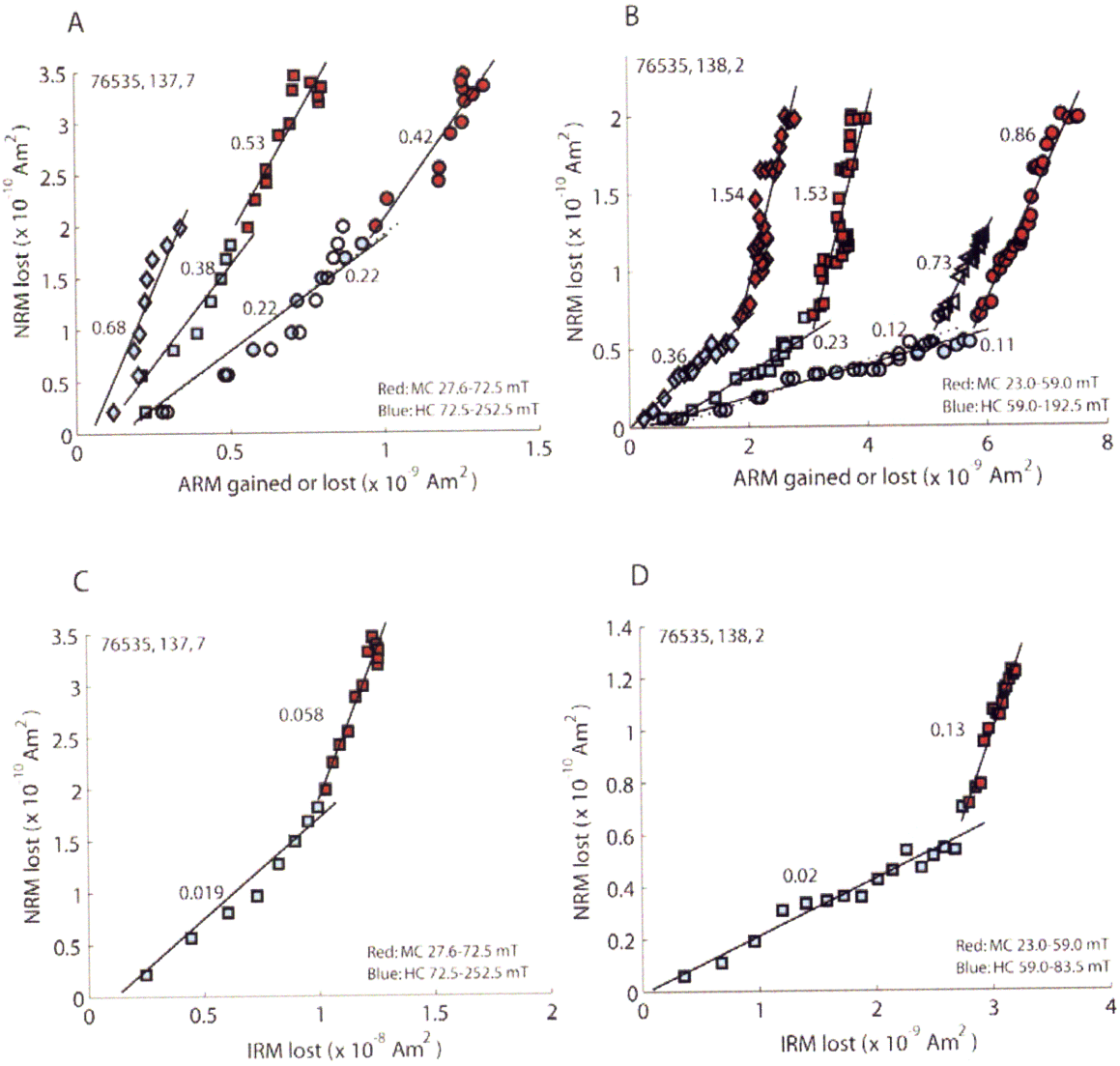

Fig. 8S.3. Paleointensity estimates for 76535. Slopes derived from linear regressions are shown next to each experiment. Blue and red points correspond to the MC and HC fits and AF steps identified in Table S1. (A, B) ARM method paleointensity estimates for 76535,137,7 and 76535,138,2. Open, uncolored points are GRM-corrected AF of ARM measurements for the MC and HC components of 76535,138,2, and the MC component of 76535,137,7, performed for AF steps below 85.0 mT. (C, D) IRM method paleointensity estimates for 76535,137,7 and 76535,138,2. AF of IRM experiment data are GRM corrected.

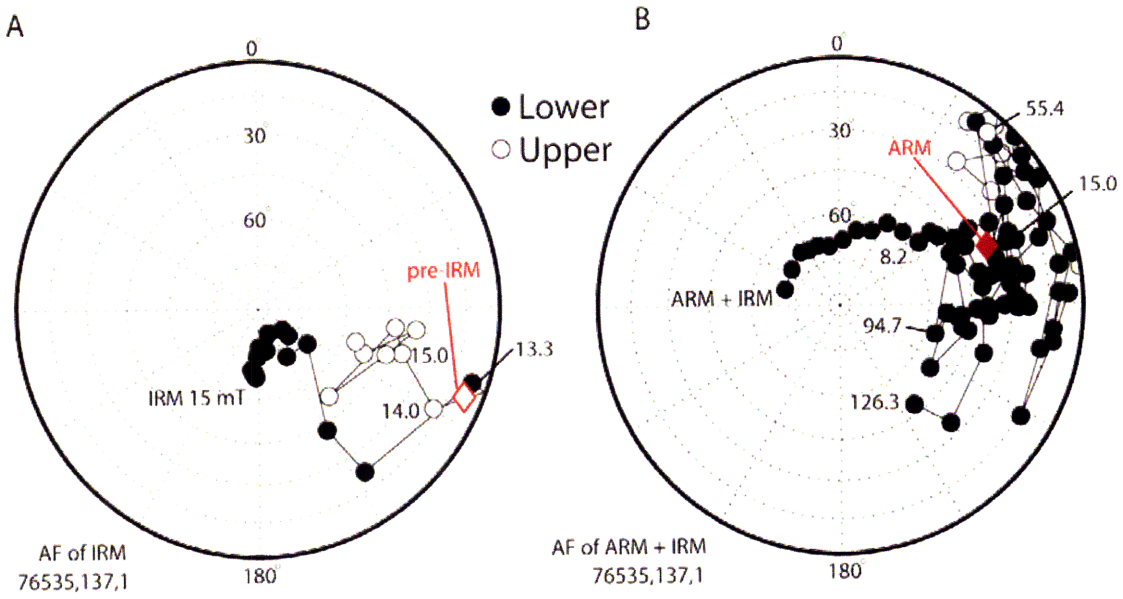

Fig. 8S.4. AF demagnetization of IRM and ARM in 76535,137,1. (A) AF demagnetization of a laboratory 15 mT IRM after demagnetization of NRM, applied 90.5° away from the pre-IRM direction. (B) AF demagnetization of a laboratory ARM (0.05 mT bias field in a peak AF field of 290 mT), plus a subsequent laboratory 15 mT IRM, both applied after demagnetization of NRM.

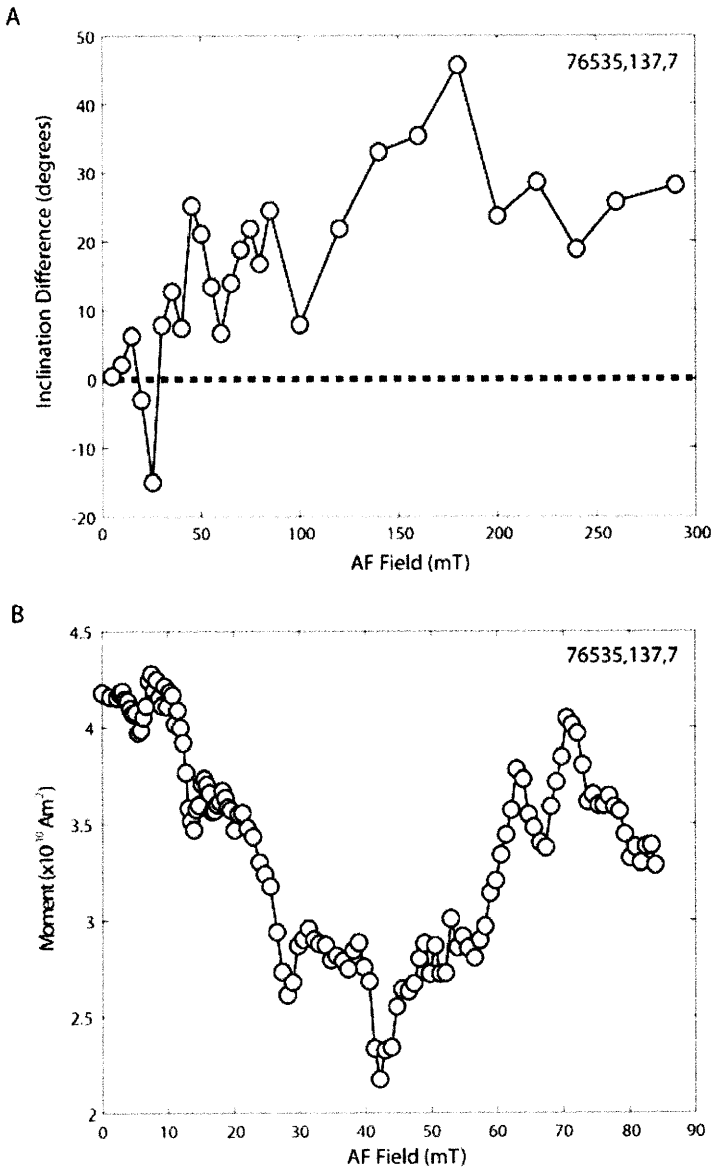

Fig. 8S.5. Evidence for gyroremanent magnetization (GRM) acquisition by 76535,137,7. (A) Difference between the average inclination of moment following uniaxial AF demagnetization in the *x*- and *y*-directions and that in the *z*-direction, as observed during NRM demagnetization. Above ~40 mT, the moment after demagnetization in the *z*-direction is increasingly shallower than after demagnetization in the horizontal directions (difference > 0 as shown by dashed line). This is consistent with GRM, which is acquired perpendicular to the AF axis. (B) Alternating field demagnetization experiment following (*S10*). Prior to the first AF step, sample NRM had been demagnetized up to 290 mT during which it acquired a GRM. This GRM is steadily demagnetized up to at least 40 mT. Beyond 40 mT, a new GRM is steadily acquired.

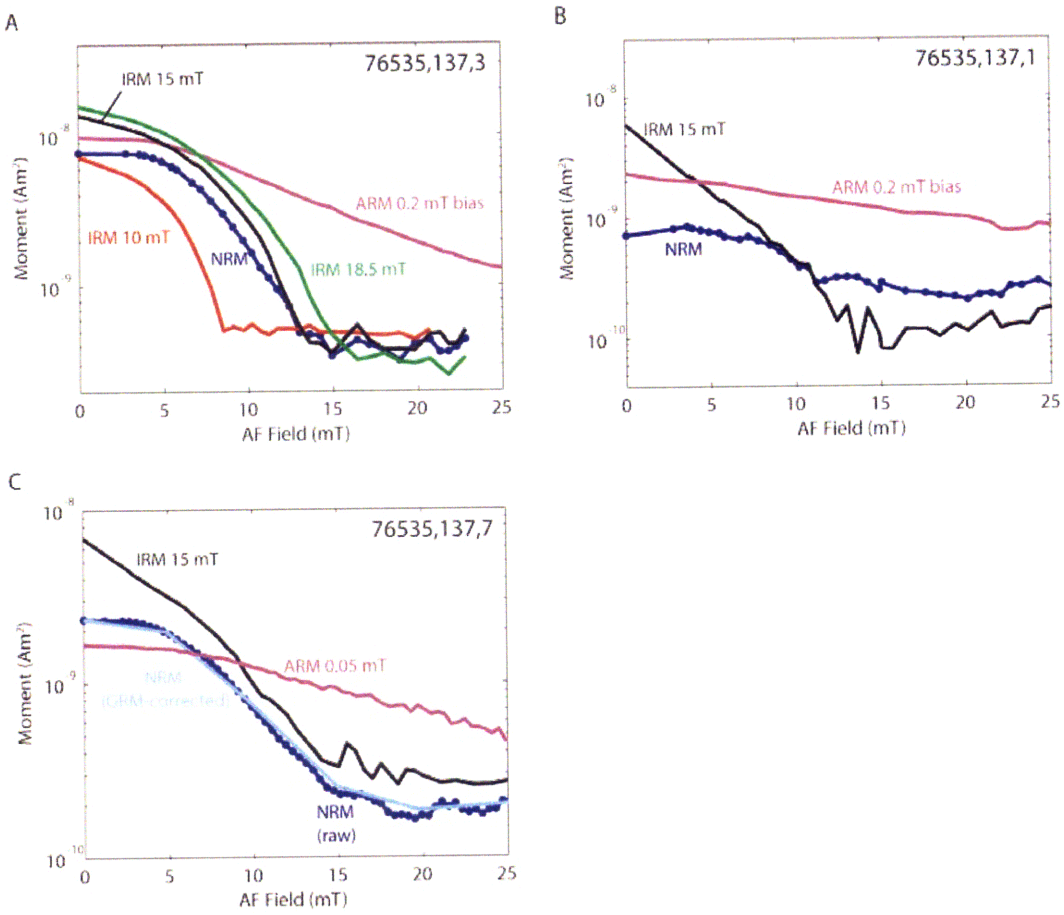

Fig. 8S.6. Remanence magnitude of 76535 during AF demagnetization. Shown is the moment as a function of peak AF field for natural remanent magnetization (NRM) (blue curves), isothermal remanent magnetization (IRM) (red and green curves), and anhysteretic remanent magnetization (purple). IRM field and ARM DC bias fields in mT are labeled. The peak ARM fields for all curves were 250 mT. (A) Subsample 76535,137,3. (B) Subsample 76535,137,3. (C) Subsample 76535,137,7.

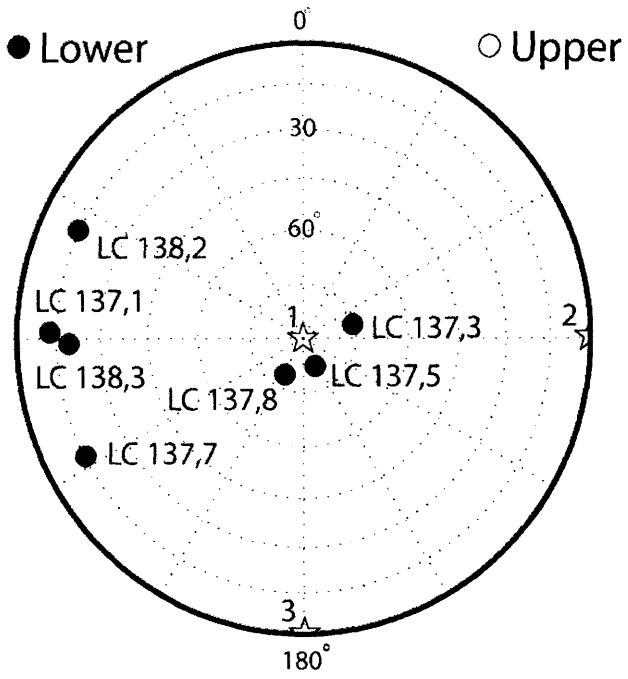

Fig. 8S.7. Stars represent the first, second, and third anisotropy ellipsoid axes for all subsamples, determined by IRM 10 mT. Circles are the LC components for each subsample (generally fit between AF steps 6-12 mT, see Table S1) in the same coordinate system as the anisotropy ellipsoid.

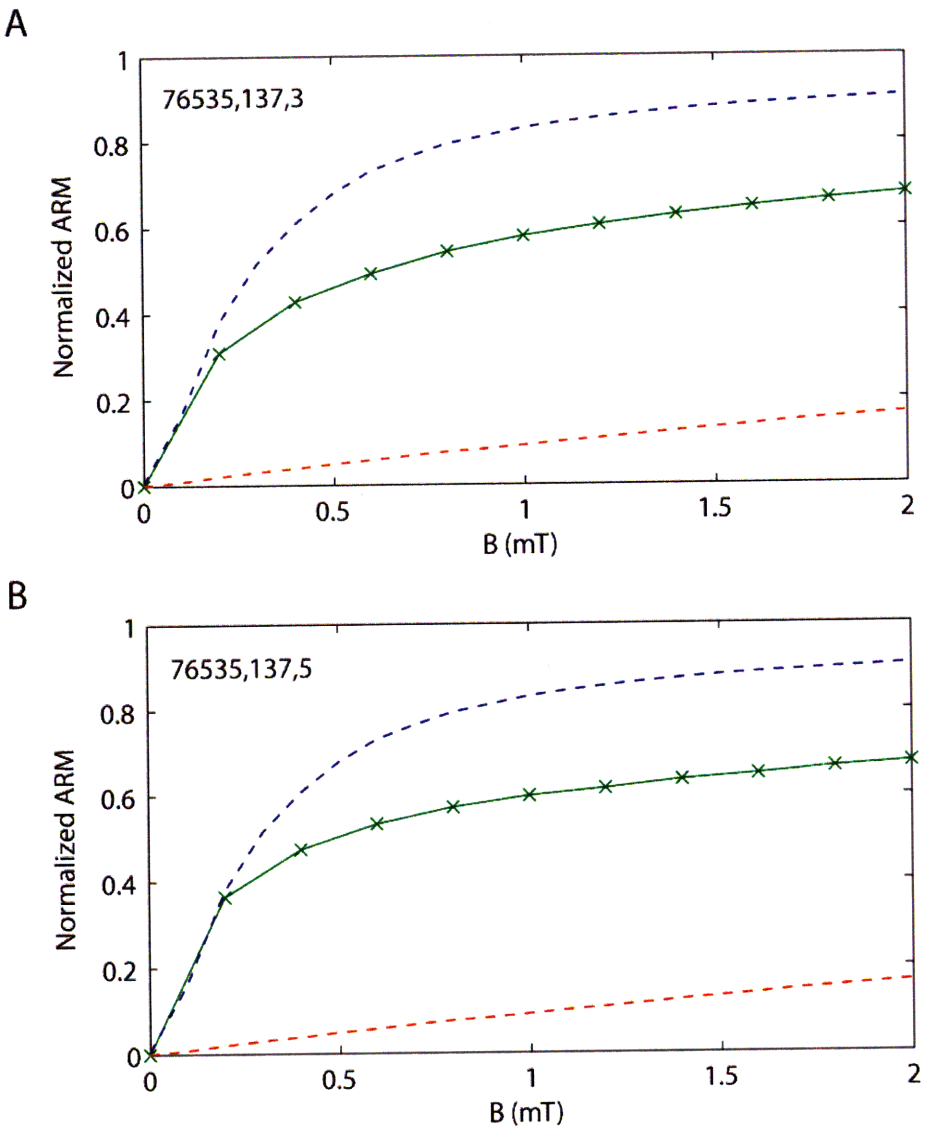

Fig. 8S.8. Anhysteretic remanent magnetization (ARM) acquisition experiments on selected subsamples of 76535. Shown is the ARM acquired in a 200 mT AC field as a function of DC bias field. Lower dotted curve is that of highly interacting chiton tooth magnetite and upper dotted curve is noninteracting magnetite in magnetotactic bacteria. (A) 76535,137,3. (B) 76535,137,5.

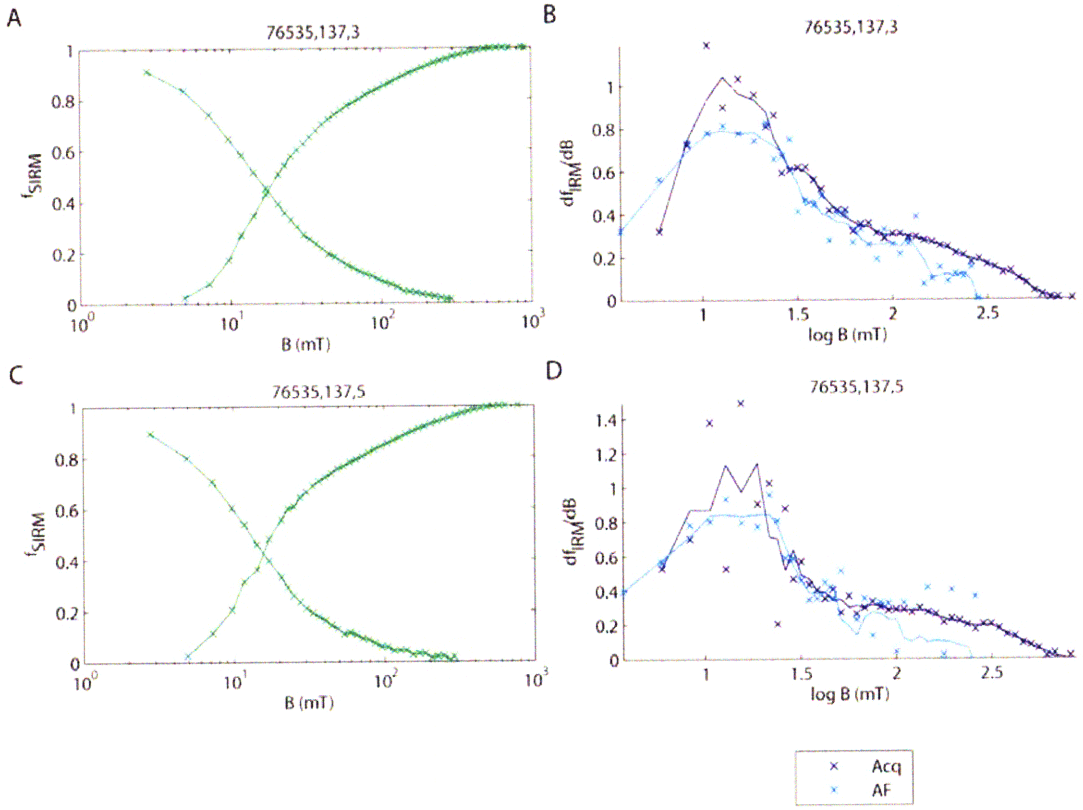

Fig. 8S.9. Isothermal remanent magnetization (IRM) acquisition and demagnetization experiments on selected subsamples of 76535. fIRM = fraction of IRM remaining/lost. (A) IRM acquisition and alternating field (AF) demagnetization of IRM by 76535,137,3. Both curves are normalized to the highest-field IRM value. (B) Derivative of IRM acquisition (purple crosses) and AF demagnetization of IRM (light blue crosses), with running average given by solid lines. (C) IRM acquisition and AF of IRM for 76535,137,5. (D) Derivatives of IRM acquisition and AF of IRM for 76535,137,5.

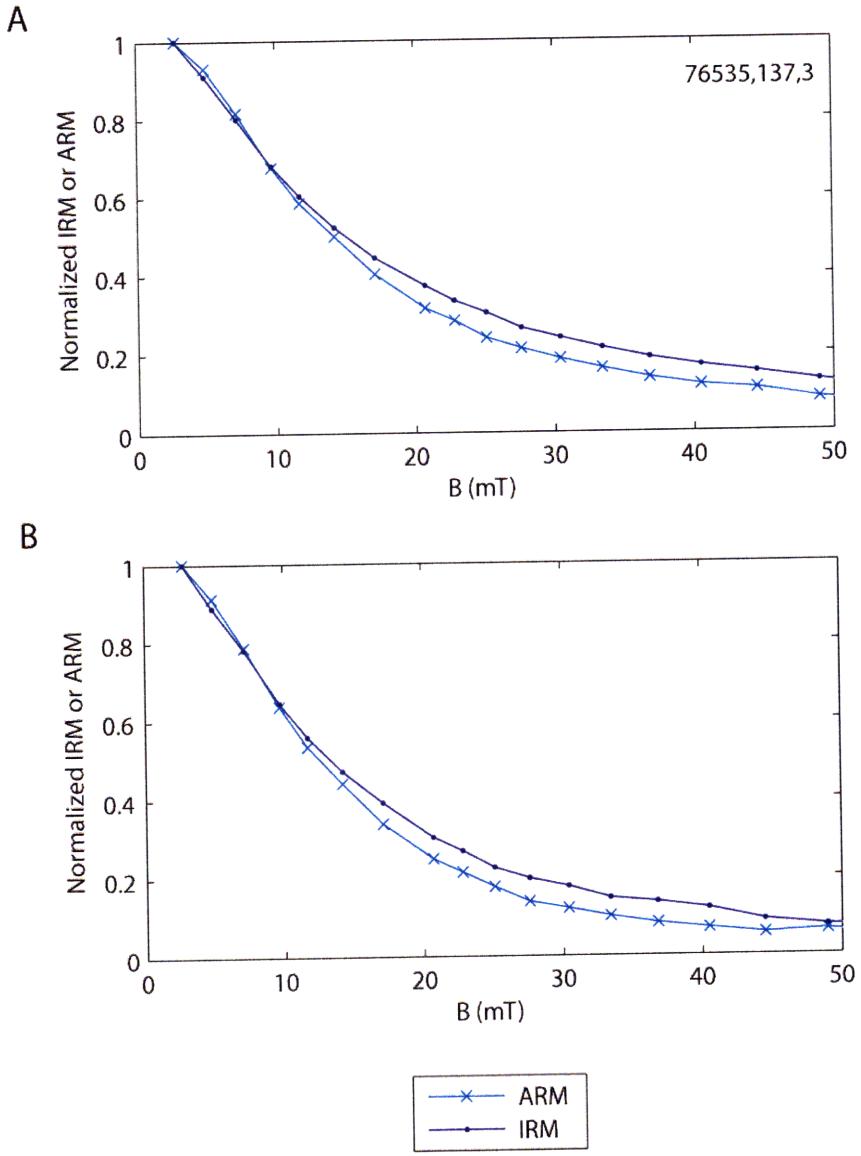

Fig. 8S.10. Lowrie-Fuller tests for selected subsamples of 76535. Shown is alternating field demagnetization of an anhysteretic remanent magnetization (ARM) acquired in a 200 mT peak AC field with 0.2 mT DC bias field (light blue symbols) and of an isothermal remanent magnetization (IRM) acquired in a 200 mT field. Both curves are normalized to the starting value just prior to AF demagnetization. (A) 76535,137,3. (B) 76535,137,5.

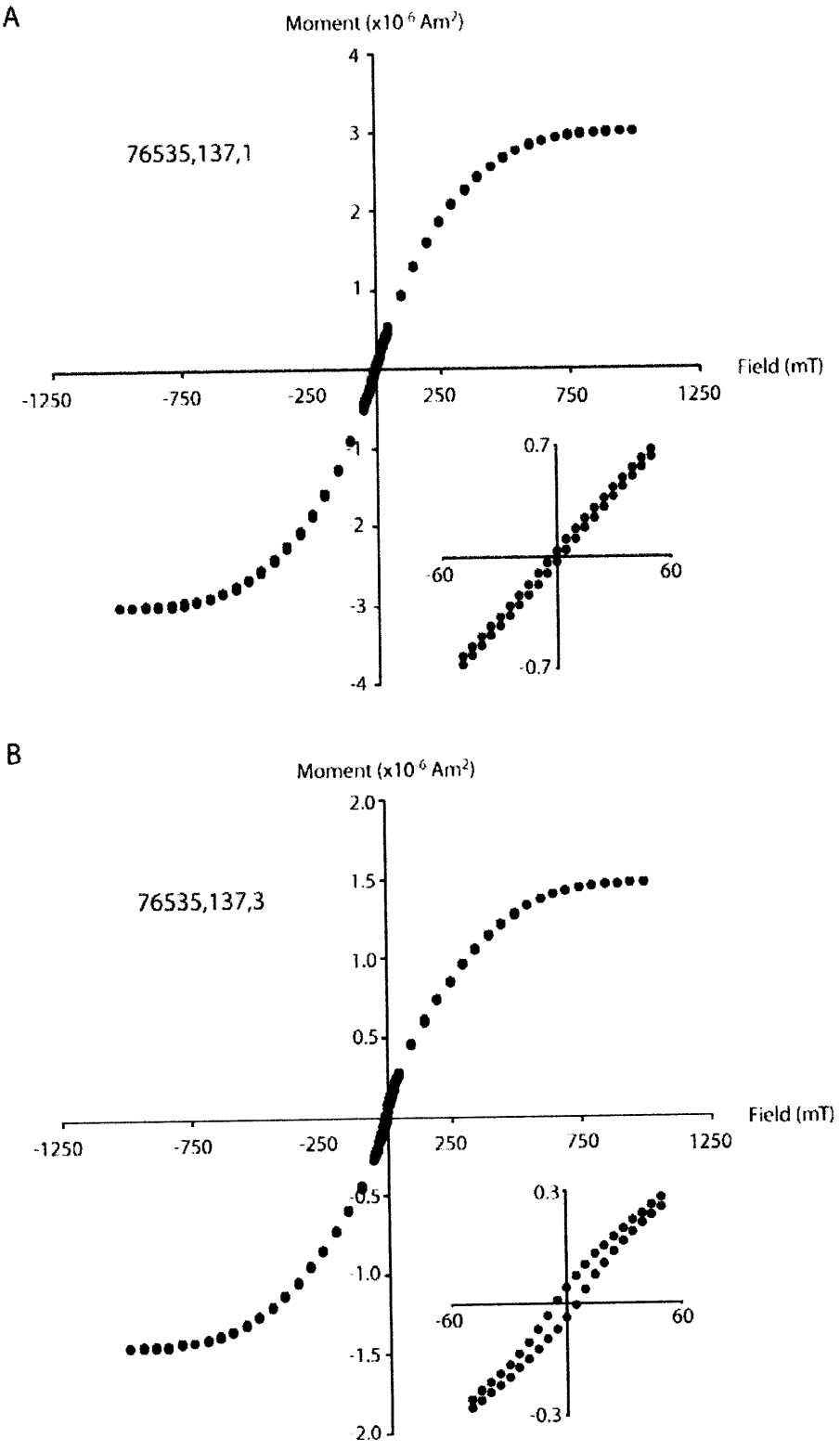

Fig. 8S.11. Room temperature hysteresis loops for 76535. Shown is the sample moment as a function of applied field. Inset shows data near origin (between -60 and 60 mT). (A) 76535,137,1. (B) 76535,137,3.

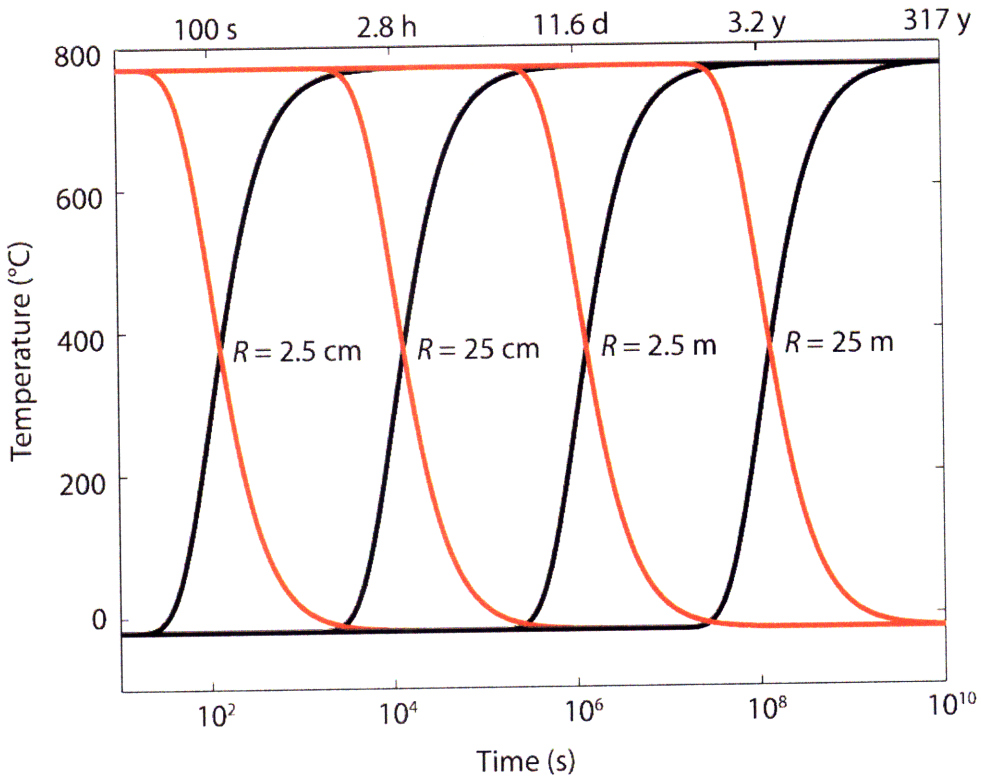

Fig. 8S.12. Diffusive heating and cooling calculations for masses of lunar rock. (A) Black curves give the temperature of a spherical rock of radius R at a radius $r = R/2$, with initial temperature T_o = –20°C, surrounded by a medium of T_o = 770°C. Curves are calculated for four values of R (2.5 cm, 25 cm, 2.5 m, and 25 m). (B) Red curves give the temperature of a spherical rock (or ejecta blanket) of radius R at a radius $r = R/2$, with initial temperature T_o = 770°C surrounded by a medium of T = -20°C. Curves are calculated for four values of R (2.5 cm, 25 cm, 2.5 m, and 25 m).